

## Getting the electrons right for O2-on-metal systems Bree, R.A.B. van

### Citation

Bree, R. A. B. van. (2025, October 21). *Getting the electrons right for O2-on-metal systems*. Retrieved from https://hdl.handle.net/1887/4279459

Version: Publisher's Version

Licence agreement concerning inclusion of doctoral

License: thesis in the Institutional Repository of the University of

<u>Leiden</u>

Downloaded from: <a href="https://hdl.handle.net/1887/4279459">https://hdl.handle.net/1887/4279459</a>

**Note:** To cite this publication please use the final published version (if applicable).

# Getting the electrons right for O<sub>2</sub>-on-metal systems

### **Proefschrift**

ter verkrijging van
de graad van doctor aan de Universiteit Leiden,
op gezag van rector magnificus prof. dr. ir. H. Bijl,
volgens besluit van het college voor promoties
te verdedigen op dinsdag 21 oktober 2025
klokke 16:00 uur

door

**Robert Anton Bernard van Bree** 

geboren te Haarlem in 1997

#### Promotores:

Prof. dr. G.J. Kroes

Dr. J. Meyer

### Promotiecommissie:

Prof. dr. M. Ubbink

Prof. dr. I.M.N. Groot

Prof. dr. S.A. Bonnet

Dr. H. J. Chadwick (Swansea University)

Dr. C. Diaz Blanco (Universidad Complutense de Madrid)

ISBN: 978-94-6473-871-1 Year of Publication: 2025

The research that is reported in this thesis has been performed in the Theoretical Chemistry group as part of the Leiden Institute of Chemistry (*Einsteinweg 55, 2333 CC Leiden, The Netherlands*) at Leiden University. This work was funded by the Leiden Institute of Chemistry and has been made possible with computer time granted by the NWO-EW 2021.12 supercomputer grant.

"My heart tells me that he has some part to play yet, for good or ill, before the end; and when that comes, the pity of Bilbo may rule the fate of many - yours not least."

J.R.R. Tolkien, The Shadow of the Past - Fellowship of the Ring, July 1954

"Don't worry about the future. Or worry, but know that worrying is as effective as trying to solve an algebra equation by chewing bubble gum. The real troubles in your life are apt to be things that never crossed your worried mind, the kind that blindside you at 4 pm on some idle Tuesday."

Mary Schmich, Chicago Tribune, June 1997.

### **Foreword**

Before the start of this thesis, it might be useful to quickly go over its scope, aims and goals. The main goal of this thesis is to convey the new scientific work of the last four and a half years regarding the "difficult" molecule-metal systems, or put more specifically: O<sub>2</sub>-on-metal systems. However, I would additionally like to use this thesis as an accessible way to cover some of the background of surface science and theoretical chemistry. I do this with the hope to make the new scientific content of Chapters 3-5 more accessible for those outside the field. Therefore, the first chapter is written in a way that I believe will be understandable for a broad audience, such that the general background of this thesis and the reasons for this work can be easily understood. Similarly, the second chapter has been somewhat extended beyond the scope commonly found in theses in this field. This is done to ensure that it forms a more complete picture of the methods and theories used in theoretical surface science. Either way, the first two chapters should form a solid context in which to place the other three scientific chapters. These three chapters are based on three scientific publications and will therefore be far more niche in their content and language. Now, with this out of the way, let's get started.

### Contents

F	Foreword 4					
1	Intro	duction	9			
	1.1	Heterogenous catalysis	9			
	1.2	Surface science	. 11			
	1.2.1	Study of the active component in heterogeneous catalysis	. 12			
	1.2.2	Surface structure	. 13			
	1.2.3	Surface interactions	. 13			
	1.2.4	Controlling reaction conditions	. 17			
	1.2.5	Surface science experiments	18			
	1.2.6	Theory in surface science	21			
	1.3	Scope of this thesis	24			
	1.4	Main results of the thesis and outlook	27			
2	Theo	ry	31			
	2.1	First steps and the Born-Oppenheimer approximation	31			
	2.2	The electronic structure	36			
	2.2.1	The variational theorem	. 37			
	2.2.2	Building a wavefunction	38			
	2.2.3	Solving the electronic structure	42			
	2.2.4	Density functional theory, Hohenberg-Kohn and Kohn-Sham	45			
	2.2.5	Exchange-correlation functional approximations	50			
	2.2.6 pseu	Periodic boundary conditions, plane waves, Bloch's theorem, a dopotentials				
	2.2.7	From electronic structure to potential energy surface	59			
	2.3	The nuclear motion and initial conditions	60			
	2.3.1	Burlisch–Stoer algorithm	61			
	2.3.2	Initial conditions of diatomic molecules	63			

3							
energy surface computed with a non-self-consistent screened hybrid density functional approach							
	3.1	Introduction					
	3.2	Methods					
	3.2.1						
	3.2.2	·					
	3.2.3						
	3.2.4	·					
	3.2.5						
	3.2.6	Hole model	79				
	3.3	Results and discussion	80				
	3.3.1	Converging a non-self-consistent field DFT calculation	80				
	3.3.2	The reaction probability	82				
	3.3.3	Sticking of rotationally aligned O <sub>2</sub>	86				
	3.3.4	The role of the energetic corrugation of the barrier height	88				
	3.3.5	The hole model	93				
	3.4	Conclusions	96				
	3.5	Appendices	98				
	3.5.1	CRP test set	99				
	3.5.2	Hole model and QCT energy shifts	100				
4		s of BOSS DFT: $O_2$ + Al(111) dynamics on a screened hybrid Var					
W		Fotential energy surface					
	4.1	Introduction					
	4.2	Methods					
	4.2.1	Electronic structure					
	4.2.2	Computational details					
	4.2.3						
	4.2.4	Fitting the PES	114				

	4.2.5	Quasi-classical trajectory dynamics	115
	4.3	Results and discussion	117
	4.3.1	Potential energy surface and barrier analysis	117
	4.3.2	Quasi-classical trajectory results	121
	4.3.3	Discussion and future prospects	123
	4.4	Conclusions	129
	4.5	Appendices	131
	4.5.1	Reaction barrier bar-plot	131
	4.5.2	Direct and indirect dissociative chemisorption	132
	4.5.3	Baule model	135
5	O <sub>2</sub> di	ssociation on Cu(111): Dynamics on a novel screened hybric	d Van der
٨	aals DF	Fpotential energy surface	137
	5.1	Introduction	139
	5.2	Methods	144
	5.2.1	The dynamical model	144
	5.2.2	Electronic structure approach	146
	5.2.3	Computational details of the DFT calculations	148
	5.2.4	Fitting the PES	150
	5.2.5	Quasi-classical trajectory dynamics calculations	151
	5.3	Results and discussion	154
	5.3.1	PES analysis	154
	5.3.2	Dynamics results	158
	5.3.3 QCT	Direct or indirect dissociation and normal energy scaling dynamics	
	5.3.4	Discussion	167
	5.4	Summary, conclusions, and outlook	169
	5.5	Appendices	170
	5.5.1	Flux weighted velocity distribution fit	170
	5.5.2	Physisorption, Van der Waals, well	174

5.5.3	Propagation-time dependent trapping	176					
References.		177					
List of abbreviations, acronyms, and symbols							
Samenvattir	ng	200					
Lijst van Nederlandstalige afkortingen, acroniemen en symbolen							
Curriculum	vitae	211					
List of public	cations	213					
Afterword		214					

### 1 Introduction

### 1.1 Heterogenous catalysis

Catalysis is one of the most vital and prevalent segments of chemistry<sup>1</sup>. From the growth of plant life<sup>2,3</sup> to the industrial production of fertiliser<sup>1,4–6</sup>, from the aptly named catalyst in most modern fuel-based cars<sup>7</sup> to the production of the building blocks of life in outer space<sup>8</sup>, catalytic processes occur all around us. Fundamentally, the presence of a catalyst in a chemical reaction will always speed up that reaction without the catalysis being altered or getting consumed by the chemical reaction<sup>9</sup>.

This speedup can be achieved because a catalyst allows for a chemical reaction to occur via a different mechanism or pathway than would be the case without the presence of a catalyst 10. A catalyst reacts with the reactants, i.e., starting chemicals, to form, bind, and stabilize the intermediate products. These intermediates convert into the final product of the chemical reaction, which is released, thereby regenerating the catalyst. This new pathway, though often more complex, is energetically more favourable, lowering the energy barrier to overcome for the reaction to occur. The entire process of consuming the reactants and regenerating the catalyst can be very fast, for an ideal catalyst very little of that catalyst is required to immensely speed up a chemical reaction 10.

The term catalysis was first used by Jöns Jakob Berzelius in 1835<sup>11</sup> to describe the acceleration of reactions by unchanged substances. The name comes from the Greek word "kataluein", comprising of two terms "kata" translating to "down", and "lyein" meaning "loosen"<sup>11,12</sup>. Although he was the first to use the term catalysis, Berzelius was not the first to describe the process of catalysis. It was Elizabeth Fulhame in 1794 who was the first to correctly describe the catalytic function of water in certain oxidation reactions<sup>13</sup>. The following centuries would, initially in conjunction with the Industrial Revolution, see a myriad of innovations and discoveries in the field of catalytic chemistry. Even now this work is still ongoing as chemists and chemical engineers try to find new

and better catalysts to overcome modern challenges in chemistry, industry, and environmental science<sup>14–22</sup>.

In general, catalysis is separated into three different categories. The first is homogenous catalysis, where the catalyst is dispersed in the same phase (gaseous, liquid, or solid) as the products and reactants of the reaction. The second category is heterogenous catalysis, where the phase of the catalysts is different from that of the products and the reactants. The third and final category is biocatalysis or enzymatic catalysis. This third category can in principle be seen as either homogenous or heterogenous depending on the type of biocatalyst or enzyme, but due to its distinctive nature from the other two types, it is generally treated as a separate category. The homogenous option may initially seem the most optimal choice for a catalyst, as it would facilitate the most efficient mixing of reactants and catalysts. However, it is often difficult to separate catalyst, reactant and product from each other. In heterogeneous catalysis, the catalyst is typically a solid compared to the liquid<sup>23</sup> or gaseous reactants and products. The different phases reduce the optimal mixing but it does facilitate easy separation of the catalysts from products and reactants.

Heterogenous catalysis is thus found in most industrial chemical production chains and processes<sup>24,25</sup>. Examples are the Haber-Bosch process for the production of ammonia (NH<sub>3</sub>) for fertilizers<sup>5,26</sup>, steam reforming where water (H<sub>2</sub>O) and methane (CH<sub>4</sub>) form hydrogen (H<sub>2</sub>) gas and carbon monoxide (CO)<sup>27-</sup> <sup>29</sup>, and the formation of more complex hydrocarbons (C<sub>c</sub>H<sub>h</sub>) from carbon dioxide (CO<sub>2</sub>) and H<sub>2</sub> via the reverse water gas shift reaction<sup>17,18,30-32</sup> and the Fischer-Tropsch reaction<sup>18,33–36</sup>. For all these examples the optimal conditions typically involve high temperatures, high pressures, carefully constructed ratios of reactants and products, and (often) complex and expensive catalysts painstakingly optimised for these reactions. These complexities make it difficult to improve a catalyst for chemical reactions and its optimisation is often achieved on a trial-and-error basis. However, further improvements are paramount as an optimal catalyst can substantially reduce the temperatures or pressures needed to attain high chemical reaction rates. This will make production more efficient and reduce the enormous energy needs of the chemical industry. It is therefore of great scientific interest to try and understand

the chemistry involved in heterogenous catalysis to ultimately achieve the ability to accurately predict the behaviour of a new or optimised catalyst based solely on its chemical composition, molecular structure, and morphology.

In this chapter the current scientific work in heterogenous catalysis is discussed, setting up the context and the relevance of this thesis. In the next section, the field of surface science will be discussed (Section 1.2.1), followed by some basics of surface structure (Section 1.2.2) and molecule-surface interactions (Section 1.2.3). Thereafter, an overview of experimental techniques is discussed. We will proceed with a discussion on how to control the molecular conditions (Section 1.2.4) and then show a brief overview of experimental techniques in surface science (Section 1.2.5). Against the backdrop of experiments the relevance and methods of theories and models in surface science are discussed (Section 1.2.6). After this, we are finally ready to discuss the scope of this work (Section 1.3) and to briefly summarise the results of this thesis (Section 1.4).

### 1.2 Surface science

In the study of heterogeneous catalysts, there are two major branches of academic science. The first is focused on understanding the catalytic performance under industrial, or *in situ*, conditions. This branch looks at macroscopic effects and conditions in the catalysis reaction<sup>37,38</sup>. The second branch, referred to as surface science, is focused on the fundamental chemical steps involved in the reaction on the catalyst-reactant interface, or surface. The chemical reaction steps involved on a surface are often a complex network of coupled elementary steps<sup>24,39</sup>. Fortunately, most heterogeneously catalysed processes are rate-limited by one of just a few elementary reaction steps<sup>6</sup>. For example, the dissociation of  $N_2$  is the rate-limiting step in the Haber-Bosch process<sup>5</sup>. Thus, in surface science, we aim to optimise heterogeneous catalysis by developing an understanding of these rate-limiting steps. Contrary to the other branch, surface science requires the elimination of as many variables as possible to study the elementary reaction steps with as few unknown parameters as possible<sup>40–45</sup>.

# 1.2.1 Study of the active component in heterogeneous catalysis

The first elimination of unknowns is achieved by restricting the surface science research to the active component of the catalysis. For heterogenous catalysis (often also for homogenous catalysis) the active component is typically a metal. This is because of the unique electronic structure of metals. This unique structure allows the metal to donate or accept electrons from reactants, intermediates, or products at low energetic "costs" 6. Both the easy acceptation and donation of electrons, in turn, make it easier for chemical bonds to be either formed or broken for molecules that are close to or adsorbed on the metal surface, lowering barriers to reactions.

This unique electronic structure of metals is a result of the formation of the metal solid. In general, a metal solid forms when enough atoms have clustered and stay rigidly together. In the process, both their occupied and unoccupied electronic orbitals will start to overlap. The overlap causes the orbitals to get smeared out, or delocalised, over the clustered atoms. This will transform the initially distinct energy levels of an atom, or molecule, into larger energy bands. These energy bands are separated by areas where there are no defined energy levels, i.e., band gaps<sup>47</sup>. The energy bands that form can be either occupied, partially occupied, or unoccupied with electrons. The boundary where an energy band goes from occupied to unoccupied in a surface is generally referred to as the Fermi-level<sup>48</sup>.

The Fermi-level of a solid surface can be positioned in a band gap, like with insulators or semiconductors, separating the energy bands into the highest occupied "valence" band and lowest unoccupied "conduction" band<sup>49</sup>. For both semiconductors and insulators exciting an electron to go from the valence to the conduction band, a so-called electron-hole-pair (ehp) excitation, takes a minimum energy equal to the size of the band gap. However, for metals, the Fermi-level is positioned inside an energy band, i.e., the band is only partially occupied. Thus, there is virtually no energetic cost for ehp excitation and the half-filled band makes it easy for the metal to exchange electrons with other compounds. It is this unique property of metals to freely "play" with the

electrons that so often makes them the active component in a catalytic reaction<sup>46</sup>.

### 1.2.2 Surface structure

The second unknown that needs to be understood is the structure of a metal (catalyst) surface. The structure of a surface can for instance influence the position of the Fermi-level of the surface, it can influence the locations on the surface where molecules can interact with the metal, and it influences where and how certain elementary steps in the reaction occur<sup>50</sup>. In the industrial applications of heterogenous catalysis the metal surface is often shaped by nanoparticles meaning the surface is complex with many types of surface facets, steps, corners kinks, and often defects. However, to properly study the effects of specific surface structures the surface of the metal catalyst needs to be very well-defined, i.e., the surface structure needs to be simple and described at atomic level precision. These types of metal surfaces are made by growing metal single-crystals that are cut and polished along the desired crystal axis to expose the right type of surface face<sup>51</sup>. These surface faces are characteristically defined by their Miller indices, for example for Cu(111) the Miller indices are (111) and they define the type of metal surface as a (111) face of a, in the case of Copper, face-centred cubic (FCC) cystal<sup>52</sup>.

#### 1.2.3 Surface interactions

At this point, it is relevant to briefly discuss what kind of interactions can occur at these well-defined metal surfaces. The basic interactions of a molecule with a metal and the general events that will occur when a molecule interacts with a surface are already known for some time<sup>53,54</sup>. However, the specifics of the exact mechanisms, interactions, selectivity, or efficiencies remain an open question to this day<sup>39,45,55,56</sup>. At present it is well understood that a molecule approaching a metal surface can largely end up doing one of two things. The molecule can either adsorb on the surface, or it can bounce back, i.e., scatter, from the surface. In turn, both scenarios can be redivided into subcategories.

There are generally three different subcategories of adsorption for molecules on metal surfaces. All three are characterised by different interactions with the metal surface. In the first option, "physisorption", the interaction between the molecule and metal is over the largest distance, i.e., it occurs when the molecule is furthest away from the surface. In physisorption, the interaction is not chemical. Thus, there is no exchange of electrons. At longer distances the interaction is governed by "Van der Waals" forces<sup>57</sup>, or more specifically London-dispersion forces<sup>57</sup>. In simple terms, the London dispersion force is induced because electrons are not static in an atom, molecule, or metal surface. The movement of electrons induces an electric field which other electrons in the area will respond to. This results in electronic motion getting correlated over a larger distance. This correlation results in an attractive force between small and opposite dipoles induced in the electronic structure of the metal and adsorbing molecule. The physisorption of molecules on a metal surface is a rather weak interaction possessing a shallow potential well (see **Figure 1.1**).

The second and third subcategories of adsorption are chemical in nature, and in both electrons or electronic density, act to form chemical bonds between the molecule and the surface, and both are called chemisorption. In molecular chemisorption, the molecule forms a chemical bond with the surface without breaking any internal bond. This chemical bond forms as the orbitals of the molecule start overlapping with the energy bands lying close to the Fermi-level of the metal<sup>42</sup>, allowing for easy electronic exchange between molecule and metal. The last subcategory of adsorption is dissociative chemisorption (DC). In such a scenario the anti-bonding orbitals of the molecule end up below the Fermi-level of the metal, thus chemical bonds in the adsorbing molecule are broken to facilitate energetically more favourable bonds with the metal surface<sup>42</sup>. These dissociative chemisorption reactions tend to result in the strongest form of interaction between the molecule (fragments) and the metal.

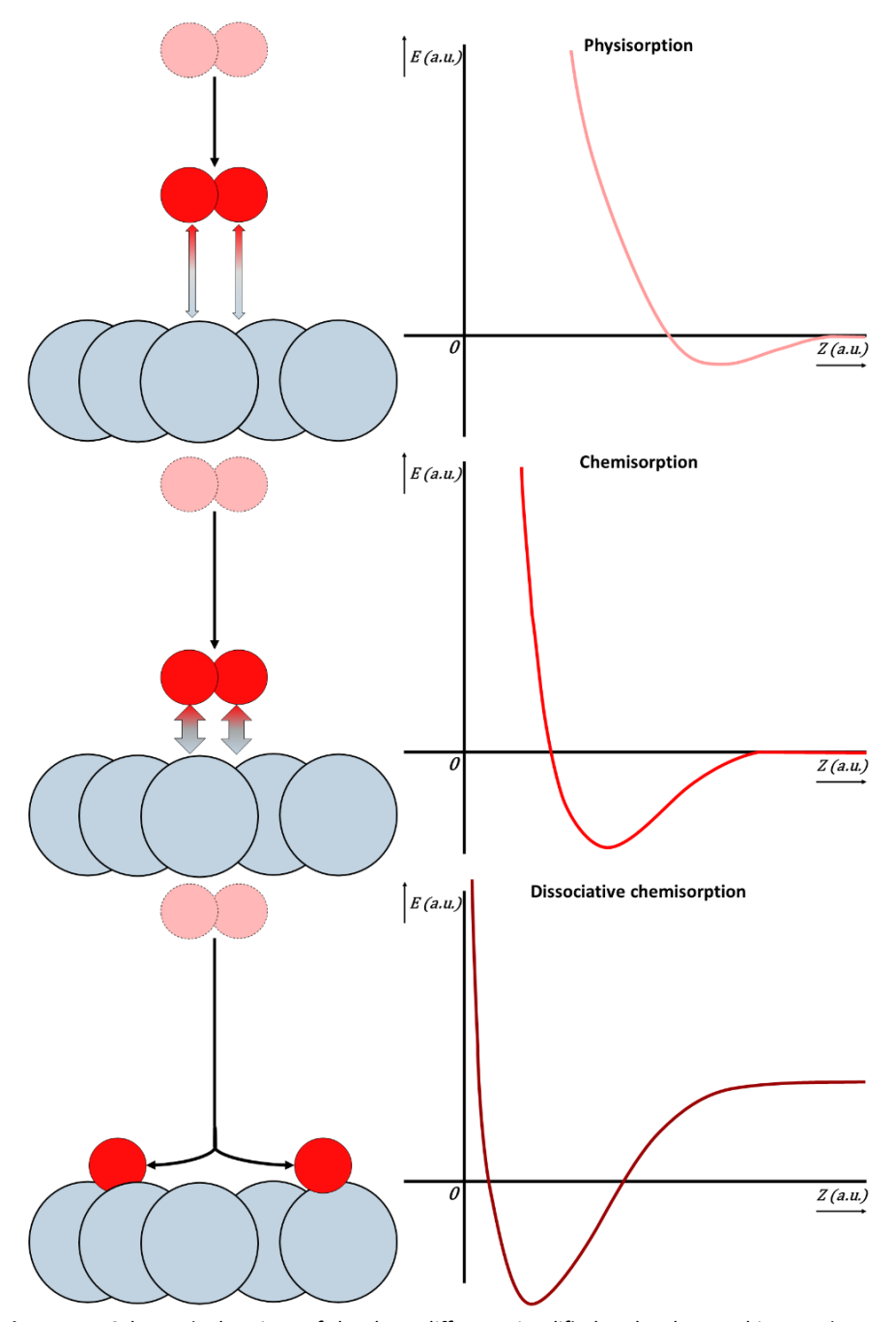


**Figure 1.1**: Schematic drawings of the three different simplified molecule-metal interaction types and their associated potential energy (E) as a function of the molecule-metal distance (Z), both in arbitrary units. All potentials are shown without additional barriers to interaction for visual and conceptual simplification.

However, the attractive interactions are not always accessible for the approaching molecule and the molecule can be repelled from the surface, or sometimes the adsorption is not strong enough and the approaching molecule has too much internal energy and returns to the gas-phase. This results in scattering processes. Scattering can occur elastically when the molecule does not lose any internal energy when it bounces back to the gas-phase. Or, if the molecule does lose or gain some energy in the collision, the scattering is called inelastic<sup>58</sup>. Energy loss to, or gain from, the surface can happen via momentum transfer with the metal surface, excitation of electronic states in the metal, i.e., ehp excitations<sup>59–61</sup>, or other more complicated, non-adiabatic, effects.

If the molecule is small enough a special type of scattering in the form of diffraction may occur<sup>62</sup>. This happens due to the interaction of the molecules with a periodic metal surface. Clean single crystal metal surfaces, as discussed in Section 1.2.2, possess repeating units. These periodic units will interact with the wavefunction of the approaching molecule (see Chapter 2) resulting in specific scattering patterns. This phenomenon is called diffraction and it is the same as how light diffracts on certain surfaces<sup>63</sup>. The larger, i.e., the heavier the molecule, the smaller its wave-function<sup>64</sup>, thus the smaller this effect. We typically only observe diffraction patterns for electrons, H<sub>2</sub>, He or other small molecules or ions.

The possibility of all of these occurrences makes the molecule-metal interactions complicated, because the occurrence of either adsorption or scattering does not exclude other events from occurring as well. Neither does adsorption need to be permanent: temporary adsorption can for example result in a form of inelastic scattering, and molecular chemisorption can be a precursor to dissociative chemisorption<sup>65</sup>. The combination of all these options means that even though the basic mechanisms for molecule-metal interactions are understood the complete detailed mechanical picture of all molecules interacting with metal surfaces is not known. In any system, any specific molecule with any (metal) surface will have their own, possibly unique, interactions with each other. The study of these interactions has therefore needed to develop into an enormous field of highly precise and systematic research.

### 1.2.4 Controlling reaction conditions

To ensure a clear picture of these complex interactions of metals and molecules in heterogeneous catalysis, the effect of many more unknowns besides the active components and surface structure needs to be eliminated. These include but are not limited to the temperature of the metal surface, the energy of the reactants, and additional molecules, or contaminations, that may influence the reaction. Moreover, any meaningful observations at the atomic scale needed to understand these complex mechanisms are very sensitive to even the smallest details. Therefore, most surface science experiments are done at ultra-high vacuum (UHV), i.e., at pressures smaller than  $10^{-10}$  mbar, only slightly more than the gas pressures in the 'busy' parts of outer space. Not only does this high vacuum ensure there is very little contamination of unwanted chemical interactions, but it is also required for some measuring equipment to properly function.

The UHV conditions eliminate a lot of contamination and unwanted interactions but experiments still need to control the conditions of the molecules that interact with the metal. These days the introduction and conditioning of the molecules interacting with the metal is often achieved with molecular beam (MB) studies<sup>66–71</sup>. A MB is created by expanding a gas from a high-pressure room to a low-pressure room through a small nozzle. Due to this expansion, all molecules in the MB travel at roughly equal velocities in the same direction, undergoing very few collisions between them. The temperature of the nozzle  $(T_N)$  influences the rovibrational temperature of the beam<sup>69</sup>, i.e., it determines the rotational and vibrational energy of the molecules in the MB. Similarly,  $T_N$  also influences the translational kinetic energy of the molecule, which in surface science is referred to as the incidence energy  $(E_I)^{71}$ .

However, often "seeding" is used to systematically influence the total  $E_i$  of the MB, without changing the rovibrational states as those can be kept constant with a constant  $T_N$ . Seeding is done by mixing the molecule of interest in a beam of inert (often noble) gases. A gas seeded with a lighter noble gas will travel faster, i.e., increase  $E_i$ , and a gas seeded with a heavier noble gas will travel slower. If only the normal component of the incidence energy, i.e., the component that is normal to the metal surface, influences the reaction of the molecule, i.e., if

normal energy scaling (NES) holds<sup>72</sup>, then the angle of the molecular beam ( $\Theta$ ) with the metal surface can also be altered to change the normal incidence energy ( $E_i^{\perp}$ ) and thereby investigate the dependence of the reaction on this energy.

In some MB studies magnetic fields, electric fields or lasers can be used to further select or excite certain molecular states<sup>73–76</sup>. It must be noted that although MBs allow for great control of the reactive molecule, not all surface experiments use or require such setups. Sometimes the direct dosing of gasses is also a fine method of introducing a gas onto the metal surface<sup>51,77,78</sup>, though this allows for far less exact control over the molecular states.

### 1.2.5 Surface science experiments

With almost all possible conditions, circumstances and variables covered, an experimentalist can work on observations and measurements. Below, a general overview of the most commonly used methods will be given. The aim is to form an idea of most of the experimental possibilities in surface science.

One of the most direct observables of the reaction of a molecule on a metal surface is the reaction probability. This can be measured in different ways but the most direct method of probing the reaction probability is by measuring the so-called "sticking probability" ( $S_0$ ).  $S_0$  can be measured by using a molecular beam and the King & Wells (K&W) method<sup>69</sup>. In principle, it is a very simple experimental setup. As the molecular beam enters the reaction chamber of the UHV setup it is initially bounced off a "flag". This flag is a metal plate placed inside the path of the MB (see Section 1.2.4). The flag blocks the molecules from reaching the metal surface and results in a certain base background pressure in the reaction chamber. This happens because the molecules are all scattered from the flag and end up bouncing around the reaction chamber, thus resulting in a certain pressure in the chamber. At a given time t' the flag is removed, thus the MB now impinges directly on the metal surface. A certain fraction of the molecules will stick to the metal surface whereas the rest will scatter off. This results in a drop in the background chamber pressure.  $S_0$  is at this point nothing more than dividing the pressure drop over the old baseline pressure when the

flag was still in place, thereby directly probing the probability that a molecule sticks to the metal surface<sup>69</sup>. The  $S_0$  may reflect a combination of reactive and non-reactive sticking, depending on the type of surface interaction (see 1.2.3), surface temperature, surface structure, etc. Other experiments are required to probe what type of sticking has occurred. Although the K&W approach sounds simple enough, running such an experiment in practice is far from trivial.

Probing the type of molecule-surface interaction, or type of sticking, or indirectly probing sticking probabilities can also be done. For example, a technique that allows us to look at possible surface structures, and thus its distortion via adsorption, would be low energy electron diffraction (LEED)<sup>42,79,80</sup>. In LEED the periodic nature of a metal surface is used to study the diffraction of an electron beam. If the periodic structure is disturbed or altered by adsorbates then this shows in the diffraction pattern. Another technique using an electron beam would be Auger electron spectroscopy (AES)<sup>81–89</sup>. In AES the electron beam is used to excite core-shell electrons in atoms at the surface. These excited electrons leave an electron-hole behind, which will be filled with a higher-shell electron, and this releases energy in the form of either an X-ray photon or the excitation of a third electron from that atom. This third electron is referred to as an Auger electron and the emission energy of Auger electrons is unique to the atom and its chemical environment<sup>81–83</sup>. Beyond measuring the Auger electron the otherwise emitted X-ray photon can also be measured and shares its chemically unique properties with the Auger electron. Measuring these photons can be done with X-ray photon spectroscopy (XPS)90-94. XPS is usually more precise to the chemical environment of the atoms. It is common to use electron beams to excite the initial core-shell electron, however, X-rays can also be used<sup>93</sup>. Regardless, both techniques allow experimentalists to observe the type of chemical species on a surface and even its chemical environment. Both techniques can, with difficulty, also be used quantitatively<sup>84–89,92,93</sup> to determine the amount of adsorbed species which can then be used to estimate the sticking probabilities.

It is also possible to use mass spectrometers to study the desorption of material from the metal surface. This is a more indirect method of investigating sticking probabilities and is far more susceptible to other surface conditions and

molecule-metal interactions as it inherently studies the product after the reaction<sup>95</sup>. However, desorption studies can still prove valuable with for example the use of transitions state theory<sup>96</sup> and well-defined reaction conditions.

One of the few techniques that can directly probe the surface on an atomic scale is scanning tunnelling microscopy or STM<sup>97,98</sup>. This method makes use of a phenomenon in quantum mechanics called "tunnelling" to sample the electronic densities at the surface. Electronic tunnelling occurs because, in the quantum mechanical description, an electron is delocalised, i.e., the wavefunction property of the electron (more in Chapter 2) means that the electron is spread over space with a given distribution. This spread can reach into potential barriers that are classically forbidden for the electron to reach. The probability of entering this classically-forbidden area decreases exponentially with the width of the potential barrier i.e., with the width of the vacuum gap between the tip of the STM and the surface. If the barrier is narrow the electron may tunnel through this barrier, as the electron is partially delocalised to the other side of the barrier. If a bias voltage is placed over the potential barrier, the tunnelling of the electrons will induce a small current that can be measured. This current is correlated to the width of the potential barrier, i.e., the distance between the microscope tip and surface 97-100. This way the tip can scan a surface and probe the electronic density and its changes over the surface. Notably, the STM does not directly distinguish between atom or molecule types. The exact functioning of this technique is out of scope for this work and we refer the reader to Refs. <sup>97–100</sup> for more information. STM is a useful technique capable of directly probing the (electronic) structure of a surface, and any possible adsorbates, down to the atomic scale. Although the technique is still improving 101-107 an STM can only probe snapshots of the surface structure with substantial time differences between sequential snapshots. As a result, it does not form a complete picture of molecule surface interactions, i.e., any "movie" made with this technique has its image frames far apart in time.

All experiments described above looked at the reacting molecules or the surface directly. Studying the molecules that do not react, i.e., scatter, can also be informative in answering the fundamental questions of molecule-metal interactions. The outcomes of scattering events, though insightful, are far more

dependent on the exact initial conditions of the scattering molecule<sup>76,108</sup>. Additionally, they usually probe the (electronic) structure of the surface in far greater detail than reactions generally will<sup>76,109,110</sup>. This makes the experimental studies even more involved than most reactive studies but also allows for far greater detail.

### 1.2.6 Theory in surface science

In the end, even experiments, like the ones described above, can still not tell the full story, and the full interaction between a molecule and surface can still not be completely observed directly. Experiments often probe average interactions or single snapshots. This is where theoretical surface science, or theoretical chemistry in general, plays a vital role. It may be possible to understand the fundamental interactions between different molecules or between molecules and metal surfaces by developing and applying accurate simulations to these problems. The ultimate goal of such simulations would be to predict the exact outcome of a chemical reaction based only on the conditions and the chemicals involved<sup>111</sup>. For now, this goal is still a little ambitious as the computational resources involved in simulations are extensive and full-dimensional quantum dynamics calculations for such large systems may even never be possible. Nevertheless, simulations can already be used to closely monitor the intricate interaction of molecules with each other and function as an instrumental tool in understanding the elementary reaction steps involved in heterogeneous catalysis.

For now, simulations and models in chemistry or surface science are not perfect and much work in the field of theoretical chemistry is currently being done to improve the accuracy of these models. Similarly to the framework of interactions of molecules and metals (see Section 1.2.3) the root of chemical simulations and models, i.e., the laws of physics, are known and well-understood for small systems. The difficulty arises from the increased complexity and the large number of degrees of freedom that arise in chemical systems. To model chemistry one has to model all the movements of the atomic nuclei and electrons. This is made even more complex as many, if not all, of the movements of the nuclei and electrons are coupled to each other. Moreover, the number of

electrons and nuclei in the system increases rapidly as the chemical system grows larger<sup>112</sup>. On top of these difficulties, there is also the small inconvenience that the interaction of small particles is predominantly governed by quantum mechanics and not classical mechanics<sup>112</sup>. As a result, the computational costs of many chemical simulations, i.e., the time it takes to simulate a chemical reaction, quickly skyrockets<sup>113–116</sup> (see also Chapters 3, 4, and 5). Consequently, theoretical chemistry as a field has to constantly balance computational costs with accuracy.

The balancing act unavoidably comes with an inherent difficulty, namely, theoreticians need to know what approximation can be made without negatively affecting the accuracy of the model, put more simply, we need to know what we can get away with without ruining our results. In resolving this difficulty there are generally two major philosophies. The first is more "a priori", it seeks to understand the exact effects or faults of each approximation made in the underlying physics of the model. Thus, the physical understanding of the approximation is necessarily put above the eventual accuracy of the model. The second is more empirical in nature, where theoretical models are often tested and benchmarked against verifiable experimental results. Here the goal is to reproduce experimental results as closely as possible, sometimes at an unavoidable cost to the understanding of the physics of the model itself.

In surface science, both philosophies still have to deal with the fact that experiments like those described in Section 1.2.5 will need to be simulated. This could bring an unwantedly large scale to the chemical simulations that need to be performed. Luckily however, the general application of UHV technologies and the defining and elimination of unknowns in surface science experiments means that we can often compute results that can be compared to experiments by constructing aggregates of many different single, i.e., small, molecule-metal systems. Put differently, we need to simulate molecule-metal systems with the desired accuracy for many different starting conditions of molecules and metals based on experimental conditions and average over those results.

Still, directly and bluntly applying quantum mechanics to all the degrees of freedom in a chemical system is, usually, not a suitable method to compute

observables. One of the first and more common, though not always allowed, approximations is to decouple the movement of the electrons and the nuclei. This approximation is called the Born-Oppenheimer approximation (BOA)<sup>117</sup>, see also Chapter 2. Put simply, this approximation exploits the mass, and thus velocity, difference of the electrons and nuclei. It assumes that the light and nimble electron can quickly, or instantly, adjust its movement to any movement of the nuclei. Thus, any movement of the nuclei will not result in immediate electronic excitations<sup>10,112,117–120</sup>. Moreover, this allows us to treat the heavier nuclei classically, as their wavefunctions, see Chapter 2, are considerably less delocalised due to their high mass. This simplifies the problem. The electronic part of the system is still treated within quantum mechanics and this results in a potential energy for the movement of the nuclei. These nuclei can then be treated classically where the forces on the nuclei are governed by the potential energy.

This, however, does not diminish the complexity of the quantum mechanical nature of the electrons. In most of chemistry and especially most of surface science the electrons are modelled using density functional theory (DFT)<sup>121</sup>. The details of DFT are discussed in Chapter 2 but putting it briefly the electrons will not be treated by wavefunctions but with an electronic density functional, i.e., they will not be described by wavefunctions of all their own distinct coordinates but by their collective density<sup>121</sup>. Mathematically, the complete density functional (DF) is proven to exist, see Chapter 2, however, its exact form is not known<sup>112,118,121,122</sup>. Generally speaking, the terms that are not fully described are the electron exchange energy and the electron correlation energy 112,118,122. These two terms are in most scenarios combined in the exchange-correlation (XC) DF. In this picture of DFT, the XC-DF is a small contribution to the total potential electronic energies<sup>112,118,122</sup>. It is, however, in these finer details that the focus for the majority of DFT-based theoretical chemistry lies  $^{112,115,130-136,118,123-129}$ . There are many different approximations to the XC-DF<sup>137–141</sup>, and many more are being developed. All these approximations come with their computational costs, errors, and (in)accuracies.

The approximations made in the XC-DF follow the common trend in theoretical chemistry: higher accuracy results in higher computational costs. In surface

science, this is especially true as the metals in molecule-metal systems come with a high number of electrons that need to be simulated. Moreover, the inherent two-phased nature of the system means that the XC-DFs which will work well for the molecule often work less well for the metal and vice versa. Generally, the so-called "generalised gradient approximation" (GGA) approach (see Chapter 2) for the XC-DF has proven to be rather reliable for many molecule-metal interactions<sup>56,124,129</sup>. For many systems<sup>129</sup> the GGA seems to be the best compromise in the description of the highly delocalised electrons in the metal surface and the more localised electrons on the molecule whilst also being computationally affordable enough to simulate many different trajectories of the molecule impinging on the metal surface to accurately reproduce K&W or other MB studies<sup>55,56</sup>.

### 1.3 Scope of this thesis

Theory in surface science has until recently been able to predominantly rely on the robust GGA framework for DFs: Specific reaction parameter (SRP) semi-empirical GGA DFs were able to describe certain molecule-metal systems within chemical accuracy, i.e., within 1 kcal/mol of experimental results<sup>55,56</sup>. For example, the reactivities of  $H_2$  + Cu (111)<sup>135</sup>,  $H_2$  + Pt(111)<sup>142,143</sup>,  $H_2$  + Pd(111)<sup>144</sup>,  $H_2$  + Ni(111)<sup>127</sup>,  $CH_4$  + Pt(111)<sup>134</sup>, and several more<sup>115,129</sup> have all been described with (near) chemical accuracy by GGA DFs.

However, recent work<sup>124,145</sup> has shown that GGA DFs will not work for all types of molecule-metal systems. For instance, systems like HCl + Au(111)<sup>124,125</sup>, O<sub>2</sub> + Al(111) (Chapters 3 and 4), O<sub>2</sub> + Cu(111) (Chapter 5), and NH<sub>3</sub> + Ru(0001)<sup>124</sup> have not yet been successfully described by theoretical models on the GGA-level of theory. In the same work, based on results for these and other systems, Gerrits  $et\ al.^{124}$  suggested that GGA DFs will fail at, or have difficulty with, the correct description of molecule-metal reaction barriers if the charge transfer energy  $(E_{CT})^{124}$  of the molecule-metal system is below  $7\ eV.\ E_{CT}$  is defined as

$$E_{CT} = \phi - EA \tag{1.1},$$

where  $\phi$  is the energy required for an electron to be extracted from the metal surface, i.e., the work function of the metal surface<sup>10</sup>, and *EA* is the electron affinity, which is the energy released by the molecule when an electron is

attached to it<sup>57</sup>. In other words,  $E_{CT}$  is the energy needed for an electron to be transferred from a metal surface to a molecule, thus indirectly representing the likelihood of electron transfer occurring during the reaction of the molecule on a metal surface<sup>124</sup>.

It is not yet fully understood why GGA fails for these specific  $E_{CT} < 7 \, eV$  systems. However, there are some possible similarities to the simulation of two molecules reacting with one another in the gas-phase<sup>124</sup>, for which the GGA level of DFT has never been able to properly describe the reaction<sup>146,147</sup>. However, even though the problems in the gas-phase community have been better known for a longer time, there still seems to be no consensus on the cause of failure for GGA DFs<sup>147–151</sup>. Regardless of the cause, the gas-phase community has resorted to working with more accurate DFs in the form of so-called "hybrid" DFs<sup>152,153</sup>.

Put simply, hybrid DFs admix a certain amount of exact exchange energy, i.e., Hartree-Fock (HF) exchange energy, to the exchange component of the XC part of a GGA DF<sup>152</sup>, see Chapter 2. However, in Kohn-Sham DFT neither the exchange nor correlation contributions can be fully separated from one another<sup>154</sup>. The exchange component will contain a given amount of correlation interaction and *vice versa*. As a result, admixing in the exact HF-exchange energy is not necessarily straightforward and remains a process based on "a priori"-based educated guesses<sup>152</sup> or on trial-and-error<sup>124</sup>.

The use of hybrid DFs is also difficult for metal surfaces as the large number of electrons and the use of plane waves (see Chapter 2 for more information) make the use of any fraction of exact exchange far more computationally expensive than the use of any regular GGA DF<sup>155–157</sup>. Lastly, the global exact exchange energy does not work well for metals due to the high delocalisation of electrons in a metal (Section 1.2.1), where the long-range interaction between electrons in the metal is generally screened by other electrons<sup>158</sup>. This means that a semi-local or fully local DF like GGA is generally more accurate in the description of the metal itself.

Regardless, Gerrits *et al.* showed that a screened hybrid DF adiabatically applied to the  $O_2 + Al(111)$  system, one of the more notorious systems with  $E_{CT} < 7$  EV,

resulted in considerable improvement of the reactivity over previously attained theoretical results<sup>124</sup>. Thus, it appears that similar to gas-phase calculations, the use of hybrid DFs, despite its difficulties, may resolve the current shortcoming of DFT in describing the more "difficult" molecule-metal systems to a large extent.

In this thesis, we aim to test and improve upon the application of screened hybrid DFs to more accurately describe the electrons and electronic structure in the "difficult" molecule-metal systems, like  $O_2$  + Al(111) and  $O_2$  + Cu(111). This entails testing a method to substantially reduce the computational costs of hybrid DFs based on a probable root cause of the error of GGA DFs(Chapter 3), and the alteration of the XC-DF with a better form of long-range electron correlation together with higher fractions of exact exchange for both  $O_2$  + Al(111) (Chapter 4) and  $O_2$  + Cu(111) (Chapter 5).

In these studies, compared to studies using the GGA the costs to compute the electronic structure of the molecule-metal system are balanced far more to the side of accuracy rather than computational efficiency. This ended up pushing the limits of current high-performance computing infrastructure to facilitate the electronic structure calculations necessary to test and verify these new DFs. Validation of the DF requires comparison to other theoretical work, i.e., benchmark studies, or experimental MB studies meaning that many different molecule-metal collisions would need to be simulated. This is done efficiently by constructing a PES using thousands of different DFT energies for different molecular geometries above the metal surface. The DFT data can then be interpolated using the corrugation-reducing procedure (CRP) to construct a continuous potential energy representation for every possible geometry of a molecule above and on a metal surface. With this PES the molecular reaction on the metal surface can then be computed using quasi-classical trajectory (QCT) dynamics calculations, i.e., single molecule-metal collision simulations. Hundreds of thousands of such trajectories are then aggregated to compute reaction probability curves that can be compared to other theoretical frameworks and experimental (reaction probability) results, mostly based on K&W experiments, to validate and test the accuracy of the screened hybrid DFs for the reactions studied.

### 1.4 Main results of the thesis and outlook

In the next few paragraphs the main results, conclusions, outlook, and contents of the following chapters are summarised. Before the main results are presented in Chapters 3-5, an inclusive overview of the theoretical models needed and employed in this work is provided in Chapter 2.

In Chapter 3, an extensive test of the non-self-consistent field (NSCF) screened hybrid DFT approach is shown. This approach computes NSCF-screened hybrid DFT energies based on self-consistent-field (SCF) GGA electronic densities. The chapter explores the accuracy of the NSCF-screened hybrid DF approach by implementing the NSCF HSE03-1/3x@RPBE DF for O<sub>2</sub> + Al(111). The molecular beam sticking probabilities ( $S_0$ ) as well as a set of sticking probabilities for rotationally aligned O<sub>2</sub> are computed using quasi-classical trajectory (QCT) calculations, and analysed. The results show that the NSCF approach yields reaction probability curves that reproduce SCF results with near-chemical accuracy, suggesting that the NSCF approach can be used advantageously for exploratory purposes. An analysis of the potential energy surface and the barriers gives insight into the cause of the disagreement between the SCF and NSCF reaction probabilities and into the changes needed in theoretical modelling to further improve the description of the  $O_2$  + Al(111) system. Additionally, an implementation of the hole model method to estimate reaction probabilities based on reaction barrier heights shows that the application of the hole model results in fair agreement with actual dynamic calculations. However, the hole model results in an increased slope of the reaction probability curve compared to the molecular dynamics, with a shift to lower or higher energies depending on whether the vibrational energy of the molecule is included in the initial energy of the molecule or not, indicating a sizable influence of dynamic effects on the  $O_2$  + Al(111) reaction.

Chapter 4 continues with the work of  $O_2$  on Al(111). So far the use of only a screened (N)SCF hybrid DF was not enough to ensure a highly accurate (i.e. chemically accurate) description of the DC of  $O_2$  on Al(111). Previous work and Chapter 3 have shown that the onset of the  $S_0$  curve was correctly described by the (N)SCF HSE03-1/3x DF, but the slope, or width, of the curve was not. Chapter 3 also discussed that the inclusion of non-local correlation in the DF may help to

resolve this shortcoming. Therefore, in Chapter 4 the use of a non-local correlation DF combined with an increased fraction of exact exchange in the screened hybrid DF is tested. This is achieved by constructing another O2 + Al(111) Born-Oppenheimer static surface (BOSS) PES, using the HSE06-1/2x-VdWDF2 DF, employing the corrugation reducing procedure (CRP), and using QCT calculations to compute the sticking probabilities. The resulting PES shows the presence of shallow Van der Waals wells in the entrance channel and the barriers to DC show slightly more corrugation and anisotropy compared to the previously used SCF HSE03-1/3x DF, but most barrier heights differ by less than 1 kcal/mol. As a result, with the use of the HSE06-1/2x-VdWDF2 DF, the onset of the  $S_0$  curve is somewhat better described than in previous work and the curve is broadened a little compared to the SCF HSE03-1/3x description, in improved agreement with experiment, but not more than seen for the NSCF approach as applied in Chapter 3. These results imply that if future theoretical methods aim to resolve the disagreement between theory and experiment then those methods would need to either result in radical changes in the PES or the shortcomings of the dynamical (BOSS) model need to be addressed. Both need to be achieved whilst keeping the computational demands of the applied method to feasible levels.

Lastly, to verify this new electronic structure approach for a different system, the computed sticking probabilities for  $O_2$  + Cu(111) based on the same HSE06-1/2x-VdWDF2 screened hybrid Van der Waals DF are presented in Chapter 5. Also in Chapter 5, a six-dimensional BOSS PES was constructed using the CRP. This PES was used to perform QCT calculations to compute the sticking probabilities of  $O_2$  + Cu(111). For the first time, DFT-based sticking probabilities are presented that underestimate the experimental sticking probabilities of  $O_2$  + Cu(111), contrasting these results to the previous Chapters 3 and 4. While reproducing the experimental results would have been even more desirable, the fact that a DF which underestimates the measured sticking probabilities was found, means that a DF using a lower fraction of exact exchange will most likely describe the  $O_2$  + Cu(111) system with high accuracy. Furthermore, the chapter shows evidence for the presence of both indirect and direct dissociative chemisorption. The indirect precursor-mediated mechanism occurs for low-incidence energy  $O_2$ . The mechanism is supplanted by a direct dissociative mechanism at higher

incidence energies. Finally, the results suggest that the Cu surface temperature may also affect the dissociation mechanism, but this still needs further verification with a different theoretical framework that allows for the simulation of surface temperature.

The outlook from the fifth chapter for the O<sub>2</sub> + Cu(111) system, though far from trivial, is fairly bright. Broady speaking three things would need to be done to come to the highest standard and (presumably) highly accurate, description of the  $O_2$  + Cu(111) system. The first is that surface motion and surface temperature need to be included in future modelling of this reaction. However, one should be careful, if this is done with an underlying DF based on the screened hybrid level then this must be done such that the number of required DFT calculations is kept to a minimum, to mitigate computational costs. This will likely exclude high dimensional neural network (HDNN) approaches previously used for, for instance, methane (CHD<sub>3</sub>) on Cu(111), as that approach requires a large dataset to train the HDNN<sup>123</sup>. It may, therefore, be fruitful to test the dynamic surface corrugation (DCM) approach<sup>159</sup>, previously successfully used for  $H_2 + Cu(111)^{160}$ . The benefit of the DCM approach is that only a small number of DFT calculations will be needed to construct the O<sub>2</sub> + Cu coupling-potential required for the implementation of this approach. The second avenue is the inclusion of ehp excitation in the dynamical model. Multiple methods currently exist like LDFA or ODF and more advanced methods are being proposed<sup>161</sup>. Whichever method may be sufficient would first need to be tested. Notably, previous work of O<sub>2</sub> + Ag(111) seems to indicate that the LDFA will not have a substantial impact on the sticking results of O<sub>2</sub><sup>162</sup>. Regardless of the approach, it is again imperative that the amount of DFT calculations required for the approach is kept to a minimum. Last but not least is the search for the new, highly accurate, DF. This DF will likely have an exact exchange fraction somewhere between the HSE06-1/2x-VdFWD2 DF, i.e. 1/2, and the RPBE DF, i.e., 0. The NSCF approach of Chapter 3 may come to mind to scan for new DFs with lower computational costs before committing again to highly costly SCF DFT calculations for a particular DF. These three avenues may, in principle, be explored in parallel as long as the final besttested results of all three avenues are combined into one complete model.

As discussed above, for the  $O_2$  + Al(111) system, the outlook is far less optimistic. It seems that any new screened hybrid DF would need to radically alter the PES to facilitate good agreement with the experiment, which is arguably unlikely, as discussed in greater detail in Chapter 4. Moreover, the high computational costs of the screened hybrid DF makes any higher-level DF an unlikely candidate to generate a new and complete PES. Lastly, Chapter 4 also presents compelling arguments that including surface motion and/or ehp excitation may represent unlikely candidate solutions to achieve further agreement with experiment, though these arguments still need to be validated. Such validation can best be done along similar lines as proposed for the  $O_2$  + Cu(111) system above, i.e., use DCM for surface atom motion and test known ehp excitation modelling approaches. It may, however, be more fruitful for the  $O_2$  + Al(111) system to proceed by finding ways to substantially lower the computational demands of the PES. Currently, the CRP requires a predefined DFT energy grid that is inefficient at (dynamically) sampling the interactions of a diatomic molecule with a metal surface. By making the sampling more efficient, and less rigid, the amount of DFT calculations needed to construct a complete PES may be reduced substantially. Additionally, an implementation of a fast and efficient machine learning algorithm, for example, based on a Δ-machine learning neural network approach<sup>163</sup>, could also be used to generate a PES with a lower number of costly DFT calculations. Either way, reducing the costs of accurate PES generation may then allow for the use of new and computationally more expensive DFs. However, before such time, it remains unlikely that the BOSS DFT approach will be able to more accurately describe the  $O_2$  + Al(111) system.

### 2 Theory

In the previous chapter the theoretical framework for molecular modelling in surface science was briefly discussed and somewhat brushed over in light of summarising the scope and main results of this thesis. However, the complete framework of theory required to accurately model chemical reactions, even for "simple" diatomic molecules, is far from trivial and comes with a large set of interwoven complexities. This chapter will discuss the needed theoretical framework more comprehensively such that the methods and new results of Chapters 3-5 may be understood more clearly. Constructing this framework is done in three major sections. Section 2.1 will discuss the starting point for any and all a priori chemical models and will discuss the first major approximation needed to reduce complexity and facilitate the splitting of the framework into the next two sections. The first of these two sections (Section 2.2) will discuss the theory needed for describing the electrons in the chemical reaction, and the second (Section 2.3) will consider the procedures for modelling the atoms (nuclei) and how to setup the initial conditions for the motion of diatomic molecules.

# 2.1 First steps and the Born-Oppenheimer approximation

Let us begin by taking a major step back: we know that chemically relevant matter in the universe will consist of three major building blocks: electrons, protons, and neutrons. Therefore, put simply, chemical interactions, i.e., chemistry, will be due to interactions of these three building blocks. Luckily, for most chemical cases the neutrons and protons are clustered together into the atomic nucleus and we can simplify this to the interactions of the negatively charged electrons with the positively charged atomic nuclei. Nevertheless, this still results in major hurdles we need to overcome. The first problem is that particles with masses as small as electrons, and sometimes light atomic nuclei as well, cannot be described as just point charges or particles, but require a wavefunction description to describe their behaviour accurately. Put differently, we need quantum mechanics to describe them<sup>10</sup>. The wave-like nature of these particles brings with it uncertainties about the locations and states of the

particles<sup>10,64</sup>. Furthermore, any system that contains three or more interacting particles will become very difficult or even impossible to solve exactly because the state of one particle will often depend on the states of all other particles but the states of all the others are dependent on the state of this same one particle, also referred to as the many-body problem<sup>10,112,164</sup>.

In this thesis, we will not dwell further on the "why" of quantum mechanics, which, although very interesting, goes far beyond the scope of this thesis. Nevertheless, the rest of this chapter, and arguably this whole thesis, is concerned more with the "how" of quantum mechanics for our specific problems.

To start, the quantum mechanical counter-part to the classical second Newtonian law of motion, i.e., the change of a system with time, for a system of N non-relativistic particles with zero spin (more about that in Section 2.2.2) is defined by the time-dependent Schrödinger equation<sup>165</sup>:

$$\mathrm{i}\hbar\frac{\partial}{\partial t}\Psi(\vec{r},t) = \widehat{H}\Psi(\vec{r},t) \tag{2.1}$$

Here  $\hat{H}$  is the (Hermitian) Hamiltonian operator,  $\hbar=h/2\pi$ , h is Planck's constant, t is time,  $\vec{r}$  is the complete spatial (coordinate) vector of all N particles, and  $\Psi$  is the function describing the complete system in a waveform, hereafter referred to as the wavefunction. The Hamiltonian ( $\hat{H}$ ) operator describes the energy of the system and will take a different form depending on the particles in the system<sup>10,112,118,164,165</sup>. Different observables, like position or momentum, are described by different operators. Furthermore, the wavefunction ( $\Psi$ ) needs to adhere to a few requirements. First, it needs to be single-valued. Second, it needs to be square-integrable. Third, it and its derivative function need to be continuous everywhere. Furthermore, probabilities of finding the particles in particular regions at a certain time t are given by the integral<sup>166</sup>:

$$\int |\Psi(\vec{r},t)|^2 d\vec{r} \tag{2.2}.$$

If the region comprises the entire space this integral is equal to 1. Lastly, note that  $|\Psi(\vec{r},t)|^2$  in Equation 2.2 describes the probability density of the system.

In chemistry, we are mostly interested in the energy of the system. The N particle Hamiltonian operator for energy can be split into two major components, the kinetic energy operator  $(\hat{T})$  and the potential energy operator  $(\hat{V})$ , such that:

$$\widehat{H} = \widehat{T} + \widehat{V} \tag{2.3}.$$

If there is no external force or torque on the system, e.g., no electric or magnetic field is applied, then the potential energy can be described by the Coulomb interaction between all the particles in the system. Then, the Hamiltonian for the energy of a chemical system with *N* particles is described by

$$\hat{\mathbf{H}} = -\sum_{i=1}^{N} \frac{\hbar^2}{2m_i} \nabla_i^2 + \underbrace{\frac{1}{2} \sum_{i=1}^{N} \sum_{i \neq j}^{N} \frac{1}{4\pi \varepsilon_0} \frac{q_i q_j}{|\vec{r}_i - \vec{r}_j|}}_{\hat{V}}$$
(2.4).

Here  $m_i$  is the mass of particular particle i,  $\nabla_i^2$  is the Laplacian operator for particle i (when using Cartesian spatial coordinates: the sum of the three unmixed second-order partial derivatives to the Cartesian coordinates),  $\varepsilon_0$  is the electric constant or vacuum permittivity,  $q_i$  the charge of particle i, and  $\vec{r}_i$  is the three-dimensional Cartesian position vector of particle i.

It follows from Equation 2.4 that the Hamiltonian in the Schrödinger equation is not explicitly dependent on time (t), and thus, if the wavefunction  $\Psi(\vec{r},t)$  is a non-degenerate eigenfunction of this Hamiltonian (Eq. 2.4) we can make the "product ansatz", i.e., the wavefunction can be taken as a product of two independent parts:

$$\Psi(\vec{r},t) = \Psi(t)\Psi(\vec{r}) \tag{2.5}.$$

The time dependency of Equation 2.5 can then be described by

$$\Psi(t) = Ce^{\pm iEt} \tag{2.6}.$$

Equation 2.6 shows us that the time dependence of the energy of a system is given by a phase-factor in the complex plane This phase-factor can be divided out to arrive at the time-independent Schrödinger equation, or commonly just referred to as the Schrödinger equation:

$$\widehat{H}\Psi(\vec{r}) = E\Psi(\vec{r}) \tag{2.7}.$$

More generally, the expectation value for the total energy ( $\langle E \rangle$ ) of a system that is described by the wavefunction  $\Psi(\vec{r})$  is described analogous to Eq. 2.2 by

$$\langle E \rangle = \int \Psi^*(\vec{r}) \widehat{H} \Psi(\vec{r}) d\vec{r}$$
 (2.8).

Furthermore, Equation 2.8 is often written as

$$\langle E \rangle = \langle \Psi | \widehat{H} | \Psi \rangle \tag{2.9},$$

using the Bra-Ket or Dirac notation, which is a shorter method of writing the integral<sup>167</sup>, and will henceforth also be used.

We can break down the Hamiltonian even further. That is, we know that the only relevant interactions in chemical systems are those of the *N* number of electrons and *M* number of atomic nuclei, thus, we can split the Hamiltonian into the relevant parts such that:

$$\widehat{H} = -\sum_{i=1}^{N} \frac{\hbar^2}{2m_e} \nabla_i^2 - \sum_{I=1}^{M} \frac{\hbar^2}{2M_I} \nabla_I^2$$

$$-\sum_{i=1}^{N} \sum_{I=1}^{M} \frac{Z_I q_e^2}{4\pi \varepsilon_0 |\vec{r}_i - \vec{R}_I|} + \sum_{i=1}^{N} \sum_{j>i}^{N} \frac{q_e^2}{4\pi \varepsilon_0 |\vec{r}_i - \vec{r}_j|}$$

$$+ \sum_{I=1}^{M} \sum_{J>i}^{M} \frac{Z_I Z_J q_e^2}{4\pi \varepsilon_0 |\vec{R}_I - \vec{R}_J|}$$
(2.10)

Although it may look like we only made Equation 2.4 longer, Equation 2.10 has a few benefits. First, the mass  $(m_e)$  and charge  $(q_e)$  of electrons are well-defined constants, such that we only need the mass  $(M_i)$  and the number of protons  $(Z_i)$  of the nuclei in the system to proceed. Moreover, note that we limit the number of calculations by avoiding double-counting the pair interactions (in Equation 2.4 this is compensated by the 1/2). Lastly, the operator is now clearly split into five different "types" of energy. Namely, the kinetic energies of the electrons and the nuclei, the attractive force between the negatively charged electrons and positively charged nuclei, the repulsion between the nuclei, and the repulsion between electrons. The use of atomic units will make it possible to simplify Equation 2.10 further. In this unit system, all the natural constants in the Hamiltonian are taken equal to 1, reducing the writing of constants that would otherwise be required  $^{168}$ .

Equations 2.7 and 2.10 show us "what" we have to solve to fully describe the energy of a chemical system but it does not show us "how". For instance, in the Hamiltonian, the Coulomb potential operator is a function of all the distances between the particles and in quantum mechanics (when solving for the energy of the system) the particle locations cannot be exactly defined because of their

delocalised wave-like nature<sup>10,112,118,164</sup>. Additionally, finding a suitable (eigen-) wavefunction to properly describe a chemical system is not trivial. Lastly, there is also still the many-body problem that will need to be addressed as well. However, setting up Equation 2.10 like this will allow us to make the first important fundamental approximation to start working on the "how" of quantum mechanics in chemical systems. This is the Born-Oppenheimer approximation (BOA)<sup>117</sup>.

The BOA means that we decouple the motion of the electrons from the motion of the nuclei, which is often allowed because the nuclei have a mass of at least three orders of magnitude higher than the electrons. The handwaving argument is that the electrons can "instantly" move and adjust to any motion of the nuclei. For a complete and detailed derivation of the BOA, the reader is referred to Refs. <sup>117,119</sup>. However, for this thesis, it is convenient to note that the BOA results in splitting the quantum mechanical problem into two, such that we have to first solve the electronic problem:

$$\widehat{H}_{Elec}\Psi(\vec{r}_{Elec}; \vec{R}_{nuc}) = E_{Elec}(\vec{R}_{nuc})\Psi(\vec{r}_{Elec}; \vec{R}_{nuc})$$
(2.11),

where the electronic energy ( $E_{Elec}$ ) is still dependent on the parametric position of the nuclei ( $\vec{R}_{nuc}$ ) as the electronic Hamiltonian is now (using atomic units)

$$\widehat{H}_{Elec} = -\sum_{i=1}^{N} \frac{1}{2} \nabla_i^2 - \sum_{i=1}^{N} \sum_{I=1}^{M} \frac{Z_I}{|\vec{r}_i - \vec{R}_I|} + \sum_{i=1}^{N} \sum_{I>i}^{N} \frac{1}{|\vec{r}_i - \vec{r}_j|}$$
(2.12).

 $E_{Elec}(\vec{R}_{nuc})$  has a set of solutions which represent the different electronic states. Often, and especially in this thesis, we are only interested in the ground-state solution, i.e., the lowest energy solution. Then, by applying the BOA and thus completely neglecting the, often small, coupling between the motion of electrons and nuclei<sup>112</sup> we can, for every value of  $\vec{R}_{nuc}$ , i.e., for every possible geometry of the nuclei, compute the potential energy for the nuclei with:

$$\hat{V}_{Pot}(\vec{R}_{nuc}) = E_{Elec}(\vec{R}_{nuc}) + E_{repulsion}(\vec{R}_{nuc}) 
= E_{Elec}(\vec{R}_{nuc}) + \sum_{I=1}^{M} \sum_{I>I}^{M} \frac{Z_I Z_J}{|\vec{R}_I - \vec{R}_J|}$$
(2.13),

such that we can now solve the Schrödinger equation for the nuclei separately using our resulting potential energy surface (PES) for the movement of the nuclei such that:

$$\left[\hat{T}_{Nuc} + \hat{V}_{Pot}(\vec{R}_{nuc})\right] \Phi(\vec{R}_{nuc}) = E_{Total} \Phi(\vec{R}_{nuc}) \tag{2.14}.$$

Note, that the use of a PES is also possible without necessarily applying the BOA, however, in this work, the BOA is the foundation of all PESs used in Chapters 3,4 and 5.

In the end, the consequence of the BOA is that we are now able to separately solve two "easier" problems instead of one more complicated one. That is, for every "snapshot" of the positions of the nuclei we need to find the energy of the resulting electronic structure. The electronic structure energy gives us the potential energy of the nuclei such that we can calculate either the total energy of the chemical system or we can use the potential energy to calculate where and how the nuclei are going to move in time. Even more powerful is that, at least for this thesis, the atomic nuclei are all considered "heavy". Therefore, we even resort to treating the motion of the nuclei with classical mechanics 112 (see Section 2.3). Thus, we only need to proceed with using quantum mechanics to build the PES for the nuclei, i.e., for a good approximation of the systems described in this thesis quantum mechanics is only required to solve the electronic structure of the system. There are known scenarios where the BOA cannot be applied, i.e., where the coupling between the motion of nuclei and electrons cannot be neglected<sup>59-61,169-171</sup>. These scenarios will be discussed in later chapters when needed.

## 2.2 The electronic structure

The electronic state has been separated from the rest of the system, specifically the motion of the nuclei, by applying the BOA and this has simplified our problem to a certain degree. Yet, the major challenges of "how" still remain, however, for the this section these challenges are limited to those of the electrons in the system. This section will discuss the basics of how electronic structure calculations can be done. It will first show that there is a strategy we can employ to find the best possible approximation for the electronic wavefunction (Section 2.2.1). Then, we will briefly discuss the basics of Hartree-Fock wavefunction-based solutions to the electronic structure(2.2.2), and the method employed to solve the resulting eigenvalue equations to come to a converged electronic energy (2.2.3). After this, we will pivot to Density

Functional Theory (DFT) (2.2.4 and 2.2.5) as an alternative approach to solving the electronic Schrödinger equation. Thereafter, the discussion will move to the DFT implementation that is best for periodic systems (2.2.6).

#### 2.2.1 The variational theorem

The exact wavefunctions for systems with at least two atoms and more than one electron, which interact, are not known, so the only path to solving the electronic structure problem is by trying a so-called "trial wavefunction", or  $\widetilde{\Psi}(\vec{r})$ . Fortunately, we can use the Hermitian nature of the Hamiltonian operator to come up with a strategy for finding the best possible trial wavefunction. By selecting a trial wavefunction that maintains the required boundary conditions of the system and adheres to the wavefunction demands of Section 2.1, we can prove that the expectation value of the energy for that trial wavefunction must always be larger than or equivalent to the true ground state energy of the system, i.e.,

$$\langle E(\widetilde{\Psi}(\vec{r})) \rangle \ge E_0(\Psi(\vec{r}))$$
 (2.15).

Equation 2.15 is easily proven by expressing the trial wavefunction as a linear combination, i.e., as a superposition, of all possible eigenfunctions of the electronic Hamiltonian and calculating the resulting expectation value using Equation 2.8.

In the end, the result of Equation 2.15 means that we can now formulate a strategy for optimising our wavefunctions. That is, the lower the expectation value of the energy of the system, the better the trial wavefunction is as an approximation of the true wavefunction of that system (as long as the boundary conditions remain satisfied). Thus, for any trial wavefunction that fulfils the normalisation constraint and that is dependent on a defined set of parameters we can optimise that trial wavefunction by minimising the expectation value of the energy as a function of those trial wavefunction parameters. This procedure is referred to as the variational method and Eq. 2.15 as the variational theorem<sup>10,112,118,164</sup>.

## 2.2.2 Building a wavefunction

Randomly trying trial wavefunctions and minimising their energy expectation value may still not be an optimal approach to finding a good trial wavefunction. It may, however, be a good idea to use solutions for more easily solvable systems as a basis for our trial wavefunction. It so happens that the Hamiltonian is fully separatable and the Schrödinger equation is exactly solvable in the context of a one-electron system that also adheres to the BOA, like an H atom,  $He^+$  ion, etc.  $^{10}$ . The resulting one-electron wavefunctions, or orbitals, could then serve as a basis for the much harder multi-electron system. This means that for a system of N electrons and M nuclei, it may be possible to start constructing a trial wavefunction by starting with a system of N non-interacting electrons such that the electrons in the wavefunction can be separated by the product ansatz, similar to Equation 2.5, i.e., we would describe the wavefunction of the system with

$$\Psi_{HP}(\vec{r}; \vec{R}) = \prod_{i=1}^{N} \psi_i(\vec{r}_i; \vec{R})$$
 (2.16).

Equation 2.16 is also referred to as the Hartree product (HP) wavefunction  $^{10,112,118,164,168}$ . The benefit of the product ansatz of the HP is that we could then express the Hamiltonian as a sum of N one-electron Hamiltonians, i.e.,

$$\widehat{H} = \sum_{i=1}^{N} \widehat{h}_i \tag{2.17}.$$

Here each one-electron Hamiltonian  $\hat{h}_i$  would then satisfy the N one-electron Schrödinger equations

$$\hat{h}_i \psi_i(\vec{r}_i; \vec{R}) = \varepsilon_i \psi_i(\vec{r}_i; \vec{R}) \tag{2.18}.$$

Then, using the HP for the wavefunction, it follows that the Schrödinger equation for the complete electronic system would be expressed as

$$\widehat{H}\Psi_{HP}(\vec{r};\vec{R}) = \sum_{i=1}^{N} \varepsilon_i \, \Psi_{HP}(\vec{r};\vec{R})$$
 (2.19).

In a real system of N electrons there will be a repulsive force between all the electrons, i.e., the N number of electrons do interact with each other. However, to maintain the ease of solving N one-electron systems this repulsive force can be approximated as the electronic repulsion force on any one electron i, as a

mean field force created by all other *N-1* electrons. This mean-field approximation will then result in the following expression for the one-electron Hamiltonians:

$$\hat{h}_{i} = -\frac{1}{2}\nabla_{i}^{2} - \sum_{I=1}^{M} \frac{Z_{I}}{|\vec{r}_{i} - \vec{R}_{I}|} + \sum_{j \neq i}^{N} \int \frac{\left|\psi_{j}(\vec{r}_{j}; \vec{R})\right|^{2}}{\left|\vec{r}_{i} - \vec{r}_{j}\right|} d\vec{r}_{j}$$
(2.20).

It can be shown that the HP of Equation 2.16 will still be an eigenfunction of the one-electron Hamiltonian of Equation 2.20. Still, the mean-field force is dependent on the one-electron wavefunctions of all other electrons in the system but each of those one-electron wavefunctions will have to be optimised, using variational calculus, with their "own" one-electron Hamiltonian which will, in turn, be dependent on the wavefunctions of all other electrons. It is here that the infamous many-body problem clearly shows up. Luckily, Hartree<sup>168</sup> came up with an iterative solution strategy to this problem that we will discuss more in Section 2.2.3, making the mean-field approximation a useful approach to deal with and 'solve' electron interactions.

Note that in Equation 2.20 we need to loop over all other electrons to compute the mean-field repulsion force but this does mean we are systematically double counting our electron-electron interaction thus, to compute the total energy of a HP(-like) solution to a many-electron system we would need to apply a Coulombic interaction correction:

$$E^{HP} = \sum_{i=1}^{N} \varepsilon_{i} - \frac{1}{2} \sum_{i=1}^{N} \sum_{j\neq i}^{N} \int \int \frac{\left| \psi_{i}(\vec{r}_{i}; \vec{R}) \right|^{2} \left| \psi_{j}(\vec{r}_{j}; \vec{R}) \right|^{2}}{\left| \vec{r}_{i} - \vec{r}_{j} \right|} d\vec{r}_{j} d\vec{r}_{j}$$
(2.21).

At this point, we need to address a larger elephant in the room. The Hartree product is still not a great approximation for electrons as it ignores a few key features of the electron<sup>10</sup>. The first key feature is the Pauli exclusion principle<sup>172</sup> which states that no two electrons can have the same set of quantum numbers. This feature can be addressed by adding the electronic spin-function into the wavefunction. Electron spin it not only added to address the Pauli exclusion principle and the spin of an electron is also observed, but for more details on the "what, why, and how" of electron spin the reader is referred to Refs.  $^{10,112,164}$ . For this thesis, it is important to note that a spin coordinate  $S_i$  needs to be added to

the wavefunction such that an N electron (HP-like) wavefunction would take the form:

$$\Psi^{HP-like}(\vec{r}, \vec{S}; \vec{R}) = \prod_{i=1}^{N} \psi_i(\vec{r}_i; \vec{R}) \sigma(S_i)$$
 (2.22).

Here  $\sigma(S_i)$  is an eigenfunction of the  $\hat{S}_z$  spin operator with only two eigenvalues, i.e.,  $\pm\hbar/2$  (or  $\pm1/2$  in atomic units), and its two orthonormal eigenfunctions are often denoted as  $\alpha$  and  $\theta$ .

However, Equation 2.22 is still not a good approximated wavefunction as we also need to account for two other important physical features of electrons. Namely, electrons are non-distinguishable, i.e., we cannot tell one apart from the other, and most importantly, we need to adhere to the fact that electrons are fermions. Crucially, this means that the total wavefunction needs to be anti-symmetric, i.e., if we were to exchange two electrons in our wavefunction then the wavefunction would need to change sign. These demands may seem a little arbitrary when we describe them here so briefly, and the "why" thereof is a very interesting piece of physics but entirely out of scope for this work, so here it is convenient to take these features as given assertions and proceed. For further clarification, the reader is encouraged to read to Refs. <sup>10,173</sup>.

To satisfy all three assertions, discussed above, the *N*-electron wavefunction needs to take the form of a Slater determinant (SD)<sup>118,174</sup> instead of an HP wavefunction or the spin-modified HP wavefunction of Equation 2.22. An N-electron SD takes the following form:

$$\Psi_{SD}(\vec{r}, \vec{S}; \vec{R}) = \frac{1}{\sqrt{N!}} \begin{vmatrix} \chi_{1}(\vec{r}_{1}, S_{1}; \vec{R}) & \chi_{2}(\vec{r}_{1}, S_{1}; \vec{R}) & \cdots & \chi_{N}(\vec{r}_{1}, S_{1}; \vec{R}) \\ \vdots & \vdots & \ddots & \vdots \\ \chi_{1}(\vec{r}_{N}, S_{N}; \vec{R}) & \chi_{2}(\vec{r}_{N}, S_{N}; \vec{R}) & \cdots & \chi_{N}(\vec{r}_{N}, S_{N}; \vec{R}) \end{vmatrix}$$
(2.23),

in which, analogously to Equation 2.22, each spin-orbital is defined by

$$\chi_i(\vec{r}_i, S_i; \vec{R}) = \varphi_i(\vec{r}_i; \vec{R}) \sigma(S_i)$$
 (2.24).

In the Slater determinant every electron i can be contained in each occupied spin-orbital ( $\chi$ ), as we cannot distinguish between electrons. Moreover, the SD

enforces that the exchange of two electrons (i and j) results in a sign change of the SD-wavefunction.

Fulfilling the three assertions means that the wavefunction has gotten more complicated and that the Coulombic electron interaction in the Hamiltonian requires a compensation component for the possible exchange of electrons, i.e., we need to subtract the exchange energy from the Coulomb potential in the Hamiltonian. The proof for this can be found in Refs. <sup>112,118</sup>. In the end, this means that the *N*-electron, *M*-nuclei (BOA, one-electron) Fock operator, as it is called, will (in atomic units) take a slightly different form to accommodate for this exchange compensation. This form is

$$\hat{f}_{i}^{HF} = -\frac{1}{2} \nabla_{i}^{2} - \sum_{I}^{M} \frac{Z_{I}}{|\vec{r}_{i} - \vec{R}_{I}|} + \underbrace{\sum_{j \neq i}^{N} \int \frac{|\chi_{j}(\vec{r}_{j}, S_{j}; \vec{R})|^{2}}{|\vec{r}_{i} - \vec{r}_{j}|} d\vec{r}_{j}}_{\hat{J}(\vec{r}_{i}, S_{i}; \vec{R})} - \underbrace{\sum_{j \neq i}^{N} \chi_{j}(\vec{r}_{i}, S_{i}; \vec{R}) \int \frac{\chi_{j}(\vec{r}_{j}, S_{j}; \vec{R})\chi_{i}(\vec{r}_{j}, S_{j}; \vec{R})}{|\vec{r}_{i} - \vec{r}_{j}|} d\vec{r}_{j}}_{\hat{K}(\vec{r}_{i}, S_{i}; \vec{R})}$$

Here  $\hat{J}(\vec{r_i}, S_i; \vec{R})$  is the Coulomb operator and  $\hat{K}(\vec{r_i}, S_i; \vec{R})$  is the exchange operator. The Fock operator has the Slater determinant as eigenfunction and the resulting eigenvalues of this operator are the orbital energies of the system where the set of N eigenfunction problems that come from this are called the Hartree-Fock (HF) equations. Similar to the Hartree operator we employ a mean-field theory to describe the electronic interactions with each other. Lastly, the total energy of the chemical system is now given by

$$E_{pot}^{HF}(\vec{r}, \vec{S}; \vec{R})$$

$$= \sum_{i=1}^{N} \left\langle \chi_{i}(\vec{r}_{i}, S_{i}; \vec{R}) \middle| -\frac{1}{2} \nabla_{i}^{2} - \sum_{I}^{M} \frac{Z_{I}}{|\vec{r}_{i} - \vec{R}_{I}|} \middle| \chi_{i}(\vec{r}_{i}, S_{i}; \vec{R}) \right\rangle$$

$$+ \sum_{i=1}^{N} \sum_{j=1}^{N/2} (2 \langle \chi_{i}(\vec{r}_{i}, S_{i}; \vec{R}) | \hat{J}(\vec{r}_{i}, S_{i}; \vec{R}) | \chi_{j}(\vec{r}_{j}, S_{j}; \vec{R}) \rangle$$

$$- \langle \chi_{i}(\vec{r}_{i}, S_{i}; \vec{R}) | \hat{K}(\vec{r}_{i}, S_{i}; \vec{R}) | \chi_{j}(\vec{r}_{j}, S_{j}; \vec{R}) \rangle ) + E_{repulsion}(\vec{R})$$
(2.26).

We can parametrize the spin-orbitals in the SD-wavefunction (Equation 2.24) and then optimise them using the variational theorem (Section 2.2.1). The parametrisation can be done in many different ways but often the orbital wavefunctions in a molecular system are set up as a linear combination of all contributing atom-centred wavefunctions (or atomic orbitals (AO)).

$$\chi_{i}(\vec{r}_{i}, S_{i}; \vec{R}) = \sum_{k}^{K} c_{k,i} \phi_{k}(\vec{r}_{i}, S_{i}; \vec{R})$$
 (2.27).

The atom-centred wavefunctions ( $\phi_k$ ), are themselves normally constructed via another linear combination of basis functions that represent the shapes of the atom-centred wavefunctions (or AOs). These basis functions come in collections that are called basis sets, and these sets can be based on so-called Gaussian-type orbitals 112,175, Slater-type orbitals 112,176, Numerical orbitals 112,164,177, or in principle any other type that will fulfil the required constraints. The choice of basis set will influence the results of the electronic structure calculations, where the general trend is that a larger, more complex, and more complete basis set will improve the results, but increase the demands of the electronic structure calculation. In the following chapters, a very different type of basis sets are used. These types are constructed with an entirely different philosophy and method in mind and these will be discussed in more detail in Sections 2.2.4, 2.2.5, and 2.2.6.

## 2.2.3 Solving the electronic structure

At this point, we have a description of the multi-electron wavefunction and a strategy to optimise that wavefunction via the variational method. Still, we need to find a way to solve the "chicken-egg problem", or many-body problem, that arose from applying the mean-field theory in the one-electron operator, the Fock operator, and the HF equations.

To start, an initial guess of the wavefunction can be made for any initial configuration or geometry of the system, i.e., nuclei positions. This guessed wavefunction is used to construct the mean-field theory (Hartree-Fock or any other) many-body operator. This initial operator, with the initial guess of the wavefunction, is used to optimise the wavefunction it works on, i.e., the wavefunction is minimised with respect to the total energy via the variational

theorem. Then, the optimised wavefunction of this new iteration is used to construct a new mean-field operator, which in turn is used to re-optimise the wavefunction for the next iteration. Then the resulting energy of the new wavefunction is tested against the energy of the previous iteration. If these energies are the same (within a certain threshold) then the calculation is considered converged and is stopped. Otherwise, the procedure is repeated, i.e. the new wavefunction will make a new operator, will make a new wavefunction, and is tested against the previous energy again. The process is continued until the energy is self-consistent, i.e., the value essentially does not change anymore between iterations. This is why this method is referred to as the self-consistent-field (SCF) method. A simplified flowchart of a SCF procedure is shown in **Figure 2.1**.

The procedure as described above, and shown in **Figure 2.1**, is in reality somewhat more complicated and especially optimising the parameters in the wavefunction is far from trivial. For a more complete understanding, the reader is encouraged to read Refs. <sup>112,118</sup>. However, for our purposes, we now have a complete picture of how to "solve" the electronic structure for multi-electron atoms and molecules. A good example of this method in practice for the "simple" H<sub>2</sub> molecule was published already in 1971 by Dewar *et al.* <sup>120</sup>.

Lastly, we must note that the HF method does not yield the exact electronic energy of a molecular system. We have thus far neglected the tendency of electrons to correlate, that is, the movement of electrons is also influenced by the presence and movement of other electrons individually and not by their average overall momentum<sup>112</sup>. This, in turn, influences the total energy of the system. This is why correlation energy is usually defined as the residual energy difference between the converged Hartree-Fock energy and the exact energy of the system. The correlation energy can be included via methods like full configuration interaction<sup>112,120</sup>, but these are computationally very demanding and out-of-scope for this work. Moreover, in Sections 2.2.4. and 2.2.5. a different method of including some correlation effects within a different electronic structure method is discussed.

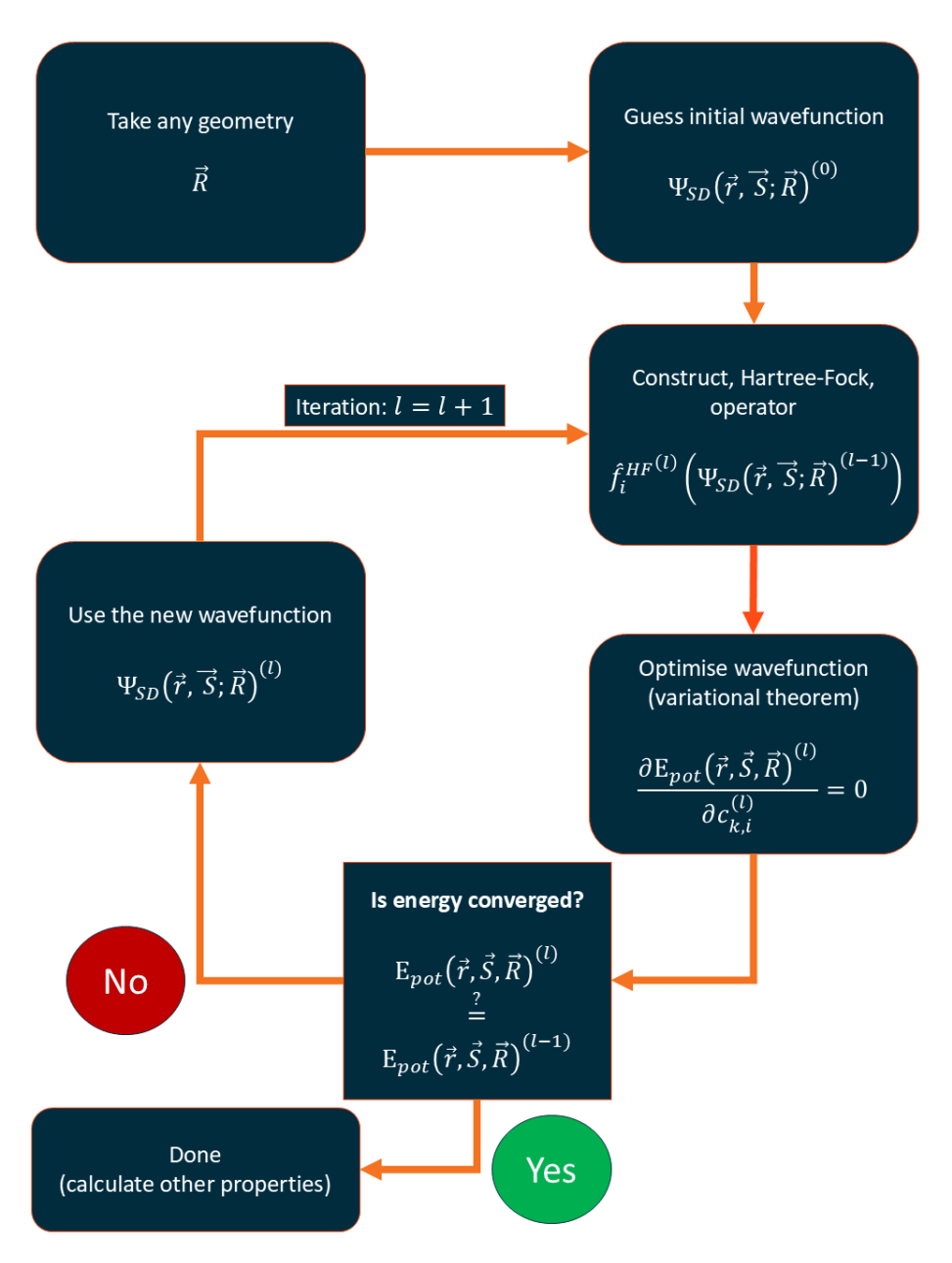


**Figure 2.1**: Simplified flow chart of the self-consistent-field method in optimising a wavefunction in the HF-theory (or other Wavefunction) method.

# 2.2.4 Density functional theory, Hohenberg-Kohn and Kohn-Sham

An observant reader may have picked up on two crucial points in the previous section. First, the complexity of the wavefunction is, thus far, very dependent on the number of electrons, such that a larger chemical system with many electrons quickly becomes unmanageable. Second, the basis functions for the wavefunction are all atom-centred. This makes our solution inherently atomically localised. This is a logical approach for molecules because the electrons are only spread over certain orbitals, and even though overlapping orbitals can share electrons over many orbitals, the electron density tends to be high only in the vicinity of the atomic nuclei. However, as discussed in Chapter 1, there are two different phases to molecule-surface systems, the first is the molecule in the gas-phase and the second is the metal solid. The electronic structure of a metal is very delocalised, such that electrons are, in principle, spread over the entire metal, forming electronic bands of electrons rather than isolated electronic levels. It is not hard to imagine that using an atom-centred wavefunction method to describe such an electronic structure may not be ideal. Furthermore, the computational scaling in HF methods is not very favourable. Computational scaling is the change in the amount of time the calculation would take if the size of the chemical system is changed. In the case of "cheap" wavefunction methods like HF, the scaling nevertheless tends to be  $O(N^4)$ , meaning a system that has two times the number of electrons will need sixteen times more time to be solved. However, most wavefunction methods that go beyond HF, i.e., which try to improve the electronic correlation, tend to scale with  $O(N^5)$  or even higher. Thus, a different approach may be needed.

It may, therefore, be fruitful to use an approach where we can describe the electronic energy with a concept that makes the calculations scale better and could possibly even amount to an observable. The concept that fits these criteria is the electronic density (see also Section 1.2.4). Such a different approach to calculating electronic structures comes in the form of density functional theory (DFT).

The density of the electrons of a system can be directly related to the total number of electrons in that system (*N*):

$$N = \int \rho(\mathbf{r})d\mathbf{r} \tag{2.28},$$

where this integral goes over all space, and  $\rho$  is the electron density as a function of r, which is a three-dimensional position vector, indicated with boldface to avoid confusion with  $\vec{r}$  (which is the complete position vector of all electrons in the system). The use of electron density is intuitive, for instance, the maxima in density could indicate the likely locations of electrons. Another benefit would be that any solution would no longer be dependent on 4N dimensions, that is the three spatial and spin dimensions, but instead, it would depend on just the three spatial coordinates of the electron density. This may, in turn, help to reduce both the complexity and the scaling of electronic structure methods.

These possibilities seem potentially useful though a mapping to an electron density would need to be proven to be possible. For that, we have to turn to the work of Hohenberg and Kohn<sup>121</sup>. They were able to prove that the electron ground state density must determine the so-called "external potential", thus determine the Hamiltonian and thus determine the energy of the system. Here the external potential is defined as:

$$v_{ext}(\mathbf{r}) = \sum_{I=1}^{M} \frac{Z_I}{|\mathbf{r} - \vec{R}_I|}$$
 (2.29),

That is, the external potential is defined as the attractive Coulomb force that the nuclei apply to the electron (density). The rest of the Hamiltonian, as seen in Equation 2.12, is governed by the number of electrons in the system (where the electrons are undistinguishable), and this is already directly related to the density via Equation 2.28. Thus, it only needs to be proven that the external potential is directly determined by the electron density.

This proof is done via *reductio ad absurdum*, i.e., the contrary results in impossibilities, and the proof is rather straightforward. Conversely, two different external potentials  $v_{ext}^a$  and  $v_{ext}^b$ , both describe the same (nondegenerate) ground state electron density  $\rho_0$ . With both external potentials, different Hamiltonians,  $\widehat{H}^a$  and  $\widehat{H}^b$ , will be associated, which both would have their

associated eigenfunctions and eigenvalues  $\Psi_0^a$ ,  $\Psi_0^b$ ,  $E_0^a$ , and  $E_0^b$ . Then the variational theorem(2.2.1) would say that:

$$E_0^a < \langle \Psi_0^b | \widehat{H}^a | \Psi_0^b \rangle \tag{2.30}.$$

This can be rewritten to:

$$E_0^a < \langle \Psi_0^b | \widehat{H}^a + \widehat{H}^b - \widehat{H}^b | \Psi_0^b \rangle \tag{2.31}$$

$$E_0^a < \langle \Psi_0^b | v_{ext}^a - v_{ext}^b | \Psi_0^b \rangle + E_0^b \tag{2.32}$$

The external potential operators are one-electron operators thus Eq. 2.32 can be expressed as a function of the ground state density  $\rho_0$ 

$$E_0^a < \int [v_{ext}^a(\mathbf{r}) - v_{ext}^b(\mathbf{r})] \rho_0(\mathbf{r}) d\mathbf{r} + E_0^b$$
 (2.33)

Then, this same procedure can be done for the ground state energy of b such that:

$$E_0^b < \int [v_{ext}^b(\mathbf{r}) - v_{ext}^a(\mathbf{r})] \rho_0(\mathbf{r}) d\mathbf{r} + E_0^a$$
 (2.34)

Now adding the two inequalities of Eqs. 2.33 and 2.34 will result in:

$$E_0^a + E_0^b < \int [v_{ext}^a(\mathbf{r}) - v_{ext}^b(\mathbf{r})] \rho_0(\mathbf{r}) d\mathbf{r} + E_0^b$$

$$+ \int [v_{ext}^b(\mathbf{r}) - v_{ext}^a(\mathbf{r})] \rho_0(\mathbf{r}) d\mathbf{r} + E_0^a$$
(2.35)

$$E_0^a + E_0^b < \int \left[ v_{ext}^a(\mathbf{r}) - v_{ext}^b(\mathbf{r}) + v_{ext}^b(\mathbf{r}) - v_{ext}^a(\mathbf{r}) \right] \rho_0(\mathbf{r}) d\mathbf{r}$$

$$+ E_0^b + E_0^a$$
(2.36)

Which will result in the following impossibility:

$$E_0^a + E_0^b < E_0^b + E_0^a \tag{2.37}$$

Thus, a non-degenerate ground state density must determine a uniquely associated external potential, Hamiltonian and energy(Hohenberg-Kohn I, HK I) <sup>121</sup>. Further work<sup>112,118</sup> has even shown HK I also holds for exited electron densities. Nevertheless, for this thesis, the ground state is already sufficient.

To effectively utilise HK I to describe electronic energies we need to prove that the variational theorem also holds for the use of an electron density, as we otherwise have no way of optimising the density function. Luckily Hohenberg and Kohn have produced a second theorem that proves just that, i.e., the electron density that minimises the total energy is the exact ground state density<sup>121</sup>. Proving this is rather trivial keeping in mind that any density of a non-degenerate ground state will correspond to a unique wavefunction and energy

(HK I) so that for a trial density  $(\tilde{\rho})$  and corresponding trial wavefunction  $(\widetilde{\Psi}[\tilde{\rho}])$  we have:

$$E[\tilde{\rho}] = \langle \tilde{\Psi}[\tilde{\rho}] | \hat{H}_0[\tilde{\rho}] | \tilde{\Psi}[\tilde{\rho}] \rangle \ge \langle \Psi_0[\rho_0] | \hat{H}_0[\rho_0] | \Psi_0[\rho_0] \rangle = E_0[\rho_0]$$

$$E[\tilde{\rho}] \ge E_0[\rho_0]$$
(2.38)
$$(2.39)$$

As such we can optimise the density of our system by minimising the total energy of the system (Hohenberg-Kohn II, HK II). There is a small caveat that changing certain approximations in the Hamiltonian (see Section 2.2.5.) may break with the variational theorem, but that is due to the introduction approximations in the Hamiltonian, and not because the variational theorem does not hold<sup>112</sup>.

A major difficulty remains though. Yes, a mapping from density to Hamiltonian to wavefunction and energy must exist (HKI), however, there is no basis for what such a mapping would be as the proof for the mapping is done via *reductio ad absurdum*. So even though it is possible to map the energy to the density, we are still not able to do so exactly. Nevertheless, there are clever tricks that can be used to achieve very good approximations with such mappings, and it was the trick of Kohn and Sham<sup>122</sup> that resulted in the most widely used variant of DFT.

Kohn-Sham (KS) DFT is constructed by initially taking a fictitious system of *N* non-interacting electrons that has the same ground-state electronic density as the real system, where the *N* electrons do interact. Kohn and Sham proposed that this is possible because electron density mapping is defined by the number of electrons and the external potential (HK I), which are taken the same for both systems. Here KS used that the exact eigenvalue problems for N non-interacting electrons can be computed exactly (see also 2.2.2). In reality, electrons do interact with each other but this can, in the Kohn-Sham framework, be corrected by adding a correction term to the total energy of the non-interacting electrons. As such, the total energy is no more than the sum of the energy of the non-interacting electrons and the addition of a correction such that the energy functional (i.e., a function that is a function of another function) will be described in full by<sup>112,118,122</sup>:

$$E[\rho(\mathbf{r})] = T_{non-i}[\rho(\mathbf{r})] + V_{nuc}[\rho(\mathbf{r})] + V_{Cee}[\rho(\mathbf{r})] + \underbrace{\Delta T_i[\rho(\mathbf{r})] + \Delta V_{Qee}[\rho(\mathbf{r})]}_{E_{xc}[\rho(\mathbf{r})]}$$
(2.40).

Here the terms are, in order of appearance: the non-interacting electronic kinetic energy, the nuclear-electron attractive Coulombic force, i.e., the external potential; the classical electron-electron Coulomb interaction; the correction on the kinetic energy term including electronic correlation; and the quantum correction to the electronic interaction including the electron exchange energy. The last two terms are generally combined into one collection of unknowns that is referred to as the exchange-correlation functional  $(E_{xc}[\rho(\mathbf{r})])^{122}$ . This term may also include other corrections to the non-interacting electron system, like a self-interaction correction<sup>112</sup>.

For the non-interacting electrons, the exact eigenfunction is the Slater determinant (see Equation 2.23) but now built up using the one-electron KS orbitals. The corresponding electron density is

$$\rho(\mathbf{r}) = \sum_{i=1}^{N} \langle \chi_i | \chi_i \rangle \tag{2.41}.$$

Here  $\chi_i$  are the KS-orbitals, which are similar, but not equal, to the AOs used in Equation 2.23. We can now represent the energy functional in atomic units as<sup>112</sup>:

$$E[\rho(\mathbf{r})] = \sum_{i=1}^{N} \left( \left( \left\langle \chi_{i} \middle| -\frac{1}{2} \nabla_{i}^{2} \middle| \chi_{i} \right\rangle \right) - \left\langle \chi_{i} \middle| \sum_{l=1}^{M} \left( \frac{Z_{l}}{|\mathbf{r}_{i} - \vec{R}_{l}|} \right) \middle| \chi_{i} \right) \right)$$

$$+ \sum_{i=1}^{N} \left( \left\langle \chi_{i} \middle| \frac{1}{2} \int \frac{\rho(\mathbf{r}')}{|\mathbf{r}_{i} - \mathbf{r}'|} d\mathbf{r}' \middle| \chi_{i} \right\rangle \right) + E_{xc}[\rho(\mathbf{r})]$$

$$(2.42).$$

This will mean it is now possible to start solving, and also optimising, a set of N number of one-electron non-interacting eigenvalue equations of the form:

$$\hat{h}_i^{KS} \gamma_i = \varepsilon_i \gamma_i \tag{2.43},$$

where the one-electron Kohn Sham Hamiltonian is given by:

$$\hat{h}_{i}^{KS} = -\frac{1}{2} \nabla_{i}^{2} - \sum_{I=1}^{M} \left( \frac{Z_{I}}{|\mathbf{r}_{i} - \vec{R}_{I}|} \right) + \int \frac{\rho(\mathbf{r}')}{|\mathbf{r}_{i} - \mathbf{r}'|} d\mathbf{r}' + V_{xc}[\rho(\mathbf{r})]$$
(2.44),

and in which

$$V_{xc}[\rho(\mathbf{r})] = \frac{\delta E_{xc}[\rho(\mathbf{r})]}{\delta \rho(\mathbf{r})}$$
(2.45)

is the functional derivative of the exchange-correlation energy as presented in 2.42<sup>112</sup>.

From this point on, solving the known parts of the KS equations is very similar to the wavefunction approach as discussed in 2.2.2 and 2.2.3, and from Equation 2.42 it is obvious that yet another self-consistent field-based approach will be required. To reiterate, the Hamiltonian determines the density but requires a density to be determined first. Thus, one has to: guess, improve, and reuse the density until it no longer changes. Solving the unknown exchange-correlation part ( $V_{xc}$ ) of the energy functional (hereafter referred to as density functional, or DF) is, however, still far from trivial. Luckily, in the KS approach, the unknowns are reduced to a smaller fraction of the total value and any error made there will influence the final result less than trying to come up with one whole new answer for a density energy mapping. The majority of research and studies done to improve the quality of DFT are all to try and find a better approximation to this  $V_{xc}$ . Some of the more common approaches will be discussed in the next section.

## 2.2.5 Exchange-correlation functional approximations

The exact form of the  $E_{xc}$  is not known, but it stands to reason that this term will, just like the one-electron potential, depend on the electron density. Thus,  $E_{xc}$  is often expressed as an integral over a product of the density and the so-called "energy-density"  $\varepsilon_{xc}$  (this is not required but is a common notational method)<sup>112</sup>. In this frame,  $E_{xc}$  is described by:

$$E_{xc}[\rho(\mathbf{r})] = \int \rho(\mathbf{r}) \varepsilon_{xc}[\rho(\mathbf{r})] d\mathbf{r}$$
 (2.46).

Here the energy density functional is often split up into contributions from exchange and correlation 112,118:

$$\varepsilon_{xc}[\rho(\mathbf{r})] = \varepsilon_x[\rho(\mathbf{r})] + \varepsilon_c[\rho(\mathbf{r})]$$
 (2.47).

However, again this is not always the case<sup>112</sup>, and it should be reiterated that the  $E_{xc}$  DF is meant to compensate for more than just exchange and correlation energy, for instance for an error due to electrons interacting with themselves (which occurs in the construction of the density). Additionally, splitting up the exchange-correlation functional also does not mean that the actual contributions are necessarily properly split, as the exact form of the  $E_{xc}$  DF is not known<sup>112,118,173</sup>.

Nevertheless, there now is a starting point for approximating the  $E_{xc}$  DF. The simplest and most logical starting point is to let the exchange-correlation be

dependent on a single value of the electron density at a given location, i.e., to let there be a *local* dependency on the density in Eqs. 2.46 and 2.47. This is referred to as the local density approximation (LDA). An example of local density exchange energy is the Slater exchange based on the uniform electron gas<sup>112,178,179</sup>:

$$\varepsilon_{x}[\rho(\mathbf{r})] = -\frac{9\alpha}{8} \left(\frac{3}{\pi}\right)^{\frac{1}{3}} \rho(\mathbf{r})^{\frac{1}{3}}$$
(2.48),

where  $\alpha$  can take either the value 1 or  $2/3^{180,181}$ , depending on the underlying derivation (see Ref. <sup>112</sup> for more information). Setting up the correlation contribution has generally always been a far more arduous task, and quickly goes beyond the scope of this work and the reader is referred to the works of <sup>182–187</sup> for detailed derivations on that end.

It is at this time a good moment to discuss that the LDA can also work for calculations where the electrons have to be spin polarised, i.e., when there are unpaired electrons in the mix. The electron spin density is simply given by the normalised spin polarization factor<sup>112</sup>:

$$\zeta(\mathbf{r}) = \frac{\rho^{\alpha}(\mathbf{r}) - \rho^{\beta}(\mathbf{r})}{\rho^{\alpha}(\mathbf{r}) + \rho^{\beta}(\mathbf{r})} = \frac{\rho^{\alpha}(\mathbf{r}) - \rho^{\beta}(\mathbf{r})}{\rho(\mathbf{r})}$$
(2.49),

where  $\rho^{\alpha}$  is the  $\alpha$ -spin density and  $\rho^{\theta}$  is the  $\theta$ -spin density. At this point, the exchange-correlation energy density can be expressed as a function of the total electron density and the spin polarisation such that <sup>112</sup>:

$$\varepsilon_{xc}[\rho(\mathbf{r}), \zeta(\mathbf{r})]$$

$$= \varepsilon_{xc}[\rho(\mathbf{r})] + \left(\varepsilon_{xc}^{Spin}[\rho(\mathbf{r})]\right)$$

$$-\varepsilon_{xc}[\rho(\mathbf{r})] \left(\frac{(1+\zeta(\mathbf{r}))^{\frac{4}{3}} + (1-\zeta(\mathbf{r}))^{\frac{4}{3}} - 2}{2(2^{\frac{1}{3}} - 1)}\right)$$
(2.50),

where  $\varepsilon_{xc}^{Spin}[\rho(r)]$  is the energy density functional based on the uniform electron gas of electrons with all uniform spin, and  $\varepsilon_{xc}[\rho(r)]$  is the regular ground state energy density. Equations 2.49 and 2.50 show that the addition of spin into DFT will make the formulation more complicated. Because it requires the evaluation of the uniform spin exchange-correlation energy functional it also slightly increased computational demands, though not by much. For the sake of clarity in formulation, the spin density terms will from now on not be discussed

in detail, but it is good to have noted that using spin densities is possible and will be used in Chapters 3-5.

The LDA is a local approximation to  $E_{xc}$ . When locally approximating any function, a Taylor expansion may quickly come to mind. As such, a common next step in improving the exchange-correlation energy is to go beyond the dependence on the local value of the density and to also include a dependence on the local first-order derivative, i.e., gradient, of the density. This brings us to the generalised gradient approximation (GGA) to the exchange-correlation DF.  $E_{xc}$  can now be expressed as:

$$E_{xc}[\rho(\mathbf{r}), \nabla \rho(\mathbf{r})] = \int \rho(\mathbf{r}) f[\rho(\mathbf{r}), \nabla \rho(\mathbf{r})] d\mathbf{r}$$
 (2.51),

where the function f can take some different forms but is often<sup>112</sup> set as:

$$f[\rho(\mathbf{r}), \nabla \rho(\mathbf{r})] = \varepsilon_{xc}^{LDA}[\rho(\mathbf{r})] + \Delta \varepsilon_{xc} \left[ \frac{|\nabla \rho(\mathbf{r})|}{\rho(\mathbf{r})^{\frac{4}{3}}} \right]$$
(2.52).

However, it should be noted that the precise implementations of GGA DFs vary greatly. It is not uncommon for semi-empirical parameters to be introduced into the exchange-correlation DF to improve the description for certain systems. For an example of a GGA DF without the use of such parameters, the reader is strongly encouraged to read the work behind the PW91<sup>188</sup> and/or PBE<sup>154</sup> DF, which are some of the most commonly applied DFs, and the PBE DF is also used further in Chapters 3-5. Going even beyond the GGA, it is possible to take the Taylor expansion further, with limited returns, to start using the second-order derivative of the density as well. These types of DFs are then referred to as meta-GGA (mGGA) DFs<sup>112</sup>. These types of DFs are moving beyond the scope of this thesis.

A quite different approach to improving the exchange-correlation description is to use the fact that we have a potentially more precise description for the exchange energy based on the HF wavefunction method (Equation 2.25, Section 2.2.2). Since the density in KS-DFT is often based on Slater-like eigenfunctions, computing the exact exchange using the  $\widehat{K}(\vec{r_i}, S_i; \vec{R})$  operator (see Eq. 2.25 and 2.26) is possible. Mixing this associated exact exchange with the semi-local exchange-correlation energy amounts to the use of a so-called hybrid functional. Note that this will increase computational demands moving from the worst-case

DFT scenario of  $O(N^3)^{112,118}$  to a worst-case of  $O(N^4)$  scaling  $^{112,118}$ . Additionally, the exchange-correlation energy is not just a correction for the exchange energy and cannot be cleanly split into two separate contributions  $^{112}$ . Thus, replacing the entire semi-local exchange contribution with exact exchange does not necessarily yield any improvement over GGA DFs. As such, the exact exchange is mixed into the (usually GGA) DFT exchange with a certain fraction  $(\alpha)^{112}$ :

$$E_{xc}^{Hybrid} = \alpha E_x^{HF} + (1 - \alpha) E_x^{DFT} + E_c^{DFT}$$
 (2.53).

One of the most straightforward global hybrid DFs, which uses PBE as the GGA backbone, is the PBE0 DF where  $\alpha$  is set to a value of  $1/4^{152,153}$ . Finally, it should be noted that the global description of exact exchange is not accurate for largerrange Coulombic systems like metals where the interaction between electrons needs to be screened at long range<sup>156,189–194</sup>. To accommodate this range-separated, or screened exchange, hybrids have been developed where the exact exchange energy is only active at short range and is fully replaced with semi-local exchange at long range, see also Chapters 3, 4 and 5.

Analogously to hybrid DFs, it is also possible to replace the correlation contribution with better approximations of non-local correlation energies. Specific non-local correlation functionals are capable of approximately describing the long-range like Van der Waals (VdW) dispersion interaction<sup>182</sup>. However, such improvements again come with additional computational demands. Furthermore, it is possible to combine the two concepts of exact exchange and long-range correlation interaction into a single DF. In Chapters 4 and 5 we have done exactly that with a screened hybrid DF, HSE<sup>156,189,190</sup> and the VdW-DF2 correlation DF<sup>183,195</sup>. These two chapters go into more detail about the implementation and the DF so there is no need to repeat that here, though it should be noted that the combination of these different DFs is not necessarily internally consistent. Only recently, work has been done to try and build an internally consistent combination of exact exchange and non-local correlation, and an example of such a DF is VdW-DF-ahcx<sup>194</sup>.

# 2.2.6 Periodic boundary conditions, plane waves, Bloch's theorem, and pseudopotentials

A proper description of metal surfaces will require a large number of atoms. Smaller clusters of atoms will inevitably exhibit nanoparticle behaviour. This type of behaviour, though interesting, is not what we want when describing a macroscopic metal surface. A clever way to resolve this is by imposing so-called periodic boundary conditions (PBC). In a PBC environment, a given unit cell is constructed and images of that unit cell are repeated infinite times in two or all three dimensions. This means that only the atoms in the cell need to be simulated but the images of the cell do ensure that atoms on the edges of the cell still "feel" like they are part of an infinite ensemble 112. In mathematical terms, PBC in three dimensions means that for any potential:

$$V(\vec{X}) = V(\vec{X} + \vec{A}) \tag{2.54}$$

$$\vec{A} = n_1 \vec{a}_1 + n_2 \vec{a}_2 + n_3 \vec{a}_3 \tag{2.55},$$

where  $\vec{X}$  are Cartesian coordinates within the cell, the  $n_i$  integers and the  $a_i$  cell-vectors in 3D Cartesian space with a given orthogonal component spanning the repeating unit cell (the three lattice vectors do not need to be fully orthogonal). A downside is that the atoms in the cell interact with the periodic images of themselves, which if the cell is not large enough may cause artefacts in the results<sup>112</sup>.

Most solid compounds, except for amorphous solids, can inherently be described by a given repeating cell. For simple non-alloy metals such unit cells can be constructed from a single atom placed inside a box spanned by three distinctly sized vectors spanning three-dimensional space. For a (metal) surface, this becomes more difficult as the periodicity will be broken in at least one direction. The interface between the bulk metal and the vacuum creates a discontinuity that needs to be dealt with. The simplest solution is to create PBC only in the direction of the surface-plane (See **Figure 2.2A** for an FCC(111) surface example, the surface-plane is indicated by the *U, V*-plane), excluding the surface normal (i.e., the *Z*-axis). This does require the resulting surface "slab" to be thick enough to properly simulate the underlying metal bulk, and it also means that the slab has two surfaces, one on the top side (higher *Z*) and one on the bottom side of the slab. If an electronic structure code will allow for this,

then this type of setup will work well enough for atomic orbital-based approaches. If the code does not allow for axis selective PBC (like two-dimensional PBC) then the other option is to include a large vacuum along the *Z*-axis such that the slab cannot interact, or hardly interacts with its periodic images. An example of such a setup can be found in **Figure 2.2B**. For this thesis, a computer program was used that imposed PBC in all three dimensions, for reasons that will be discussed below. Thus, in this thesis, all metal slabs will be separated with a minimum of 10 Å vacuum. Further slab-specific details can be found in the method sections of the relevant chapters.

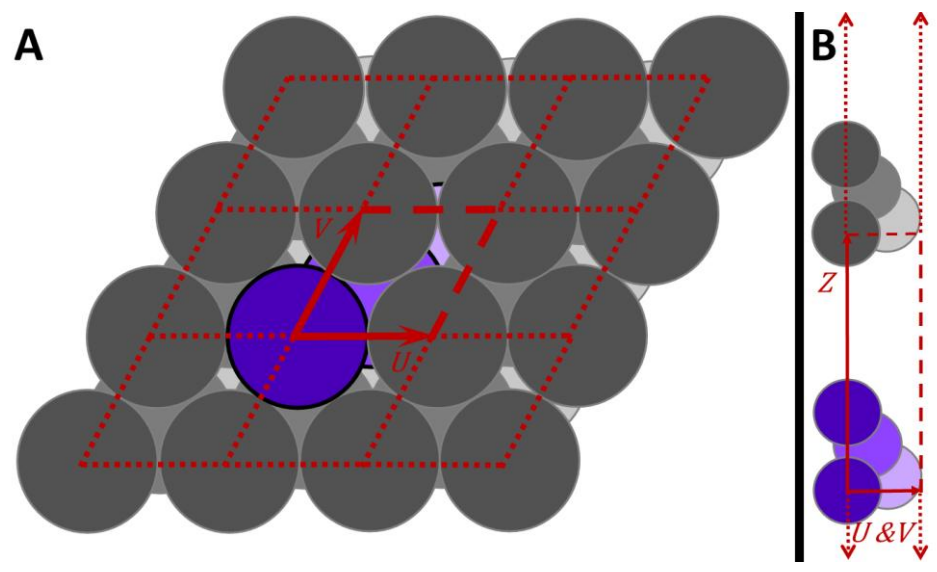


**Figure 2.2:** Schematic description of a periodic metal FCC(111) surface. Purple shades indicate the original atoms in the repeating cell, grey depicts periodic images and red arrows indicate the relevant axes where the red dashed lines close the repeating unit, red dots show the periodic images of the cell translated to different locations; **A**: periodicity in the surface (U,V-) plane; **B**: periodicity along the surface normal (Z axis) for a 4 layer surface slab, including the layer of vacuum in-between surfaces.

PBC allow for an elegant trick to ease the description of the electrons in a periodic potential (like that of metals) via Bloch's theorem<sup>181</sup>. This theorem states that any eigenfunction of the Schrödinger equation in a periodic potential can be expressed as a plane wave such that:

$$\psi_{\vec{k}}(\mathbf{r}) = \mu_{\vec{k}}(\mathbf{r})e^{i\vec{k}\mathbf{r}} \tag{2.56}.$$

In Equation 2.56  $\mu_{\vec{k}}(r)$  is a periodic function that obeys the periodicity of the lattice, i.e., the potential as defined in Equation 2.54, and  $\vec{k}$  is a wave vector in

the first Brillouin zone. The Brillouin zone is the reciprocal version of the periodic unit cell.

Using Bloch's theorem the KS-orbitals, as defined in Equations 2.41 and 2.42, and for a given sample point in k-space, the KS-orbital can be expanded as a Fourier-series, i.e., plane wave basis set, such that:

$$\chi_{i,\vec{k}}(r) = N \sum_{\vec{G}} c_{i,k}(\vec{G}) e^{i(\vec{k}+\vec{G})r}$$
(2.57).

Here N is the normalisation constant  $c_{i,k}$  are the expansion coefficients, and  $\tilde{G}$  are reciprocal lattice vectors. For an infinite sampling of the reciprocal lattice this series is exact, however, computationally the series is limited by a discretisation over a k-space grid and a "cut-off" energy such that:

$$\frac{1}{2}\left|\vec{k} + \vec{G}\right|^2 \le E_{cut-off} \tag{2.58}.$$

In practice, this means that the k-point grid and cut-off energy need to be chosen wisely to ensure proper sampling of the periodic electronic state and thereby ensure convergence of the total energy. Put simply, more k-points mean more plane waves and a higher cut-off energy also means more plane waves. More plane waves mean that the basis set further approaches the limit of the exact solution, but at a greater computational cost.

The plane wave basis set is quite useful for efficiently describing the periodic nature of metals and for describing the highly delocalised electrons in the metals. However, it comes with a certain computational cost. For one, the plane wave approach means periodicity needs to be ensured in all three dimensions and that the size of the vacuum separating the slabs (see above) will increase the periodic unit cell size thus increasing the number of plane waves required. That is, in a plane-wave electronic structure method we "pay" computational costs for the size of the vacuum. An additional downside is the large costs associated with hybrid DFs as solving the exact exchange operator (Eq. 2.25) using plane waves can be a rather demanding task. Lastly, the description of larger atoms, that is atoms with many electrons, and thus many nodes in the wavefunction of valence electrons (because of orthogonality demands) can quickly require very large basis sets to properly describe the highly oscillatory behaviour of such wavefunctions.

The complexity of the basis set for many-electron atoms can be reduced by the use of pseudopotentials<sup>196,197</sup>. The idea is that the electrons close to the nuclei of heavy, many-electron atoms, also referred to as the "core-electrons", are not chemically relevant. Therefore a more simplistic description of those electrons and the resulting effective potential can be used to limit the size of the basis set for the valence electrons. Pseudopotentials additionally allow for the inclusion of relativistic effects of the core-electrons. Thus far, relativistic effects have not been discussed in this thesis, and the reader is referred to Ref. <sup>198</sup> for more information. Briefly, electrons close to the nuclei move fast enough that such effects will start to influence the electronic structure. The use of pseudopotentials incorporating such effects is a way to approximately include these effects without altering the electronic structure method.

A principal idea behind pseudopotentials is that the chemically relevant valence electrons do not interact with the full charge of the nuclei as the electrons in between the nuclei and the valence electrons shield, or screen, the charges of the nuclei and the core-electrons. Also, the core-electrons do not affect the chemistry much. As such we can describe the nuclei and core electrons by one, different, effective potential with a given 'core' radius  $r_c$ . The nuclei and the core-electrons within this core radius are no longer distinctly described but are described by a pseudo-potential. This will simplify the calculation with the wavefunction describing the valence electrons, as it no longer needs to be made orthogonal to wavefunctions describing the core-electron wavefunctions. (see **Figure 2.3** for a schematic drawing).

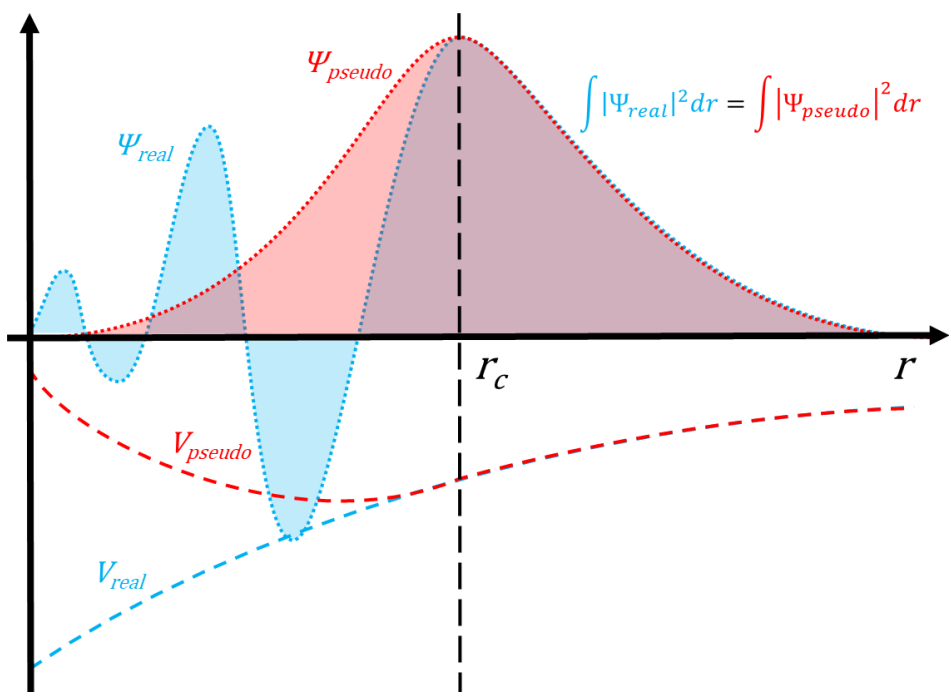


**Figure 2.3**: Schematic drawing of a pseudopotential and how it compares to a real potential. Pseudo potential and wavefunction in red, real potential and wavefunction in light blue. The horizontal axis measures the distance of the electron to the nucleus. The shading serves as a guide to the eye.

To ensure that the chemical state of the atom is not altered pseudopotentials are usually constrained such that the wavefunction and potential outside of  $r_c$  is described the same as the real wavefunction and potential. Furthermore, the pseudopotentials are often norm-conserving, meaning that the norm of the pseudo-wavefunction is kept the same as that of its real counterpart, i.e.,

$$\int |\Psi_{real}|^2 dr = \int |\Psi_{pseudo}|^2 dr \tag{2.59}.$$

However, to further reduce the basis set size this last constraint is not always adhered to. The electronic structure calculations in the following chapters have all used a slightly different approach with the same aim, namely the Projector Augmented Wave (PAW)<sup>199</sup> method to describe the core-electrons. In this method, a linear transformation is used to transform the rapidly oscillating (KS)-wavefunction near the core of the atom to a smooth function. This is done in such a way that the wavefunction is only transformed within the cutoff radius, similar to other pseudopotentials. However, in the PAW method, there is no

norm-conserving. Furthermore, all-electron observables can still be computed with the PAW method by simply reversing the linear transformation. The finer details of PAW pseudopotentials are outside the scope of this thesis but further reading is available at Refs. <sup>199,200</sup>.

#### 2.2.7 From electronic structure to potential energy surface

All of the last six sub-sections put together mean that it is possible to calculate accurate electronic energies (within the DF approximation) for a given geometry of the nuclei. This still leaves two possible classes of methods to use this electronic structure to compute any motion of the nuclei, i.e., to simulate the chemistry that occurs. The first and maybe the most straightforward class of methods is *ab initio* or Born-Oppenheimer molecular dynamics (AIMD/BOMD). In this approach, the forces on the nuclei are calculated from the electronic structure "on-the-fly". Whenever the nuclei are at a given position the electronic structure is computed, which will, in turn, govern the potential and forces on the nuclei (see Section 2.3). The AIMD/BOMD approach may at face value seem logical but it comes with large computational demands when thousands of molecular trajectories need to be simulated because each trajectory then requires hundreds of electronic structure calculations in sequence. As such, for lower dimensional systems, i.e., smaller molecules, there is a more efficient class of methods.

When dealing with a limited number of degrees of freedom (DOF) it may be more efficient to pre-compute the electronic structure for a large grid of molecular geometries as a function of the DOFs of the system and use interpolative techniques or fitting to form a continuous energy representation. Put differently, a potential energy surface (PES) is computed in advance, after which, this PES is used to solve the equations of motion efficiently. Note that with more degrees of freedom, this approach may quickly become less efficient, as the initial sampling of geometries to form the PES will grow fast with the number of degrees of freedom.

In the following chapters, all molecular dynamics (MD) calculations are limited to that of diatomic molecules whilst the metal surface is kept static. Thus, the

calculations are limited to six dimensions, see Chapters 3, 4, and 5 for the relevant breakdown of the DOF. For such a setup the construction of a PES is most efficient. In this thesis, the discreet electronic structure energies are turned into a continuous PES description based on the corrugation-reducing procedure  $(CRP)^{201,202}$ . In the CRP the six-dimensional (6D) molecule-metal potential energy  $(V^{6D})$  is set up such that:

$$V^{6D}(\vec{\Gamma}) = I^{6D}(\vec{\Gamma}) + \sum_{l=1}^{2} V_l^{3D}(\vec{\gamma}_l)$$
 (2.60)

$$V_l^{3D}(\vec{\gamma}_l) = I^{3D}(\vec{\gamma}_l) + \sum_{m=1}^{M} V_{l,m}^{1D}(d_{lm})$$
 (2.61).

Here  $\vec{\Gamma}$  are the six coordinates of the molecule,  $\vec{\gamma}_l$  the three coordinates of the atom I (which can be calculated from  $\vec{\Gamma}$ ),  $d_{lm}$  is the distance between the atom I of the diatomic molecule and a surface atom m, the total number of metal surface atoms taken into account is M, I<sup>6D</sup> is the molecular six-dimensional interpolation function,  $I^{3D}$  is the atomic three-dimensional interpolation function, and  $V^{1D}$  is the one-dimensional corrugation reduction function.  $V^{1D}$  is fitted to the atom-surface interaction of a geometry in which atom I is put above a top surface atom and its distance to the surface atom is varied. This procedure is set up to ease the interpolation procedure, produce a six-dimensional function ( $I^{6D}$ ) that contains less corrugation than  $V^{6D}$  and is, therefore, easier to interpolate, and thereby limit the number of electronic structure calculations needed to construct a smooth PES. Put differently it reduces the number of oscillations that will occur in the interpolation functions when only a limited amount of electronic structure data is available. This procedure has been developed previously and in this thesis it is only further applied, thus the procedure is described in more detail in the following Refs. <sup>201–204</sup>.

# 2.3 The nuclear motion and initial conditions

The potential energy surface that results from the electronic structure calculations as discussed in Section 2.2 can be used directly to influence the movement of the nuclei via Newtonian physics. It is generally assumed that the atomic nuclei, with the possible exception of the nuclei of hydrogen or helium, tend to be too heavy for the quantum mechanical effects associated with their

motion to be relevant. Moreover, the mass difference between the electrons and the nuclei is so large that the motion of the nuclei can be approximated by the motion of the atom as a whole. Therefore, the acceleration of any atom, i.e., atomic nucleus, I with atomic mass  $M_I$  will be given by:

$$\vec{a}_I(\vec{R}_I(t)) = \frac{-\nabla_I V_I^{Elec}[\vec{R}(t)]}{M_I} = \frac{d^2 \vec{R}_I(t)}{dt^2}$$
(2.62).

The acceleration at a given time t can be used to update the positions of the atoms with a given time step  $\Delta t$  via a simple Taylor expansion truncated at the second order in the position:

$$\vec{R}_{I}(t + \Delta t) = \vec{R}_{I}(t) + \frac{d\vec{R}_{I}(t)}{dt} \Delta t + \frac{1}{2!} \frac{d^{2}\vec{R}_{I}(t)}{dt^{2}} \Delta t^{2}$$
 (2.63).

This can be rewritten as

$$\vec{R}_I(t+\Delta t) = \vec{R}_I(t) + \vec{v}_I(t)\Delta t + \frac{-\nabla_I V_I^{Elec}[\vec{R}(t)]}{2M_I}\Delta t^2$$
 (2.64).

Here  $\vec{v}_I(t)$  is the velocity of an atom I and the potential energy determining the force working on the atom at a given time t is dependent on the positions of all other atoms in the system at that same time t. There are several methods to effectively solve the time propagation in nuclear dynamics, the most famous perhaps being the velocity-Verlet algorithm<sup>205</sup>. In this thesis however, a more complicated algorithm, the Burlisch–Stoer algorithm<sup>206</sup>, is used to improve numerical stability as one needs to be careful with selecting the size of the timestep ( $\Delta t$ ) when the gradient of the PES changes fast with the change of positions of the atoms, i.e., when the gradient of the acceleration is far away from zero. The algorithm used for this thesis is discussed in some more depth in Section 2.3.1 below. After that, Section 2.3.2 will discuss the sampling of the initial molecular conditions used to start the MD trajectories.

## 2.3.1 Burlisch–Stoer algorithm

In this thesis, the time propagation for the MD trajectories is all done using the Burlisch–Stoer algorithm (BuSA)<sup>206</sup>. The exact functionality of this algorithm is out of the scope of this work, and the reader is referred to <sup>207</sup> for a detailed overview. However, below a few key points will be briefly discussed to give an inkling of the procedure and its benefits. The BuSA works by implementing

Hamiltonian mechanics for propagating nuclear motion. This means that de change of position of an atom in time will be governed by:

$$\frac{d\vec{R}}{dt} = \frac{\partial \hat{H}(\vec{R}, \vec{P})}{\partial \vec{P}} \tag{2.65},$$

while its change of momentum is determined by

$$\frac{d\vec{P}}{dt} = -\frac{\partial \hat{H}(\vec{R}, \vec{P})}{\partial \vec{R}} \tag{2.66},$$

in which

$$\widehat{H}(\vec{R}, \vec{P}) = \frac{\vec{P}^2}{2\underline{M}} + \widehat{V}(\vec{R})$$
 (2.67).

Here  $\vec{P}$  is the momentum vector of all atoms in the system,  $\hat{V}$  is the potential as defined by the electronic structure and M is the mass of the respective atom. From 2.65-2.67, it follows that  $^{206,207}$ :

$$\frac{d\vec{R}}{dt} = \frac{\partial \hat{T}(\vec{P})}{\partial \vec{P}} = \frac{\vec{P}}{M} = \vec{v}$$
 (2.68),

$$\frac{d\vec{P}}{dt} = -\frac{\partial \hat{V}(\vec{R})}{\partial \vec{R}} \tag{2.69}.$$

In the end, Hamiltonian mechanics is a reformulation of the previously mentioned Newtonian mechanics but for the BuSA it is the more useful formalism. Additionally, it turns one second-order differential equation into two separate first-order differential equations.

The BuSA uses the above equations to propagate the atoms in time via a predictor-corrector method. In such an integration method there are always two distinct steps, the first is to use an arbitrary fit to previous function values and derivatives to extrapolate the value of the next function value. The second step will use an interpolative method, often based on the predicted value, to improve the initial fit approximation.

In the BuSA this procedure is along the following lines<sup>206</sup>. First, an initial large time step S is chosen such that a new position for t+S is extrapolated (updating velocities where required with Equation 2.68) by subdividing S into N smaller sub-steps  $S_n$  and using Richardson extrapolation<sup>208</sup> to find

$$\vec{R}(t_2) = \vec{R}(t_1 + S)$$
 (2.70),

by extrapolating  $N_{max}$  times:

$$\vec{R}(t_{i+n}) = \vec{R}(t_i + s_n)$$
 (2.71).

These results can then be fitted to a rational function to estimate an error of the Richardson extrapolation. If the error is not yet sufficiently small the number of substeps  $N_{max}$  is increased such that over time:

$$s_n \to 0 \land N_{max} \to \infty$$
 (2.72).

The more steps used in the Richardson extrapolation the more accurate it will be<sup>208</sup>. In practise the extrapolation error will eventually fall below a preset threshold for a given amount of substeps and the approximation is stopped there, or a maximum number of iterations ( $iter_{max} = 9$ )<sup>209</sup> is reached. In this last scenario, the initial timestep S may have been too large and is halved after which the process is repeated. If the first scenario is encountered the solution to the differential equations (Eqs. 2.65 and 2.66) will have been found for the next point in time, and a new step size S for the next step will be chosen based on<sup>209</sup>:

$$S_{new} = \begin{cases} 1.5S; & if: iter \le 6 \\ 0.6^{iter-0.6} * 1.5S; & if: iter > 6 \end{cases}$$
 (2.73).

This way the step size of the time integration will always adapt to the gradient of the potential, i.e., if the potential is very steep or, more generally, shows many oscillations, the timestep will be reduced until accurate results are obtained, or a minimum size threshold is reached resulting in an error message. If the potential is, however, shallow and "stable" then the timestep can be increased in size again. This algorithm allows us to mitigate the risks associated with the choice of a poor, constant, timestep for the MD.

#### 2.3.2 Initial conditions of diatomic molecules

Equation 2.63 has two parameters that define the starting location and velocity, or kinetic energy of the atoms, which can be derived from known or chosen initial conditions of the atoms. All dynamics calculations in this thesis are quasiclassical trajectory (QCT) calculations<sup>210,211</sup>. This means that the molecule is propagated through time classically but the initial conditions of the molecule are defined according to the quantisation of the rovibrational states of the molecule. As a result of this, the initial condition of the molecule will include zero point energy (ZPE)<sup>173</sup>. The translational kinetic energy of the entire molecule is not

quantised and can be selected according to a few different methods depending on the type of experiment that is being simulated or the experimental data that is available, see the respective chapters for more details.

Rovibrational initial conditions, however, are defined via three quantum numbers v, j, and  $m_j$ . The population distribution of these states is governed by model simulations of the diatomic molecules, and the states are populated according to input settings like rotational and/or vibrational temperatures. The population of a given v, j state is given by:

$$F_{v,j} = \frac{2j+1}{Z(T_{vib}, T_{rot})} e^{-\frac{E_{v,j=0} - E_{v=0,j=0}}{k_B T_{vib}}} e^{-\frac{E_{v,j} - E_{v,j=0}}{k_B T_{rot}}}$$
(2.74).

Here  $Z(T_{vib}, T_{rot})$  is the partition function for given vibrational and rotational temperatures,  $E_{v,j}$  is the energy of a given (v, j) state, and  $T_{vib}$  and  $T_{rot}$  are the vibrational and rotational temperatures. In molecular beam experiments (see Section 1.2.4) these temperatures are related to the nozzle temperature. Initial intramolecular distances and momenta are computed from a quasi-classical full-cycle vibrational simulation of the molecule in the gas-phase. The rotational state is selected according to the rotational population of the initial angular momentum which is defined by

$$L = \hbar \sqrt{j(j+1)} \tag{2.75},$$

and the orientation of L is randomly sampled with the constraint that

$$\cos(\theta_L) = \frac{m_j}{\sqrt{j(j+1)}} \tag{2.76}.$$

Here  $\theta_L$  is the angle between L and the surface normal. The  $m_j$  states are all sampled with equal probability as these states are degenerate for homonuclear diatomic molecules in the absence of a magnetic field. It must be noted that, depending on the nuclear spin statistics of the diatomic molecule in question, not all j states are allowed, e.g., even j states are not permitted for  $O_2^{173}$ . Put very briefly this is due to the combination of the Pauli principle, as also briefly discussed in Section 2.2.2, and the fact that undistinguishable nuclei may get interchanged in the rotation of a molecule. That is, nuclei have their own spin, which depending on the number of protons and neutrons in the nuclei can be either integral or fractional, i.e., the nucleus will behave like a fermion or a boson. This means the sign of the wavefunction has to either change sign (like with electrons, i.e. fermions) or remain the same (for bosons) when two nuclei

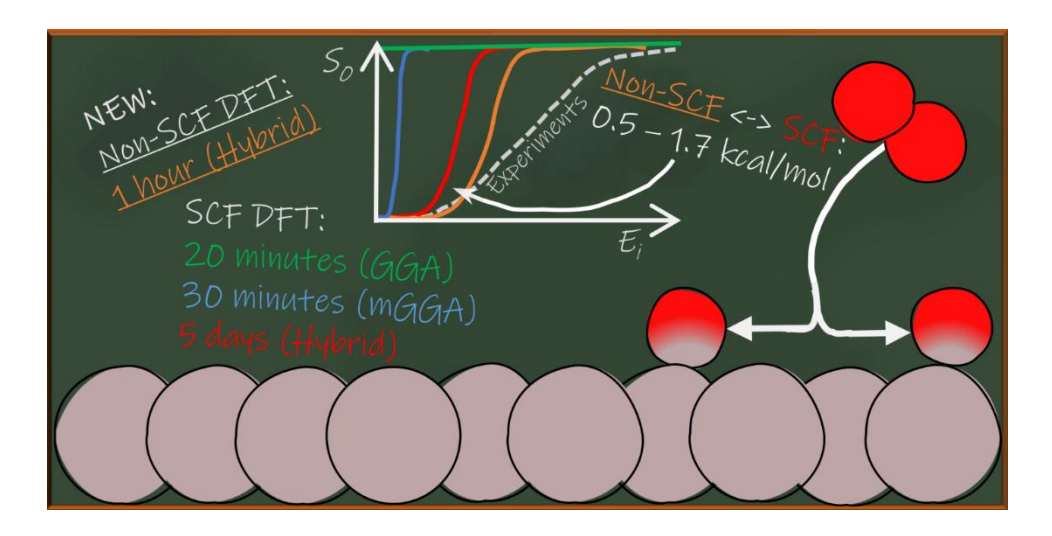
are interchanged by the rotation. This means that certain types of rotational transitions and rotation states may be less occupied (for  $H_2$ ) or completely forbidden (for  $O_2$ ). The details of this are beyond the scope of this thesis and the reader is referred to Ref. <sup>173</sup> for a more detailed explanation. Chapter 3 includes a table in Section 3.2.5 with the rovibrational occupations for an  $O_2$  beam of  $T_{vib}$  = 300 K and  $T_{rot}$  = 9 K. The temperature conditions, i.e.,  $T_{vib}$  and  $T_{rot}$ , are consistent in all three further chapters of this thesis. Further details of the initial conditions of the molecules in QCT dynamics are given in the respective chapters.

Lastly, although in the initial conditions of the molecule, quantisation is taken into account in QCT, the classical time propagation means that quantisation may be lost and energy may leak from states where this would normally not be allowed. This generally does not happen in the QCT for a diatomic molecule in isolation but this may occur when the molecule is interacting with other molecules or with a metal surface.

3 Dissociative chemisorption of O<sub>2</sub> on Al(111): Dynamics on a potential energy surface computed with a non-self-consistent screened hybrid density functional approach

#### This chapter is based on:

van Bree, R. A. B.; Gerrits, N.; Kroes, G.-J. Dissociative Chemisorption of  $O_2$  on Al(111): Dynamics on a Potential Energy Surface Computed with a Non-Self-Consistent Screened Hybrid Density Functional Approach. *Faraday Discuss.* **2024**, *251*, 361–381. https://doi.org/10.1039/D3FD00165B.



## Abstract

Density functional theory (DFT) at the generalised gradient approximation (GGA) level is often considered the best compromise between feasibility and accuracy for reactions of molecules on metal surfaces. Recent work, however, strongly suggests that density functionals (DFs) based on GGA exchange are not able to describe molecule-metal surface reactions for which the work function of the metal surface minus the electron affinity of the molecule is less than 7 eV. Systems for which this is true exhibit an increased charge transfer from the metal

to the molecule at the transition state, increasing the delocalisation of the electron density. This enlarged delocalisation can cause GGA-DFT to underestimate energy values relative to the gas-phase and thus underestimate the barrier height, similar to what has been observed for several gas-phase reactions. An example of such a molecule-metal surface system is  $O_2 + Al(111)$ . Following a similar strategy as for gas-phase reactions, previous work showed results of increased accuracy when using a screened hybrid DF for  $O_2 + Al(111)$ . However, even screened hybrid DFs are computationally expensive to use for metal surfaces. To resolve this, we test a non-self-consistent field (NSCF) screened hybrid DF approach. This approach computes screened hybrid DFT energies based on self-consistent-field (SCF) GGA electronic densities. In this chapter, we explore the accuracy of the NSCF screened hybrid DF approach by implementing the NSCF HSE03-1/3x@RPBE DF for O<sub>2</sub> + Al(111). We compute and analyse molecular beam sticking probabilities as well as a set of sticking probabilities for rotationally aligned O2. Our results show that the NSCF approach results in reaction probability curves that reproduce SCF results with near-chemical accuracy, suggesting that the NSCF approach can be used advantageously for exploratory purposes. An analysis of the potential energy surface and the barriers gives insight into the cause of the disagreement between the SCF and NSCF reaction probabilities and into the changes needed in theoretical modelling to further improve the description of the  $O_2$  + Al(111) system. Finally, the hole model yields fair agreement with dynamics results for the reaction probability curve, but results in an increased slope of the reaction probability curve compared to the molecular dynamics, with a shift to lower or higher energies depending on whether the vibrational energy of the molecule is included in the initial energy of the molecule or not.

#### 3.1 Introduction

The dissociative chemisorption (DC) of a molecule reacting on a surface is often rate-controlling step in heterogeneously catalysed processes<sup>6,212,213</sup>, for instance in ammonia production<sup>1,5</sup>, and steam reforming<sup>27,28</sup>. Moreover, the DC of an O<sub>2</sub> molecule is the initial and often the rate-determining step in oxide formation, corrosion, and catalytic oxidation reactions<sup>214–218</sup>. Understanding the elemental steps at play in the DC of O<sub>2</sub>, or other diatomic molecules, is thus of great practical importance. In addition, there is also an intrinsic scientific interest in understanding the breaking and formation of chemical bonds at surfaces<sup>1,55,56,219,220</sup>. In the literature, the H<sub>2</sub> on Cu(111) system is often mentioned as the benchmark system for H<sub>2</sub> dissociation<sup>55,110,135,221</sup>. Similarly, O<sub>2</sub> on Al has over the years become the benchmark system for the oxidation of metals<sup>214,222–227</sup>. However, theoretical work on the DC of O<sub>2</sub> on Al(111) has thus far not been able to come to an overall consensus on the barrier height for dissociation, the origin of the barrier, and even the reaction mechanism at play<sup>228–235</sup>.

The foremost reason for the disagreement in the theoretical community is that density functionals (DFs) at the generalised gradient approximation (GGA) level of density functional theory (DFT) fail to yield even a qualitatively correct description of the O<sub>2</sub> + Al(111) reaction. The workhorse GGA DF for modelling gas metal interactions<sup>56</sup>, the PBE<sup>154</sup> DF, fails to predict any barriers for DC of O<sub>2</sub> on Al(111)<sup>236–238</sup>. Moreover, even one of the most repulsive (and therefore 'least reactive') DFs that can be used for molecule-metal systems at the GGA DFT level, the RPBE functional<sup>239</sup>, fails to predict any significant barrier for the dissociation of O<sub>2</sub> on Al(111)<sup>236–238</sup>. GGA-level functionals generally incorrectly predict unit reaction probabilities for all incidence energies, i.e., GGA DFs predict a nonactivated reaction<sup>124</sup>. This is in contrast with experimental evidence, which shows that the DC of O<sub>2</sub> on Al(111) is an activated reaction<sup>224</sup>. Going beyond semi-local (GGA) functionals to resolve this (or for gas-metal systems in general) is still challenging as computational costs increase quickly and the dual nature of the system, i.e. the presence of both molecule and metal surface, makes the choice of functional more difficult. As such, a solution to the theoretical description of the O<sub>2</sub> on Al(111) system is not readily found.

The failure of GGA-DFT to describe the barrier of O<sub>2</sub> dissociation on Al(111) has, over the years, been attributed to different origins. Behler et al. 231,240 argued that the reaction should proceed in an almost diabatic fashion, with spin-orbit coupling only being strong enough to quench the triplet spin of the oncoming O<sub>2</sub> molecule once the barrier on the corresponding 'triplet potential energy surface' has already been passed. They argued that in GGA or other adiabatic DFT approaches, this quenching (which is forbidden in the absence of spin-orbit coupling) incorrectly happens continuously, already occurring for O<sub>2</sub> still far from the surface. This should then be why the sticking probability should be overestimated at the adiabatic RPBE-GGA level of theory, as found in Ref. <sup>231</sup>. Using an RPBE-DFT approach for computing the potential energy surface (PES) in which the spin state on O<sub>2</sub> was locally constrained to the triplet ground state, they obtained semi-quantitative agreement with sticking experiments in classical molecular dynamics (MD) calculations<sup>231,240</sup>. Carbogno et al.<sup>234,235</sup> later made predictions for experiments on the scattering of singlet O<sub>2</sub> from Al(111) that can be used to verify the proposed mechanism, but these experiments have not yet been carried out.

Later, Carter and co-workers argued that the barrier for dissociation of O2 on Al(111) does not find its origin in spin selection rules but in the occurrence of charge transfer<sup>228</sup>. As Carter and co-workers showed, they were able to compute rather accurate DC barriers for O<sub>2</sub> + Al(111) using an adiabatic approach<sup>228–230</sup> employing an embedded correlated wavefunction (ECW) method<sup>241</sup>. In these calculations, a second-order multi-reference perturbation theory method, i.e., CASPT2<sup>242,243</sup>, was used to model the interaction of O<sub>2</sub> with an embedded Al cluster. Carter and co-workers attributed<sup>228</sup> the errors in approaches based on GGA DFs to the lack of derivative discontinuities<sup>244</sup> and the self-interaction error<sup>245</sup>. Dynamics calculations based on an embedded CASPT2 PES were in semi-quantitative agreement with sticking experiments<sup>230</sup>, thereby showing that modelling non-adiabatic effects associated with spin-orbit coupling may not be necessary. A disadvantage of their method is that CASPT2 calculations are rather expensive computationally, with the cost scaling as  $O(N^5)$  where N is a measure of the size of the system<sup>246</sup>. Perhaps due to high computational costs, the PES was fitted using a minimum of data points, and as a result, a fitting method with limited accuracy (the flexible periodic London-Eyring-Polanyi-Sato,

FPLEPS<sup>210,247,248</sup> method) had to be used. Furthermore, this unfavourable scaling has possibly stood in the way of achieving further progress using this method for molecules interacting with transition metal surfaces<sup>116,129</sup>, though recent calculations on  $H_2$  + Cu(111) show much better results with the embedded NEVPT2 method<sup>249</sup>.

One method to correct for the self-interaction error, at least approximately, is to mix exact non-local exchange with semi-local exchange to obtain a hybrid DF This approach has been used successfully to obtain DFs that are more accurate for gas-phase reaction barriers<sup>137,139</sup>. This idea was further supported by preliminary hybrid DFT calculations on  $O_2 + Al(111)$ , showing that barriers for dissociation do occur when employing (screened) hybrid functionals to calculate the electronic structure<sup>226</sup>. The suggestion to go beyond the use of semi-local functionals for  $O_2 + Al(111)$  also comes from recent work suggesting a correlation between the failure of GGA-DFs for DC on metal surfaces with the so-called charge transfer energy of the system ( $E_{CT}$ ). This energy may be defined as:<sup>124</sup>

$$E_{CT} = \phi - EA \tag{3.1}.$$

Here,  $\phi$  is the work function of the metal surface, and *EA* is the electron affinity of the molecule. Gerrits *et al.* estimated<sup>124</sup> that the divide between GGA DF failure and success can be found at about  $7\,eV$ , i.e., if the charge transfer energy of a system is below  $7\,eV$ , charge transfer from metal to the molecule is more likely and an error in the semi-local GGA-DF is expected to occur and lead to underestimated barrier heights<sup>124</sup>. At  $3.76\,eV$  the charge transfer energy of the  $O_2$  on Al(111) system is far below  $7\,eV^{124}$ , and from previous work<sup>236,237</sup>, it is clear that a manner of delocalization of the  $O_2$  orbitals occurs at the Al surface, which has been pointed to as a cause for underestimating the barrier heights<sup>146,250,251</sup>. However, we do note that the work of Ref. <sup>124</sup> suggests that errors in the density are not necessarily the major cause of the underestimation of the barrier heights, as will be discussed further below.

The above-described correlation of the charge transfer energy of the system with the likely success of GGA functionals, the above-mentioned 'fix' for gasphase reactions, and preliminary results for  $O_2$  interacting with Al clusters<sup>230</sup> led to dynamics calculations using a screened hybrid DFT PES for  $O_2$  + Al(111)<sup>124</sup>. Hybrid DFT has a more favourable computational scaling with system size (as

 $O(N^4))^{252}$  than CASPT2. A screened hybrid functional was used as global hybrid DFs have severe shortcomings for metals, e.g., their use leads to an underestimated density of states at the Fermi level<sup>158</sup>. The screened hybrid functional dynamics calculations achieved semi-quantitative agreement with experimental sticking coefficients for  $O_2 + Al(111)^{124}$ .

The presented solution in Ref. 124 is promising, nevertheless, the use of screened hybrid functionals for gas-metal systems (even for simple metals like AI) is computationally expensive. Nonetheless, if the error of the GGA functional would be mostly functional-driven<sup>253</sup> as opposed to density-driven<sup>124,253</sup>, the electron densities (and Kohn-Sham wavefunction) found from converged GGA DFT calculations might remain accurate. Consequently, using the GGA-DF electron density (and Kohn-Sham wavefunction) to non-self-consistently compute the energy with a screened hybrid functional might represent a viable (i.e., affordable) approach to systems with low electron transfer energies like O<sub>2</sub> + Al(111). This would enable us to avoid the majority of the computationally expensive cycles with the screened hybrid functional that would be required for self-consistency, and instead achieve results of (near) screened hybrid-level accuracy at only a fraction of the costs. Ref. 124 already suggested that this approach might be viable, by showing, for a limited number of configurations, that a non-self-consistent field (NSCF) hybrid calculation can indeed closely reproduce the self-consistent hybrid barrier heights 124,145 This finding suggests that the GGA error in the barrier heights for O<sub>2</sub> + Al(111) must be largely functional driven.

In this chapter, we explore the potential of the NSCF-screened hybrid functional approach by constructing and analysing an NSCF screened hybrid potential energy surface (PES) for  $O_2$  on Al(111) and using it in dynamics calculations. The resulting NSCF sticking probabilities are compared with SCF results and with results of supersonic beam experiments on sticking of ordinary and rotationally aligned beams. We will show that the NSCF approach reproduces SCF results to within  $2 \, kcal/mol$ . The NSCF results are unintentionally in even better agreement with experiments than the SCF results. Furthermore, an analysis of the PES and the reaction barriers, and an analysis using the hole model of Holloway and Nørskov and co-workers<sup>254</sup> give insight into the cause of the disagreement

between SCF and NSCF reaction probabilities. Our analysis also shows what type of additions in the theoretical modelling of this challenging benchmark system may be required in future work to improve upon the agreement presently achieved for  $O_2 + Al(111)$ .

This chapter is set up as follows. The next section, i.e., 3.2, presents the methods employed. Thereafter Section 3.3 presents the results in several sub-sections. The first sub-section, 3.3.1, discusses the importance of a strict convergence of the self-consistent calculations producing the GGA densities. The next two sub-sections, i.e., 3.3.2 and 3.3.3, present and discuss the results of the dynamics calculations using the NSCF PES for sticking of ordinary and rotationally aligned  $O_2$  in supersonic beams, also comparing to SCF and experimental results. After this, we discuss the role of the energetic corrugation of the barrier height in Section 3.3.4. Finally, Section 3.3.5 discusses results for  $O_2$  + Al(111) that are obtained with the hole model. After this the chapter is summarised in Section 3.4 and Section 3.5 presents two appendices.

#### 3.2 Methods

This section of Chapter 3 discusses the methods and computational details used for this work. This section is divided into six subsections. Section 3.2.1 discusses the coordinate system and dynamical model used, Section 3.2.2 the details of both DFs in use, Section 3.2.3 briefly highlights the computational details of the DFT calculations, 3.2.4 discusses the procedure for constructing the PES, 3.2.5 the relevant details for the QCT calculations, and lastly Section 3.2.6 discusses the computational implementation of the hole model.

#### 3.2.1 Coordinate system and dynamical model

The coordinate system used in this chapter is as used in previous work on diatomic molecules reacting on (111) surfaces of FCC metals, see Ref. <sup>55</sup> for a detailed account. For the dynamics calculations in this chapter, we make use of the Born-Oppenheimer static surface (BOSS) approximation, which means that we employ both the Born-Oppenheimer approximation (BOA) and keep all Al(111) surface atoms fixed in their ideal lattice position<sup>56</sup>. This way, we only have

to consider the six degrees of freedom associated with the diatomic molecule  $(O_2)$ . Therefore, we can use the molecule's centre-of-mass (COM) centralised coordinate system for the molecule's degrees of freedom. In this coordinate system, the COM's position is expressed in the coordinates X and Y for motion along the surface, and Z is the distance of the molecule's COM to the surface. The distance between the oxygen atoms is given by the r coordinate. The azimuthal angle  $\varphi$  defines the orientation of the molecule's projection on the surface, i.e., on the horizontal-(X, Y)-plane, and the polar angle  $\theta$  defines the angle of the  $O_2$  bond axis with the Z-axis. For a visual representation see **Figure 3.1A**.

The surface unit cell of a (111) surface of an FCC metal is illustrated in **Figure 3.1B**. In this figure, the most relevant high-symmetry sites are also indicated. Note that the angle between the U and V axes can be taken as either 60 or 120 degrees; in **Figure 3.1B** the  $60^{\circ}$  version is demonstrated. As we are describing a unit cell, the U and V coordinates within this cell are taken as normalised (between 0 and 1). The X and Y coordinates of the COM of  $O_2$  are transformed to U, V-space to properly describe the position of the COM of  $O_2$  above a (111) FCC surface and its high symmetry sites, with the X vector being along U.

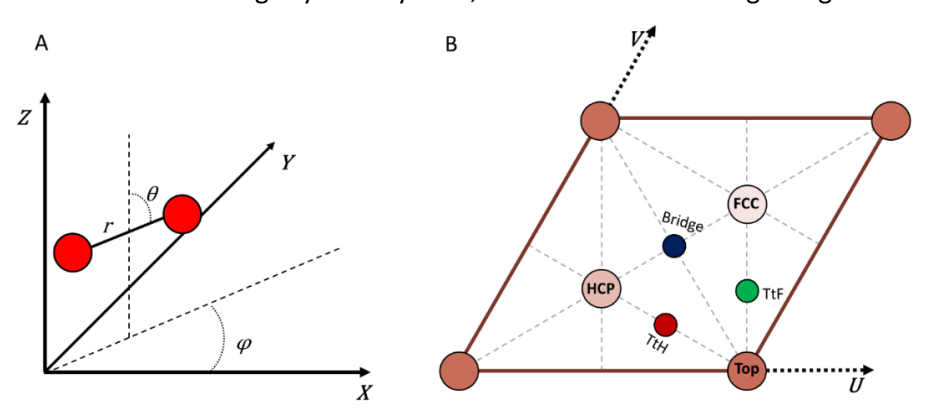


**Figure 3.1**: The coordinate system in use and its relation with the Al(111) surface unit cell. **A**: The centre-of-mass coordinate system used for the description of  $O_2$  interacting with Al(111). See the text for an explanation of the coordinates shown. **B**: The unit cell of a (111) surface of an FCC metal (Al), in which the high symmetry surface sites are indicated.

#### 3.2.2 Density functionals

The density functionals used for this chapter are the RPBE<sup>239</sup> DF at the generalised gradient approximation (GGA) rung and the HSE03-1/3x DF<sup>189</sup> at the hybrid rung of DFT. The RPBE DF may be viewed<sup>239</sup> as a variant of the non-empirical GGA PBE DF<sup>154</sup>, with the RPBE DF originally designed to improve the description of chemisorption energies of atoms and molecules on metal surfaces. Hammer *et al.* constructed the RPBE DF in such a way that the same non-empirical constraints imposed on the PBE-DF are also imposed on RPBE<sup>239</sup>. Importantly for metals, the recovery of the uniform electron gas limit at zero gradient of the density is included<sup>255</sup>. In general, we can consider the RPBE functional as more 'repulsive' than the PBE functional, i.e., the RPBE barriers for both gas-phase reactions and dissociative chemisorption reactions on metals are higher than the PBE DF barriers<sup>135,256</sup>. This generally results in lower reactivity when describing a gas-metal system with the RPBE functional<sup>56</sup>.

The HSE03-1/3x DF is a screened hybrid functional. It is a hybrid DF because a fraction of exact exchange (also somewhat ambiguously called Hartree-Fock exchange) is admixed to the GGA exchange<sup>152</sup>. It is screened because the exact exchange is turned off at long range. This means that at long range the functional behaves like a PBE DF<sup>154</sup>, whereas at short range it will behave as a PBE0-like hybrid DF<sup>153</sup>. The screening of the exact exchange in metals is vital, because without it a myriad of descriptive issues can occur, not the least of which is a reduction of the density of states of the electrons at the Fermi level<sup>158</sup>.

The HSE03-1/3x DF is similar to the original HSE03 DF<sup>189,190</sup>, i.e., to the HSE03 DF that has been corrected for an implementation error<sup>190</sup>. The HSE03 DF only differs from the better-known HSE06 functional through the use of a slightly different screening range parameter<sup>189,190</sup>. The difference between the HSE03-1/3x DF and the HSE03 DF in Ref. <sup>189</sup> is that we implemented a different maximum fraction of exact exchange ( $\alpha$ ). The  $\alpha$ -values for PBE0 and HSE03 were originally set to 1/4, whereas we use  $\alpha = 1/3$ . Increasing the exact exchange is an accepted approach to improve the performance for gas-phase reaction barrier heights<sup>139,257</sup>, and was thus used already in earlier work on O<sub>2</sub> + Al(111)<sup>124</sup> to improve over the description of the O<sub>2</sub> on Al(111) system obtained with the original HSE03 functional.

Here a non-self-consistent field (NSCF) HSE03-1/3x@RPBE calculation is performed by first initialising and converging a self-consistent field (SCF) calculation with the lower level RPBE functional to obtain a well-converged electron density. The higher level HSE03-1/3x density functional<sup>189</sup> is then applied once to this density (using its Kohn-Sham wavefunction) to compute the HSE03-1/3x@RPBE energy. Vital to achieving an accurate and converged result in this type of calculation is that a high enough level of convergence is achieved for the energy (and thereby the density) at the lower (RPBE) level of theory. We have found that this requires a tougher energy tolerance than usually needed in a self-consistent calculation, presumably because the RPBE density is not equal to the density that corresponds to the variational minimum energy that would be obtained with the self-consistent HSE03-1/3x functional.

#### 3.2.3 Computational details

All DFT calculations are performed with the Vienna Ab initio Simulation Package (VASP) version 5.4.4 $^{200,258-262}$ . The initial SCF GGA spin-polarised DFT calculations are done with the RPBE $^{239}$  functional. The calculations use a 2x2 Al(111) supercell with 4 layers and a vacuum distance of 10 Å. The Al surface is described by a lattice constant of 4.022 Å and interlayer distances of  $d_{12} = 2.356$  Å,  $d_{23} = 2.248$  Å, and  $d_{34} = 2.353$  Å, which are the same as the values used in Ref.  $^{124}$  for the SCF HSE03-1/3x DF calculations. A plane wave cut-off energy of 400 eV and an 8x8x1  $\Gamma$ -centred k-point grid is used. The core electrons are represented by the projector augmented wave (PAW) $^{199}$  method, and first-order Methfessel-Paxton smearing with a width of 0.2 eV is employed to improve convergence. The energy convergence criterium for the RPBE functional is set to  $10^{-9}$  eV. This stringent convergence criterium is specifically chosen with the erratum $^{145}$  on the work of reference  $^{124}$  in mind and is discussed further in Section 3.3.1.

To complete an NSCF HSE03-1/3x@RPBE calculation we perform another single-point calculation by applying the HSE03-1/3x DF one time to the pre-converged RPBE density. This calculation uses mostly the same DFT settings as the SCF GGA single-point calculations. The notable difference, however, is the use of the screened hybrid HSE03<sup>189</sup> functional with an exact exchange fraction of 1/3. (see

also Section 3.2.2) In this calculation, the SCF-RPBE density and Kohn-Sham wavefunction of the previous calculation are used, and the HSE03-1/3x is not applied in a self-consistent manner but only once to compute the screened hybrid energy from the converged RPBE density.

#### 3.2.4 Constructing the PES

In the most common approach to performing quasi-classical trajectory (QCT) dynamics calculations a continuous and global PES is used that is fitted to electronic structure calculations using the DF of which the accuracy is evaluated. As discussed in Section 3.2.1, the PES in this work is dependent on the six degrees of freedom of the diatomic (O<sub>2</sub>) molecule. A continuous representation of this six-dimensional PES is obtained by applying the corrugation-reducing procedure (CRP)<sup>201,202</sup> to a grid of DFT single-point energies. In this approach, atom-surface PESs are subtracted from the full 6D PES such that the 6D rest function is less corrugated and easier to interpolate. In previous studies, this procedure led to off-grid interpolation errors that were no larger than 30 meV  $^{202}$  (2.9 kJ/mol) and 0.7 kcal/mol  $^{115}$  (2.9 kJ/mol). Moreover, in the work of Smeets et al. a large test set of 4900 samples was used to test the interpolation error of the CRP method<sup>130</sup>. This resulted in a root mean squared error (RMSE) of 31 meV (3.0 kJ/mol). However, this RMSE was reduced to 8 meV (0.8 kJ/mol) if the interaction energies between molecule and metal were smaller than 4 eV 130. For  $O_2 + Al(111)$ , most interaction energies are within 4 eV in the configuration space relevant to the reaction dynamics (see also Figure 3.7 in Section 3.3.4). Furthermore, **Table 3.3** in Section 3.5.1 shows a comparison of reaction barrier energies extracted from the CRP PES (as also shown in Table 3.2 in Section 3.3.4) with values directly calculated for the corresponding CRP barrier geometries using DFT (the NSCF HSE03-1/3x@RPBE DF). The RMSE of 0.61 kJ/mol is consistent with the value of 0.8 kJ/mol for total interaction energies smaller than 4 eV in the earlier cited study, with the largest deviation between a CRP and a DFT barrier being about 3.0 kJ/mol, in what is a clear outlier in the set. The CRP procedure used in this chapter is along similar lines as in e.g. the work of Ref. 263, except for two distinctions.

First, we did not employ an equidistant (r, Z)-grid. Instead, we used a similar grid as used in Ref. <sup>124</sup> for the calculations with the SCF HSE03-1/3x functional, i.e., Z = [1.00, 1.50, 2.00, 2.25, 2.50, 2.75, 3.00, 3.25, 3.50] Å, and r = [1.0, 1.1, 1.15, 1.175, 1.2, 1.225, 1.25, 1.3, 1.4, 1.5, 1.6] Å. This grid limits the number of single points necessary for a good representation whilst maintaining high accuracy for the description of the molecule in the gas-phase and at the transition sate (TS). We opted to use the same grid as the earlier  $O_2 + Al(111)$  work of Gerrits  $et\ al$ . to enable an optimal comparison with the calculations using the SCF HSE03-1/3x DF PES, in the sense that differences should not be attributable to the use of a different grid of points.

The second distinction is that, similar to reference <sup>124</sup>, we employ the atomic 3D PES computed with the MS-RPBEI DF<sup>128</sup> instead of an atomic PES obtained with the (NSCF) HSE03-1/3x functional. This is done to maintain comparative PESs between the NSCF and SCF DF. Regardless, the three-dimensional atomic PES will not influence the 6D PES itself as long as the 3D potential is physically reasonable, since the 3D atomic PES is used only to decrease the corrugation of the 6D PES during the fitting procedure, as also discussed in Ref. <sup>124</sup>.

#### 3.2.5 Quasi-classical trajectory calculation

A global PES as produced by the CRP allows for performing quasi-classical trajectory (QCT)<sup>210,211</sup> dynamics calculations, along similar lines as in previous work<sup>124,125,130</sup>. With QCT we take into account the molecule's initial zero-point energy, after which the molecular trajectory is propagated classically in time. If the bond length of  $O_2$  exceeds the threshold of  $1.59 \, \text{Å}$  in a trajectory, we count that trajectory as reacted. If the value of Z increases beyond the value of Z at the starting point of the trajectory (i.e., if  $Z > 5.0 \, \text{Å}$ ) we consider the molecule to be scattered. The reaction probability ( $P_r$ ) is calculated using:

$$P_r = \frac{N_r}{N_{total}} \tag{3.2}$$

where  $N_r$  is the number of trajectories that correspond to a reaction and  $N_{total}$  is the total number of trajectories run.

Two types of molecular beams were simulated for this chapter. This first type is used to simulate the experiments of Österlund et al.<sup>224</sup>, for which supersonic molecular beams with a nozzle temperature  $(T_N)$  equal to room temperature, i.e., 300 K, were used. In simulating the experiments the vibrational temperature of the molecules can be taken equal to the value of  $T_N$  in the experiments<sup>224</sup>. Due to the high rotational cooling in the oxygen molecular beams employed, the rotational temperature of  $O_2$  is only  $9K^{264}$ , resulting in a rovibrational state population presented in Table 3.1 (see Refs. 130,136 for more information). In the QCT calculations, we used a single value for the incidence energy of the molecule and allowed initial states with v = 0 - 3, and i = 1 - 49 to be populated. However, **Table 3.1** shows that O<sub>2</sub> molecules in a beam with  $T_N = 300 \text{ K}$  mostly occupy the rovibrational ground state (v=0, j=1). Note that we only consider the odd j states, because the even j states are forbidden according to nuclear spin statistics<sup>173</sup>. For this beam simulation, we ran 10,000 trajectories for each incidence energy to compute the reaction probability  $(P_r)$  per incidence energy with converged statistics.

**Table 3.1**: Rovibrational state population in an  $O_2$  molecular beam with a nozzle temperature of 300 K.

v state	j state	Rovibrational energy (eV)	Population
0	1	0.10687	80.6546 %
0	3	0.10865	18.8495 %
0	5	0.11186	0.47049 %
0	7	0.11650	0.00160 %
1	1	0.31449	0.02632 %
1	3	0.31626	0.00627 %
1	5	0.31944	0.00016 %

The second type of beam is used to simulate the experiments of Kurahashi and Yamauchi<sup>227</sup>, for which we employed a state-specific initial condition of v=0, j=1, with appropriate averaging over  $m_j=-1$ , 0, 1, according to the particular experiment simulated. We ran 2800 trajectories per incidence energy to compute the sticking probability. We then use the  $m_j$  state-specific reaction probabilities and the equations provided in the work of Kurahashi and

Yamauchi<sup>227</sup> to compute the reaction probabilities measured for particular rotational alignments. We refer the reader to reference <sup>227</sup> for the details.

#### 3.2.6 Hole model

The hole model<sup>254</sup> is a method to compute the sticking probability from the barrier corrugation and anisotropy without the usage of dynamics<sup>56</sup>. In this chapter we used the well-defined NSCF PES to compute the reaction, or sticking, probability, as described by the hole model<sup>56,254</sup>:

$$S_{0}(E_{mol}) = \frac{\int H\{E_{mol} - E_{B}(X, Y, \theta, \varphi)\} dU dV d\cos(\theta) d\varphi}{\int dU dV d\cos(\theta) d\varphi}$$

$$H\{\Delta E\} = \begin{cases} 1 \text{ if } \Delta E \ge 0 \\ 0 \text{ if } \Delta E < 0 \end{cases}$$
(3.3)

Here  $E_{mol}$  is the sum of the internal energy of the molecule (as defined by the temperature of the molecular beam) and the incidence energy of the molecule, and  $E_B(X, Y, \theta, \varphi)$  is the energy of the barrier for a given molecular geometry  $(X, Y, \theta, \varphi)$ .

In practice, we opt to use a Monte-Carlo-like approach to solving this integral. Analogously to Section 3.2.5, we compute the reaction probability as Equation 3.2, though now we do not use quasi-classical trajectory outcomes but distinct samples such that:

$$P_{r}(E_{i}) = \frac{N_{r}(E_{i})}{N_{total}} = \frac{\sum_{j}^{N_{total}} H\{E_{j}^{mol}(E_{i}) - E_{j}^{B}(U_{j}, V_{j}, \cos(\theta)_{j}, \varphi_{j})\}}{N_{total}}$$

$$E_{j}^{mol}(E_{i}) = E_{i} + E_{j}^{vibration} + E_{j}^{rotation}$$
(3.5)

where  $E_i$  is the incidence energy of the molecule,  $E^{vibration}$  and  $E^{rotation}$  are the vibration energy and rotation energy of the molecule for each sample j chosen randomly via the  $T_N=300K\,\rm O_2$  molecular beam population distribution (see also **Table 3.1**),  $N_{total}$  is the total number of samples used, H is the same Heaviside function as in Equation 3.4, and U, V,  $cos(\theta)$ ,  $\varphi$  are chosen randomly from uniform distributions for each j as defined in Section 3.2.1 (Note that in Equations 3.5 we use the U, V coordinates instead of X, Y see also Section 3.2.1). If  $N_{total}$  is chosen to be large enough (here it is chosen to be  $10^{\circ}$ ) Equation 3.5 should approach the results of Equation 3.3.

For each sample j, a molecular energy and molecular geometry (U, V,  $\theta$ ,  $\varphi$ ) are thus chosen according to the same initial conditions as in the QCT calculations. The geometry is used to compute the reaction barrier in r and Z via a simple two-dimensional barrier searching algorithm applied to the (NSCF) PES. The barrier search is in principle a basic saddle-point searching algorithm, assuming that only one saddle-point, or barrier, will exist per r, Z-elbow cut of the PES. The saddle points are found by starting a modified Powell method<sup>265,266</sup> root finding algorithm on the Jacobian of the two-dimensional (r, Z) PES from an initial guess on the elbow. This critical point is then verified to be a saddle point via a second-order derivative test with the hessian of the two-dimensional (r, Z) PES on the critical point (i.e., the discriminant of the hessian needs to be smaller than zero). If the critical point is not a saddle point, a new root search in the Jacobian is started from a different initial guess. This algorithm is basic but robust if the corrugation of the PES not to large so that extra critical points or saddle points are not present (to avoid the occurrence of false critical or saddle points).

#### 3.3 Results and discussion

Below the results of this chapter are presented. This is done with a few subsections. The first, i.e., section 3.3.1 discusses the need for stringent convergence of the RPBE density. Section 3.3.2 then follows this by presenting the sticking results from QCT calculations and comparing those results to the SCF HSE03-1/3x results, and other previous theoretical and experimental work. Section 3.3.3 then briefly discusses the sticking probability of rotationally resolved  $O_2$  molecules. This is followed by Section 3.3.4 where the differences in sticking probability are related to the differences in the PESs of both the SCF and NSCF DF. Lastly, in Section 3.3.5 the sticking results computed with the hole model are presented and analysed.

## 3.3.1 Converging a non-self-consistent field DFT calculation

As discussed in Section 3.2.2 it is important to achieve a high convergence of the DFT energy in the lower rung calculation of the electron density, to ensure that this density is stable. We found this to be particularly true for geometries in

which O<sub>2</sub> is still far away from the Al(111) surface. The NSCF energies can be quite dependent on the convergence of the GGA RPBE density used to evaluate the HSE03-1/3x@RPBE DF. An example of potential problems with less converged densities is shown in Figure 3.2. In this figure three different cuts through the potential energy surface are shown, plotting the total energy value of  $O_2$  + Al(111) for different bond lengths of  $O_2$  in the gas-phase, i.e., at 5.0 Å above the surface. In Figure 3.2A, results obtained with the SCF HSE03-1/3x functional are shown for an energy tolerance  $\Delta E_{Tol} = 10^{-5} \text{ eV}$ . In Figure 3.2B and C results obtained with the NSCF HSE03-1/3x@RPBE functional are shown for the RPBE tolerance of  $\Delta E_{Tol} = 10^{-5}$  eV in panel **B** and  $\Delta E_{tol} = 10^{-9}$  eV in panel **C**. Figure 3.2 clearly shows that obtaining accurate and converged results with the NSCF calculations requires a much lower value of  $\Delta E_{Tol}$  in the GGA primer calculation (a better-converged GGA electron density) than needed in an SCF calculation. As also discussed in Section 3.2.2. we attribute the much larger dependence of the NSCF energy on small changes in the GGA density to the GGA electron density probably not being equal to the electron density corresponding to the variational minimum for the higher-level functional. In this situation, one would expect to see a much larger dependence of the energy on small variations in the density.

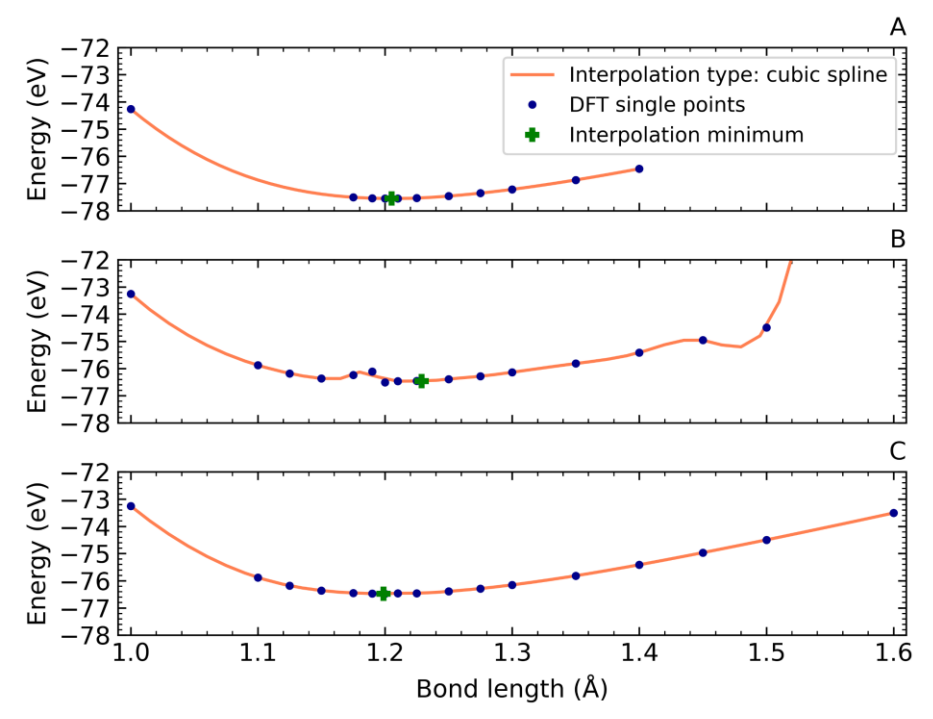


**Figure 3.2**: Three (cubic spline interpolated) potential energy cuts for  $O_2$  at 5 Å above the Al(111) surfaces, where all degrees of freedom are kept constant except for the oxygen bond length; **A**: HSE03-1/3x with an  $\Delta E_{Tol}$  of 10<sup>-5</sup> eV; **B**: NSCF HSE03-1/3x@RPBE with RPBE with an  $\Delta E_{Tol}$  of 10<sup>-5</sup> eV; **C**: NSCF HSE03-1/3x@RPBE with RPBE with an  $\Delta E_{Tol}$  of 10<sup>-9</sup> eV.

#### 3.3.2 The reaction probability

In **Figure 3.3** the reaction probability computed with the NSCF hybrid functional (HSE03-1/3x@RPBE) is plotted as a function of incidence energy. We compare these results with reaction probabilities computed with SCF HSE03-1/3 $x^{124}$ , wavefunction theory embedded in DFT<sup>230</sup>, RPBE<sup>231,240</sup>, MS-RPBEI (a meta-GGA)<sup>124</sup>, and with experimental results<sup>224</sup>.

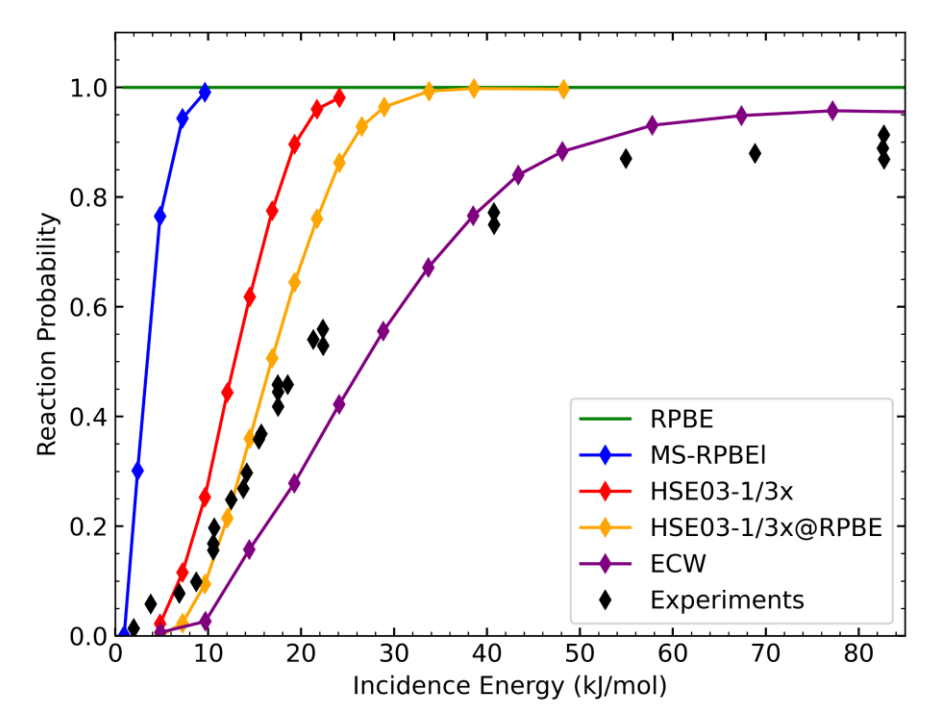


**Figure 3.3**: The reaction probability as a function of incidence energy as computed with the SCF HSE03-1/3x functional (red) $^{124}$ , the NSCF HSE03-1/3x @RPBE functional (orange), the embedded correlated wavefunction method (purple) $^{230}$ , and as measured in experiments (black) $^{224}$ , is compared with the reaction probability computed with the RPBE DF(green) $^{231,240}$ , and with the MS-RPBEI DF(blue) $^{124}$ .

Importantly, the NSCF results reproduce the SCF reaction probabilities within near-chemical accuracy (2 kcal/mol), but not within chemical accuracy (1 kcal/mol). The NSCF reaction probabilities appear to be shifted towards somewhat higher incidence energies. This energy shift is not constant: it is larger for higher incidence energies. The increase of the shift also means that the slope of the NSCF reaction probability curve is smaller. This somewhat reduced slope of the NSCF reaction probability curve corresponds to a small broadening of the sticking probability curve relative to the SCF results.

The difference in incidence energy dependency of the NSCF and SCF HSE03-1/3x sticking curves is visualised in **Figure 3.4** where we have plotted the incidence energy shift (or  $\Delta$ ) that the SCF HSE03-1/3x reaction probabilities would need to be shifted by to higher energies to morph into the NSCF HSE03-1/3x@RPBE

result. At low incidence energy, the energy shift required is small (2.4 kJ/mol) and well within chemical accuracy ( $1 \text{ kcal/mol} \approx 4.2 \text{ kJ/mol}$ ), but for larger incidence energies the required shift increases considerably (to 7.2 kJ/mol). Based on the energy shift we can say that the NSCF results reproduce the SCF results to within chemical accuracy up to an incidence energy of 14 kJ/mol. The energy shift of the NSCF curve also means that these results reproduce the initial onset of the experimental sticking curve less well (at  $E_i < 7 \text{ kJ/mol}$ ) than the SCF results, but the agreement of the NSCF results with experiments is unintentionally improved in the range of 10 - 23 kJ/mol (see **Figure 3.3**).

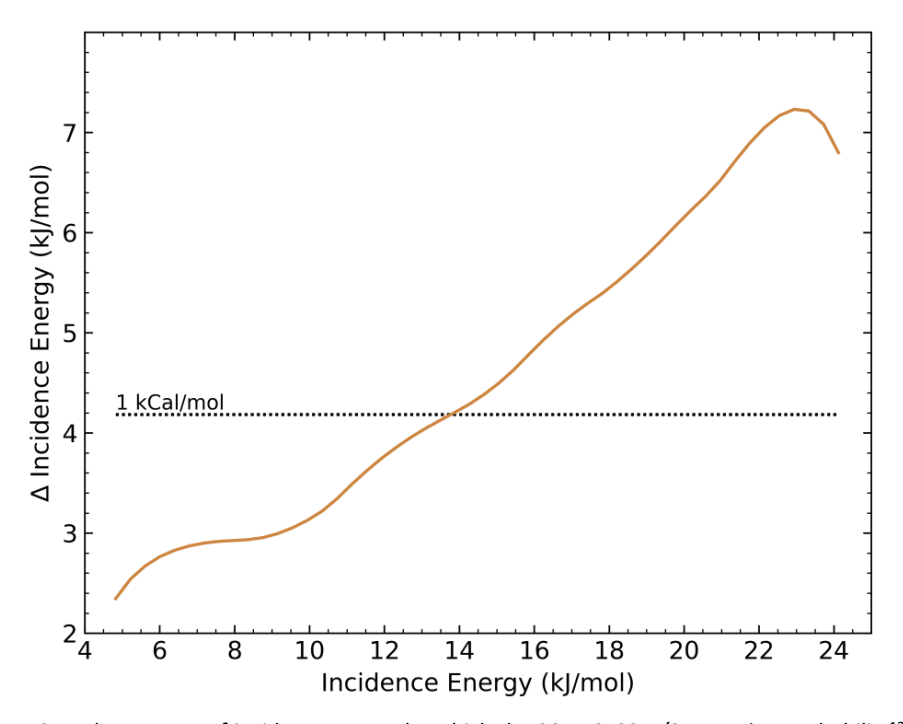


**Figure 3.4**: The amount of incidence energy by which the SCF HSE03-1/3x reaction probability<sup>124</sup> would have to be shifted to morph into the NSCF HSE03-1/3x@RPBE reaction probability curve is shown as a function of the incidence energy of the SCF reaction probability.

The disagreement between the SCF HSE03-1/3x and the NSCF HSE03-1/3x@RPBE results may be surprising when looking back at Ref. <sup>124</sup> where (originally) near exact agreement between SCF and NSCF barriers was reported. Such an agreement would suggest that reaction probability curves would also be

in excellent agreement with one another. However, this is, as shown above, not the case. The problem is resolved through the recent Erratum<sup>145</sup> published on the work of Ref. <sup>124</sup>, which corrected the reported NSCF 1D potential and further clarified the exact settings used for the published NSCF calculations. It appears that the input parameters in reference <sup>124</sup> for the SCF RPBE in the NSCF HSE03-1/3x@RPBE functional were set at values not yet sufficiently stringent to obtain a stable NSCF energy. The limited convergence of the GGA density likely resulted in energetic noise in the gas-phase description of the  $O_2 + Al(111)$  model (see also **Figure 3.2**). This, in turn, has most likely resulted in incorrect molecule-surface interaction energies, as an unstable result for  $O_2$  in the gas-phase was subtracted from the energy of the combined system. All in all, this resulted in a down-shifted barrier height, thereby presenting a too optimistic picture of the NSCF-screened hybrid DF barrier description.

We found that, when using a plane wave code like VASP for the O<sub>2</sub> on Al(111) system, only a small fraction of the computation time for an NSCF hybrid single point is spent on generating a well-converged SCF GGA density. A very stringent convergence setting in the SCF GGA calculation is therefore of little influence on the total computation time. Moreover, the computational cost of an NSCF hybrid single-point calculation is between  $1/20^{th}$  to  $1/200^{th}$  of the cost of a full SCF hybrid single-point calculation. It is, therefore, encouraging to see that the NSCFscreened hybrid results represent a considerable improvement over the RPBE GGA and the MS-RPBEI mGGA results<sup>124</sup> shown in **Figure 3.3**, at a computational cost that is more than an order of magnitude lower than the SCF hybrid DFT calculations. Specifically, we observe that a single application of the screened hybrid functional to a well-converged GGA (i.e., RPBE) density is capable of altering the sticking probability curve to a result much closer to the desired, experimental, outcome and reproduces the SCF Hybrid DF with near-chemical accuracy. This last point strengthens the argument made in earlier work<sup>124</sup> that the errors made with GGA functionals when describing systems with a low charge transfer energy, like the O<sub>2</sub> + Al(111) system investigated here, are likely to be mostly functional-driven, with only a small density-driven component.

It would obviously be more elegant if the NSCF results would reproduce the SCF results even more closely so that the HSE03-1/3x@RPBE results could be cast as

a very good approximation to the HSE03-1/3x results. In that case, our dynamics calculations would directly test the quality of the DF as used self-consistently, and the comparison with the experiment would be more telling of the quality of the functional itself. The remaining disagreement between SCF and NSCF results does suggest that the DF errors are not entirely functional driven, and that part of the GGA failure is due to errors in the GGA density. This then raises the question of how the density-driven part of the error is related to the system we are treating. Would the disagreement between NSCF and SCF-screened hybrid calculations, where the NSCF calculations are based on GGA densities, be smaller if the functionals were applied to systems with smaller charge transfer energies? And would electron densities from mGGA DFs improve the description further? It may be fruitful to explore the answer to these and other related questions, and thereby hopefully learn more about how problems with DFT are related to the type of system to which it is applied, and how such problems may be solved.

Nevertheless, the NSCF-screened hybrid results are in semi-quantitative agreement with experiments and reproduce the SCF results within near-chemical accuracy. This suggests that the NSCF approach could be used in explorative research aimed at extracting reaction barrier heights for difficult dissociative-chemisorption-on-metal systems (i.e., systems that require hybrid DF's for a proper description at great computational costs, with charge transfer energies < 7~eV). This way, hopefully, the best DFs for a given system can be identified in the same fashion as used earlier for 'easy' systems (with charge transfer energies > 7~eV), see Refs. S6,129. As discussed there, this would allow minimum reaction barrier heights to be extracted for such systems, as experimental reaction probability curves should only be reproduced if the barriers in the PES are correctly described (this argument can be based on the hole model 254, as also discussed in Ref. S6).

## 3.3.3 Sticking of rotationally aligned O<sub>2</sub>

In 2013 Kurahashi and Yamauchi showed that the sticking of  $O_2$  on Al(111) depends strongly on the alignment of the  $O_2$  molecule relative to the surface<sup>227</sup>. Using a single spin-rotational state-selected  $O_2$  beam their work differentiates the sticking between the two different DC mechanisms of  $O_2$  that are at play<sup>227</sup>.

Here the first mechanism is direct DC, which can occur when the molecule is parallel to the surface<sup>267</sup> e.g., in a helicoptering state. The second mechanism occurs when the molecule is mostly perpendicular to the surface, in which case abstraction can occur<sup>219,268–271</sup>. Kurahashi *et al.* showed that, for lower incidence energies of  $O_2$ , only a small fraction of the  $O_2$  reacts through the abstraction mechanism<sup>227</sup> (see also **Figure 3.5**).

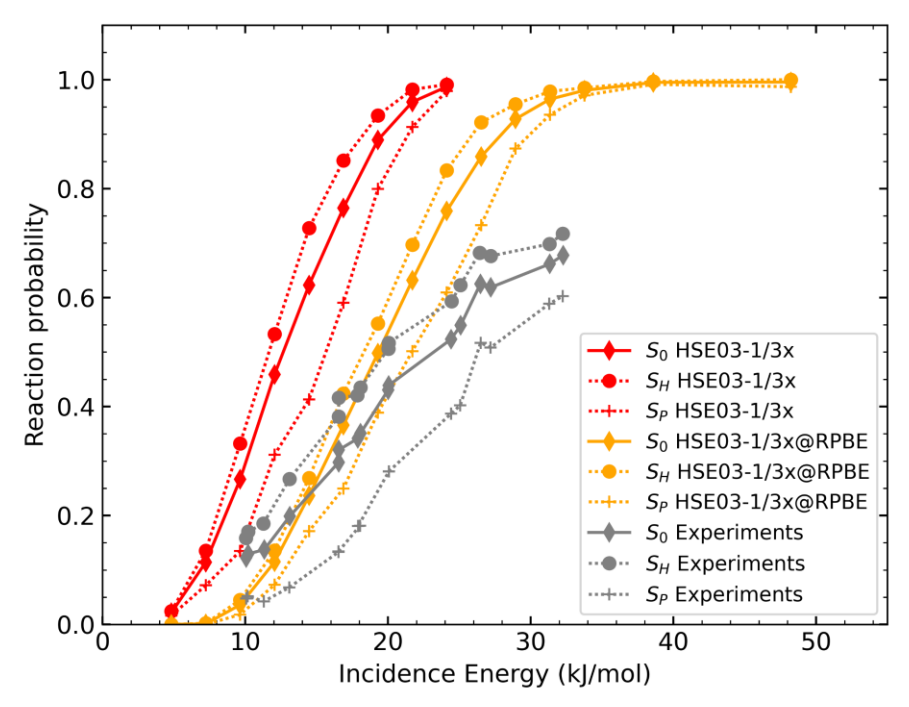


**Figure 3.5**: Total and rotationally resolved sticking curves as a function of incidence energy (kJ/mol) for molecular beams of  $O_2$  in the v=0, j=1 (V=0, J=2, K=1) state only; as computed with the SCF HSE03-1/3x (red)<sup>124</sup>, and NSCFHSE03-1/3x@RPBE (orange) functional are compared with the measured reaction probabilities(grey)<sup>227</sup>. Diamonds and solid lines represent the unaligned state reaction probability ( $S_0$ ). The circles represent the sticking curve of helicoptering molecules that rotate in a plane parallel to the surface ( $S_H$ ) and the plus symbols represent the sticking of molecules that are preferentially aligned perpendicular to the surface ( $S_P$ ).

Similarly to Ref.  $^{124}$ , we simulate the orientationally aligned state-selected  $O_2$  experiments using our NSCF hybrid functional. We ran quasi-classical trajectories for each of the three specific rovibrational states (v=0, j=1, and  $m_j=-1$ , 0, 1) and used Equations 1-5 from the work of Kurahashi $^{227}$  to combine the  $m_j$  state-specific reaction probabilities to obtain sticking probabilities for the two orientationally aligned states prepared experimentally. Note that in

spectroscopic terms the rovibrational spin state of  $O_2$  is indicated by V=0, J=2, K=1, and  $M_K=-1$ , O, O, O is the O ought not to be confused with O, which is the angular momentum associated with the rotation of the molecule. The sticking probabilities computed for the two rotationally aligned states with the SCF HSE03-1/3x DF (red)<sup>124</sup>, and NSCF HSE03-1/3x@RPBE DF (orange) are compared with experiment (grey)<sup>227</sup> in **Figure 3.5**.

# 3.3.4 The role of the energetic corrugation of the barrier height

To explain the difference between the NSCF and SCF reaction probabilities, we tabulated the reaction barriers of both DFs, and their difference ( $\Delta$ ) for each elbow cut used to fit the CRP PES in **Table 3.2**, and we plotted a sample set of the barrier heights for both approaches (SFC and NSCF) in **Figure 3.6**. This figure (as well as **Table 3.2**) shows that all barriers generated using the NSCF approach (orange) are higher in energy than those generated by the SCF approach (red). However, it remains hard to discern a pattern to the shifts in barrier height. There seems to be no constant shift or addition, and the barriers also do not universally scale with a single scalar. There also does not seem to be a clear dependence of the shifts on barrier geometry, nor does the type of surface site seem to influence the shift of the barrier height. However, a consistent trend is that large barriers obtained with the SCF functional correlate with large barriers computed with the NSCF functional and with larger shifts.

The lowest barrier height seen in **Table 3.2** and **Figure 3.6** (Bridge-P,  $\varphi$ :  $O^{\circ}$ ) corresponds roughly with the sticking curve onset seen in **Figure 3.3**. The minimum SCF barrier height is about  $4.7 \, kJ/mol$  and the SCF sticking onset is at approximately the same incidence energy. The NSCF minimum barrier can be found at around  $6.6 \, kJ/mol$  and the onset of the NSCF sticking curve is somewhat below  $7 \, kJ/mol$ . From these results, it is clear that an incidence energy approximately equal to the minimum barrier height is enough to initialise dissociation for a parallel-oriented  $O_2$  molecule (see also Section: 3.3.3.). This is also in agreement with the barriers to dissociation generally being in the entrance channel (see also the potential elbows in **Figure 3.7** for the barrier locations) of the reaction, with Polanyi's rules<sup>273</sup> dictating that the  $10.28 \, kJ/mol$ 

of initial vibrational energy (for the ground state  $O_2$ , see also Section 3.2.5., **Table 3.1**) is not used to overcome this barrier. As such, for a molecular beam with a rotational temperature of only  $9 K (0.03 \, kJ/mol \, \text{for } j=1, 80\% \, \text{populated}$ , see **Table 3.1**) the incidence energy should be the only significant component of the molecule's energy that can be used to overcome the barrier.

**Table 3.2**: Barrier heights computed with the SCF HSE03-1/3 $x^{124}$ , the NSCF HSE03-1/3x@RPBE DFs, and their difference ( $\Delta$ ) are presented for all elbow cuts used to fit the CRP PES. See **Figure 1.1B** for the name and location of the high symmetry sights; the  $O_2$  orientation is indicated with P(parallel) for  $\theta$ =90°, N(Normal) for  $\theta$ =0°, and T(Tilted) for  $\theta$ =45°.

High Symmetry geometry	SCF, HSE03-1/3x Barrier height ( <i>kJ/mol</i> ) <sup>124</sup>	NSCF HSE03-1/3x@RPBE Barrier height ( <i>kJ/mol</i> )	∆ Barrier height (kJ/mol)
Top N	26.8	29.8	3.0
Top P, φ: 0°	22.7	24.4	1.7
Top P, φ: 30°	22.5	24.4	1.9
Bridge N	19.5	25.5	6.0
Bridge P, φ: 0°	4.7	<u>6.6</u>	1.8
Bridge P, φ: 60°	19.6	29.7	10.1
Bridge P, φ: 90°	29.5	51.4	21.8
TtF N	22.9	29.1	6.2
TtF Τ, φ: 150°	26.0	38.0	11.9
TtF Τ, φ: 240°	12.5	16.7	4.1
TtF Τ, φ: 330°	14.4	16.6	2.2
TtF P, φ: 240°	23.6	28.7	5.1
TtF P, φ: 330°	10.7	12.8	2.1
TtH N	21.9	27.7	5.8
TtH Τ, φ: 30°	14.4	16.8	2.4
TtH Τ, φ: 120°	12.8	16.9	4.1
TtH Τ, φ: 210°	25.3	36.3	11.1
TtH P, φ: 30°	10.1	12.3	2.2
TtH P, φ: 120°	23.7	37.8	14.1
FCC N	26.9	38.5	11.6
FCC T, φ: 150°	24.6	32.5	7.9
FCC T, φ: 330°	<u>39.9</u>	<u>60.0</u>	20.1
FCC P, φ: 0°	11.5	13.5	2.0
FCC P, φ: 330°	12.4	14.6	2.2
HCP N	22.8	34.6	11.9
HCP Τ, φ: 210°	23.3	31.0	7.7
HCP Τ, φ: 30°	<u>39.9</u>	56.2	16.3
HCP P, φ: 0°	10.4	12.7	2.3
HCP P, φ: 30°	11.4	13.7	2.3

The barrier height analysis might additionally help with explaining the results of the sticking of rotationally aligned  $O_2$ , as the minimum barrier height is found for the parallel orientation above a bridge site, and barriers for the reaction with  $O_2$  normal to the surface are found at several kJ/mol higher energy. It is therefore not surprising that in the limit of low incidence energy the direct DC mechanism, in which the molecule is parallel to the surface, is favoured.

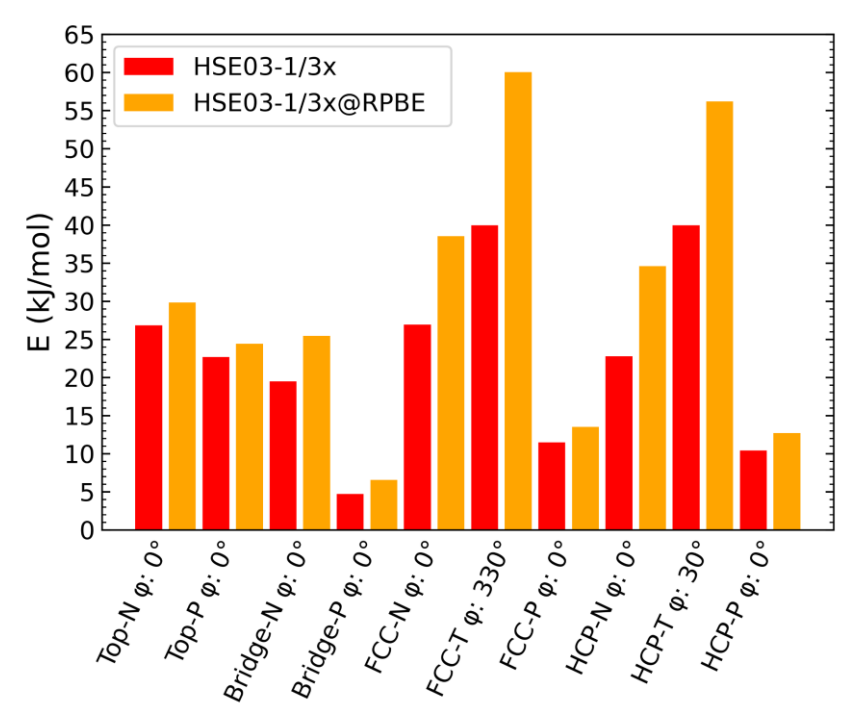


**Figure 3.6**: The barrier heights (in kJ/mol) calculated with the SCF HSE03-1/3x (red) and the NSCF (orange) HSE03-1/3x@RPBE functional are shown for a large set of different geometries. See **Figure 3.1** for the name and location of the high-symmetry sites. The  $O_2$  orientation is indicated with P(parallel) for  $\theta$ =90°, N(normal) for  $\theta$ =0°, and T(tilted) for  $\theta$ =45°.

The analysis of the barrier heights explains why the widths of the sticking probability curves differ for the NSCF and the SCF results. The energetic corrugation of the barrier height is increased with the NSCF approach over the SCF approach, because, as observed in **Figure 3.6** and **Table 3.2**, higher barriers in the SCF approach are correlated with larger positive energy shifts of the NSCF barrier heights relative to the SCF barrier heights. As a result, the difference between the minimum and maximum barrier height for HSE03-1/3x@RPBE in **Table 3.2** is much larger (*53.5 kJ/mol*) than the analogous difference for the self-

consistent HSE03-1/3x DF (*35.2 kJ/mol*), see also the underlined barrier heights in **Table 3.2**. The higher energetic corrugation of the barriers in the NSCF approach is likely the cause of the increased width (i.e., reduced slope) of the NSCF sticking curve relative to that of the SCF curve, as observed in **Figure 3.3**<sup>254</sup>.

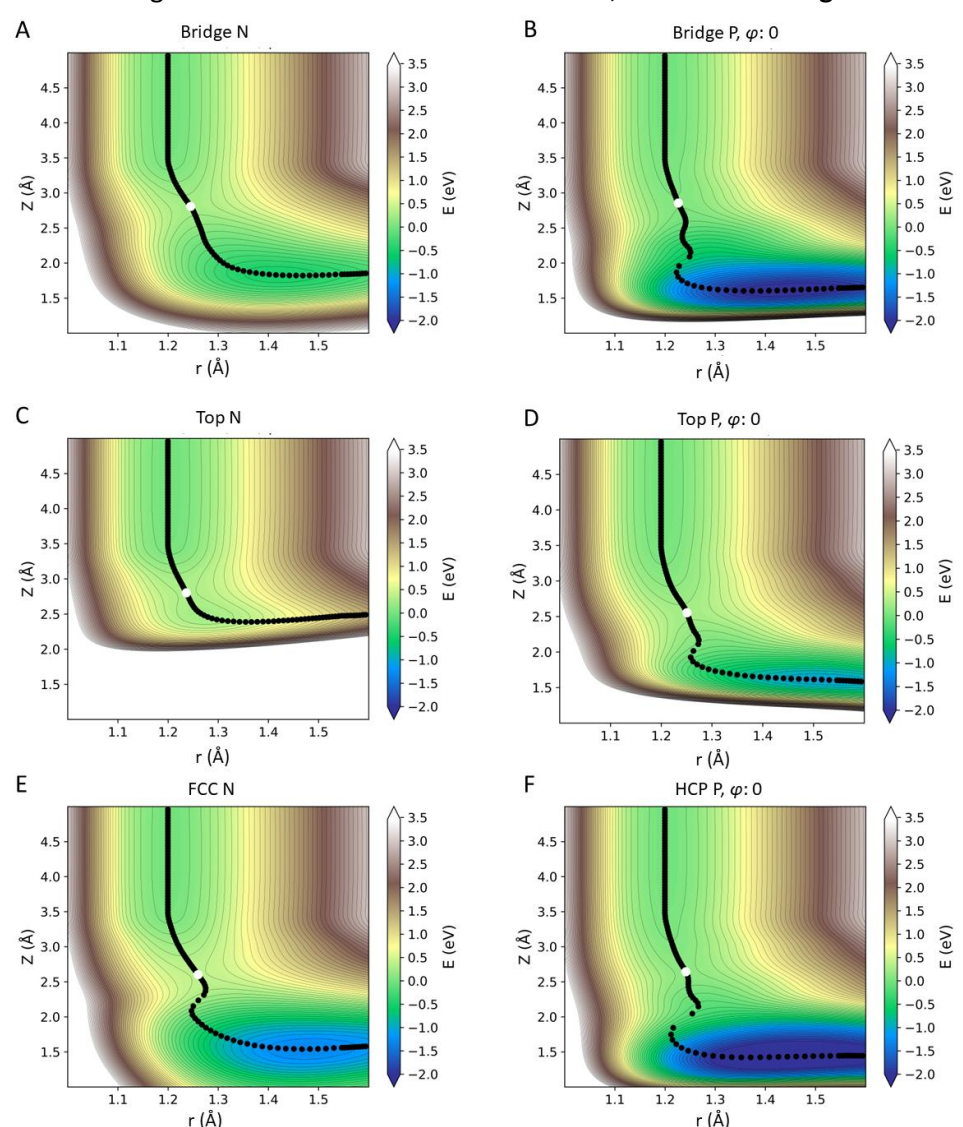


**Figure 3.7**: Set of 6 'elbow cuts', showing slices through the PES as a function of the molecule's bond length (r) and the distance of  $O_2$  to the surface (Z) for six different geometries (sampling four different surface sites and two different molecular orientations). Contour lines are separated by 2 kcal/mol. Each elbow shows the approximate minimum energy path with black dots. The white dots show the location of the transition state in reduced dimensionality; **A**: Bridge N, **B**: Bridge P- $\varphi$ : 0°, **C**: Top N, **D**: Top P- $\varphi$ : 0, **E**: FCC N, **F**: HCP P- $\varphi$ : 0°.

The rather small change of the QCT reaction probability curve width despite the substantial increase of the barrier corrugation (obtained with the NSCF potential) raises concerns about a suggestion made in earlier work<sup>124</sup>. Increasing the energetic corrugation of the barrier height and increasing the anisotropic dependency of the barriers by adding in the attractive van der Waals interaction has been suggested as a way to resolve the difference in slope between the sticking probability curve computed with the HSE03-1/3x functional and the experimental curve<sup>124</sup>. However, with our NSCF approach, we have already inadvertently but considerably changed the barrier corrugation and anisotropy and this is seen to lead only to a minor increase in the width of the sticking curve. Yet, it is unclear what effects Van der Waals correlation would have on the dynamics of the reaction. For future theoretical work of O<sub>2</sub> on Al(111), it may still be relevant to not only attempt to increase the energy corrugation or affect the dynamics with the addition of Van der Waals correlation but also to look more closely at non-adiabatic effects that may occur in this system, which may also affect the slope of the sticking curve: Systems in which charge transfer is likely, like  $O_2$  on Al(111), may also be more prone to electron-hole-pair excitation 124,136,170,171. Additionally, it is not yet known whether or not the thermal displacement of the surface atoms could influence the reaction barriers or whether the sudden approximation will hold for O<sub>2</sub> on Al(111)<sup>221,274,275</sup>. Therefore, we might also need to study the effect of thermal displacements of the surface atoms and of energy transfer to surface atom motion. Conversely, experiments show little influence of the surface temperature on the reaction probability<sup>224</sup> indicating a limited influence of surface motion. However, this has not yet been checked with theory, nor do we know whether the reaction probability can be diminished by energy dissipation to the surface atoms at higher incidence energies. Further theoretical work should address these points.

Although the change in the barrier corrugation appears to be considerable, as stated before the change of the slope (or width) of the reaction probability curve is rather small in **Figure 3.3**. This could also suggest that dynamical effects such as steering play an active role in the reaction, as was also previously suggested by Carter and co-workers<sup>229,230</sup>. Steering effects have also been indicated in other DC systems of slowly rotating molecules incident on a surface at low translational

energies<sup>59,276–278</sup>. The importance of steering effects can be investigated with the hole model, as will now be discussed.

#### 3.3.5 The hole model

An interesting way to test for the importance of dynamical effects is by applying the hole model<sup>254</sup>. Put simply, the hole model states that for a particular geometry, a reaction will occur if the translational plus internal energy of the molecule is equal to or greater than the barrier height<sup>56</sup>. Using the hole model the reaction probability can be computed using Equation 3.3. The method does not include any dynamical effects, but it does include the effect of the distribution of the initial rovibrational  $O_2$  states through its dependence on the initial energy of the molecule. It also includes the effects of the minimum barrier height, the corrugation of the barrier, and the anisotropy of the barrier. The Monte-Carlo-like implementation of the hole model we use is described in detail above, in Section 3.2.6.

In Figure 3.8 we show reaction probability curves computed with four different interpretations of the hole model, where each point on the curve is based on  $10^6$  samples of initial  $O_2$  energies and geometries taken on the HSE03-1/3x@RPBE PES, and compared them to QCT results obtained with the same PES. The uppermost curve implements the regular hole model (i.e., initial vibrational energy included, gold upward triangles interpolated by a dotted line), and the lowest curve shows hole model results where we excluded the vibrational energy of the molecule (light green downward triangles, dotted line). Lastly, Figure 3.8 presents these same reaction probability curves shifted horizontally with  $6.73\ kJ/mol$  and  $-3.54\ kJ/mol$  respectively (darker colour variants and dashed lines) to achieve optimal agreement with QCT results.

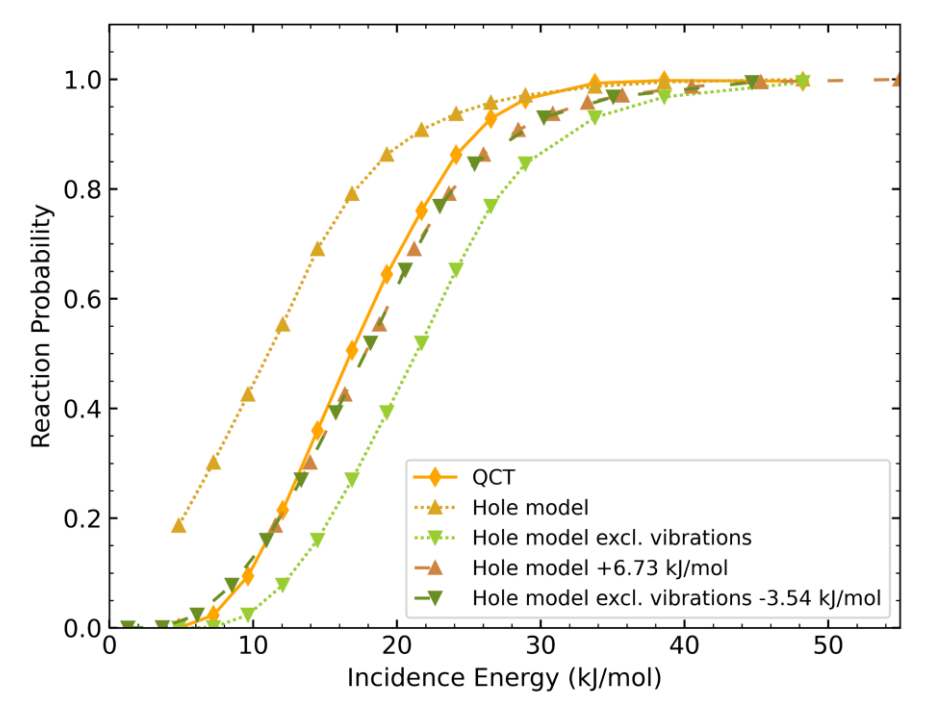


**Figure 3.8**: Reaction probability as a function of incidence energy for the HSE03-1/3x@RPBE DF PES. The results of the QCT method (orange diamonds and solid line), the hole model including vibrational energy (triangles down), and the hole model excluding vibrational energy (triangles up) are shown with dotted lines. The dashed lines represent shifted reaction probabilities obtained with these versions of the hole model. The shift in incidence energy is 6.73 kJ/mol to the right for the hole model including vibrational energy, and 3.54 kJ/mol to the left for the hole model excluding vibrational energy.

The agreement between the regular hole model and the QCT results is reasonable, although it seems that the regular hole model yields a slightly wider reaction probability curve, and systematically overestimates the QCT reaction probability. However, this overestimation is not unexpected. The hole model assumes that all of the internal energy of the molecule is available to overcome the reaction barrier. This includes zero point energy (ZPE), which cannot all be used to overcome a barrier. Additionally, we know from Polanyi's rules<sup>273</sup> that converting vibrational energy into motion along the reaction path should be inefficient for an early barrier reaction. We therefore also included hole model results where we excluded the initial vibrational energy from the total energy of  $O_2$ , which leads to a reaction probability curve that is shifted to higher energy by

about 10 kJ/mol relative to the regular hole model curve. This shift is approximately equal to the vibrational energy of  $O_2$  in v=0 (99% of  $O_2$  is in v=0 at  $T_N=300$  K, see **Table 3.1**). These results, predictably, now underestimate the QCT reaction probability. Excluding all vibrational energy of the molecule is of course a slight overcorrection on Polanyi's rules, as the early barrier is often found at slightly expanded bond lengths (see also **Figure 3.7**). It is also an overcorrection for the ZPE, as the gas-phase ZPE of the  $O_2$  molecule is not the same as, and typically higher than, the ZPE of  $O_2$  at the TS in reduced dimensionality if only r and Z are considered.

To best evaluate the different hole model results we shifted the two different hole model curves horizontally to match the onset of the QCT curve as well as possible (the lowest value of the regular hole model is at a reaction probability of 0.186, thus we match the curves in  $E_i$  to this value of the reaction probability) Figure 3.9 and Figure 3.10 in the Section 3.5.2 show the continuous energy shifts required to superimpose the reaction probability curves for the incidence energy range of 5-30 kJ/mol similar to Figure 3.4). Matching the curves with the QCT results required shifting the regular hole model curve to higher energies by 6.7 kJ/mol, and shifting the hole model curve excluding the effect of the vibration by 3.5 kJ/mol to lower energies. Based on this we can say that the amount of vibrational energy used to overcome the barrier is roughly one-third that of the vibrational energy of O<sub>2</sub> in the gas-phase. Interestingly, shifting the hole model curves like this reveals a small but clear difference between the widths (or slopes) of the reaction probability curves: the hole model reaction probability curves are broader than the QCT reaction probability curve. This suggests that dynamical effects, possibly related to steering, occur and that these favour the dissociation of O<sub>2</sub> on Al(111) most at the low incidence energies where there is time for the forces acting on the molecule to steer it to more favourable geometries for reaction. At the same time, this effect appears to be rather small, suggesting that the hole model can be used as a computationally cheaper screening tool to test electronic structure methods for  $O_2$  + Al(111), or more generally systems where dynamical effects are limited. The use of the hole model allows for savings on computation time not only because dynamics calculations can be skipped, but also because the PES is not required beyond the barrier geometries (i.e., in the exit channel).

#### 3.4 Conclusions

 $O_2$  + Al(111) is a benchmark system for modelling  $O_2$  dissociation on metal surfaces and oxide formation. Thus far, the theoretical community has not been able to come to a consensus on the fundamental mechanisms at play in the dissociative chemisorption of  $O_2$  on Al(111). One underlying cause is that GGA functionals (the most commonly used functionals in the study of gas-metal surface interactions) are unable to describe barriers of  $O_2$  dissociative chemisorption on metals correctly if the charge transfer energy ( $\Phi$  - EA) is smaller than  $T eV^{124}$ . Recent work<sup>124</sup> suggested that using a screened hybrid DF will yield better results than GGA functionals even if the screened hybrid DF is applied in an NSCF manner to a GGA electron density. Here we tested this idea for  $O_2$  + Al(111).

Our results show that the NSCF approach to a screened hybrid density functional (DF) (HSE03-1/3x@RPBE) is indeed a major improvement over GGA (RPBE) or even meta-GGA (MS-RPBEI) DFs for describing the dissociative chemisorption of  $O_2$  on Al(111), while also limiting the extra computational cost by at least one order of magnitude compared to fully self-consistent hybrid calculations. The sticking curves generated with the NSCF-DF are within near chemical accuracy of the SCF-DF results for both full molecular beam simulations and rotationally aligned sticking. Moreover, with the NSCF approach, the quantitative agreement with experiments was inadvertently improved over that obtained with the SCF HSE03-1/3x approach.

The NSCF-screened hybrid DF was not able to exactly reproduce the SCF-screened hybrid functional results. The onset of the NSCF DF reaction probability at low incidence energy is within chemical accuracy of the SCF results. The NSCF approach leads to a slightly reduced slope of the reaction probability curve, resulting in a slightly increased disagreement with the SCF results at larger incidence energies. This can be traced back to the differences in barrier heights between the SCF and NSCF methods. The NSCF barrier heights are shifted to higher energies relative to the SCF barriers by a minimum of 1.8 kJ/mol, with the difference increasing with the SCF barrier height. Overall the anisotropic variation of the barrier height and the corrugation of the barrier height have been increased by the NSCF approach relative to the SCF HSE03-1/3x DF case.

This has resulted in a minor decrease in the slope of the reaction probability curve and, conversely, a slight increase in its width.

Irrespective of the small quantitative disagreement of sticking probabilities and barrier heights obtained with the NSCF and SCF approaches, the argument that originally inspired us to explore the NSCF approach (accurate while much cheaper computationally) still holds considerable credence based on the results of this chapter. It is clear that based on only a GGA density we can achieve a vast improvement of the interaction energy of  $O_2 + Al(111)$  simply by non-self-consistently applying a screened hybrid functional to a GGA electron density once. Based on the small differences between the SCF and the NSCF results, we conclude that the greater part of the error in describing the  $O_2 + Al(111)$  system with a GGA DF is functional-driven and not density-driven. However, the remaining disagreement between the SCF and NSCF results suggests that a small density-driven error from using a GGA-level functional is still present.

Increasing the width of the sticking curve of  $O_2$  on Al(111) remains a priority for future work as the onset of the sticking curve is described with good agreement with both the SCF and NSCF functionals. Previous work suggested that this could be achieved by increasing the corrugation and anisotropy of barriers by incorporating Van der Waals correlation into the DF. The QCT and hole model reaction probability comparison suggests that the corrugation and anisotropy of the barrier may, however, not be the only factors influencing the width of the sticking curve. Nonetheless, the effect of including Van der Waals correlation in the DF on the dynamics should still be investigated. At the same time, due to the low charge transfer energy, electron-hole-pair excitations may need to be taken into account in future work, which could help to further broaden the sticking curve. Furthermore, introducing surface atom motion could also affect the width of the computed sticking probability curve for  $O_2$  on Al(111) by either influencing the barriers via thermal surface atom displacements or through energy transfer between the motions of  $O_2$  and the Al surface atoms.

## 3.5 Appendices

This chapter has two minor appendices. The first (Section 3.5.1) compares the barrier energies extracted from the CRP-PES to the corresponding HSE03-1/3x@RPBE DFT energy and shows the difference in energy and the RMSE. The second appendix (Section 3.5.2) shows two figures presenting the different energy shifts between the QCT and hole model sticking probabilities.

## 3.5.1 CRP test set

**Table 3.3:** Barrier energies as extracted from the CRP PES, and computed with DFT single point calculations for the CRP barrier geometries, the deviation ( $\Delta$ ) between them, and the resulting root mean squared error based on the deviations. See **Figure 3.1B** for the name and location of the high symmetry sites; the  $O_2$  orientation is indicated with P(parallel) for  $\theta$ =90°, N(Normal) for  $\theta$ =0°, and T(Tilted) for  $\theta$ =45°.

Top N         29.833         29.735         -0.098           Top P, $\varphi$ : 0°         24.423         24.152         -0.271           Top P, $\varphi$ : 30°         24.409         24.189         -0.220           Bridge N         25.451         25.334         -0.117           Bridge P, $\varphi$ : 0°         6.559         6.533         -0.027           Bridge P, $\varphi$ : 60°         29.727         29.470         -0.257           Bridge P, $\varphi$ : 90°         51.360         54.332         2.972           TtF N         29.108         29.127         0.019           TtF T, $\varphi$ : 150°         37.979         37.285         -0.694           TtF T, $\varphi$ : 330°         16.625         16.686         -0.003           TtF T, $\varphi$ : 330°         16.625         16.625         0.000           TtF P, $\varphi$ : 240°         28.736         28.527         -0.209           TtH T, $\varphi$ : 330°         16.821         16.632         0.011           TtH T, $\varphi$ : 30°         16.821         16.832         0.011           TtH T, $\varphi$ : 120°         36.335         35.837         -0.498           TtH P, $\varphi$ : 210°         37.847         37.466         -0.381           FCC N         38.521         38.982	High Symmetry geometry	CRP HSE03-1/3x@RPBE Barrier height ( <i>kJ/mol</i> )	DFT HSE03-1/3x@RPBE Barrier height ( <i>k]/mol</i> )	Δ (DFT-CRP) Barrier height ( <i>k]/mol</i> )
Top P, $\varphi$ : $30^{\circ}$ $24.409$ $24.189$ $-0.220$ Bridge N $25.451$ $25.334$ $-0.117$ Bridge P, $\varphi$ : $0^{\circ}$ $6.559$ $6.533$ $-0.027$ Bridge P, $\varphi$ : $60^{\circ}$ $29.727$ $29.470$ $-0.257$ Bridge P, $\varphi$ : $90^{\circ}$ $51.360$ $54.332$ $2.972$ TtF N $29.108$ $29.127$ $0.019$ TtF T, $\varphi$ : $150^{\circ}$ $37.979$ $37.285$ $-0.694$ TtF T, $\varphi$ : $240^{\circ}$ $16.688$ $16.686$ $-0.003$ TtF P, $\varphi$ : $330^{\circ}$ $16.625$ $16.625$ $0.000$ TtF P, $\varphi$ : $330^{\circ}$ $12.835$ $12.624$ $-0.212$ TtH N $27.718$ $27.690$ $-0.028$ TtH T, $\varphi$ : $120^{\circ}$ $16.821$ $16.832$ $0.011$ TtH T, $\varphi$ : $210^{\circ}$ $36.335$ $35.837$ $-0.498$ TtH P, $\varphi$ : $120^{\circ}$ $36.335$ $35.837$ $-0.498$ TtH P, $\varphi$ : $120^{\circ}$ $37.466$ $-0.381$ FCC N, $\varphi$ : $330^{\circ}$ $32.487$		29.833	29.735	-0.098
Bridge N $25.451$ $25.334$ $-0.117$ Bridge P, $\varphi$ : 0° $6.559$ $6.533$ $-0.027$ Bridge P, $\varphi$ : 60° $29.727$ $29.470$ $-0.257$ Bridge P, $\varphi$ : 90° $51.360$ $54.332$ $2.972$ TtF N $29.108$ $29.127$ $0.019$ TtF T, $\varphi$ : $150^\circ$ $37.979$ $37.285$ $-0.694$ TtF T, $\varphi$ : $240^\circ$ $16.688$ $16.686$ $-0.003$ TtF T, $\varphi$ : $330^\circ$ $16.625$ $16.625$ $0.000$ TtF P, $\varphi$ : $240^\circ$ $28.736$ $28.527$ $-0.209$ TtF P, $\varphi$ : $330^\circ$ $12.835$ $12.624$ $-0.212$ TtH N $27.718$ $27.690$ $-0.028$ TtH T, $\varphi$ : $30^\circ$ $16.821$ $16.832$ $0.011$ TtH T, $\varphi$ : $210^\circ$ $36.335$ $35.837$ $-0.498$ TtH P, $\varphi$ : $30^\circ$ $12.313$ $12.031$ $-0.282$ TtH P, $\varphi$ : $120^\circ$ $37.847$ $37.466$ $-0.381$ FCC N $38.521$ $38.982$	Top P, φ: 0°	24.423	24.152	-0.271
Bridge $P, \varphi: 0^{\circ}$ $6.559$ $6.533$ $-0.027$ Bridge $P, \varphi: 60^{\circ}$ $29.727$ $29.470$ $-0.257$ Bridge $P, \varphi: 90^{\circ}$ $51.360$ $54.332$ $2.972$ TtF $N$ $29.108$ $29.127$ $0.019$ TtF $T, \varphi: 150^{\circ}$ $37.979$ $37.285$ $-0.694$ TtF $T, \varphi: 240^{\circ}$ $16.688$ $16.686$ $-0.003$ TtF $P, \varphi: 330^{\circ}$ $16.625$ $16.625$ $0.000$ TtF $P, \varphi: 330^{\circ}$ $12.835$ $12.624$ $-0.212$ TtH $N$ $27.718$ $27.690$ $-0.028$ TtH $T, \varphi: 30^{\circ}$ $16.821$ $16.832$ $0.011$ TtH $T, \varphi: 120^{\circ}$ $16.920$ $16.930$ $0.009$ TtH $P, \varphi: 210^{\circ}$ $36.335$ $35.837$ $-0.498$ TtH $P, \varphi: 30^{\circ}$ $12.313$ $12.031$ $-0.282$ TtH $P, \varphi: 120^{\circ}$ $37.847$ $37.466$ $-0.381$ FCC $N$ $38.521$ $38.982$ $0.460$ FCC $P, \varphi: 330^{\circ}$ $59.569$ $-0.457$ FCC $P, \varphi: 0^{\circ}$ $13.507$ $13.21$	Top P, φ: 30°	24.409	24.189	-0.220
Bridge $P, \varphi: 60^{\circ}$ $29.727$ $29.470$ $-0.257$ Bridge $P, \varphi: 90^{\circ}$ $51.360$ $54.332$ $2.972$ $TtF N$ $29.108$ $29.127$ $0.019$ $TtF T, \varphi: 150^{\circ}$ $37.979$ $37.285$ $-0.694$ $TtF T, \varphi: 240^{\circ}$ $16.688$ $16.686$ $-0.003$ $TtF T, \varphi: 330^{\circ}$ $16.625$ $16.625$ $0.000$ $TtF P, \varphi: 340^{\circ}$ $28.736$ $28.527$ $-0.209$ $TtF P, \varphi: 330^{\circ}$ $12.835$ $12.624$ $-0.212$ $TtH N$ $27.718$ $27.690$ $-0.028$ $TtH T, \varphi: 30^{\circ}$ $16.821$ $16.832$ $0.011$ $TtH T, \varphi: 120^{\circ}$ $16.920$ $16.930$ $0.009$ $TtH P, \varphi: 30^{\circ}$ $12.313$ $12.031$ $-0.282$ $TtH P, \varphi: 30^{\circ}$ $12.313$ $12.031$ $-0.282$ $TtH P, \varphi: 120^{\circ}$ $37.847$ $37.466$ $-0.381$ $FCC N$ $38.521$ $38.982$ $0.460$ $FCC T, \varphi: 330^{\circ}$ $60.026$ $59.569$ $-0.457$ $FCC P, \varphi: 0^{\circ}$ $13.50$	Bridge N	25.451	25.334	-0.117
Bridge $P, \varphi: 90^\circ$ $51.360$ $54.332$ $2.972$ $TtF N$ $29.108$ $29.127$ $0.019$ $TtF T, \varphi: 150^\circ$ $37.979$ $37.285$ $-0.694$ $TtF T, \varphi: 240^\circ$ $16.688$ $16.686$ $-0.003$ $TtF T, \varphi: 330^\circ$ $16.625$ $16.625$ $0.000$ $TtF P, \varphi: 240^\circ$ $28.736$ $28.527$ $-0.209$ $TtF P, \varphi: 330^\circ$ $12.835$ $12.624$ $-0.209$ $TtH N$ $27.718$ $27.690$ $-0.028$ $TtH T, \varphi: 30^\circ$ $16.821$ $16.832$ $0.011$ $TtH T, \varphi: 120^\circ$ $36.335$ $35.837$ $-0.498$ $TtH T, \varphi: 210^\circ$ $36.335$ $35.837$ $-0.498$ $TtH P, \varphi: 30^\circ$ $12.313$ $12.031$ $-0.282$ $TtH P, \varphi: 120^\circ$ $37.847$ $37.466$ $-0.381$ $FCC N$ $38.521$ $38.982$ $0.460$ $FCC T, \varphi: 150^\circ$ $32.487$ $32.623$ $0.136$ $FCC P, \varphi: 0^\circ$ $13.507$ $13.218$	Bridge P, φ: 0°	6.559	6.533	-0.027
$TtFN$ $29.108$ $29.127$ $0.019$ $TtFT, \varphi: 150^{\circ}$ $37.979$ $37.285$ $-0.694$ $TtFT, \varphi: 240^{\circ}$ $16.688$ $16.686$ $-0.003$ $TtFT, \varphi: 330^{\circ}$ $16.625$ $16.625$ $0.000$ $TtFP, \varphi: 240^{\circ}$ $28.736$ $28.527$ $-0.209$ $TtFP, \varphi: 330^{\circ}$ $12.835$ $12.624$ $-0.212$ $TtHN$ $27.718$ $27.690$ $-0.028$ $TtHT, \varphi: 30^{\circ}$ $16.821$ $16.832$ $0.011$ $TtHT, \varphi: 120^{\circ}$ $16.920$ $16.930$ $0.009$ $TtHT, \varphi: 210^{\circ}$ $36.335$ $35.837$ $-0.498$ $TtHP, \varphi: 30^{\circ}$ $12.313$ $12.031$ $-0.282$ $TtHP, \varphi: 120^{\circ}$ $37.847$ $37.466$ $-0.381$ $FCCN$ $38.521$ $38.982$ $0.460$ $FCCT, \varphi: 150^{\circ}$ $32.487$ $32.623$ $0.136$ $FCCT, \varphi: 330^{\circ}$ $60.026$ $59.569$ $-0.457$ $FCCP, \varphi: 330^{\circ}$ $14.612$ $14.289$ $-0.289$ $FCCP, \varphi: 300^{\circ}$ $34.616$	Bridge P, φ: 60°	29.727	29.470	-0.257
$TtFT, \varphi: 150^{\circ}$ $37.979$ $37.285$ $-0.694$ $TtFT, \varphi: 240^{\circ}$ $16.688$ $16.686$ $-0.003$ $TtFT, \varphi: 330^{\circ}$ $16.625$ $0.000$ $TtFP, \varphi: 240^{\circ}$ $28.736$ $28.527$ $-0.209$ $TtFP, \varphi: 330^{\circ}$ $12.835$ $12.624$ $-0.212$ $TtHN$ $27.718$ $27.690$ $-0.028$ $TtHT, \varphi: 30^{\circ}$ $16.821$ $16.832$ $0.011$ $TtHT, \varphi: 120^{\circ}$ $16.920$ $16.930$ $0.009$ $TtHP, \varphi: 30^{\circ}$ $12.313$ $12.031$ $-0.282$ $TtHP, \varphi: 30^{\circ}$ $12.313$ $12.031$ $-0.282$ $TtHP, \varphi: 120^{\circ}$ $37.847$ $37.466$ $-0.381$ $FCCN$ $38.521$ $38.982$ $0.460$ $FCCT, \varphi: 150^{\circ}$ $32.487$ $32.623$ $0.136$ $FCCP, \varphi: 0^{\circ}$ $13.507$ $13.218$ $-0.289$ $FCCP, \varphi: 330^{\circ}$ $14.612$ $14.289$ $-0.332$ $HCPN$ $34.616$ $34.929$ $0.313$ $HCPT, \varphi: 30^{\circ}$ $56.217$ $56.139$ $-0.$	Bridge P, φ: 90°	51.360	54.332	2.972
$TtFT, \varphi: 240^\circ$ $16.688$ $16.625$ $16.625$ $0.000$ $TtFT, \varphi: 330^\circ$ $16.625$ $16.625$ $0.000$ $TtFP, \varphi: 240^\circ$ $28.736$ $28.527$ $-0.209$ $TtFP, \varphi: 330^\circ$ $12.835$ $12.624$ $-0.212$ $TtHN$ $27.718$ $27.690$ $-0.028$ $TtHT, \varphi: 30^\circ$ $16.821$ $16.832$ $0.011$ $TtHT, \varphi: 120^\circ$ $16.920$ $16.930$ $0.009$ $TtHT, \varphi: 210^\circ$ $36.335$ $35.837$ $-0.498$ $TtHP, \varphi: 30^\circ$ $12.313$ $12.031$ $-0.282$ $TtHP, \varphi: 120^\circ$ $37.847$ $37.466$ $-0.381$ $FCCN$ $38.521$ $38.982$ $0.460$ $FCCT, \varphi: 150^\circ$ $32.487$ $32.623$ $0.136$ $FCCT, \varphi: 330^\circ$ $60.026$ $59.569$ $-0.457$ $FCCP, \varphi: 0^\circ$ $13.507$ $13.218$ $-0.289$ $FCCP, \varphi: 330^\circ$ $14.612$ $14.289$ $-0.332$ $HCPT, \varphi: 210^\circ$ $30.969$ $31.125$ $0.156$ $HCPT, \varphi: 30^\circ$ $12.707$ <t< td=""><td>TtF N</td><td>29.108</td><td>29.127</td><td>0.019</td></t<>	TtF N	29.108	29.127	0.019
$TtF T, \varphi: 330^{\circ}$ $16.625$ $16.625$ $0.000$ $TtF P, \varphi: 240^{\circ}$ $28.736$ $28.527$ $-0.209$ $TtF P, \varphi: 330^{\circ}$ $12.835$ $12.624$ $-0.212$ $TtH N$ $27.718$ $27.690$ $-0.028$ $TtH T, \varphi: 30^{\circ}$ $16.821$ $16.832$ $0.011$ $TtH T, \varphi: 120^{\circ}$ $16.920$ $16.930$ $0.009$ $TtH P, \varphi: 30^{\circ}$ $12.313$ $12.031$ $-0.282$ $TtH P, \varphi: 120^{\circ}$ $37.847$ $37.466$ $-0.381$ $FCC N$ $38.521$ $38.982$ $0.460$ $FCC T, \varphi: 150^{\circ}$ $32.487$ $32.623$ $0.136$ $FCC T, \varphi: 330^{\circ}$ $60.026$ $59.569$ $-0.457$ $FCC P, \varphi: 0^{\circ}$ $13.507$ $13.218$ $-0.289$ $FCC P, \varphi: 330^{\circ}$ $14.612$ $14.289$ $-0.332$ $HCP N$ $34.616$ $34.929$ $0.313$ $HCP T, \varphi: 30^{\circ}$ $56.217$ $56.139$ $-0.078$ $HCP P, \varphi: 30^{\circ}$ $12.707$ $12.455$ $-0.252$ $HCP P, \varphi: 30^{\circ}$ $13.700$ <td>TtF Τ, φ: 150°</td> <td>37.979</td> <td>37.285</td> <td>-0.694</td>	TtF Τ, φ: 150°	37.979	37.285	-0.694
$TtF P, \varphi: 240^{\circ}$ $28.736$ $28.527$ $-0.209$ $TtF P, \varphi: 330^{\circ}$ $12.835$ $12.624$ $-0.212$ $TtH N$ $27.718$ $27.690$ $-0.028$ $TtH T, \varphi: 30^{\circ}$ $16.821$ $16.832$ $0.011$ $TtH T, \varphi: 120^{\circ}$ $16.920$ $16.930$ $0.009$ $TtH T, \varphi: 210^{\circ}$ $36.335$ $35.837$ $-0.498$ $TtH P, \varphi: 30^{\circ}$ $12.313$ $12.031$ $-0.282$ $TtH P, \varphi: 120^{\circ}$ $37.847$ $37.466$ $-0.381$ $FCC N$ $38.521$ $38.982$ $0.460$ $FCC T, \varphi: 150^{\circ}$ $32.487$ $32.623$ $0.136$ $FCC T, \varphi: 330^{\circ}$ $60.026$ $59.569$ $-0.457$ $FCC P, \varphi: 30^{\circ}$ $13.507$ $13.218$ $-0.289$ $FCC P, \varphi: 330^{\circ}$ $14.612$ $14.289$ $-0.332$ $HCP N$ $34.616$ $34.929$ $0.313$ $HCP T, \varphi: 210^{\circ}$ $30.969$ $31.125$ $0.156$ $HCP P, \varphi: 30^{\circ}$ $12.707$ $12.455$ $-0.252$ $HCP P, \varphi: 30^{\circ}$ $13.700$ </td <td>TtF Τ, φ: 240°</td> <td>16.688</td> <td>16.686</td> <td>-0.003</td>	TtF Τ, φ: 240°	16.688	16.686	-0.003
$TtF P, \varphi: 330^{\circ}$ $12.835$ $12.624$ $-0.212$ $TtH N$ $27.718$ $27.690$ $-0.028$ $TtH T, \varphi: 30^{\circ}$ $16.821$ $16.832$ $0.011$ $TtH T, \varphi: 120^{\circ}$ $16.920$ $16.930$ $0.009$ $TtH T, \varphi: 210^{\circ}$ $36.335$ $35.837$ $-0.498$ $TtH P, \varphi: 30^{\circ}$ $12.313$ $12.031$ $-0.282$ $TtH P, \varphi: 120^{\circ}$ $37.847$ $37.466$ $-0.381$ $FCC N$ $38.521$ $38.982$ $0.460$ $FCC T, \varphi: 150^{\circ}$ $32.487$ $32.623$ $0.136$ $FCC T, \varphi: 330^{\circ}$ $60.026$ $59.569$ $-0.457$ $FCC P, \varphi: 0^{\circ}$ $13.507$ $13.218$ $-0.289$ $FCC P, \varphi: 30^{\circ}$ $14.612$ $14.289$ $-0.332$ $HCP N$ $34.616$ $34.929$ $0.313$ $HCP T, \varphi: 210^{\circ}$ $30.969$ $31.125$ $0.156$ $HCP P, \varphi: 30^{\circ}$ $12.707$ $12.455$ $-0.252$ $HCP P, \varphi: 30^{\circ}$ $13.700$ $13.551$ $-0.149$	TtF Τ, φ: 330°	16.625	16.625	0.000
$TtH N$ $27.718$ $27.690$ $-0.028$ $TtH T, \varphi: 30^{\circ}$ $16.821$ $16.832$ $0.011$ $TtH T, \varphi: 120^{\circ}$ $16.920$ $16.930$ $0.009$ $TtH T, \varphi: 210^{\circ}$ $36.335$ $35.837$ $-0.498$ $TtH P, \varphi: 30^{\circ}$ $12.313$ $12.031$ $-0.282$ $TtH P, \varphi: 120^{\circ}$ $37.847$ $37.466$ $-0.381$ FCC N $38.521$ $38.982$ $0.460$ FCC T, $\varphi: 150^{\circ}$ $32.487$ $32.623$ $0.136$ FCC T, $\varphi: 330^{\circ}$ $60.026$ $59.569$ $-0.457$ FCC P, $\varphi: 0^{\circ}$ $13.507$ $13.218$ $-0.289$ FCC P, $\varphi: 330^{\circ}$ $14.612$ $14.289$ $-0.332$ HCP N $34.616$ $34.929$ $0.313$ HCP T, $\varphi: 210^{\circ}$ $30.969$ $31.125$ $0.156$ HCP T, $\varphi: 30^{\circ}$ $56.217$ $56.139$ $-0.078$ HCP P, $\varphi: 30^{\circ}$ $12.707$ $12.455$ $-0.252$ HCP P, $\varphi: 30^{\circ}$ $13.700$ $13.551$ $-0.149$	TtF P, φ: 240°	28.736	28.527	-0.209
$TtH T, \varphi: 30^{\circ}$ $16.821$ $16.832$ $0.011$ $TtH T, \varphi: 120^{\circ}$ $16.920$ $16.930$ $0.009$ $TtH T, \varphi: 210^{\circ}$ $36.335$ $35.837$ $-0.498$ $TtH P, \varphi: 30^{\circ}$ $12.313$ $12.031$ $-0.282$ $TtH P, \varphi: 120^{\circ}$ $37.847$ $37.466$ $-0.381$ $FCC N$ $38.521$ $38.982$ $0.460$ $FCC T, \varphi: 150^{\circ}$ $32.487$ $32.623$ $0.136$ $FCC T, \varphi: 330^{\circ}$ $60.026$ $59.569$ $-0.457$ $FCC P, \varphi: 30^{\circ}$ $13.507$ $13.218$ $-0.289$ $FCC P, \varphi: 30^{\circ}$ $14.612$ $14.289$ $-0.332$ $HCP N$ $34.616$ $34.929$ $0.313$ $HCP T, \varphi: 210^{\circ}$ $30.969$ $31.125$ $0.156$ $HCP T, \varphi: 30^{\circ}$ $56.217$ $56.139$ $-0.078$ $HCP P, \varphi: 0^{\circ}$ $12.707$ $12.455$ $-0.252$ $HCP P, \varphi: 30^{\circ}$ $13.700$ $13.551$ $-0.149$	TtF P, φ: 330°	12.835	12.624	-0.212
$TtH T, \varphi: 120^{\circ}$ $16.920$ $16.930$ $0.009$ $TtH T, \varphi: 210^{\circ}$ $36.335$ $35.837$ $-0.498$ $TtH P, \varphi: 30^{\circ}$ $12.313$ $12.031$ $-0.282$ $TtH P, \varphi: 120^{\circ}$ $37.847$ $37.466$ $-0.381$ $FCC N$ $38.521$ $38.982$ $0.460$ $FCC T, \varphi: 150^{\circ}$ $32.487$ $32.623$ $0.136$ $FCC T, \varphi: 330^{\circ}$ $60.026$ $59.569$ $-0.457$ $FCC P, \varphi: 0^{\circ}$ $13.507$ $13.218$ $-0.289$ $FCC P, \varphi: 30^{\circ}$ $14.612$ $14.289$ $-0.332$ $HCP N$ $34.616$ $34.929$ $0.313$ $HCP T, \varphi: 210^{\circ}$ $30.969$ $31.125$ $0.156$ $HCP T, \varphi: 30^{\circ}$ $56.217$ $56.139$ $-0.078$ $HCP P, \varphi: 0^{\circ}$ $12.707$ $12.455$ $-0.252$ $HCP P, \varphi: 30^{\circ}$ $13.700$ $13.551$ $-0.149$	TtH N	27.718	27.690	-0.028
$TtH T, \varphi: 210^{\circ}$ $36.335$ $35.837$ $-0.498$ $TtH P, \varphi: 30^{\circ}$ $12.313$ $12.031$ $-0.282$ $TtH P, \varphi: 120^{\circ}$ $37.847$ $37.466$ $-0.381$ $FCC N$ $38.521$ $38.982$ $0.460$ $FCC T, \varphi: 150^{\circ}$ $32.487$ $32.623$ $0.136$ $FCC T, \varphi: 330^{\circ}$ $60.026$ $59.569$ $-0.457$ $FCC P, \varphi: 0^{\circ}$ $13.507$ $13.218$ $-0.289$ $FCC P, \varphi: 330^{\circ}$ $14.612$ $14.289$ $-0.332$ $HCP N$ $34.616$ $34.929$ $0.313$ $HCP T, \varphi: 210^{\circ}$ $30.969$ $31.125$ $0.156$ $HCP T, \varphi: 30^{\circ}$ $56.217$ $56.139$ $-0.078$ $HCP P, \varphi: 0^{\circ}$ $12.707$ $12.455$ $-0.252$ $HCP P, \varphi: 30^{\circ}$ $13.700$ $13.551$ $-0.149$	TtH T, φ: 30°	16.821	16.832	0.011
$TtH P, \varphi: 30^{\circ}$ $12.313$ $12.031$ $-0.282$ $TtH P, \varphi: 120^{\circ}$ $37.847$ $37.466$ $-0.381$ $FCC N$ $38.521$ $38.982$ $0.460$ $FCC T, \varphi: 150^{\circ}$ $32.487$ $32.623$ $0.136$ $FCC T, \varphi: 330^{\circ}$ $60.026$ $59.569$ $-0.457$ $FCC P, \varphi: 0^{\circ}$ $13.507$ $13.218$ $-0.289$ $FCC P, \varphi: 330^{\circ}$ $14.612$ $14.289$ $-0.332$ $HCP N$ $34.616$ $34.929$ $0.313$ $HCP T, \varphi: 210^{\circ}$ $30.969$ $31.125$ $0.156$ $HCP T, \varphi: 30^{\circ}$ $56.217$ $56.139$ $-0.078$ $HCP P, \varphi: 0^{\circ}$ $12.707$ $12.455$ $-0.252$ $HCP P, \varphi: 30^{\circ}$ $13.700$ $13.551$ $-0.149$	TtH T, φ: 120°	16.920	16.930	0.009
$TtH P, \varphi: 120^{\circ}$ $37.847$ $37.466$ $-0.381$ $FCC N$ $38.521$ $38.982$ $0.460$ $FCC T, \varphi: 150^{\circ}$ $32.487$ $32.623$ $0.136$ $FCC T, \varphi: 330^{\circ}$ $60.026$ $59.569$ $-0.457$ $FCC P, \varphi: 0^{\circ}$ $13.507$ $13.218$ $-0.289$ $FCC P, \varphi: 330^{\circ}$ $14.612$ $14.289$ $-0.332$ $HCP N$ $34.616$ $34.929$ $0.313$ $HCP T, \varphi: 210^{\circ}$ $30.969$ $31.125$ $0.156$ $HCP T, \varphi: 30^{\circ}$ $56.217$ $56.139$ $-0.078$ $HCP P, \varphi: 0^{\circ}$ $12.707$ $12.455$ $-0.252$ $HCP P, \varphi: 30^{\circ}$ $13.700$ $13.551$ $-0.149$	TtH T, φ: 210°	36.335	35.837	-0.498
FCC N $38.521$ $38.982$ $0.460$ FCC T, $\varphi$ : $150^\circ$ $32.487$ $32.623$ $0.136$ FCC T, $\varphi$ : $330^\circ$ $60.026$ $59.569$ $-0.457$ FCC P, $\varphi$ : $0^\circ$ $13.507$ $13.218$ $-0.289$ FCC P, $\varphi$ : $330^\circ$ $14.612$ $14.289$ $-0.332$ HCP N $34.616$ $34.929$ $0.313$ HCP T, $\varphi$ : $210^\circ$ $30.969$ $31.125$ $0.156$ HCP T, $\varphi$ : $30^\circ$ $56.217$ $56.139$ $-0.078$ HCP P, $\varphi$ : $0^\circ$ $12.707$ $12.455$ $-0.252$ HCP P, $\varphi$ : $30^\circ$ $13.700$ $13.551$ $-0.149$	TtH P, φ: 30°	12.313	12.031	-0.282
FCC T, φ: 150°       32.487       32.623       0.136         FCC T, φ: 330°       60.026       59.569       -0.457         FCC P, φ: 0°       13.507       13.218       -0.289         FCC P, φ: 330°       14.612       14.289       -0.332         HCP N       34.616       34.929       0.313         HCP T, φ: 210°       30.969       31.125       0.156         HCP T, φ: 30°       56.217       56.139       -0.078         HCP P, φ: 0°       12.707       12.455       -0.252         HCP P, φ: 30°       13.700       13.551       -0.149	TtH P, φ: 120°	37.847	37.466	-0.381
$FCC\ T, \varphi: 330^\circ$ $60.026$ $59.569$ $-0.457$ $FCC\ P, \varphi: 0^\circ$ $13.507$ $13.218$ $-0.289$ $FCC\ P, \varphi: 330^\circ$ $14.612$ $14.289$ $-0.332$ $HCP\ N$ $34.616$ $34.929$ $0.313$ $HCP\ T, \varphi: 210^\circ$ $30.969$ $31.125$ $0.156$ $HCP\ T, \varphi: 30^\circ$ $56.217$ $56.139$ $-0.078$ $HCP\ P, \varphi: 0^\circ$ $12.707$ $12.455$ $-0.252$ $HCP\ P, \varphi: 30^\circ$ $13.700$ $13.551$ $-0.149$	FCC N	38.521	38.982	0.460
FCC P, $\varphi$ : 0°       13.507       13.218       -0.289         FCC P, $\varphi$ : 330°       14.612       14.289       -0.332         HCP N       34.616       34.929       0.313         HCP T, $\varphi$ : 210°       30.969       31.125       0.156         HCP T, $\varphi$ : 30°       56.217       56.139       -0.078         HCP P, $\varphi$ : 0°       12.707       12.455       -0.252         HCP P, $\varphi$ : 30°       13.700       13.551       -0.149	FCC Τ, φ: 150°	32.487	32.623	0.136
FCC P, $\varphi$ : 330°       14.612       14.289       -0.332         HCP N       34.616       34.929       0.313         HCP T, $\varphi$ : 210°       30.969       31.125       0.156         HCP T, $\varphi$ : 30°       56.217       56.139       -0.078         HCP P, $\varphi$ : 0°       12.707       12.455       -0.252         HCP P, $\varphi$ : 30°       13.700       13.551       -0.149	FCC Τ, φ: 330°	60.026	59.569	-0.457
HCP N       34.616       34.929       0.313         HCP T, φ: 210°       30.969       31.125       0.156         HCP T, φ: 30°       56.217       56.139       -0.078         HCP P, φ: 0°       12.707       12.455       -0.252         HCP P, φ: 30°       13.700       13.551       -0.149	FCC P, φ: 0°	13.507	13.218	-0.289
HCP N       34.616       34.929       0.313         HCP T, φ: 210°       30.969       31.125       0.156         HCP T, φ: 30°       56.217       56.139       -0.078         HCP P, φ: 0°       12.707       12.455       -0.252         HCP P, φ: 30°       13.700       13.551       -0.149	FCC P, φ: 330°	14.612	14.289	-0.332
HCP T, φ: 30°       56.217       56.139       -0.078         HCP P, φ: 0°       12.707       12.455       -0.252         HCP P, φ: 30°       13.700       13.551       -0.149		34.616	34.929	0.313
HCP P, φ: 0°       12.707       12.455       -0.252         HCP P, φ: 30°       13.700       13.551       -0.149	HCP Τ, φ: 210°	30.969	31.125	0.156
HCP P, φ: 30° 13.700 13.551 -0.149	HCP Τ, φ: 30°	56.217	56.139	-0.078
	HCP P, φ: 0°	12.707	12.455	-0.252
RMSE - 0.614	HCP P, φ: 30°	13.700	13.551	-0.149
	RMSE	-	-	0.614

## 3.5.2 Hole model and QCT energy shifts

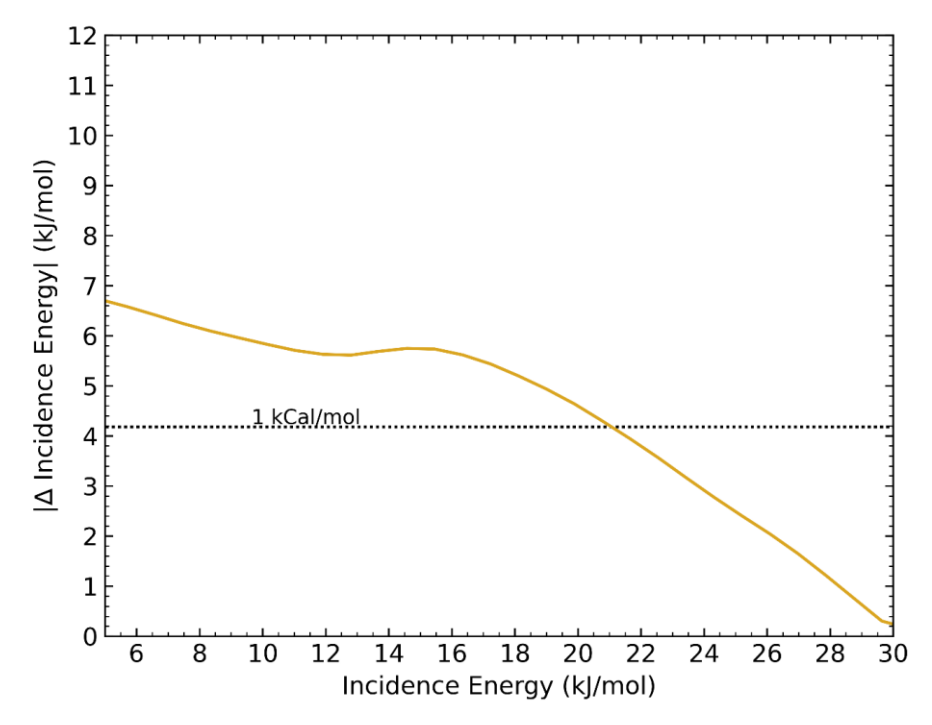


**Figure 3.9**: The absolute difference of incidence energy between the hole model reaction probability and the QCT reaction probability curve as a function of the incidence energy of the Hole model, moving the reaction probability curves in **Figure 3.8** from left (hole model) to right(QCT).

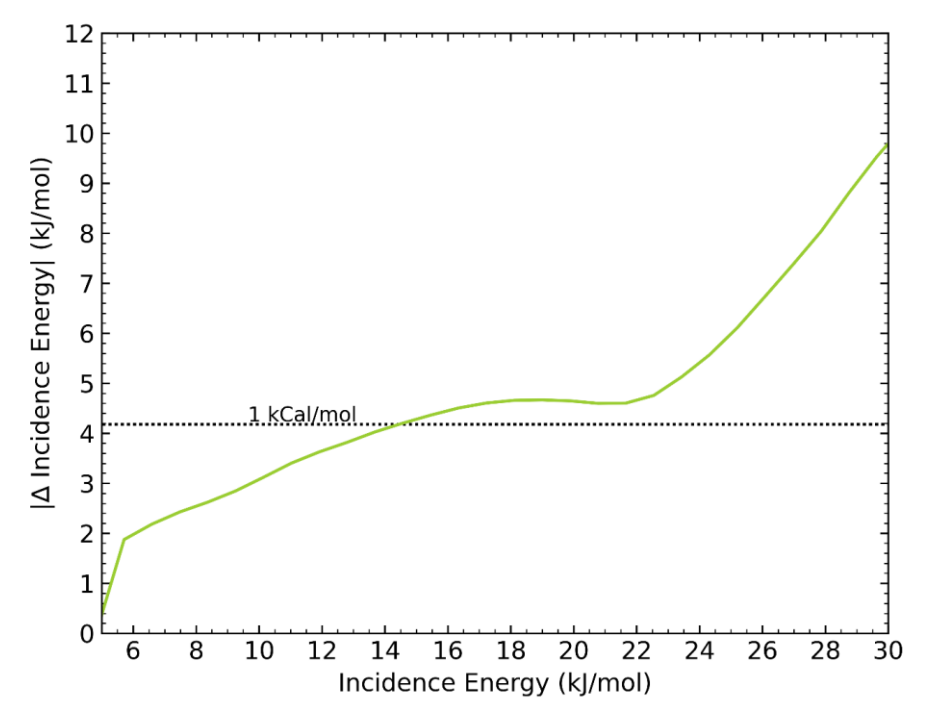
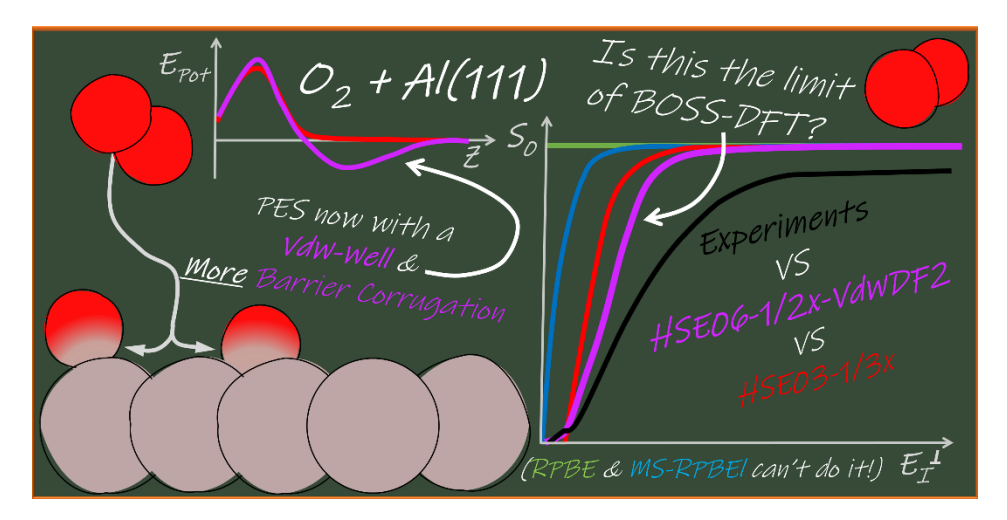


**Figure 3.10**: The absolute difference of incidence energy between the QCT reaction probability and the reaction probability curve of the hole model excluding vibrational energies as a function of the incidence energy of the QCT, moving the reaction probability curves in **Figure 3.8** from left(QCT) to right (hole model Excl. Vibrations).

## 4 Limits of BOSS DFT: O<sub>2</sub> + Al(111) dynamics on a screened hybrid Van der Waals DFT potential energy surface

#### This chapter is based on:

van Bree, R. A. B.; Kroes, G. J. Limits of BOSS DFT: O<sub>2</sub> + Al(111) Dynamics on a Screened Hybrid Van der Waals DFT Potential Energy Surface. *J. Phys. Chem. C* **2025**, *129* (11), 5408–5421. https://doi.org/10.1021/acs.jpcc.5c00327.



### **Abstract**

The activated dissociative chemisorption (DC) of  $O_2$  on Al(111) is a thoroughly studied benchmark system for oxygen–metal interactions. However, research based on density functional theory (DFT) has not yet been able to accurately determine the electronic structure, and theory as a whole has so far been unable to reproduce measured sticking probabilities with chemical accuracy. Previous work has argued that this is likely due to the inability of DFT at the generalised gradient approximation (GGA) level to describe the barriers to DC of  $O_2$  on Al(111) correctly. The argument is that the most commonly applied electronic structure approach in surface science, which involves the use of GGA-DFT, yields too low reaction barriers for the DC of  $O_2$  on Al(111). Moreover, it seems that GGAs will generally fail to accurately predict barriers for systems with low charge transfer energy, i.e., systems for which charge transfer from metal to molecule

at the transition state is likely. Subsequent work on both  $O_2$  + Al(111), i.e., Chapter 3, and O<sub>2</sub> + Cu(111), i.e., Chapter 5, has suggested that screened hybrid density functionals (DF) yield more accurate barrier heights for DC on metal surfaces. However, so far the use of only a screened hybrid DF was not enough to ensure a highly accurate description for O<sub>2</sub> + Al(111). Even though the onset of the sticking probability  $(S_0)$  curve was correctly described, the slope, or width, of the curve was not. The use of a non-local correlation DF combined with an increased fraction of exact exchange in the screened hybrid exchange DF was believed to further improve the description of the electronic structure by increasing the energetic corrugation of the barrier. This approach was assumed to increase the width of the sticking curve without lowering the incidence energy for the reaction onset, thus reducing the slope of the sticking curve. To test this, we present quasi-classical trajectory (QCT) calculations on the  $O_2$  + Al(111) system based on a potential energy surface (PES) computed with the HSE06-1/2x-VdWDF2 screened hybrid Van der Waals DF, using the Born-Oppenheimer static surface (BOSS) model. The resulting PES shows the presence of shallow Van der Waals wells in the entrance channel. Furthermore, the barriers to DC show a slightly higher energetic corrugation than the previously used HSE03-1/3x screened hybrid DF, although most differences are smaller than 1 kcal/mol. These minor alterations in the PES with respect to previous work mean that the  $S_0$  computed for  $O_2$  + Al(111) using the HSE06-1/2x-VdWDF2 DF are somewhat improved over the previous results. Specifically, the onset of the  $S_0$  curve is now somewhat better described and the curve is broadened a little compared to the HSE03-1/3x description. These results, in combination with previous studies, imply that future electronic structure methods would need to provide larger changes in the PES, or a different dynamical model would need to be used to bring theory in better agreement with the experiment. Moreover, future higherlevel theory also needs to address the currently very demanding computational costs of screened hybrid plane-wave-DFT for molecule-metal interactions.

#### 4.1 Introduction

The rate of heterogeneously catalysed processes is often controlled by the dissociative chemisorption (DC) of a molecule on the active centre of the catalyst  $^{6,212,213}$ . Furthermore, for oxidative catalysis or oxide formation, the DC of  $O_2$  is often the first and most critical step $^{214-216,218}$ . The key interactions that are at play in the DC of  $O_2$  on metals are not yet fully understood  $^{124,229,231}$  and are therefore of substantial scientific interest  $^{1,55,56,219}$ . The  $O_2$  + Al(111) system has over the years become a benchmark for the DC of  $O_2$  on metal systems  $^{214,222-227}$ . However, unlike the perhaps better-known  $H_2$  + Cu(111) benchmark system $^{55,110,135}$ , theoretical models are not yet able to describe the DC of  $O_2$  on Al within chemical accuracy  $^{124}$ , nor is there a clear scientific consensus on the origins of the barrier to DC for this system $^{228-235}$ .

Both the failure of theoretical models to describe the DC of  $O_2$  on Al(111) and the ongoing discussion on the origin of the barrier to reaction can be related to the inability of the most commonly applied density functional theory (DFT) method in surface science to compute the DC barrier<sup>124,228,240,229–231,234–238</sup>. The generalised gradient approximation (GGA) approach to the density functional (DF) remains the most commonly used approach to compute reaction barriers<sup>56</sup> within surface science because it represents a good compromise between accuracy and computational costs. However, recent work<sup>124</sup> strongly suggests that the GGA approach will fail to compute accurate reaction barriers if the charge transfer energy ( $E_{CT}$ ) is below T eV, where  $E_{CT}$  is defined as:

$$E_{CT} = \phi - EA \tag{4.1}.$$

Here  $\phi$  is the work function of the metal surface, and EA is the electron affinity of the molecule reacting on that surface<sup>124</sup>. If  $E_{CT}$  is below  $7\,eV$  even one of the most "repulsive" (i.e., a "more repulsive DF" is a DF generally predicting higher DC barriers) GGA DFs (i.e., RPBE<sup>239</sup>) tends to underestimate the barrier height to DC<sup>55,56,129,161</sup>. This means that, when constructing a chemically accurate semi-empirical DF using the specific reaction parameter approach, i.e., an SRP DF, basing this DF on GGA DFs will probably not be possible<sup>124,129</sup>. For O<sub>2</sub> + Al(111)  $E_{CT} = 3.8\,eV^{124}$ , and all GGA DFs fail to compute any relevant barrier. This in turn results in computed reaction probabilities that are always equal or close to one and thereby in disagreement with the experiment, which shows activated

dissociation for  $O_2$  on Al(111)<sup>124,236–238</sup>. Likewise, meta-GGA DFs, which are on the next rung up on Jacob's ladder<sup>279</sup>, show only a minor improvement over GGA results for  $O_2$  + Al(111)<sup>124</sup>.

At this time it is not fully understood why  $E_{CT} < 7 \text{ eV}$  results in a failure of DFs containing semi-local exchange for DC on metals. The failure of GGA DFs to accurately predict barriers for molecule-metal reactions may be related to the more general failure of GGA DFs to predict barriers for gas-phase reactions, as also previously discussed by Gerrits et al. 124. The commonly applied reasoning is that GGA DFs favour the delocalised nature of a transition state (TS) and thus result in TS-energies that are too low compared to the reactants, resulting in too low or even eliminating the barriers. For gas-phase reactions such a "densitydriven" error could then be and has been resolved by using semi-local DFs in a non-self-consistent-field (NSCF) manner by applying a GGA-DF once to a converged density obtained with a hybrid DF, i.e., a "HF-based density", where HF stands for Hartree-Fock<sup>147–149,253</sup>. However, the explanation that this approach yields more accurate barriers due to correcting for density-driven errors has come under scrutiny as recent work indicates that the improved agreement is due to a cancellation between both density-driven and "functional-driven" errors 150,151. Moreover, the explanation in terms of only density-driven errors is also at odds with previous results from Chapter 3 for O<sub>2</sub> + Al(111), which showed that good sticking probabilities can be computed with both SCF- and NSCFscreened hybrid approaches, where in the latter a screened hybrid DF is applied just once to a converged GGA density. This implies that the greater part of the GGA-DFT error for  $O_2$  + Al(111) should be functional-driven <sup>147,253,280</sup>, see also Chapter 3.

Regardless of the origin of the error of the semi-local exchange DF, previous work suggests that the failure of these types of DFs for  $O_2$  + Al(111) should be avoided by employing a screened hybrid DF instead<sup>124,280</sup>. The use of the screened hybrid HSE03-1/3x DF resulted in reaction probabilities that were in semi-quantitative agreement with the experiments. Especially the reaction probabilities at lower normal incidence energy ( $E_i^{\perp}$ ) closely reproduce experimental results<sup>124,145,280</sup>. However, at higher  $E_i^{\perp}$  the computed sticking probabilities still overestimate the experimentally determined sticking probabilities. This resulted in a reaction

probability curve that is too steep, or too narrow<sup>124,280</sup>, as also seen in Chapter 3. To find a DF that can reproduce experiments with chemical accuracy for systems like  $O_2 + Al(111)$ , this problem still needs to be fixed.

Several alternative possibilities could contribute to a too-narrow reaction probability curve. The first few are due to the use of the Born-Oppenheimer static surface (BOSS) model. In the Born-Oppenheimer approximation, the electronic energy is decoupled from nuclear motion, and in the static surface approximation, the surface atoms of the metal are kept fixed in their ideal surface lattice positions. Because experiments indicate a limited influence of surface temperature on the reaction probability of  $O_2$  on Al(111)<sup>224</sup>, it is not immediately expected that the inclusion of surface phonon motion will substantially influence the reactivity 124,224,280. Furthermore, if the barrier location as described by the HSE03-1/3x DF is to be taken as accurate, which is likely according to previous work<sup>129</sup>, then the O<sub>2</sub> + Al(111) system will generally have "early" barriers, i.e., the barriers will be located at large molecule-surface distances<sup>124,145,228–230,280</sup>. Such early barriers tend to limit the effects of energy dissipation from the motion of the molecule to surface atom motion<sup>124,274,275</sup>. Furthermore, the early barrier and the high mass of O<sub>2</sub> also suggest that the effects of electron-hole pair (ehp) excitation, which can be described with electronic friction approaches, should be small<sup>162,170,281</sup>. This likely also eliminates the effects of ehp excitation as a possible important cause for the disagreement between theory and experiments for  $O_2 + Al(111)$ .

If we assume that the BOSS model is not to blame for the currently deficient theoretical description of the DC of  $O_2$  on Al(111), only the electronic structure description remains a likely cause of error, as also previously argued in Chapter 3 and Refs. <sup>124,280</sup>. As stated above it was expected that the inclusion of longrange Van der Waals (VdW) correlation in the exchange-correlation functional could result in a broadening of the reaction probability curve, but this has so far not yet been corroborated. This hypothesis is supported by the argument that the introduction of a VdW well will increase both the energetic and geometric corrugation of the barrier sight varies with the impact point of the surface and the orientation of the molecule and this strongly influences the width of the reaction probability

curve<sup>161,254</sup>. Additionally, a VdW well could alter the dynamics of O<sub>2</sub> impinging on the surface by accelerating the molecule towards the metal surface before dissociation<sup>132</sup>.

In this chapter, we aim to investigate the simultaneous effects of the inclusion of VdW correlation and of admixing a larger amount of exact exchange on the potential energy surface (PES) as well as the dynamics of the DC of O<sub>2</sub> on Al(111), by computing and analysing a PES based on the HSE06-1/2x-VdWDF2 DF and comparing quasi-classical trajectory (QCT) dynamics results based on this PES to experiments and previous theoretical studies. The aim of applying this DF is to hopefully resolve the current shortcomings in the description of the DC of O<sub>2</sub> + Al(111). This chapter is set up as follows: Section 4.2.1 will discuss the details of the DF used to compute the electronic structure, Section 4.2.2 the computational details of the DFT calculations, Section 4.2.3 the Al(111) lattice details, Section 4.2.4 the PES fitting technique, and Section 4.2.5 the QCT calculations. Thereafter, the DFT results are shown in Section 4.3.1, and in Section 4.3.2 the QCT dynamics results are shown. Section 4.3.3 then discusses the results in the context of previous work and presents an outlook for future work. The chapter is summarised and conclusions are provided in Section 4.4. Lastly, the appendixes to the chapter are presented in Section 4.5.

## 4.2 Methods

In this chapter, the Born-Oppenheimer static surface (BOSS) model is employed  $^{56}$ . In short, this signifies that the motion of the nuclei is decoupled from the motion of the electron via the Born-Oppenheimer approximation, and that the Al surface atoms are kept static in their ideal (111) surface lattice positions. As a result, the dynamics of the  $O_2$  on the Al(111) system only requires a description of the motion in the remaining six molecular degrees of freedom. These six degrees of freedom in addition to a description of the high symmetry sites on the Al(111) surface are shown in **Figure 4.1** and discussed in greater detail in other work  $^{55,124,280}$ , see also Chapter 3.

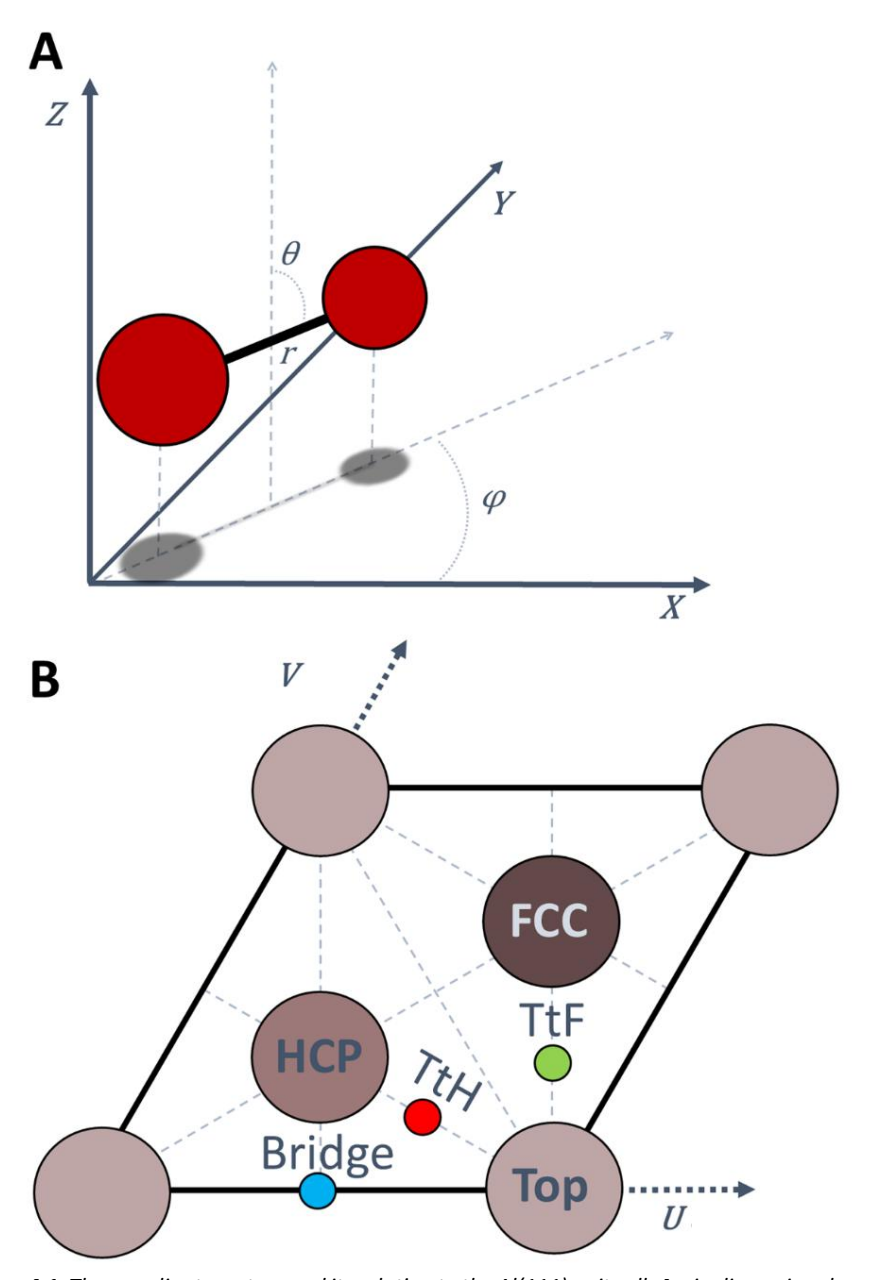


**Figure 4.1**: The coordinate system and its relation to the Al(111) unit cell; **A**: six-dimensional centre-of-mass coordinate system for the  $O_2$  molecule; **B**: (111) surface unit cell for an FCC metal (Al) with all high symmetry sites indicated. A darker shade represents an atom that is in a deeper layer in the slab.

#### 4.2.1 Electronic structure

For this chapter, a combination of two different types of DFs is used to improve the description of the electronic structure. Specifically, the non-local Van der Waals-DF2 (VdWDF2)<sup>183,195</sup> correlation functional and the screened exact exchange DF of the HSE06<sup>189,190</sup> DF are combined. Below we will briefly discuss these DFs, first as standalone DFs and then quickly as their combination.

Local or semi-local DFs will inherently not be able to describe the longer-range electronic correlation necessary to accurately describe effects like VdW forces. Several different approaches have been developed to correct the long-range correlation of the exchange-correlation functional for such shortcomings. For instance, approaches that use a pair-wise potential based on time-dependent DFT to include VdW interaction have been developed by Grimme and coworkers<sup>185,186</sup>. Initial work of Lundqvist *et al.*<sup>182</sup>, forms the basis for multiple different VdW methods better suited for metal-molecule interactions, like the VV10<sup>187</sup>, rVV10<sup>184</sup>, VdWDF1<sup>183</sup>, and VdWDF2<sup>195</sup> DFs. Of these DFs VdWDF1 represents a truly non-empirical DF., i.e., this method is not based on fitted adjustable parameters.

In this chapter we use the VdWDF2<sup>195</sup> approach, in which a non-local (*NL*) longerrange correlation energy is added to a local (LDA) correlation energy, resulting in the following expression for the correlation functional:

$$E_C^{VdWDF2} = E_C^{LDA} + E_C^{NL,VdWDF2}$$
 (4.2).

Note that an exchange DF ( $E_x$ ) can be added to this DF that can be local, semilocal or even a non-local DF including exact exchange. The Van der Waals correction to the correlation energy can be written as

$$E_C^{NL,VdWDF2} = \int d\mathbf{r} \int d\mathbf{r}' \, \rho(\mathbf{r}) \Phi(\mathbf{r},\mathbf{r}') \rho(\mathbf{r}')$$
(4.3).

Here r is the position vector of the electron density,  $\rho(r)$  the electronic density, and  $\Phi(r,r')$  the Van der Waals kernel describing the electron density-density interactions. A full discussion of this kernel is out of scope for this chapter and the reader is referred to Refs.  $^{183,195}$  for more details.

The effects of the VdWDF2 correlation on the PES are not known *a priori*, although its addition will generally improve the description of longer-range interactions and improves over PBE in describing the adsorption of molecules on metals<sup>56,282</sup>. The presumption is that a longer-range attraction, i.e., a Van der Waals well will form in the PES<sup>126</sup>, although it is not uncommon for the middle-range interaction to become slightly more repulsive<sup>132</sup>. As the barriers for  $O_2$  on Al(111) are far away from the surface, it is expected that the use of VdW correlation will tend to reduce the barrier height<sup>124</sup>.

Moving on to the screened hybrid exchange functional, we use the HSE06<sup>190</sup> DF. This DF is very similar to the HSE03 DF<sup>189</sup>, the expression of which was later revised to obtain the HSE06 DF<sup>190</sup>. The HSE06 DF is a hybrid DF because a fraction ( $\alpha$ ) of exact (Hartree-Fock) exchange is admixed with the semi-local PBE<sup>154</sup> exchange-correlation functional according to

$$E_{XC}^{PBE0} = \alpha E_X^{HF} + (1 - \alpha) E_X^{PBE} + E_C^{PBE}$$
 (4.4).

This makes the HSE06 DF similar to the better-known PBE0<sup>153</sup> DF. However, unlike the PBE0 DF, the HSE06 DF also screens the exact exchange at longer electron-electron distances. As a result, at short distances, the DF behaves like PBE0 but at longer distances like PBE. This screening is done with a continuous and quick switching function between a long-range (*LR*) and short-range (*SR*) part in the Hartree-Fock (HF) exchange potential, such that the coulomb operator splits into:

$$\frac{1}{r_{ij}} = \underbrace{\frac{1 - \operatorname{erf}(\omega, r_{ij})}{r_{ij}}}_{SR} + \underbrace{\frac{\operatorname{erf}(\omega, r_{ij})}{r_{ij}}}_{LR}$$
(4.5),

where  $r_{ij}$  is the distance between electrons i and j,  $\operatorname{erf}(\omega, r_{ij})$  is the Gaussian error function, and  $\omega$  is the screening length parameter<sup>189,190</sup>. The result of this adaptation of the HF exchange potential is that the HSE06 exchange-correlation functional can also be partitioned into a short and long-range part, such that:

$$E_{XC}^{HSE06} = \alpha E_X^{HF,SR}(\omega) + (1 - \alpha) E_X^{PBE,SR}(\omega) + E_X^{PBE,LR}(\omega) + E_C^{PBE}$$
 (4.6)

The screening of the HF exchange for longer distances is needed to reduce computational costs<sup>189</sup>, and the screening is required to obtain a good description of the metal surface itself. Without it, the density of states of the electrons at the Fermi level would be artificially reduced<sup>158</sup>.

The implementation of the screened hybrid exchange functional in this chapter has an important difference from that of the original HSE06 DF<sup>190</sup>: In this chapter, we use a larger fraction of exact exchange. Originally, the HSE06 DF comes with a maximum exact exchange fraction  $\alpha$  of 1/4. Previous work with an HSE03-like DF used  $\alpha = 1/3^{124}$  but still resulted in overestimated sticking probabilities, suggesting that  $\alpha$  should be increased further. In this work, we therefore opted to use an exact exchange fraction  $\alpha$  of 1/2. Increasing the fraction of exact exchange is a common approach to improve the performance of the DF for gasphase barriers by increasing the barrier height<sup>139,257,283</sup>. An exact exchange fraction of 1/2 could also result in an overestimation of the barrier height<sup>283</sup>, as it did in similar work on  $O_2 + Cu(111)^{284}$ , see also Chapter 5. However, at the outset, we realised that we might need to compensate for a barrier-lowering effect by replacing the PBE correlation with the Van der Waals correlation<sup>124,126</sup>, as also discussed above, and for this, an increased fraction of exact exchange over the previously used value of 1/3 was deemed necessary.

The combination of both the screened hybrid exchange and the Van der Waals correlation DF results in the HSE06-1/2x-VdWDF2 DF

$$E_{XC}^{HSE06-VdWDF2} \tag{4.7}.$$
 
$$= \frac{1}{2} E_X^{HF,SR}(\omega) + \frac{1}{2} E_X^{PBE,SR}(\omega) + E_X^{PBE,LR}(\omega) + E_C^{VdWDF2}$$

It is expected that the HSE06-1/2x-VdWDF2 DF will adequately describe longer-range interactions and thereby result in the presence of a VdW well in the entrance channel, whilst hopefully also still correctly describing the barrier height. In the next chapter, i.e., Chapter 5, the DF defined by Equation 4.7 is presented as the first hybrid-VdW DF to yield dynamics results for the DC of  $O_2$  on Cu(111). For that system the DF tended to underestimate the reaction probability, i.e., it overestimated the barrier heights<sup>284</sup> (see also Chapter 5). Although for  $O_2$  + Cu(111) this was the first DFT result to ever underestimate sticking, we do not expect that the HSE06-1/2x-VdWDF2 would also result in an underestimated sticking probability for the  $O_2$  + Al(111) system based on the previous results obtained with  $\alpha = 1/3^{124,280}$ , and on  $O_2$  + Al(111) having only a single barrier to reaction in the entrance channel, unlike the  $O_2$  + Cu(111) system which also has a second barrier in the exit channel.

Lastly, it is important to differentiate the HSE06-1/2x-VdWDF2 DF from screened hybrid VdW DFs where the exchange part of the DF is not tailored to or made consistent with the Van der Waals correlation functional, e.g., VdW-DF2-ahbr<sup>193</sup>. The HSE06-1/2x-VdWDF2 DF does not represent a completely new screened hybrid VdW DF, as provided by the recent work of Hyldgaard and coworkers<sup>193,194</sup>. Instead, our DF is simply a combination of two established exchange and correlation DFs, as described above.

## 4.2.2 Computational details

All DFT calculations are done with the Vienna Ab Initio Simulation Package (VASP) version 6.3.2<sup>200,258–262</sup> using the Van der Waals DFT implementation of Klimeš *et al.*<sup>285,286</sup>. In this chapter, all energies from the HSE06-1/2x-VdWDF2 DF are based on three distinct successive self-consistent-field (SCF) single-point calculations. The computational costs of converging the electronic structure energy with the HSE06-1/2x-VdWDF2 DF from scratch are high. Therefore, two pre-calculations, or "primers", have been performed to set up initial guesses for the electronic density and Kohn-Sham (KS) wavefunction. The first SCF primer uses the PBE-VdWDF2 DF, the second SCF calculation the HSE06-1/2x-VdWDF2 DF with a sparse HF integration grid, and the third and final SCF single point calculation uses a normal HF integration grid to improve accuracy.

All three SCF calculations, that is the two primers and the final SCF calculation, are spin-polarised calculations and use a 2x2 4-layer Al supercell (see the next section for the lattice details) with 15.0 Å vacuum above the slab. All three use a 10x10x1  $\Gamma$ -centred k-point grid and a cutoff energy of 400 eV. The core electrons of both Al and O are described by the projector augmented wave  $(PAW)^{199}$  method, as developed for the PBE DF. Methfessel-Paxton smearing with a width of 0.2 eV is used to improve convergence. The PBE-VdWDF2 primer uses the "conjugate" algorithm<sup>287,288</sup> with a convergence tolerance of  $10^{-9}$  eV, as done in other work<sup>280,284</sup>, see also Chapters 3 and 5. After this primer is finished, its electron density and KS-wavefunction are used for the next primer with the HSE06-1/2x-VdWDF2 DF, using the damped algorithm, as without this algorithm numeric stability is limited, and a convergence criteria of  $10^{-5}$  eV, or a limit of 240 SCF steps is used. Furthermore, the "Fast", i.e., sparse HF integration grid is

employed<sup>289</sup>. This final primer single-point calculation will, if all goes well, usually consume the bulk of the computational time. After this, another HSE06-1/2x-VdWDF2 single-point calculation is started using the previous KS-wavefunction with a normal HF integration grid to improve the accuracy of the final result. This final SCF single point is then converged to  $10^{-5}$  eV again. Converged results were obtained for all but one data point (U = 0, V = 0,  $\theta = 90^{\circ}$ ,  $\varphi = 30^{\circ}$ , Z = 4.0 Å, r = 1.175 Å), the energy of which was interpolated based on surrounding data points. Despite the use of these tricks, the computational demands for this project are still large: we have consumed upwards of 30 million CPU hours for this PES, where a single point typically takes a minimum of one week but can easily take two weeks or longer on a modern dual socket AMD EPYC 7351 32 core node, depending on the difficulty of the convergence.

#### 4.2.3 Lattice details

The Al bulk lattice has been relaxed using the HSE06-1/2x-VdWDF2 DF, using a 1x1x1 bulk supercell with 11x11x11  $\Gamma$ -centred k-points, whilst maintaining the other computational settings as described above. The lattice constant is relaxed at 4.041 Å. This is in good agreement with the experimental lattice constant of 4.032 Å $^{290}$ . The surface lattice structure was then further relaxed using a 1x1, 4-layer supercell with the bottom 2 layers frozen and 15 Å of vacuum using a 20x20x1  $\Gamma$ -centred k-point grid. This resulted in interlayer distances of  $d_{12} = 2.376$ ,  $d_{23} = 2.306$ , with  $d_{34} = 2.333$ . **Table 4.1** presents comparisons of this lattice expansion/contraction to other works, which shows that the top layer expansion is in good agreement with experimental and other theoretical work. To maintain consistency with the 2x2 unit cell the number of k-points parallel to the Al surface is halved for the PES production, see the computational details above.

**Table 4.1**: Comparing Al(111) surface layer expansion and contractions of this work with experiments and other theories.

	LEED Experiments on $160  \mathrm{K}^{\mathrm{291}}$	HSE03-1/3x <sup>124</sup>	LDA <sup>292</sup>	HSE06-1/2x-VdWDF2 (this work)
d <sub>12</sub>	1.7 % ± 0.3 %	1.4 %	1.18 %	1.83 %
$d_{23}$	0.5 % ± 0.7 %	-	-0.40 %	-1.16 %
$d_{34}$	-	-	0.22 %	-

## 4.2.4 Fitting the PES

The interaction of  $O_2$  + A(111) is described with a continuous six-dimensional (6D) PES that is interpolated from the electronic structure calculations performed with the above-described HSE06-1/2x-VdWDF2 density functional. To obtain a good interpolation quality the corrugation reduction procedure (CRP)<sup>201,202</sup> is used. In this procedure, two three-dimensional (3D), or atomic. PESs are subtracted from the 6D diatomic PES. This is done to obtain a residual PES with reduced corrugation, which is easier to interpolate accurately. After this, the 3D PESs are added back to the full interpolated result. The resulting error of the CRP for predicting energies of points not part of the interpolation grid used to obtain the PES should be minor 115,130,202,280: previous work using the same  $(U, V, \theta, \phi)$  geometries and comparably fine grids in r and Z has shown an RMSE of 0.8 kJ/mol (0.2 kcal/mol) as long as interaction energies of the molecule with the metal are smaller than 4  $eV^{130}$ , with outliers usually below 3 kJ/mol<sup>115,202,280</sup>, see also Chapter 3. The CRP as implemented in this chapter is similar to that of Refs. <sup>124,263,280</sup>. However, a few distinctions will be highlighted below.

First, the atomic PES is not based on the HSE06-1/2x-VdWDF2 DF but on the PBE-VdWDF2 DF. This is done to mitigate the computational cost. Additionally, the atomic PES is based on spin unpolarised DFT, unlike the 6D molecular PES. This avoids convergence issues as the open-shell nature of an O atom results in significant noise in the DFT energies far away from the Al surface. Computing the 3D atomic PES with spin-unpolarised DFT does not affect the accuracy of the full 6D PES as subtracting the 3D atomic PESs from the full 6D PES merely serves to yield a 6D residual term with decreased corrugation and anisotropy. Adding the 3D atomic correction terms back on to the residual PES then yields the spinpolarised 6D DFT data at the points used for interpolation. Furthermore, the convergence criteria are slightly lighter than in the primer calculations, as discussed in Section 4.2.2, and are set to 10<sup>-8</sup> eV. These nuances are possible because the atomic PES does not need to be very accurate as long as it is physically reasonable, as also discussed in Refs. 124,280,284. For instance, by using the cheaper to evaluate PBE-VdWDF2 DF we ensure that the long-range interactions are described. As a result, one or two orders of magnitude in computational costs can be saved for the atomic potential. The U, V grid for this

3D atomic PES is similar to that used in earlier CRP work<sup>124,263,280</sup>, and the *Z*-Grid is an equidistant grid between -1.20 and 8.50  $\mathring{A}$  with a 0.05  $\mathring{A}$  spacing, leading to a total of 194 grid points for each of the 10 different surface sites.

Second, the 6D PES grid is not equidistant as in Ref. <sup>263</sup>. Instead a similar grid structure as in Chapters 3 and 5, and references <sup>124,280</sup> is used but extended to allow for longer-range interactions captured by the addition of the VdW-DF2 DF. Thus, this results in the grid: Z = [1.00, 1.50, 2.00, 2.25, 2.50, 2.75, 3.00, 3.25, 3.50, 3.75, 4.00, 4.25, 4.50, 4.75, 5.00] Å, and r = [1.000, 1.100, 1.150, 1.175, 1.190, 1.200, 1.225, 1.250, 1.300, 1.400, 1.500, 1.600] Å. To clarify this point further, these Z and r grids are used for each U, V,  $\theta$ , and  $\varphi$  geometry employed, and the values of the coordinates of the relevant geometries are shown in **Table 4.2**. The PES in the gas-phase is extrapolated beyond S.00 Å up to S.750 Å via a switching function to a 2D potential, similar to previous work <sup>263</sup>. This grid spacing limits the total number of required single points whilst maintaining enough details near the transition state and in the gas-phase to properly describe both the dissociative chemisorption and the Van der Waals interaction. All in all, this makes for a total of 5260 different single points used to interpolate the PES.

**Table 4.2**: The different combinations of the U, V,  $\theta$ , and  $\phi$  coordinates that are used in the grid to interpolate the PES. The U and V coordinates are shown in **Figure 4.1**.

Site name	U	V	[ heta,arphi]
Тор	0	0	[0, 0], [90, 0], [90, 30]
Bridge	1/2	0	[0, 0], [90, 0], [90, 60], [90, 90]
HCP	1/3	1/3	[0, 0], [45, 30], [45, 210], [90, 0], [90, 30]
TtH	1/6	1/6	[0, 0], [45, 30], [45, 120], [45, 210], [90, 30], [90, 120]
TtF	1/3	-1/6	[0, 0], [45, 150], [45, 240], [45, 330], [90, 240], [90, 330]
FCC	2/3	-1/3	[0, 0], [45, 150], [45, 330], [90, 0], [90, 330]

# 4.2.5 Quasi-classical trajectory dynamics

The continuous 6D CRP-PES can be used to compute the reaction probabilities of  $O_2$  on Al(111) with dynamics calculation using the quasi-classical trajectory (QCT) method <sup>210,211</sup>. QCT calculations include the zero-point energy of the molecule through the initial conditions imposed, after which the equations of motion are propagated classically in time<sup>210,211</sup>. The molecule is initially placed at

7.00  $\mathring{A}$  above the surface with a given incidence energy, with its velocity vector pointing along the surface normal. The trajectory is counted as reacted if the O<sub>2</sub> bond length exceeds 1.59  $\mathring{A}$ , or it is considered scattered if the molecule-surface distance exceeds 7.00  $\mathring{A}$  and the velocity of the molecule points away from the Al surface. The reaction probability is then calculated as:

$$P_r = \frac{N_r}{N_T} \tag{4.8},$$

where  $N_T$  is the total number of trajectories, and  $N_r$  the number of trajectories that reacted. See Refs.<sup>124,125,130</sup> for further details on the implementation of the QCT dynamics.

To assess the quality of the DF, computed sticking probabilities need to be compared to King and Wells experiments<sup>55,69,126</sup>. In this chapter, we compare with the supersonic molecular beam experiments of Österlund et al.<sup>224</sup>. The experimentalist varied the nozzle temperature  $(T_N)$  and used seeding in He and anti-seeding in Xe to vary the  $E_i^{\perp}$ . For the sticking curve that we aim to reproduce the authors stated that all O<sub>2</sub> molecules were in the vibrational ground state. However, no time of flight measurements are available for this study<sup>224</sup>. Moreover, previous theoretical studies used a  $T_N = 300 \ K^{124,280}$ , thus, to fairly compare the effect of the incidence energy on the DC of O2 we computed the reaction probabilities as a function of single  $E_i^{\perp}$  values with the vibrational temperature of O<sub>2</sub> taken to be the same as in the previous chapter, i.e., 300  $K^{124,280}$ . To describe the effect of the high rotational cooling of O<sub>2</sub> the rotational temperature is simply taken as having a single value of 9  $K^{264}$ ; this represents an approximation. In the QCT of this chapter, we have allowed the states v = 0 - 3and i = 1 - 49 to get occupied. This results in an 80% occupation of the rovibrational ground state: v = 0, i = 1, see Ref. <sup>130,136</sup> or Chapter 3 for more information. Note that even j states are forbidden via nuclear spin statistics for O<sub>2</sub> in the electronic ground state. The supporting information (SI) of Ref. <sup>280</sup> provides a breakdown of all the occupied initial states (or see the previous chapter Section 3.2.5.). To compute the reaction probabilities  $(P_r)$  with converged statistics we ran at least  $10^5$  trajectories per  $E_i^{\perp}$ .

## 4.3 Results and discussion

Below the results will be discussed in three distinct sections. In the first section, the effects of the DF on the electronic structure description and potential energy surface are discussed. The second section discusses the QCT results and compares them to previous work. Lastly, the impact of the new HSE06-1/2x-VdWDF2 DF is discussed in the context of the literature and what these results mean for future descriptions of this system.

## 4.3.1 Potential energy surface and barrier analysis

Before discussing the new QCT dynamics results, it may be insightful to discuss the effects of the VdW correlation and the increased exact exchange fraction of the HSE06-1/2x-VdWDF2 DF on the electronic structure of the  $O_2$  + Al(111) system, and the resulting changes of the PES compared to previous electronic structure calculations with  $\alpha$  = 1/3 and using PBE correlation 124,145,280.

The most immediate and important change is the consistent presence of a VdW well. This well appears in the entrance channel, i.e., at larger molecule-surface distances than where the barrier to dissociation is found, at about 3.5 Å above the Al(111) surface. In **Figure 4.2** a selection of potential curves including VdW wells are plotted as a function of the molecule-surface distance (Z) for  $O_2$  at a constant bond length r=1.19 Å. The PES cuts shown in **Figure 4.2** differ in the surface site (U, V) and  $O_2$  orientation given by  $\theta$  and  $\varphi$ . **Figure 4.2** shows that the VdW well appears to be almost completely independent of the  $O_2$  adsorption site and  $\varphi$ . However, the depth and location in Z of the well do depend on  $\theta$ . The well-depth depends on whether the molecule is orientated parallel or normal to the surface. The well tends to be shallowest and furthest away from the surface for  $O_2$  orientated normal to the surface, and deepest and closest to the surface for the planar orientation. These results are reminiscent of the VdW wells that are computed for  $O_2$  + Cu(111), see Chapter 5, with the same HSE06-1/2x-VdW DF as used here<sup>284</sup>.

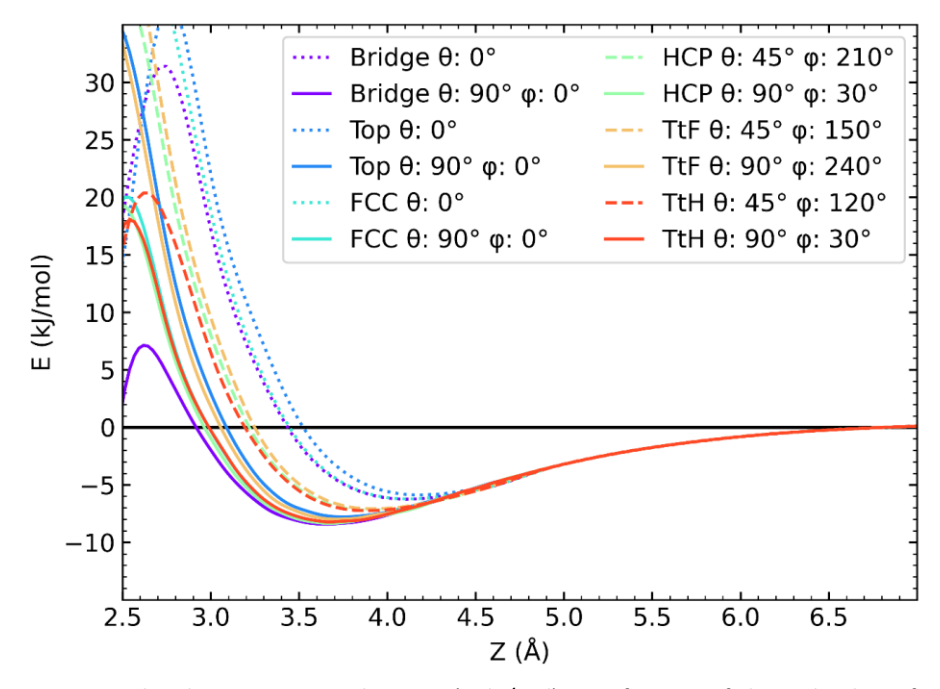


**Figure 4.2**: The electronic potential energy (in kJ/mol) as a function of the molecule surface-distance Z for a fixed  $O_2$  bond length of 1.19 Å at different U, V impact sites and for different molecular orientations (see also **Figure 4.1**).

Unlike the surface site independence of the VdW well, Figure 4.2 also shows a glimpse of a different dependence effect, i.e., a strong dependence of the barrier height on the impact site of the molecule. Although the bond length is kept constant in Figure 4.2 the results obtained at lower Z values strongly suggest that the barriers vary greatly depending on the  $O_2$  geometries. The actual barriers to dissociation occur at slightly elongated bond lengths as also found earlier  $^{280}$  in Chapter 3. The actual barrier heights are presented in Table 4.3. This table also compares with the barrier heights obtained with the HSE03-1/3x DF  $^{124}$  and the non-self-consistent field (NSCF) approach implemented through the HSE03-1/3x@RPBE DF (see Chapter 3), which amounts to obtaining the electronic energy through a single application of the HSE03-1/3x DF to a converged RPBE density  $^{280}$ . Furthermore, the left column of the table is colour-coded depending on the relative difference of barrier heights between the results of the HSE06-

1/2x-VdWDF2 DF and the HSE03-1/3x DF to aid the reader in judging the shifts in barrier heights.

**Table 4.3**: Barrier heights (in kJ/mol) computed for specific U, V, θ, φ geometries for  $O_2$  + Al(111) with the HSE06-1/2x-VdWDF2 DF, the HSE03-1/3x DF<sup>124</sup>, and the NSCF HSE03-1/3x@RPBE DF(Chapter 3)<sup>280</sup>. The colour of the barrier location tab indicates the difference between the barrier height computed with the HSE06-1/2x-VDWDF2 DF and the HSE03-1/3x DF. Red indicates a higher barrier energy for the HSE06-1/2x-VdWDF2 DF and blue a lower energy. A deeper/darker colour indicates a larger effect. Colour distinctions are made, i.e., binned per 0.5 kcal/mol (≈ 2 kJ/mol). For each DF the lowest and highest values of the barrier height computed with the DF are indicated with single and double underlining, respectively.

Location	HSE06-1/2x-VdWDF2	HSE03-1/3x	HSE03-1/3x@RPBE
	( <i>kJ/mol</i> )	( <i>kJ/mol</i> )	( <i>kJ/mol</i> )
<i>TtF θ: 0°</i>	26.7	22.9	29.1
TtF θ: 45° φ: 150°	25.4	26.1	38.0
TtF θ: 45° φ: 240°	13.4	12.5	16.7
TtF θ: 45° φ: 330°	15.9	14.4	16.6
TtF θ: 90° φ: 240°	26.4	23.6	28.7
TtF θ: 90° φ: 330°	9.9	10.7	12.8
<i>TtH θ: 0°</i>	26.1	21.9	27.7
TtH θ: 45° φ: 120°	14.1	12.8	16.9
TtH θ: 45° φ: 210°	24.9	25.3	36.3
TtH θ: 45° φ: 30°	15.9	14.4	16.8
TtH θ: 90° φ: 120°	25.8	23.7	37.9
TtH θ: 90° φ: 30°	9.3	10.1	12.3
FCC θ: 0°	34.4	26.9	38.5
FCC θ: 45° φ: 150°	25.0	24.6	32.5
FCC θ: 45° φ: 330°	39.1	<u>39.9</u>	<u>60.0</u>
FCC θ: 90° φ: 0°	11.0	11.5	13.5
FCC θ: 90° φ: 330°	12.4	12.4	14.6
Bridge θ: 0°	23.0	19.5	<i>25.5</i>
Bridge θ: 90° φ: 0°	<u>2.0</u>	<u>4.7</u>	<u>6.6</u>
Bridge θ: 90° φ: 60°	21.0	19.6	29.7
Bridge θ: 90° φ: 90°	30.7	29.5	51.4
<i>HCP θ: 0°</i>	28.6	22.8	34.6
HCP θ: 45° φ: 210°	23.9	23.3	31.0
HCP θ: 45° φ: 30°	<u>39.2</u>	<u>39.9</u>	56.2
HCP θ: 90° φ: 0°	9.8	10.4	12.7
HCP θ: 90° φ: 30°	11.2	11.4	13.7
<i>Top θ: 0°</i>	30.9	26.8	29.8
<i>Top θ: 90° φ: 0°</i>	25.4	22.7	24.4
Top θ: 90° φ: 30°	25.2	22.5	24.4

The results presented in **Table 4.3** are also shown in the form of a bar plot in **Figure 4.5** in Section 4.5.1. Both **Table 4.3** and **Figure 4.5** show that the barrier

heights to DC computed with the HSE06-1/2x-VdWDF2 are not very different from the values computed with the HSE03-1/3x DF: The majority of the barrier heights are within  $\pm 1$  kcal/mol ( $\approx 4.2$  kJ/mol), of one another. This is true except for three configurations in which  $O_2$  is oriented normal to the surface and impinges on an HCP, FCC, or TtH site. The barrier heights at these geometries differ by more than 1 kcal/mol. Another noteworthy element is that the difference in barriers does not seem to follow any clear trend, i.e., some barriers are lower when computed with the HSE06-1/2x-VdWDF2 DF but most are slightly higher in energy. The overall effect is that the energy range over which the barriers are spread is increased slightly when employing the HSE06-1/2x-VdWDF2 DF, or, put differently, the energetic corrugation of the barrier is increased meaning that the barrier height varies more strongly with impact site and orientation of the molecule.

The increased energetic corrugation may result in a slight broadening of the sticking probability curve. This is what was both desired and expected from the use of the screened hybrid Van der Waals DF. However, we should note that the effect on the barriers by switching DFs is small. As discussed above, most barriers are within 1 kcal/mol of the old results and thus the effectiveness of this increased energetic corrugation may be limited. Furthermore, Table 4.3 also shows the barrier heights as computed in Chapter 3 with the NSCF HSE03-1/3x@RPBE DF<sup>280</sup>. Switching to the NSCF approach only results in higher barriers than obtained with the SCF HSE03-1/3x DF, but generally seems to increase the energetic corrugation of the barrier more than switching to the HSE06-1/2x-VdWDF2 DF does. The differences between the sticking curves computed based on the NSCF and SCF HSE03-1/3x DFs were minor<sup>280</sup> and thus, the effectiveness of increasing the barrier corrugation and anisotropy by the use of the HSE06-1/2x-VdWDF2 may be expected to be limited. This concern was also raised in the previous chapter. Thus, the effectiveness of changing to the HSE06-1/2x-VdWDF2 DF might be smaller than we had hoped for unless, e.g., the presence of the VdW well would substantially alter the nature of the dynamics.

## 4.3.2 Quasi-classical trajectory results

The QCT dynamics calculations were performed for 491 different normal incidence energies varying from  $0.020 \, eV$  to  $1.000 \, eV$  with steps of  $0.002 \, eV$ . For every incidence energy, a total of  $10^5$  trajectories were simulated using a maximum propagation time of  $1 \, ns$ . The resulting sticking probabilities ( $S_0$ ) are presented in purple in **Figure 4.3**. The experimental  $S_0$  and the  $S_0$  computed by other theories are also presented as a comparison.

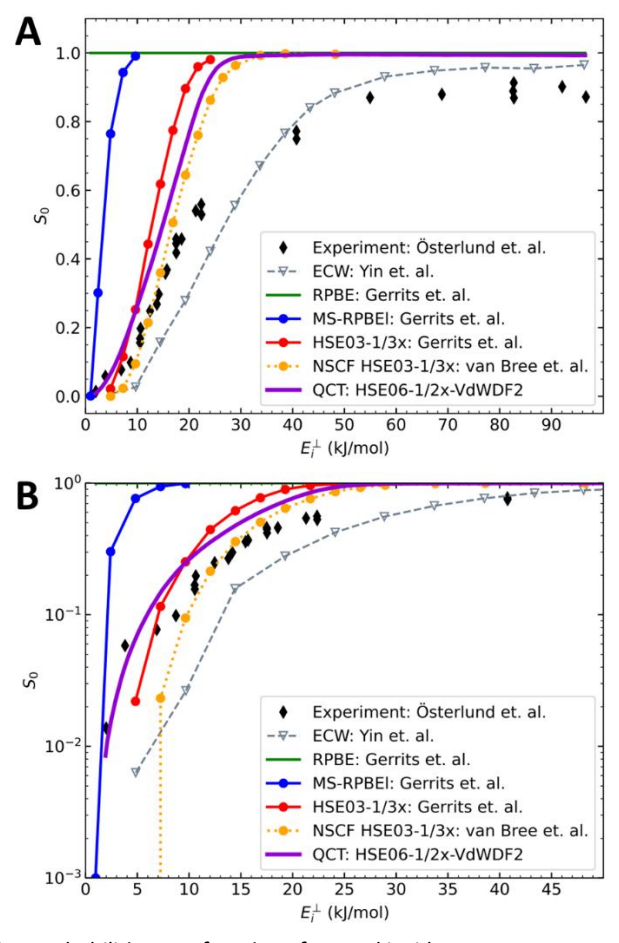


**Figure 4.3**: Sticking probabilities as a function of normal incidence energy; **A**: normal y-axis; **B**: Log y-axis, and shorter range of the x-axis, for clarity. Plotted are the sticking probabilities of the experiments (black diamonds) by Österlund et al.<sup>224</sup>, ECW results of Yin et al.<sup>230</sup>(Grey dashed line), results using the RPBE DF (green solid line), MS-RPBEI DF(blue solid line), and the HSE03-1/3x DF (red solid line) of Gerrits et al.<sup>124</sup>, the NSCF HSE03-1/3@RPBE DF (orange dotted line) of Chapter 3, and the HSE06-1/2x-VdWDF2 DF (this work, purple solid line).

The onset of  $S_0$  for the HSE06-1/2x-VdWDF2 DF is best seen in the log plot of **Figure 4.3B** and shows that some reaction already occurs at  $E_i^{\perp} = 2 \text{ kJ/mol}$ . The reactivity then quickly increases to 1 over the range of 2 - 32 kJ/mol, as seen in both **Figure 4.3A** and **Figure 4.3B**. For higher  $E_i^{\perp}$  the  $S_0$  remains constant around 1, although a maximum of 0.996 is found at  $E_i^{\perp} \approx 57 \text{ kJ/mol}$  after which  $S_0$  seems to consistently drop slowly, with a tiny amount, to 0.992 for  $E_i^{\perp} = 100 \text{ kJ/mol}$ .

The low energy threshold to the reactivity is not unexpected as the corresponding normal incidence energy of 2 kJ/mol is similar to the smallest barrier height found in Table 4.3 (see the singly underlined minimum barrier). As discussed earlier<sup>280</sup> in Chapter 3, the shape of the PES and the lack of accessible rovibrational energy for the DC of O2 means that most of the dissociation will be driven by the normal incidence energy of the molecule. Furthermore, the maximum barrier height found in **Table 4.3** is only a few *kJ/mol* higher than the value of  $E_i^{\perp}$  at which the computed sticking probability appears saturated. Unlike found for the dissociation of  $O_2$  on  $Cu(111)^{284}$  in the next chapter, the overwhelmingly greater part (by more than one order of magnitude) of the DC of O<sub>2</sub> on Al(111) occurs via a direct mechanism (Section 4.5.2. and **Figure 4.6**). The minor drop in reactivity for very high  $E_i^{\perp}$  is most likely caused by an effect similar to the bobsled effect<sup>273,293,294</sup> where the fast O<sub>2</sub> molecules barrel beyond the early barrier to hit a potential wall behind it and are forced to scatter back before the O<sub>2</sub> bond length becomes large enough for dissociation. However, it is clear that this effect is very small, and therefore not worthy of much discussion.

The QCT results based on the HSE06-1/2x-VdWDF2 DF are close to the HSE03-1/3x results of Gerrits *et al.*<sup>124</sup>. The onset of sticking obtained with the HSE06-1/2x-VdWDF2 DF occurs at somewhat lower  $E_i^{\perp}$  and the saturation of the sticking occurs at a somewhat higher energy. That is, the sticking curve undergoes a slight broadening, which is expected when looking at the increased energetic corrugation of the barriers seen in **Table 4.3** and **Figure 4.5**. Like the previous HSE03-1/3x result, the HSE06-1/2x-VdWDF2 curve represents a substantial improvement over previous GGA or mGGA-based results. The newly computed curve captures the onset of the experimentally determined  $S_0$  very well, although it is still not able to describe the  $S_0$  accurately for larger  $E_i^{\perp}$ .

# 4.3.3 Discussion and future prospects

The comparison of the quality of the different DFs is further aided by **Figure 4.4**. In this figure, the estimated energy shift of the  $S_0$  curve obtained for a specific DF from the experimental curve is plotted as a function of the  $E_i^{\perp}$  of the experimental reference. This means that for any  $E_i^{\perp}$  shown on the x-axis in **Figure 4.4**, the energy shift shown on the y-axis needs to be applied to the experimental result for that  $E_i^{\perp}$  to match the  $S_0$  values computed with the specific DF.

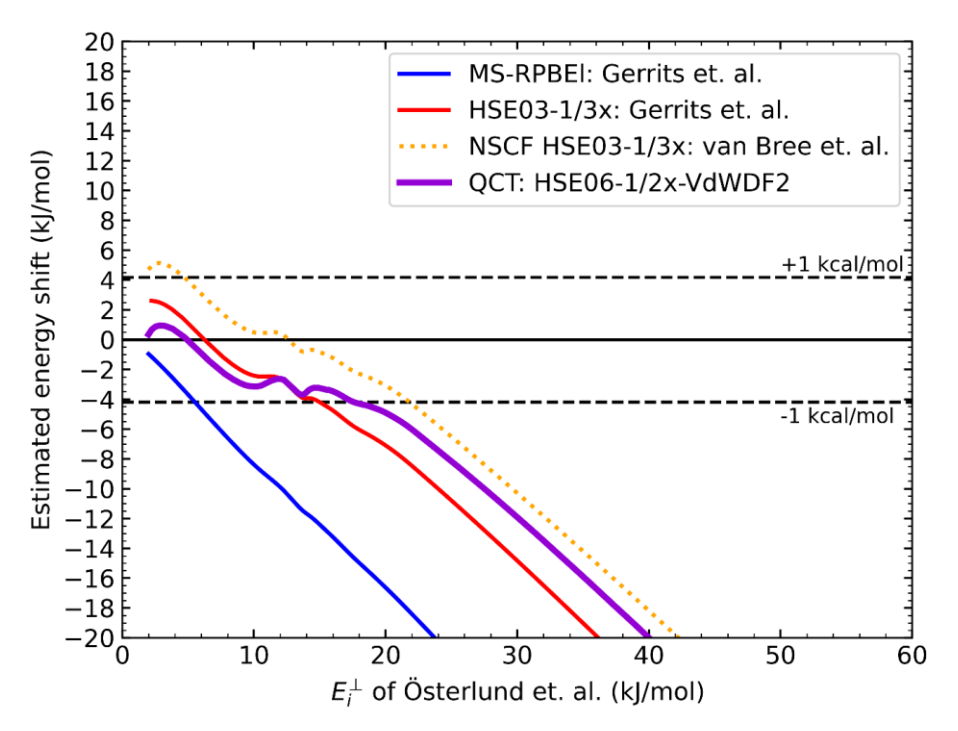


**Figure 4.4:** Estimated normal incidence energy shift (in kJ/mol) of the computed sticking probabilities relative to the experimental results of Österlund et al.<sup>224</sup> as a function of the normal incidence energy of the same experimental reference. The 1 kcal/mol boundary is indicated by dashed lines. Shown are results based on the MS-RPBEI DF (blue) of Gerrits et al.<sup>124</sup>, HSE03-1/3x DF (red) of Gerrits et al.<sup>124</sup>, the NSCF HSE03-1/3x@RPBE DF (orange dotted) of Chapter 3, and the HSE06-1/2x-VdWDF2 used here (purple). The x-axis is cut off at 60kJ/mol and energy shifts smaller than -20 kJ/mol are not plotted for clarity of the plot.

**Figure 4.4** shows very clearly that the onset of the  $S_0$  curve is described very accurately by the HSE06-1/2x-VdWDF2 DF. Even though the description of the HSE03-1/3x DF was already within chemical accuracy for the onset, the HSE06-1/2x-VdWDF2 is a better match to the experimental onset, as can also be seen

in **Figure 4.3**. However, the results depicted in **Figure 4.4** are very sobering for the impact of the combined effect of using VdW correlation and increasing the fraction of exact exchange on the 6D dynamics. The overall improvement over the HSE03-1/3x DF is limited as both DFs quickly deviate from the experimental  $S_0$  once the incidence energy in the experiments exceeds  $22 \, kJ/mol$ . It is clear that the minor broadening of the sticking curve that resulted from the implementation of the VdW correlation, although present, is not enough to lead to agreement with experiments within chemical accuracy over the entire energy range shown.

In the end, these results raise a major question for the  $O_2$  + Al(111) system: what does this mean for the ability of DFT combined with the BOSS model to accurately describe O<sub>2</sub> + Al(111)? In this chapter, we have employed one of the least reactive forms of a screened hybrid VdW DF that can be constructed based on the generic HSE06 expression. Any reduction of the fraction of exact exchange will result in more GGA-like results, thus increasing the reactivity. Using even higher mixing ratios seems doubtful as there are formal reasons for limiting the fraction of exact exchange to values equal to 1/n with n a whole number 152, and the use of n=1 would be completely replacing the semi-local exchange with exact exchange. Furthermore, the VdW-DF2 description of electron correlation remains one of the better methods to describe long-range molecule-metal interactions 126,129. Yet, the composite DF tested here with  $\alpha = 1/2$  yields only marginal improvements over the previously used screened hybrid DF with  $\alpha =$ 1/3. Lastly, the NSCF HSE03-1/3x@RPBE approach<sup>280</sup> yielded a larger energetic corrugation of the barrier than either SCF approach, yet still resulted in only small changes in the computed  $S_0$  curve relative to the SCF curve. Thus, an improvement of the computed  $S_0$  for  $O_2$  on Al(111), by any new DF, would need to come from a larger increase of the energetic corrugation of the barrier, or another large change of an aspect of the PES of which the importance is not foreseen at present. However, the similarities between the HSE06-1/2x-VdWDF2 and HSE03-1/3x barriers cast doubt on the possibility of any other screened hybrid-based DF to achieve such radical changes. Therefore, we argue that it is unlikely that the combination of screened HF exchange with VdW correlation DFs shall result in an accurate description of the  $O_2$  + Al(111) system if one also sticks to the use of the BOSS model for the dynamics.

To improve the accuracy of the theoretical description we could try to go beyond the hybrid level of DFT. However, we emphasise the already high computational demands of plane-wave screened hybrid DFT for this system and for O<sub>2</sub> + Cu(111)<sup>284</sup>, see also Chapter 5. These high costs make the brute-force use of any higher level of theory impractical at this time. This means that DFT methods like the random phase approximation (RPA) or other types of theory like Quantum Monte Carlo remain unfeasible to be used for more than the calculation of a few barrier heights. Although these types of calculations can be insightful to benchmark a select few barrier heights 114,115,249,295, such calculations will not allow for QCT dynamics to compute sticking curves. Another option to possibly improve the quality of the screened hybrid DF is to mix mGGA exchange instead of GGA exchange with exact exchange <sup>157,296</sup>. This type of mGGA-hybrid DF is still untested for molecule-metal systems. One could also try the recent DFs in which screened exchange DFs that are tailored to and are consistent with VdW-DFs combined with them<sup>193,194</sup>. However, before mapping out a completely new PES with a new DF and then testing it with dynamics calculations one might also attempt the QMC-DF approach<sup>115</sup>, in which one would try to reproduce the barrier height computed with diffusion Monte-Carlo by fitting a parameter in the generic, well-chosen, combination of a screened hybrid DF with a VdW correlation DF. For a proper description of the energetic barrier corrugation one might need to verify beforehand whether the energetic corrugation is well described with this approach of at least a few different barrier geometries.

If the construction of a PES at the screened hybrid or higher level of theory will remain as computationally expensive as in this chapter, then choosing a more advanced electronic structure method cannot be done lightly, as already explained. Thus, before trying yet another new DF or electronic structure approach to improve the description of DC of  $O_2 + Al(111)$  it may be more fruitful to briefly explore the effects and limitations of the approximations made in the BOSS model. Eliminating unfounded approximation in the BOSS model may, at this point, prove computationally less demanding than any further advancements in electronic structure calculations.

Surface temperature  $(T_5)$  effects, whether associated with surface phonons or electronic excitations in the metal, remain an unlikely cause for the disagreement with experiment, as the experiments of Österlund et al.<sup>224</sup> have shown no discernible influence of  $T_s$  on the reactivity over a  $T_s$  range of 90 - 650 $K^{224}$ . Thus, only a minor effect of surface atom displacements arising from the non-zero surface temperature in the experiments would be expected on  $S_0$ . Furthermore, the barriers to DC are generally located early in the entrance channel, i.e., at molecule-metal distances commonly larger than 2.5 Å, which also means that the perturbation of surface atom motion due to the incoming molecule may be limited<sup>274,275</sup>. This suggests a limited effect of any energy loss of the impinging molecule to surface atom motion that might occur before overcoming the barrier. As an additional test, the expected upper bound of the effect surface atom motion can be calculated using the simple, Baule model<sup>297</sup> and we show the effect in Figure 4.7 in Section 4.5.3. The Baule method treats the molecule and the surface atoms as hard spheres, and will likely result in an overestimated effect of surface atom motion. Nevertheless, Figure 4.7 does indicate that including surface atom motion may result in better agreement of the computed  $S_0$  with experiments for low incidence energies, i.e.,  $E_i^{\perp} < 26$ kJ/mol. For larger  $E_i^{\perp}$  the influence of surface atom motion will likely remain too small to result in an improved agreement with experiments. Therefore, the effect of the static surface approximation, i.e., of using an ideal and static surface in the dynamical model, may be relatively small.

If using the static surface approximation would not have a large impact, could making the Born-Oppenheimer approximation still be a cause of concern? Systems with low charge transfer energies may be more susceptible to, e.g., ehp excitation  $^{170,281,298}$ . Ehp excitation is commonly modelled by the use of electronic friction techniques  $^{299}$ , but the effect of electronic friction has not yet been modelled for the  $O_2$  + Al(111) system in conjunction with a PES obtained using a DF featuring screened exact exchange. One reason for this may be that there are two strong arguments against electronic friction having a substantial effect. First, the barrier is early, so the  $O_2$  will likely not sample higher electronic densities of the metal, thus limiting the effectiveness of electronic friction. Second, electronically adiabatic calculations on DC of  $O_2$  on Ag(111) $^{162}$ , in which reaction occurs at much higher energies than on Al(111) $^{162,224}$ , and calculations employing

the local density friction approximation (LDFA) on DC of N<sub>2</sub> on a metal surface<sup>171,300</sup> suggest that the DC of these "heavier molecule", i.e. heavier than H<sub>2</sub>, is not much affected by ehp excitation, likely due to the lower velocities exhibited by molecules heavier than H<sub>2</sub><sup>300</sup>. This might seem to suggest that ehpexcitation may also have only a small influence on reducing reactivity. There are two reasons why this preliminary conclusion might not hold. Firstly, calculations using a different electron friction model, e.g., orbital dependent friction (ODF), suggest a much larger influence of ehp excitation on DC of N<sub>2</sub> + Ru(0001) than calculations using the LDFA model<sup>171</sup>. Currently, it is not yet known which of the two electronic friction methods is best, or whether either of the two methods is accurate for modelling the effect of ehp excitation on DC on metals<sup>161</sup>. Secondly, for low  $E_{CT}$  systems, a strong electronically non-adiabatic effect can also occur through jumps of electrons between electronic states in which either the neutral molecule or the molecular anion interacts with the surface<sup>301</sup>. The non-adiabatic couplings between such states are quite strong, and modelling of the associated non-adiabaticity requires a method that is suited to deal with the associated "strong-coupling case", like the independent electron-surface hopping (IESH) method of Tully and co-workers<sup>59,302</sup>.

An argument in favour of the BOSS model is the semi-quantitative agreement achieved with experiment of sticking probabilities computed with the BOSS model using a PES calculated with the embedded correlated wavefunction (ECW) approach by Yin *et al.* who used CASPT2 for the embedded cluster<sup>230</sup> (see also **Figure 4.3**). This would seem to suggest that an accurate sticking probability curve can be computed within the BOSS dynamical model, but leaves open the questions of whether this can be done with DFT, and how accurate the ECW method employing CASPT2 for the active site actually is.

In summary, the low  $E_{CT}$  of  $O_2$  + Al(111) may still imply the presence of non-adiabatic effects in the DC of  $O_2$  on Al(111) that can, per definition, not be captured by the currently employed BOSS model. Moreover,  $O_2$  incidence energy loss, whether through ehp excitation or dissipation to surface atom motion, would be expected to have its largest effect on the reactivity in the higher incidence energy range, i.e., the energy range currently most poorly described by our current BOSS-DFT approach. For future work, it should therefore be

insightful to test the effect of allowing surface-atom motion, and of ehp excitation, if only for the purpose of elimination, before looking into further alterations of the DF used.

A computationally cheap method to model the effects of surface atom motion may be the dynamic corrugation method, previously successfully implemented for  $H_2$  + Cu(111)<sup>159</sup>. For this method, we would only need a few hundred additional DFT single-point calculations to construct the coupling potential<sup>159</sup>. Alternatively one could use a high-dimensional neural network (HDNN) approach to fit the PES<sup>303,304</sup>. The cheapest method to treat electronically nonadiabatic effects is the LDFA method<sup>281</sup>, but one should also test the ODF approach<sup>171</sup>, and possibly a recently suggested electronic friction approach called scattering potential friction<sup>161</sup>. Lastly, any future work with screened hybrid DFs will have to deal with the high computational demands. Future work could try to further reduce the amount of DFT data needed for the CRP method when building the PES, as the direct product and rigid grid now used require multiple geometries that are of limited use for fitting the dynamically relevant parts of the PES. The possibilities of a Δ-machine learning neural network approach, for example, as previously implemented for liquid H<sub>2</sub>O<sup>163</sup>, come to mind to further decrease the amount of computationally demanding calculations using a screened hybrid DF. In such an approach one might first fit a GGA-VdW potential energy surface to a large amount of points and then upgrade to a screened hybrid-VdW quality PES by fitting and using the difference of energies computed for far lesser points. To our knowledge, such an approach has not yet been tested on the DC of molecules on metal surfaces.

Finally, one may look for errors in the procedure used by the experimentalists to estimate the sticking probabilities for  $O_2$  at fixed energies. The experimentalists calculated what they called the "beam energy" from the known heat capacities of He,  $O_2$ , and Xe, which is an approximate procedure<sup>224</sup>. According to the experimentalists<sup>224</sup> the spread in the incidence energy of the beams employed, and the rotational temperature used in an experiment were estimated from earlier work<sup>305</sup>. These approximate procedures to obtain the results to which we compare here may all have led to errors. Given the important role of  $O_2$  + Al(111) as a benchmark system it might be useful if the experiments were repeated, with

time-of-flight measurements to more accurately determine the energy distributions of  $O_2$  in He-seeded and Xe anti-seeded beams and more accurate determination of their rotational and vibrational temperature than was possible before.

#### 4.4 Conclusions

The combination of a DFT approach for the electronic structure of the PES and the use of the BOSS dynamical model has thus far not been able to accurately describe the DC of  $O_2$  on Al(111). Past work has strongly suggested that this is due to the inability of the workhorse electronic structure approach in surface science, i.e., GGA-DFT, to accurately describe systems for which the charge transfer energy is below  $7 \, eV$ . Although the cause of the failure of GGA-DFT is still debated, several prior works suggest that the use of hybrid DFT leads to substantial improvement in the description of systems characterised by a low charge transfer energy. Previous work on  $O_2$  + Al(111) additionally suggested that the description of this system could be improved further by increasing the energetic corrugation of the barrier. It was believed that this could be achieved by including improved long-range, VdW-, electronic correlation while simultaneously increasing the fraction of exact exchange in the exchange-correlation DF.

To test this assumption, this chapter used the HSE06-1/2x-VdWDF2 DF. This DF is a screened hybrid DF that includes a maximum admixing of  $\alpha = 1/2$  of exact exchange and relies on the VdWDF2 electronic correlation description. To test this DF a 6D static surface PES was fitted to DFT energies for over five thousand different  $O_2 + Al(111)$  configurations, using the CRP. This PES was used to perform QCT dynamics calculations for different initial  $O_2$  conditions to compute the  $S_0$  of  $O_2$  on Al(111) as a function of  $E_i^{\perp}$ , using the BOSS dynamical model.

The use of VdWDF2 correlation and the increase of the fraction of exact exchange results in two changes in the PES relative to the previous HSE03-1/3x screened hybrid PES. Firstly, a VdW well now appears in the entrance channel of the PES. This well is generally only dependent on the angle the  $O_2$  molecule makes with the surface normal. Secondly, the reaction barriers also change. The

barriers of HSE06-1/2x-VdWDF2 in some cases shift to lower but in most cases to higher energies. This results in a slight increase of the energetic corrugation of the barrier, although the changes remain small and are smaller than the changes seen in the barriers when applying the HSE03-1/3x DF in the NSCF approach to an RPBE density, as has been done previously.

The small changes in the PES from the use of the HSE06-1/2x-VdWDF2 DF do result in some changes in the  $S_0$ . The onset of the sticking curve moves to a somewhat lower energy and the sticking curve has undergone a slight broadening, due to the increase in the energetic corrugation of the barrier. However, the changes are not very large, and the distinction between the SCF and NSCF application of a hybrid DF is more substantial. As such, even though the changes in the PES and  $S_0$  are as expected, the small magnitude of these changes means that the use of the HSE06-1/2x-VdWDF2 DF has not yet resulted in the desired degree of improvement of the description of sticking of  $O_2$  on Al(111).

Furthermore, based on the comparison of the three different DF-approaches, i.e., SCF HSE03-1/3x, NSCF HSE03-1/3x@RPBE, and HSE06-1/2x-VdWDF2, we argue that much larger changes in the PES will be required to more closely reproduce the experimental  $S_0$  with the use of the BOSS-model. The results obtained here at high computational cost signal that it is unlikely that the combined BOSS and DFT approach, as currently implemented, can be made accurate enough for the DC of  $O_2$  + Al(111).

Given the above, we suggest that future work on  $O_2$  + Al(111) would first aim at eliminating the possible influences and errors associated with the dynamical approximations inherent in the BOSS model. Addressing the effects of surface atom motion can be cost-effectively done by applying the dynamical corrugation method, while one might also use the HDNN method to obtain a PES incorporating the effect of surface atom motion. The influence of electronically non-adiabatic effects like ehp excitation can be modelled with different electron friction approaches or with a method more appropriate for strong non-adiabatic electron coupling, like the IESH method, in combination with the QCT method. Future work would also do best to try and address the mounting computational

costs associated with screened hybrid DFT or other higher-level electronic structure approaches. Finally, given the important role of the  $O_2$  + Al(111) as a benchmark system, it would be good if the experiments were to be repeated to investigate the quality of the approximate procedure used by the experimentalist to arrive at initial-rovibrational-state-selective sticking probabilities for specific single incidence energies.

# 4.5 Appendices

This chapter has three appendices. The first appendix presents a visual aid for **Table 4.3**, by plotting the barrier heights displayed in the table as a bar plot. The second appendix is a brief overview of the deconvolution of the indirect and direct reaction mechanism as simulated in the QCT calculations and shows that an indirect mechanism has a minor and negligible contribution to the total sticking probability. The third appendix briefly discusses the Baule model to molecule-metal surface energy transfer and presents a figure showing an expected lower bound for the reactivity of the  $O_2 + Al(111)$  system if energy transfer to the Al surface phonons were to be included.

# 4.5.1 Reaction barrier bar-plot

The barriers to dissociative chemisorption as presented in **Table 4.3** of the main text are shown in a bar plot in **Figure 4.5** as an additional visual aid to understanding the differences in energetic corrugation of the barrier. Also plotted are the reaction barriers based on the SCF HSE03-1/3x DF of Gerrits *et al.*<sup>124</sup> and the NSCF HSE03-1/3x@RPBE DF of Chapter 3. **Figure 4.5** shows that some barriers described by the HSE06-1/2x-VdWDF2 DF are lower than those of the HSE03-1/3x DF, but most others are higher. Furthermore, **Figure 4.5** shows that there are no clear patterns based on surface site or O<sub>2</sub> geometry as to the screened hybrid VdW DF resulting in either a lower or higher barrier energy. Lastly, the NSCF results are also presented. The NSCF DF inadvertently but considerably increased the energetic corrugation of the barrier<sup>280</sup> and can thus also function as a useful DF for assessing the effect of the energetic corrugation on the sticking.

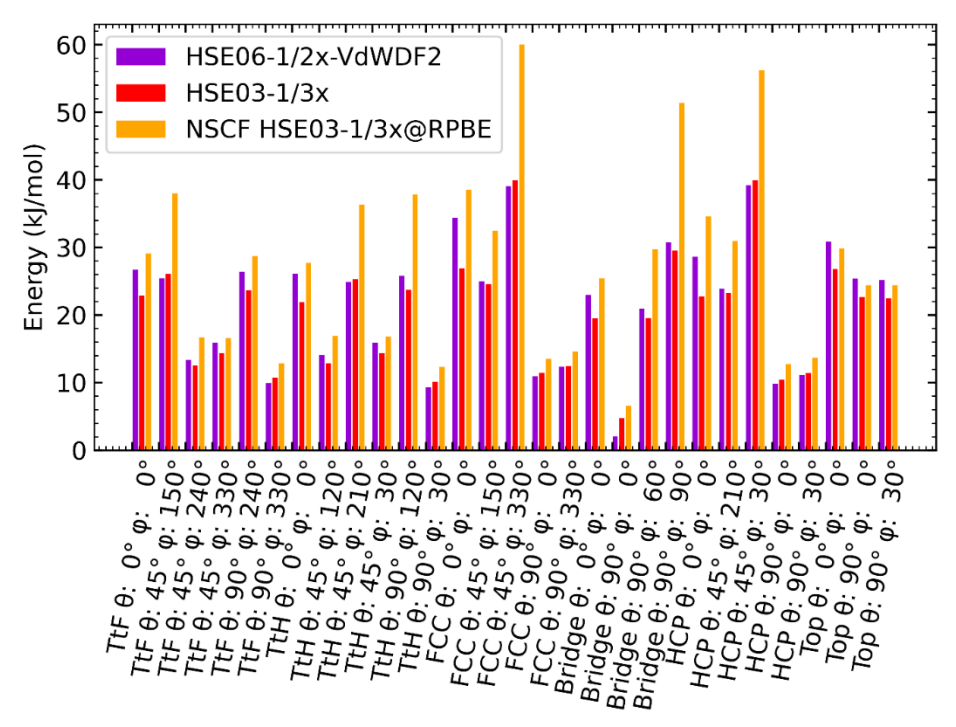


**Figure 4.5**: Barplot comparing barrier heights for twenty-nine different  $O_2$  + Al(111) geometries computed with the HSE06-1/2x-VdWDF2 DF (purple), HSE03-1/3x DF (red) as adapted from the work of Gerrits et al.<sup>124</sup>, and the non-self-consistent field HSE03-1/3x@RPBE DF (orange) as taken from Chapter 3.

# 4.5.2 Direct and indirect dissociative chemisorption

The reaction probability of  $O_2$  on Al(111) can be divided into contributions of different types of events in a similar way as was done for  $O_2 + Cu(111)$  in previous work<sup>284</sup>, i.e. Chapter 5. In short, the total reaction probability is the sum of both the direct and the indirect reaction probability where the sticking probability is the sum of the total reaction probability and the trapping probability:

$$S_0 = 1 - P_S = P_r^T + P_t = P_r^D + P_r^I + P_t$$
 (4.9).

Here  $P_s$  is the scattering probability. Any probability of a specific event is computed analogously to Equation 8 of the main text, and the conditions for reaction and scattering are described in Section 4.2.5 of the main text. Furthermore, a molecule is considered trapped if it has neither scattered nor reacted after the limit of  $1 \, ns$  propagation time has been reached. The reaction

probability is considered indirect if the molecule makes more than one "bounce" on the surface. A bounce is defined by a sign change in the momentum vector of the COM of the  $O_2$  molecule along the surface normal. For more details, the reader is referred to Chapter 5.

If the  $S_0$  shown in **Figure 4.3** of the main text is divided into the probabilities of the separate sticking events as described by Equation 4.9 then this results in **Figure 4.6**. From this figure, it is immediately clear that no trapping of  $O_2$  on the Al(111) surface occurs within the time limit we use, i.e., 1 ns. That is, all  $O_2$  molecules will either scatter or react within this timeframe. Furthermore, the contribution of indirect reaction is minimal, i.e., always one order of magnitude smaller than the contribution of direct dissociative chemisorption. The influence of the indirect mechanism is thus small although not entirely negligible.

Moreover, the indirect mechanism only occurs in an  $E_i^\perp$  regime where the  $E_i^\perp$  can be either higher or lower than an encountered reaction barrier, i.e., within the barrier energy range, see also **Table 4.3** or **Figure 4.5**. As such, one can assume that the indirect mechanism occurs via the  $O_2$  molecule impinging the surface at a geometry for which the barrier is slightly too high, with the initial collision leading to, e.g., enhanced molecular rotational motion, which leads to temporary adsorption if not enough energy is left in translational motion normal to the surface for the molecule to escape to the gas-phase. Once the molecule returns to the surface it may find a more favourable geometry for reaction, but since it has experienced at least one bounce with the Al(111) surface the reactive event will be classified as indirect.

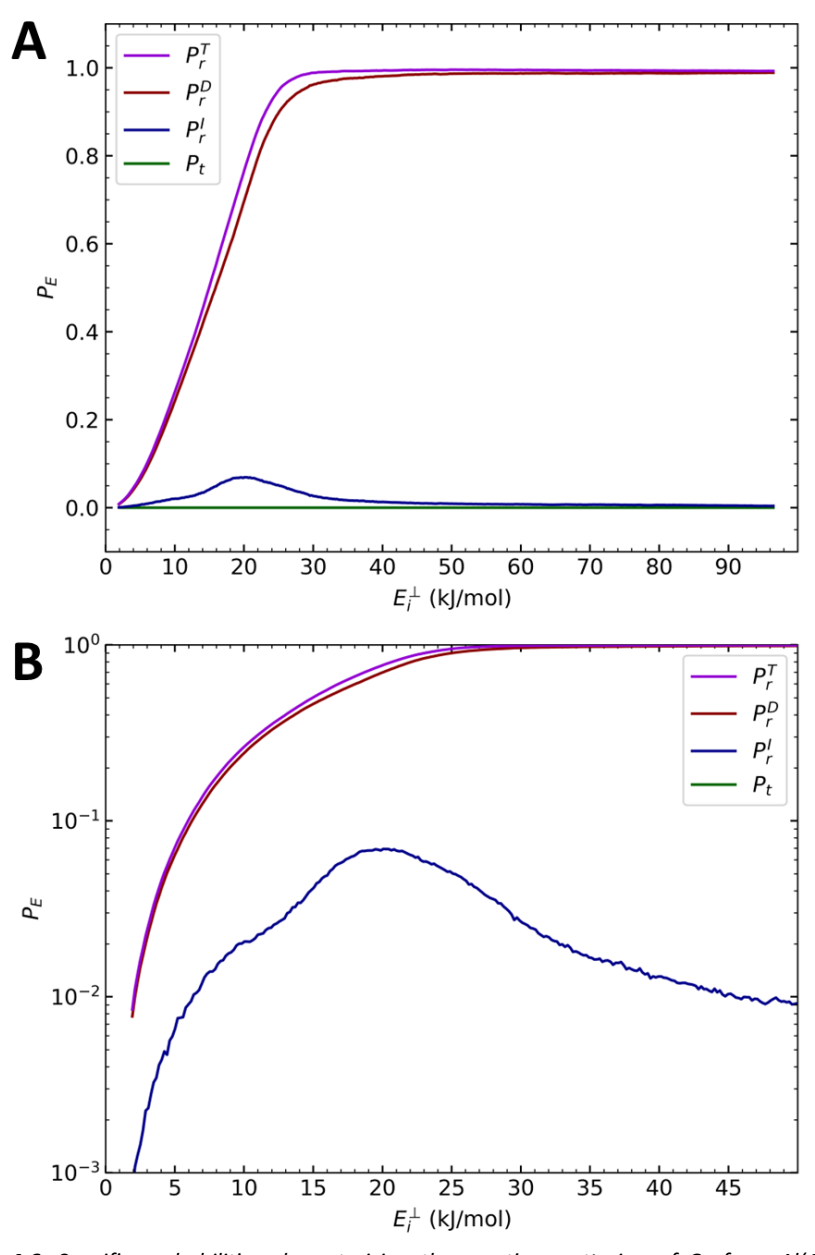


**Figure 4.6**: Specific probabilities characterising the reactive scattering of  $O_2$  from Al(111) as computed by quasi-classical trajectory calculations using the HSE06-1/2x-VdWDF2 PES. The probabilities are plotted as a function of normal incidence energy ( $E_r^{\perp}$ ), and plotted are the total reaction probability ( $P_t^{\text{T}}$ ), the direct reaction probability ( $P_t^{\text{D}}$ ), the indirect probability ( $P_t^{\text{D}}$ ) and the trapping probability ( $P_t^{\text{D}}$ ). For definitions of each type of event see the text and Ref. <sup>284</sup> or Chapter 5.

#### 4.5.3 Baule model

An expected upper bound of energy transfer between  $O_2$  and an Al surface atom can be estimated using the Baule model<sup>297</sup>, along similar lines as done in the work of Nattino *et al.* to estimate the effect of allowing surface atom motion on the inelastic scattering of  $N_2$  from W(110)<sup>131</sup>. The energy transfer in the Baule model can be computed as

$$\Delta E = \frac{4\mu}{(1+\mu)^2} E_I \tag{4.10}$$

with

$$\mu = \frac{2 * 15.999 \, u}{26.982 \, u} = 1.1859 \tag{4.11}$$

thus,

$$\Delta E = \frac{4 * 1.1859}{(1 + 1.1859)^2} E_I = 0.992 E_I \tag{4.12}.$$

We estimate that for sticking only half the total energy transfer occurs before the barrier is crossed, as only "half" a collision occurs before the system "decides" that sticking occurred. The estimated shift of  $S_0$  of **Figure 4.3** can then be estimated by shifting the  $S_0$  through changing its argument  $E_i^{\perp}$  as follows:

$$E_I^{\perp} + \frac{1}{2} \Delta E = (1 + \frac{0.992}{2}) E_I^{\perp}$$
 (4.13).

The sticking probability shifted in this way, along with the experimental and original QCT-based  $S_0$  is presented in **Figure 4.7**. This figure shows that we may still expect a non-trivial drop in  $S_0$  if the motion of surface atoms is included in future models. However, we note that the Baule model is simplistic and may well overestimate the energy transfer to surface atom motion, as was also previously shown for the scattering of  $N_2$  from  $W(110)^{131}$ . Furthermore, the barriers to reaction for  $O_2 + Al(111)$  are so early in the entrance channel that the barriers tend to be encountered before a "hard-sphere-like" collision of the molecule and the surface atoms actually can take place as the Baule model would imply. Thus, it is more likely that any future  $S_0$  computed with the inclusion of the effects of surface atom motion will end up somewhere between the QCT results of the current chapter and the lower bound as calculated with the Baule model. This area is indicated as the grey area in **Figure 4.7**.

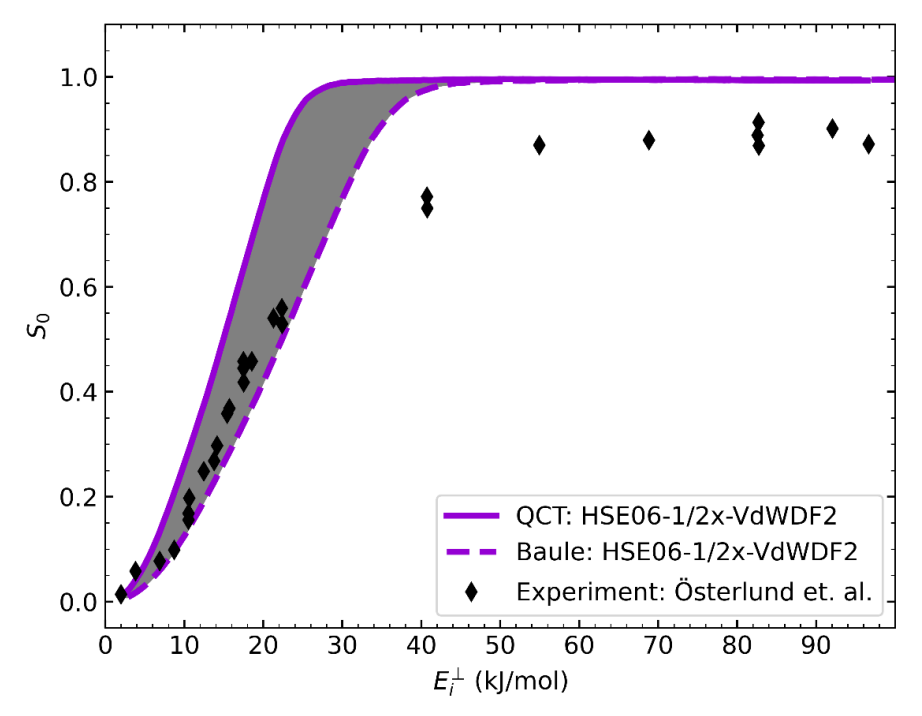


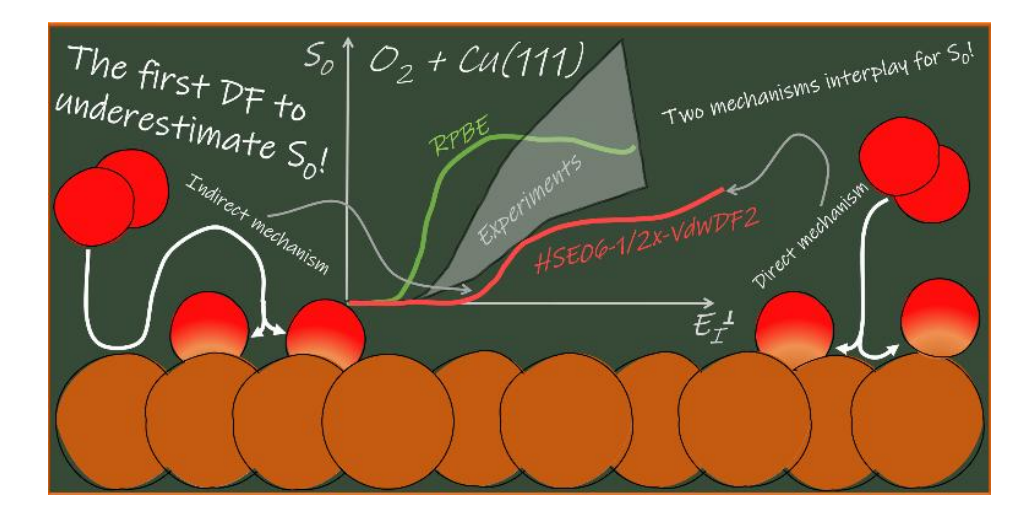
**Figure 4.7**: Sticking probabilities as a function of normal incidence energy. Plotted are the sticking probabilities measured in the experiments (black diamonds) by Österlund et al.<sup>224</sup>, as computed with the HSE06-1/2x-VdWDF2 DF using the static surface model (purple solid line), ), and as estimated from the latter by taking into account energy transfer to surface atom motion as calculated by the Baule model (purple dashed line). The grey shaded area estimates future computational results including the effects of surface atom motion.

Application of the Baule model shows that, with the use of the HSE06-1/2x-VdWDF2 DF and quasi-classical dynamics for molecular motion, the addition of surface atom motion to the model may result in substantially better agreement with experiment for incidence energies up to about  $E_i^{\perp} = 26 \text{ kJ/mol}$ . However, based on these results it seems that surface atom motion will be an unlikely candidate to improve agreement much for any higher  $E_i^{\perp}$ .

# 5 O<sub>2</sub> dissociation on Cu(111): Dynamics on a novel screened hybrid Van der Waals DFT potential energy surface

#### This chapter is based on:

van Bree, R. A. B.; Kroes, G. J. O<sub>2</sub> Dissociation on Cu(111) Dynamics on a Novel Screened Hybrid Van der Waals DFT Potential Energy Surface. *J. Phys. Chem. C* **2024**, *128* (45), 19182–19196. https://doi.org/10.1021/acs.jpcc.4c05466.



## **Abstract**

The dissociative chemisorption (DC) of  $O_2$  on Cu(111) has been extensively studied by both theory and experiment. Different experiments disagree on the underlying mechanisms (direct or indirect) for the sticking of  $O_2$ . Thus far, studies based on density functional theory (DFT) favour the indirect mechanism. However, DFT has not fully resolved the discussion, as DFT based on the generalised gradient approximation (GGA) has always substantially overestimated the reactivity and sticking probabilities of  $O_2$  on Cu(111) and other Cu surfaces. Recent work indicated that this overestimation is due to the failure of GGA DFT to describe molecule-metal systems where the charge transfer energy ( $E_{CT}$ ), i.e., the work function of the metal surface minus the electron affinity of the molecule, is below  $7 \, eV$ .  $O_2 + Cu(111)$  is one such system. This chapter presents computed sticking probabilities for  $O_2 + Cu(111)$  based on

the HSE06-1/2x-VdWDF2 screened hybrid Van der Waals density functional (DF), which is applied self-consistently. A six-dimensional static surface potential energy surface (PES) was constructed using the corrugation-reducing procedure. This PES was used to perform quasi-classical trajectory calculations to compute the sticking probabilities of  $O_2$  + Cu(111). For the first time, we present DFTbased sticking probabilities that underestimate the experimental sticking probabilities. While reproducing the experimental results would have been even more desirable the fact that we found a DF which underestimates the measured sticking probabilities means a DF using a lower fraction of exact exchange will most likely describe the  $O_2$  + Cu(111) system with high accuracy. Furthermore, our work shows evidence for the presence of both indirect and direct dissociative chemisorption. The indirect precursor-mediated mechanism occurs for low-incidence energy O2. The mechanism is supplanted by a direct dissociative mechanism at higher incidence energies. Lastly, our work suggests that the Cu surface temperature may also effect the dissociation mechanism, but this still needs further verification with a different theoretical framework that allows for the simulation of surface temperature.

## 5.1 Introduction

The adsorption or dissociative chemisorption (DC) of oxygen molecules  $(O_2)$  on metal surfaces is the first step in many oxygen-related chemical processes <sup>6,212,213</sup>. These can be useful processes as seen in, for instance, the heterogeneous catalysis of methanol formation<sup>27,29</sup> or oxidative catalysis reactions<sup>215–218</sup>. But processes can also be undesired, for example in unwanted oxide formation during catalysis or in the corrosion of metal materials<sup>215,216,218,306,307</sup>. As a result, the study of the DC of O<sub>2</sub> on metal surfaces is not only of fundamental but also of high practical importance<sup>1,218</sup>. Furthermore, copper (Cu) is one of the most widely studied transition metals for catalytic activity, both experimentally 68,76,308-<sup>315</sup> and theoretically 55,56,126,129,316-320. In addition, the H<sub>2</sub> on Cu(111) system is well known as a benchmark system for activated DC reactions on transition metal surfaces $^{55,56,110,221,263,321}$ . However, the electronic structure of  $O_2$  + Cu(111) is considerably more complicated than that of  $H_2$  + Cu(111) due to the high electron affinity of the molecule and the triplet-spin ground state of the molecule $^{124,145,228,231,280,319}$ . The O<sub>2</sub> on Cu(111) system has seen plenty of experimental and theoretical development<sup>313,319,322-325</sup> and is as a useful benchmark system for the interaction of O<sub>2</sub> with transition metals.

The majority of studies on  $O_2$  + Cu(111) and other Cu surfaces have focused on the initial sticking probability ( $S_0$ ) of  $O_2$  impinging on the Cu surface<sup>313–315,318,319,324–326</sup>. The studies generally show that the (110) and (100) surfaces have a higher reactivity towards  $O_2$  than the (111) surface, i.e., the sticking probability as a function of the normal component of the incidence energy of the  $O_2$  molecule is highest for the more "open" (110) and (100) faces<sup>314,315,324–326</sup>. The literature generally describes two possible mechanisms for the sticking of  $O_2$  on Cu surfaces, where the sticking of the molecule to the metal surface can proceed via a direct DC reaction or via a non-dissociative chemisorbed (or even physisorbed) precursor state.

The first of these two mechanisms is discussed in the work of Hall et~al. for  $O_2$  on  $Cu(100)^{326}$  and of Zhang et~al. for  $O_2 + Cu(111)^{325}$ . Both provide evidence that  $O_2$  sticking on Cu(100) and Cu(111) takes place largely through direct activated  $DC^{325,326}$ . Additionally, the  $S_0$  on both surfaces appear to follow normal energy scaling (NES), i.e., the  $S_0$  only depends on the normal component of the

incidence energy of the molecule ( $E_i^{-1}$ ). Both works<sup>325,326</sup> also found that the  $S_0$  is positively and linearly correlated with the Cu surface temperature ( $T_s$ ). Interestingly, the work of Zhang  $et\ al.$ <sup>325</sup> seems to indicate a deviation from this linearity of  $O_2$  sticking on Cu(111) at the lowest  $T_s$  shown (90 K), however, the exact  $T_s$  at which such a deviation of linearity starts to occur is not clearly determined<sup>325</sup>. Hall  $et\ al.$  also showed evidence for a considerable energy transfer from the incidence energy ( $E_i$ ) of the impinging  $O_2$  to the Cu(100) surface atoms<sup>326</sup>. It is plausible that such energy transfer also occurs for  $O_2$  sticking on Cu(111), but the work of Zhang  $et\ al.$  did not specify this.

Importantly, the work of Zhang  $et\ al.^{325}$  seems to be in stark disagreement with the  $O_2$  on Cu(111) sticking measurements of Minniti  $et\ al.^{324}$  which predate the work of Zhang  $et\ al.^{325}$  by about ten years. Although the work of Minniti  $et\ al.$  was focused on the sticking of  $O_2$  and  $H_2$  on Cu monolayers on a Ru(0001) surface, they also reported  $O_2$  sticking probabilities for a clean Cu(111) surface. The  $S_0$  measured by Zhang  $et\ al.^{325}$  are considerably higher than those of Minniti  $et\ al.^{324}$ . The authors of Ref.  $^{325}$  also noted this discrepancy but were unable to explain the major disagreements between measurements, even though both experiments were similar in conditions and both used the King and Wells (K&W) technique  $^{69}$ . This does raise the question of what the actual reactivity of  $O_2$  on Cu(111) is.

The second, indirect, mechanism for the sticking of  $O_2$  is supported by the experimental and theoretical works of Refs.  $^{313-315,318,319,322,323}$ . This second mechanism, which proceeds via a precursor state, usually occurs at low  $E_i$ . Already in 1979, Habraken *et al.* published work<sup>313</sup> studying the  $O_2$  chemisorption on Cu(111) using low energy electron diffraction (LEED) and ellipsometry. Based on the dependence of the  $S_0$  on both  $T_5$  and the  $O_2$  surface coverage they argued that  $O_2$  would have to dissociate on Cu(111) via a "mobile" precursor state. Additionally, in 1993 Hodgson *et al.* extensively discussed sticking results for  $O_2$  on  $Cu(110)^{315}$  obtained with the K&W technique<sup>69</sup> and distinctively identified two separate DC channels. The first channel, which occurs for low  $E_i$ , seems to be a precursor-mediated dissociation, and the second at higher  $E_i$  was identified as direct DC. A similar two-channel observation was made in 2004 for the sticking of  $O_2$  on Cu(100) by Junell *et al.*<sup>314</sup>. Furthermore,

in 1996 Sueyoshi *et al.* identified the existence of an adsorbed molecular  $O_2$  species on a 100 K Cu(111) surface<sup>322</sup> using high-resolution electron energy loss spectroscopy (HREELS). This chemisorbed  $O_2$  species dissociated upon annealing the Cu surface to 170 - 300  $K^{322}$ .

The second mechanism, and the presence of at least two reaction channels for O<sub>2</sub> on low index faces of Cu, is similarly supported in theoretical work <sup>318,319,323</sup>. In support of the work of Sueyoshi et al.<sup>322</sup>, Xu et al.<sup>323</sup> used density functional theory (DFT)<sup>121,122</sup> calculations at the generalised gradient approximation (GGA) level with the PW91<sup>188</sup> density functional (DF) to calculate the binding energies of molecularly chemisorbed O<sub>2</sub> on Cu(111). They found energy barriers to dissociation from this precursor state of about 16 - 22 kJ/mol, depending on whether or not the Cu(111) surface is allowed to relax in response to the presence of the adsorbed O<sub>2</sub><sup>323</sup>. Also using the PW91 DF, Martin-Gondre et al. constructed a complete six-dimensional (6D) static surface potential energy surface (PES) for O<sub>2</sub> + Cu(100), using the FPLEPS model<sup>210,247,248</sup> to fit the DFT data, and simulated the DC with quasi-classical trajectory (QCT) calculations<sup>318</sup>. The computed reaction probabilities considerably overestimated the existing experimental results. The authors also identified two distinct reaction channels (direct and indirect), with the fractional contribution of the indirect channel being greatest at low  $E_i^{\perp}$  and declining as  $E_i^{\perp}$  increases<sup>318</sup>.

Lastly, in an attempt to reproduce the experimental work of Minniti *et al.*<sup>324</sup> Ramos *et al.*<sup>319</sup> used the more repulsive, i.e., less reactive, RPBE<sup>239</sup> GGA DF to compute the sticking probabilities of  $O_2$  on Cu(111) (and also  $O_2$  on  $Cu_{ML}$ /Ru(0001)) with the QCT method. They used the corrugation reducing procedure (CRP)<sup>201,202</sup> to fit the DFT data and the Cu surface atom motion was modelled using the generalised Langevin oscillator (GLO)<sup>327</sup> method. Their computed  $S_0$ <sup>319</sup> overestimated the experimental  $S_0$  of both Ref. <sup>324</sup> and Ref. <sup>325</sup>. However, Ramos *et al.* likewise identified the existence of a precursor-mediated dissociation channel in  $O_2$  + Cu(111). Moreover, they found that at  $T_S$  = 100 K the greater part of the  $S_0$  is caused by the non-dissociative chemisorption of  $O_2$  molecules on the Cu(111) surface, in contrast to  $T_S$  = 350 K, where nearly all chemisorption was dissociative<sup>319</sup>.

To properly understand the two reaction mechanisms or channels and distinguish between them, it will probably be necessary to compute the reaction probabilities within chemical accuracy, i.e. within an accuracy of  $1 \text{ kcal/mol}^{55,56}$ . However, the substantial overestimation of the measured  $S_0$  for  $O_2$  on Cu(111) with even the least reactive GGA DF<sup>319</sup>, i.e., RPBE, is concerning, as this suggests that a chemically accurate description of the reaction is likely not possible at the semi-local (GGA) DFT level<sup>319</sup>. This problem is not unique to the dissociation of  $O_2$  on Cu surfaces but is also a well-documented issue for the activated direct dissociative chemisorption of  $O_2$  on Al(111) considered in an electronically adiabatic framework<sup>124,228–230,234–238,240</sup>. Moreover, the failure of semi-local GGA DFT is likely caused by the same origin<sup>124</sup>, and may also be resolved by the same solution as tried recently for  $O_2$  + Al(111)<sup>124,226,280</sup>.

The failure of semi-local (GGA or meta-GGA) DFs to accurately describe the reaction of  $O_2$  on Al(111) has been attributed to the charge transfer energy ( $E_{CT}$ ) of the system being below  $7 eV^{124}$ . Here  $E_{CT}$  is defined as the work function of the metal surface minus the electron affinity of the molecule.  $E_{CT}$  is a measure to investigate the likelihood of electron transfer from the metal surface to the molecule during their collision 124. It is not yet fully understood why  $E_{CT} < 7 \text{ eV}$ results in a failure of semi-local DFs for DC on metals. As discussed in Ref. 124, for gas-phase reactions it has been argued that semi-local exchange-correlation (XC) DFs generally favour, i.e., yield a lower energy for, situations where charge delocalisation occurs<sup>146,328</sup>. This would then result in transition state energies being too low relative to the energies of the reactants and would explain why semi-local DFs applied to Hartree-Fock densities tend to give much better results for gas-phase reactions<sup>147–149,253</sup>. Consequently, such errors have been labelled as "density-driven"<sup>147–149,253</sup>, i.e., as resulting from errors in semi-local densities. However, this explanation is at odds with calculations on O<sub>2</sub> + Al(111), which showed that quite reasonable results can be obtained for this system using semilocal densities provided that a screened hybrid functional was applied to these densities in a non-self-consistent way  $^{124,145,280}$ . The error made for  $O_2$  + Al(111) should then be labelled as "functional-driven" 124,145,147,253,280. Interestingly, the explanation that the underestimation of gas-phase reaction barriers by semilocal density functionals should be due to density-driven errors is now under scrutiny: recent papers argue that the improved agreement resulting from the

non-self-consistent application of semi-local density functionals to Hartree-Fock densities is due to cancellation between functional-driven and density-driven errors<sup>150,151</sup>.

The  $E_{CT}$  of  $O_2$  + Cu(111) is approximately  $4.4 \ eV^{124}$ , thus also substantially below the  $7 \ eV$  boundary. This could be a good reason why one of the least reactive GGA DFs (RPBE) is still too reactive to describe the  $O_2$  + Cu(111) reaction<sup>319</sup>. As such, the employment of a non-local XC in the form of a screened hybrid DF may, similarly to  $O_2$  + Al(111)<sup>124</sup>, help to resolve the overestimation of the reactivity.

The goal of the present chapter is to investigate whether the use of a screened hybrid DF may result in a better description of the experimentally determined reactivity of  $O_2$  on Cu(111). We do this by constructing a static surface PES using the screened HSE06-1/2x-VdW-DF2 DF, applied self-consistently, and by comparing the resulting sticking probabilities, as computed with QCT, to experiments and other theoretical work. We will show that we were able to, for the first time, compute reaction probabilities that underestimate instead of overestimate the experimental sticking probabilities of  $O_2$  on Cu(111). This indicates that a non-local DF that can describe the measured sticking probability with high accuracy must be within reach. Furthermore, we show that for a static surface there seems to be a significant contribution of the indirect reaction channel to the DC for lower incidence energies of  $O_2$ , and that the indirect reaction does not follow normal energy scaling in contrast to the direct reaction.

This chapter proceeds as follows: Section 5.2.1 will briefly discuss the Born-Oppenheimer static surface (BOSS) approximation, Section 5.2.2 will broadly discuss the choice of screened hybrid DF, and 5.2.3 will discuss the computational setup for the DFT calculations. Then, Section 5.2.4 will discuss the CRP PES fitting method, and the details concerning the QCT calculations are found in Section 5.2.5. Thereafter, Section 5.3.1 will discuss the resulting screened hybrid PES, 5.3.2 will compare our computed  $S_0$  with experimental and other computed  $S_0$ , Section 5.3.3 will discuss the direct and indirect components of  $S_0$  and investigate the NES of both components and, lastly, Section 5.3.4 will discuss our results within the framework of current literature. Section 5.4 presents conclusions and an outlook.

### 5.2 Methods

## 5.2.1 The dynamical model

The dynamics calculations are done with the motion of the nuclei decoupled from the motion of the electrons via the Born-Oppenheimer approximation. The Cu atoms are also kept static in their relaxed, or ideal (i.e.,  $0 ext{ K}$ ) lattice position. This results in a total of six degrees of freedom for the motion of the O-atoms (**Figure 5.1A**). The centre of mass (COM) of the diatomic molecule is described by its Cartesian coordinates. Here, Z indicates the distance between the surface and the COM of  $O_2$ , and X and Y describe the projection of the COM on the Cu(111) surface. X and Y are represented in U, V-space such that the angle between the two axes is taken as  $60^\circ$  (see **Figure 5.1B**) to describe the (111) surface unit cell. Furthermore, r is the bond length of the molecule,  $\theta$  the polar angle the  $O_2$  bond makes with the Z-axis, and  $\varphi$  the azimuthal orientation angle of the molecular relative to the Cu surface, as indicated in **Figure 5.1A**. **Figure 5.1B** additionally shows the locations of the high symmetry sites of Cu(111).

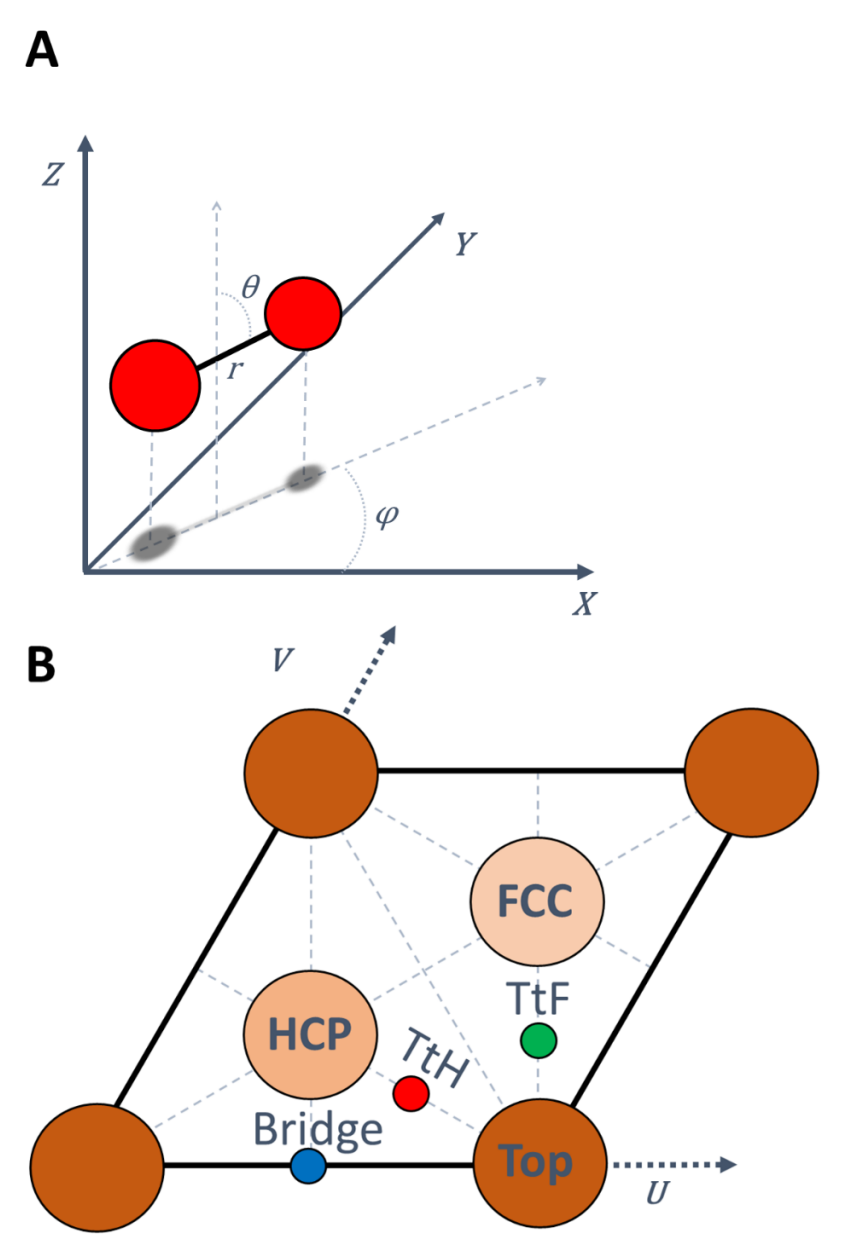


**Figure 5.1**: Coordinate system and its relation to the Cu(111) unit cell; **A**: six-dimensional centre-of-mass coordinate system for the  $O_2$  molecule; **B**: (111) surface unit cell for an FCC metal (like Cu) with all high symmetry sites indicated. A lighter shade represents an atom that is in a deeper layer in the slab.

### 5.2.2 Electronic structure approach

The exchange-correlation functional chosen for this work consists of a combination of two distinct DFs. The first part is the exchange part of the screened hybrid DF named  $HSE06^{189,190}$  but using a fraction of 1/2 of screened exact exchange instead of 1/4. The second part is the Van der Waals DF2 correlation function<sup>195</sup>. Below we will discuss both components and their combination.

The HSE06 DF, based on the better known PBE0<sup>152,153</sup> DF, is a hybrid DF, meaning that a certain fraction ( $\alpha$ ) of exact (i.e., Hartree Fock) exchange( $E^{HF}$ ) is mixed into the PBE<sup>154</sup> exchange-correlation energy ( $E_{XC}$ ) such that

$$E_{XC} = E_C^{PBE} + \alpha E_Y^{HF} + (1 - \alpha) E_Y^{PBE}$$
 (5.1),

here the two  $E_x$  contributions taken together form the exchange part of the exchange-correlation functional and  $E_c$  is the correlation part. HSE06 is distinct from PBE0<sup>152,153</sup> as described by Equation 5.1, due to the addition of screening. Such screening is required for a more physically correct, and more computationally efficient, description of the metal slab<sup>155–157,189</sup>. For example, without screening, the electronic density of states would be substantially and artificially reduced at the Fermi-level<sup>158</sup>.

The screening of the exact exchange is done by introducing a continuous switching function (based on the screening parameter  $\omega$ ) in the coulomb operator describing the electron-electron interaction<sup>189,190</sup>, such that the long-range electron-electron interaction is only described with the semi-local exchange DF<sup>189,190</sup>. This results in the following description:

$$E_{XC}^{HSE06}$$

$$= E_c^{PBE} + \alpha E_x^{HF,SR}(\omega) + (1 - \alpha) E_x^{PBE,SR}(\omega) + E_x^{PBE,LR}(\omega)$$
(5.2),

where SR indicates a short-range interaction relative to the screening parameter  $\omega$  and LR a long-range interaction.

In this work, we opted to use  $\alpha = 1/2$ , calling the corresponding exchange DF HSE06-1/2x. The original HSE06 DF comes with an  $\alpha$  of  $1/4^{152,153,189,190}$ . However, previous work on the interaction of  $O_2$  + Al(111) showed that even  $\alpha = 1/3$  resulted in reaction probabilities that overestimated the experimental results  $^{124,280}$ . Therefore, we opted to increase the  $\alpha$  to 1/2 (in principle the

maximum mixing value<sup>152</sup>), assuming that a higher fraction of exact exchange should also be required to reproduce the barrier height for  $O_2 + Cu(111)^{283}$ . This value may seem high but we note that the BH&HLYP and MPW1K functionals, with values of  $\alpha$  of 0.5 and 0.428, respectively, were found to perform quite well on gas-phase barriers in the work of Truhlar and co-workers<sup>329</sup>. Moreover, keeping in mind the addition of the Van der Waals correlation in the DF, as described below, we anticipated that we might require a high fraction of exact exchange to compensate for the expected effect<sup>56,124,126,132,282</sup> this correlation might have on the barrier heights, and thus on the computed reaction probabilities.

In the HSE06-1/2x DF, the correlation functional is the PBE correlation functional. However, semi-local DFs like PBE are not able to describe long-range interactions between electrons and the non-local or global nature of the (screened) hybrid DF does not include a correct description of the attractive Van der Waals correlation. Therefore we opted to use a non-empirical Van der Waals (VdW) DF as correlation DF<sup>183,195</sup> to improve the long-range correlation description of the functional. To obtain the so-called PBE-VdWDF2 DF, which we use as a 'primer' (see Section 5.2.3), the addition of Van der Waals correlation is rather straightforward:

$$E_{XC} = E_C^{LDA} + E_C^{VdWDF2} + E_X^{PBE}$$
 (5.3).

Here the correlation part of the DF is now split between that of the local density approximation (LDA) and a purely non-local VdW correlation correction <sup>195</sup>. This correction is computed with

$$E_c^{VdWDF2} = \int d\mathbf{r} \int d\mathbf{r}' \, \rho(\mathbf{r}) \Phi(\mathbf{r}, \mathbf{r}') \rho(\mathbf{r}')$$
(5.4),

in which r and r' are the position vectors of the electron density,  $\rho(r)$  the electron density of the electron at r, and  $\Phi(r,r')$  is the Van der Waals kernel describing the electron density-density interaction. The details of this kernel are complex and out of scope for this chapter and we refer the interested reader to Refs.  $^{183,195}$  for more information.

The addition of the VdW correlation is expected to introduce a VdW well in front of the barrier in the entrance channel<sup>56,126,130,282</sup>. A VdW-well would speed up the molecule as it approaches the Cu(111) surface (during dynamics calculations) and this could influence the dynamics of the reaction<sup>126,130</sup>. The replacement of

PBE correlation with VdW-DF2 correlation may lower the reaction barrier. Anticipating that this may lead to a too-low barrier we decided to use a high fraction of exact exchange, as discussed above. However, it must be noted that a lowering of the barrier does not always occur and replacing PBE with VdW-correlation has in the past sometimes caused the opposite to happen<sup>132</sup>. As the results will show, choosing the maximum fraction of exact exchange,  $\alpha$ , to "tune" a barrier height is still a trial-and-error-based approach.

In conjunction, the combination of exact exchange and VdW-correlation leads to the following expression for the screened hybrid VdW exchange-correlation energy of the HSE06-1/2x-VdWDF2 DF:

$$E_{XC}^{HSE06-1/2x-VdWDF2} = E_{C}^{LDA} + E_{C}^{VdWDF2} + \frac{1}{2}E_{x}^{HF,SR}(\omega) + \frac{1}{2}E_{x}^{PBE,SR}(\omega) + E_{x}^{PBE,LR}(\omega)$$
(5.5).

It is important to distinguish this DF from other screened hybrid VdW DFs, as a simple combination of two established DFs, as described above. Our functional does not represent a completely new screened hybrid VdW DF, like the recent VdW-DF2-ahbr DF as developed by Hyldgaard and co-workers in such a way that the exchange part of the functional is matched to the Van der Waals part<sup>193</sup>. It was expected that the HSE06-1/2x-VdWDF2 DF would adequately describe longer-range interactions and thereby result in the presence of a VdW-well before the barrier<sup>126124</sup>, and we hoped that it would correctly describe the barrier height<sup>124</sup>.

### 5.2.3 Computational details of the DFT calculations

The DFT calculations are done with the Vienna Ab Innitio Simulation Package (VASP) version 6.3.2<sup>200,258–262</sup>, with the Van der Waals implementation of J. Klimeš *et al.*<sup>285,286</sup>. All computed DFT energies are based on two different successive self-consistent field (SCF) spin-polarised single-point calculations. The first is a "primer" calculation done with the PBE-VdWDF2 DF to establish a decent estimate for the electron densities and Kohn-Sham (KS) wavefunctions. After this, the HSE06-1/2x-VdWDF2 SCF single-point calculation is started using the previously converged PBE-VdWDF2 KS wavefunction. This is done to

meaningfully improve the convergence speed of the calculation with the screened hybrid DF.

Both calculations use a 2x2 4-layer Cu(111) slab with 15 Å of vacuum separating the slabs. The lattice constant for Cu was converged with the HSE06-1/2x-VdWDF2 DF to 3.698 Å, and relative to the bulk the top interlayer distance was reduced by 1.0%. This interlayer relaxation is chosen based on experimental work, which indicates that at the interface with the vacuum changes in the interlayer spacings of Cu(111) are only significant between layers one and two, the relevant change being about 1.0% for low-temperature Cu(111)<sup>330</sup>. Moreover, experimental Cu lattice interlayer distances have been used successfully in theoretical work in the past<sup>321</sup>. An energy cutoff of 440 eV and an 8x8x1 Γ-centred k-point grid is used. The core electrons are represented with the augmented wave (PAW) method<sup>199</sup>. Specifically, the GW projector pseudopotentials developed for PBE as implemented in VASP were used. The GW versions were used to both improve convergence and improve upon the lattice description of Cu using the HSE06-1/2x-VdWDF2 DF. To ease convergence even more, Methfessel-Paxton smearing with a width of 0.2 eV is used.

The primer (PBE-VdWDF2) single point energy was converged using the conjugate algorithm implemented in VASP, using a very tight convergence criterion, i.e.,  $10^{-9}$  eV. This is done to best approach the variational minimum of the electronic density, thus possibly making it a better KS wavefunction starting point for the screened hybrid single point, in line with earlier published work for  $O_2$  on Al(111)<sup>280</sup>, i.e., Chapters 3 and 4. Finally, the HSE06-1/2x-VdWDF2 single-point energy is converged self-consistently using the damped algorithm to within  $10^{-5}$  eV, using a sparser (or as indicated in VASP; fast) FFT-grid (fast Fourier transform-grid) for the exact exchange (HF) calculations. The faster grid was chosen as the computational cost with the normal FFT grid would not be manageable, i.e., we would not get the calculations converged. Based on a section of PES data points for  $O_2$  + Al(111) presented in Chapter 4, i.e., 4035 out of the complete 5250, we estimated that the root mean squared error(RMSE) introduced in the PES by using the sparser HF-FFT-Grid is about 0.9 kJ/mol. We assume that the error for  $O_2$  + Cu(111) will be of a similar magnitude, therefore,

this should not be detrimental to the accuracy of results published in this chapter.

### 5.2.4 Fitting the PES

The  $O_2 + Cu(111)$  6D interaction is described by a continuous spline interpolation of 5260 computed DFT single points. These 5260 points make up a grid describing the  $O_2$  + Cu(111) interaction and a grid describing the molecule in the gas-phase above the surface. The interaction grid spans 29 combinations of Cu surface sites and  $O_2$  orientations, i.e., 29 different sets of U, V,  $\theta$  and  $\varphi$ coordinates (see Figure 5.1) as also used in previous chapters and other, similar, work<sup>124,130,280</sup>. For each combination of surface site and molecular orientation, the same r and Z grid is set up (see Figure 5.1); where r = [1.000, 1.100, 1.150,1.175, 1.190, 1.200, 1.225, 1.250, 1.300, 1.400, 1.500, 1.600]  $\mathring{A}$  and Z = [1.00, 1.00]1.50, 2.00, 2.25, 2.50, 2.75, 3.00, 3.25, 3.50, 3.75, 4.00, 4.25, 4.50, 4.75, 5.00] Å. The computational time involved in converging the calculations of the 5260 DFT single points with the HSE06-1/2x-VdWDF2 DF was more than 25 million CPU hours (300 – 330 elapsed hours per single point using dual-processor nodes, i.e., using nodes containing two octo core 2.4GHz EM64T Xeon E5 processors (E5-2630 v3), or two octo core 2.6GHz EM64T Xeon E5 processors (E5-2650 v2)), thus starting to push the limits of computational feasibility.

The continuous PES spline-interpolation fitting quality was improved by employing the corrugation-reducing procedure (CRP) $^{201,202}$  as also done in previous chapters and Refs.  $^{124,263,280}$  Herein, two atom-surface, 3D, PESs of O interacting with the Cu(111) surface, are subtracted from the molecular, 6D, PES to obtain a 6D function with less corrugation. This function therefore easier to fit accurately. After fitting, the atomic PES is re-added to the fitted result. The procedure is implemented for this chapter along similar lines as in Refs.  $^{124,280}$ . Previously, the application of the CRP resulted in a fitting RMSE of  $0.8 \, kJ/mol$  as long as the interaction energies were smaller than  $4 \, eV^{126}$ , where outliers often remain below  $2.9 \, kJ/mol^{115,202}$ . This error is generally small enough to ensure that using the CRP-PES tests the quality of the underlying DFT data.

The atomic 3D PES as needed for the CRP does not necessarily need to be very accurate as it (and its possible inaccuracies) are first subtracted and later readded to the molecular PES. However, for the procedure to work it does need to be physically reasonable<sup>124</sup>, based on a dense Z-grid, and free of unwanted fluctuations, inconsistencies, and discontinuities. Achieving these standards with spin-polarised calculations and a computationally demanding DF is difficult for an open shell system like atomic O + Cu(111). To resolve this we make use of the flexibility in the accuracy, i.e., we opted to use spin unpolarised DFT calculations using the PBE-VdWDF2 DF and to impose a fairly tight convergence criteria of  $5.0 \cdot 10^{-7}$  eV to calculate the O + Cu(111) 3D PES. All other computational details were kept consistent with the previously discussed "primer" single-point calculations. A CRP 6D PES computed with a similar procedure has been successfully developed and tested for  $O_2 + Al(111)^{124,280}$ . Additionally, we believe that the PBE-VdWDF2 DF will capture the longer range O + Cu(111) interaction well enough not to disrupt the CRP interpolation and that it will allow us to achieve the high precision standard needed without excessively consuming computational resources.

## 5.2.5 Quasi-classical trajectory dynamics calculations

With the continuous 6D PES it is possible to run dynamics calculations of  $O_2$  impinging on the Cu(111) surface. Here the dynamics calculations are performed with the quasi-classical trajectory (QCT)<sup>210,211</sup> method. In QCT the  $O_2$  molecule is given an initial zero-point energy after which its reaction with the Cu surface is propagated classically through time<sup>210,211</sup>. More extensive details on our implementation of the QCT method can be found in Refs. <sup>130,136</sup>. Here, the  $O_2$  molecule is given an initial rovibrational energy (or assigned to a rovibrational state) at  $7.0\,\text{Å}$  above the Cu(111) surface with a given incidence energy, along an incidence vector pointing towards the surface at an angle  $\Theta$  with the surface normal.

The outcome of a trajectory is determined by the molecule encountering specific conditions that also lead to the termination of the trajectory. The first is when the bond length (r) of the  $O_2$  molecule exceeds  $1.59\,\text{Å}$ . At this point, the molecule is considered dissociated and thus the trajectory is counted as reacted. If the

molecule-surface distance exceeds  $7.0\,\text{Å}$  and the molecule moves away from the surface the trajectory is considered scattered. Lastly, if the propagation time limit of  $1\,\text{ns}$  is reached without encountering either state, the molecule is considered trapped on the surface. However, we observed that the majority of  $O_2 + Cu(111)$  interactions lead to scattering or reaction within the first  $10\,\text{ps}$ .

Both in scattering and reaction we make an additional distinction between direct and indirect events. Indirect events occur when the  $O_2$  molecule makes an extra bounce on the surface before reaching terminating conditions. A bounce is defined by a sign change from negative to positive along the *Z*-component of the momentum vector of the COM of the  $O_2$  molecule, i.e., a bounce occurs whenever the molecule changes from going towards the surface to away from the surface. An event is considered indirect if the number of bounces is larger than one. For direct scattering the number of bounces is thus equal to one and for direct dissociative chemisorption the number of bounces can be equal to or smaller than one. We note that with our definition of indirect trajectories, their associated timespan may be too short to directly detect their presence experimentally.

All together, we distinguish between direct scattering, indirect scattering, direct reaction, indirect reaction, and trapping as possible events. The probability of a particular event,  $P_E$ , is easily defined as

$$P_E = \frac{N_E}{N_{Total}} \tag{5.6},$$

where  $N_E$  is the number of trajectories counted as resulting in a particular event and  $N_{Total}$  is the total number of trajectories run. Furthermore, if trapping is a relevant event one needs to define the total sticking probability ( $S_0$ ) as the sum of contributions from dissociative chemisorption and trapping, such that

$$S_0 = 1 - P_s = P_r + P_t (5.7),$$

where  $P_s$  is the scattering probability (direct plus indirect),  $P_t$  is the trapping probability and  $P_r$  is the reaction probability (direct plus indirect).

Experimental sticking probabilities are usually extracted from molecular beam studies. In a molecular beam, the  $O_2$  molecules are not in a single rovibrational state but rather in a distribution of states according to experimental conditions. The rovibrational state distribution of the  $O_2$  molecule follows from the nozzle

The (normal) incidence energy of the molecule is experimentally varied by either changing the seeding ratio of the molecular beam (by mixing the  $O_2$  with lighter or heavier nobles gasses) or by varying the incidence angle  $\Theta$ . With the QCT method, we can look at "monoenergetic" beams, i.e., beams with a constant incidence energy, where we can vary  $\Theta$ . However, if the experimental time of flight (TOF) spectra of the  $O_2$  beams are known we can more closely simulate the experiment by simulating the flux-weighted incidence velocity distribution (N(V)) using

$$N(V)dV = K_V V^3 e^{-\frac{(V - V_S)^2}{(\Delta V_S)^2}} dV$$
 (5.8),

where  $K_V$  is a proportionality constant, V is the velocity of the molecule,  $V_S$  is the stream velocity and  $\Delta V_S$  the width of the velocity distribution<sup>67</sup>. This can be rewritten to an energy distribution by using the kinetic energy velocity relation:

$$E_S = \frac{1}{2} m V_S^2 (5.9),$$

and by defining:

$$\frac{\Delta E_S}{E_S} \equiv \frac{2\Delta V_S}{V_S} \tag{5.10},$$

such that the flux-weighted incidence energy distribution is written as 67

$$N(E)dE = \frac{1}{K_F} E e^{-4E_S \frac{(\sqrt{E} - \sqrt{E_S})^2}{(\Delta E_S)^2}} dE$$
 (5.11),

where  $K_E$  is a normalisation constant. In practice, this means that, just like the incidence velocity distribution, the distribution of the incidence energy of  $O_2$  is described by a slightly skewed Gaussian. The velocity distribution

characterisations for the experiments of Zhang *et al.*<sup>325</sup>, and our fitted parameters characterising their beams are described in the first appendix, i.e., Section 5.5.1 We refer the reader to the work and electronic supporting information of Zhang *et al.*<sup>325</sup> for more details regarding their molecular beam time-of-flight measurements, velocity distributions, and energy distributions.

### 5.3 Results and discussion

### 5.3.1 PES analysis

Six different two-dimensional "elbow" cuts through the PES are shown in **Figure 5.2**, to get an impression of the PES. Geometries (U, V,  $\theta$ ,  $\varphi$ , r, Z) and heights of the barriers shown in **Table 5.1** represent the barriers shown with the white dots in **Figure 5.2**.

**Table 5.1**: Barrier in r, Z, and E per elbow cut, as displayed in **Figure 5.2**; if available the barrier height of Ramos et al.<sup>319</sup> is displayed in brackets. Energies in eV, distances in Å, the underlined barrier is the lowest barrier found for all 29 different elbow cuts, see Section 5.2.4.

Geometry	r <sub>barrier</sub> (Å)	Zbarrier (Å)	Ebarrier (Ebarrier Ramos et al. 319) (eV)
Bridge, $\theta$ : 90°, $\varphi$ : 0°	1.22	2.43	<u>0.28</u> (0.097)
Top, θ: 0°	n/a	n/a	n/a
Bridge, $\theta$ : 90°, $\varphi$ : 60°	1.22	2.29	0.35
Top, θ: 90°, φ: 0°	1.26	2.14	0.41
Bridge, $\theta$ : 90°, $\varphi$ : 90°	1.23	2.21	0.39
FCC, θ: 90°, φ: 0°	1.22	2.24	0.32 (0.202)

Following an incoming  $O_2$  molecule, the elbow cuts show a few general trends. First, coming from the gas-phase a small and shallow ( $\approx 2~kcal/mol$ ) well appears between 5 and 3 Å above the surface. The distance of the Van der Waals well to the surface and its depth is, to a large extent, independent of the  $O_2$  (U, V) impact site above the Cu(111) surface (see **Figure 5.2**, and **Figure 5.10** of Section 5.5.2). However, the Van der Waals interaction does depend on the polar angle of orientation of the molecule. The well is shallower and further from the surface if the molecule is not oriented parallel to the surface (see **Figure 5.10**). The dependence noted suggests that trapping of the molecule will occur through a mechanism in which energy in translational motion normal to the surface is temporarily converted to rotational energy. If the molecule is not orientated

along the surface normal, it encounters a barrier to molecular chemisorption at a slight bond elongation and  $Z \approx 2.3 \,\text{Å}$ . The barrier height is dependent on surface site and molecular orientation but its location remains roughly similar. Once this barrier is overcome the molecule enters what looks like a molecular chemisorption-well (except for the upright geometry in Figure 5.2B), where the  $O_2$  bond length is expanded to between 1.3 and 1.5  $\mathring{A}$  at about 2  $\mathring{A}$  above the surface. Some channels (Figure 5.2C and Figure 5.2E) seem to allow for further dissociation (i.e. expansion of the bond length beyond the value of 1.59 Å, where it is considered dissociated in the dynamics) without the need for overcoming an additional barrier that is higher than the entrance-barrier (Figure 5.2C and Figure 5.2E). However, for most other combinations of molecular orientation and surface site the second (exit channel) barrier, if present, would appear to be higher than the first barrier encountered, for example, in Figure 5.2D and Figure 5.2F. This seems to indicate that for molecules with low-incidence energy a pathway to dissociation is possible as long as the molecularly chemisorbed O<sub>2</sub> species (i.e., after crossing the first barrier) can change its geometry  $(U, V, \theta)$ , and  $\varphi$ ) to one in which the second barrier is low enough to allow dissociation. An important assumption made in this chapter is that once the first barrier to molecular chemisorption is crossed and the bond length (r) exceeds 1.59 Å the molecule will find its way over the second barrier to the state where two separate O-atoms remain chemisorbed to the surface (see also below).

The lowest entrance barrier that we found has a height of 0.28 eV (27 kJ/mol) and is located at the bridge site with  $\theta = 90^{\circ}$  and  $\varphi = 0^{\circ}$  (**Figure 5.2A** and **Table 5.1**). However, similar to the findings of Ramos  $et~al.^{319}$  the second, i.e., exit channel, barrier is very high for this geometry, meaning that at low  $E_i$  a change in  $O_2$  adsorption location or orientation is needed to facilitate full dissociation. Unlike the work of Ramos  $et~al.^{319}$ , we seem to find our lowest exit barrier at a different molecular orientation and surface site than the site and orientation of their lowest exit channel barrier. Still, our PES suggests that for low-incidence energies of  $O_2$ , a precursor-mediated pathway to full dissociation is not unexpected.

We note that our PES employs a shorter r-grid(see **Figure 5.2** and Section 5.2.4) than the previous work of Ramos *et al.*<sup>319</sup>. The chosen limit of r of 1.60  $\mathring{A}$  was

initially based on previous work on  $O_2$  on Al(111). However, for  $O_2$  + Cu(111) the shorter r-grid compared to the work of Ramos et al. 319 means we may artificially underestimate the second, or exit channel, barrier. This artificial underestimation would be the consequence of cutting-off the r-grid before describing the highest point of the barrier, thus lowering the threshold for full dissociation. This may result in increased dissociative reactivity of the PES. However, any increase of the r-grid to improve the second barrier description to the same size as Ramos et al. would come at computational costs that are prohibitive for our present work. For example, if we were to adhere to the current rigorous implementation and methods of the CRP-PES each additional rvalue in the r-grid would come with an additional 435 DFT single-point calculations. This is because the r-grid would need expansion into the full 15point Z-grid and for all 29 combinations of surface site and molecular orientation. Furthermore, at the lowest minimum r-grid accuracy standard of a  $\Delta r$  of 0.1 Å, we would need 9 additional r-values in the r-grid (to expand 1.6 Å to the value of 2.5 Å used in Ref. <sup>319</sup>). Based on the computational costs of this PES (300 - 330 elapsed hours per single point calculation, see Section 5.2.4) we estimate that we would need an additional 18 million CPU hours to facilitate such an r-grid extension.

Lastly, we note that all elbow cuts with parallel orientations (i.e.,  $\theta$ : 90°) through the fitted PES share a small defect in the PES for higher bond lengths further away from the Cu(111) surface. This is due to some DFT calculations in the 3D atomic PES that have not converged as well as others. However, this defect appears in an area where the classical dynamics should hardly ever sample the PES (at  $+1.50\,eV$  in potential energy). Thus, we do not expect to see any influence of this defect on our QCT results.

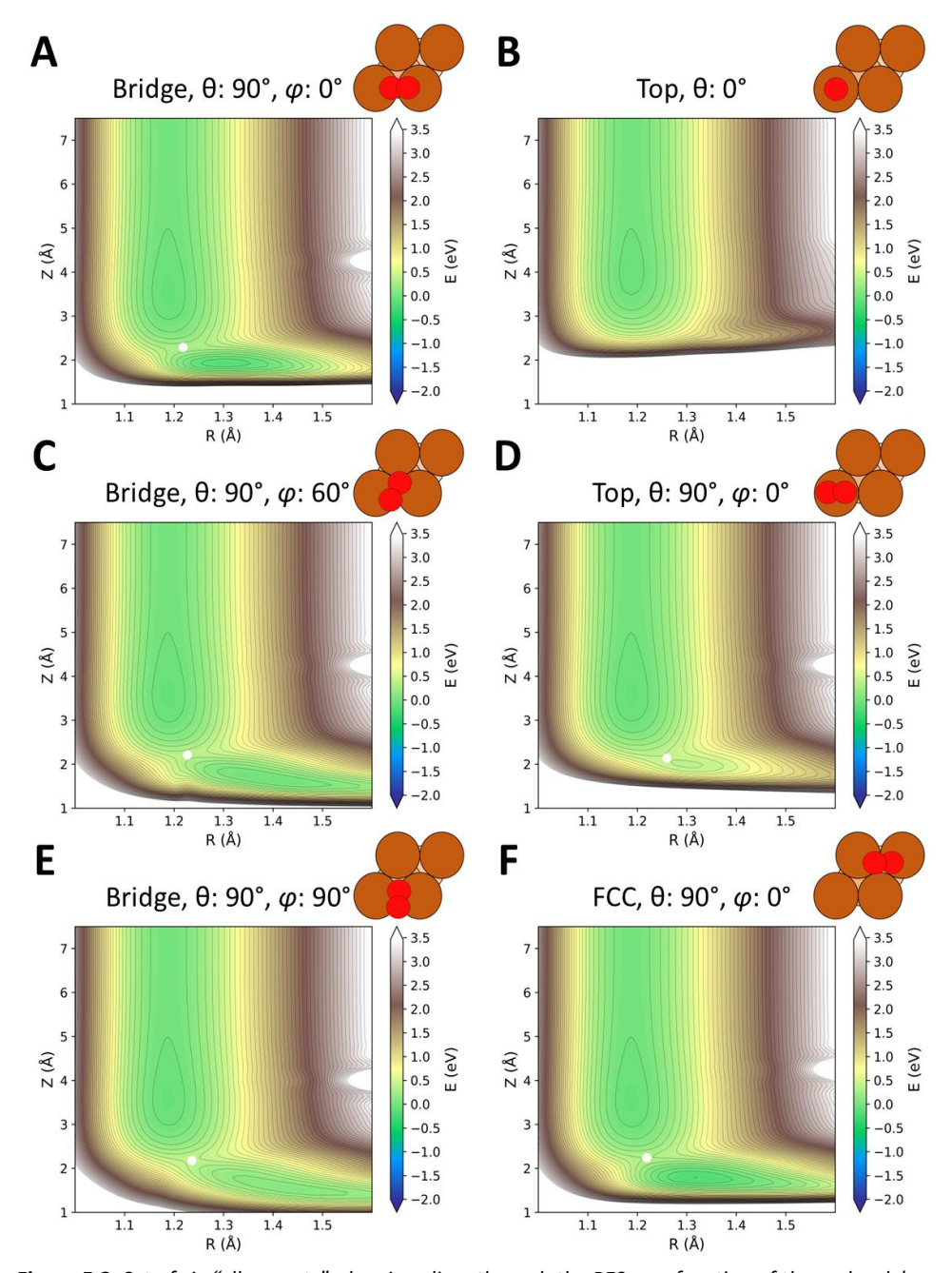


**Figure 5.2**: Set of six "elbow cuts", showing slices through the PES as a function of the molecule's bond length (r) and the distance of  $O_2$  to the surface (Z) for six different geometries (sampling three different surface sites and three different molecular orientations). Contour lines are separated by 2 kcal/mol. The white dots show the location of the barrier(if present) in reduced dimensionality.

### 5.3.2 Dynamics results

The initial conditions of the  $O_2$  beam for the K&W experiments of Zhang et al.<sup>325</sup> are simulated as closely as possible with our QCT calculations. The flux-weighted velocity distributions from the work of Ref. 325 are fitted with Equation 5.8 using a least-squared fitting method, see Section 5.5.1. The fitting of the velocity distribution results in slightly different average incidence translational energies than those presented by Zhang et al. but the difference is within 10 meV. In addition to the  $O_2$  in He seeding ratios, the incidence angle  $\Theta$  was varied to change the  $E_i^{\perp}$  (similar to the work of Zhang et al.). The resulting  $S_0$  (based on 500k trajectories per  $E_i^{\perp}$ ) are presented in **Figure 5.3**. The corresponding error bars are generally smaller than the representation of the datapoint. The figure additionally shows the experimental  $S_0$  of Minniti et al.<sup>324</sup>(blue diamonds) and Zhang et al. 325 (black diamonds), and the semi-local RPBE DF sticking probabilities of Ramos et al.  $^{319}$  (green solid line) for comparison. We also present calculated  $S_0$ for single values of  $E_i^{\perp}$ , where 100k trajectories were run for every 4 meV (0.39) kJ/mol) of normal incidence energy ranging from 12 meV to 2000 meV (see Figure 5.3 and Figure 5.4). In Figure 5.3B and C these results were cut off at 65 kJ/mol for clarity of the plot.

Our "beam simulated" and "mono-energetic"  $S_0$  overlap substantially, where the beam simulated  $S_0$  starts showing reactivity at a lower average  $E_i^\perp$  and increases slightly slower than the mono-energetic  $S_0$  to eventually reach the same plateau at  $S_0 \approx 0.180$ . Especially at low  $E_i^\perp$ , this is not unexpected as the use of the actual velocity distribution will slightly smear out sticking probability results, as can be inferred from Equation 5.11 and the steep increase of the monoenergetic  $S_0$  at low  $E_i^\perp$ .

More importantly, our results underestimate the  $S_0$  compared to all other  $S_0$  presented in **Figure 5.3**. However, the qualitative agreement with the results of Ramos *et al.*<sup>319</sup> is noteworthy. Both theoretical studies indicate a plateau in  $S_0$  after an initial steep rise of the reactivity. Our barriers to sticking are substantially higher than those of Ramos *et al.* (as also seen in **Figure 5.2** and **Table 5.1**) thus considerably reducing the sticking probability. Agreement with the experiment is best with the results of Minniti *et al.*, as their  $S_0$  are lower than those of Zhang *et al.* 

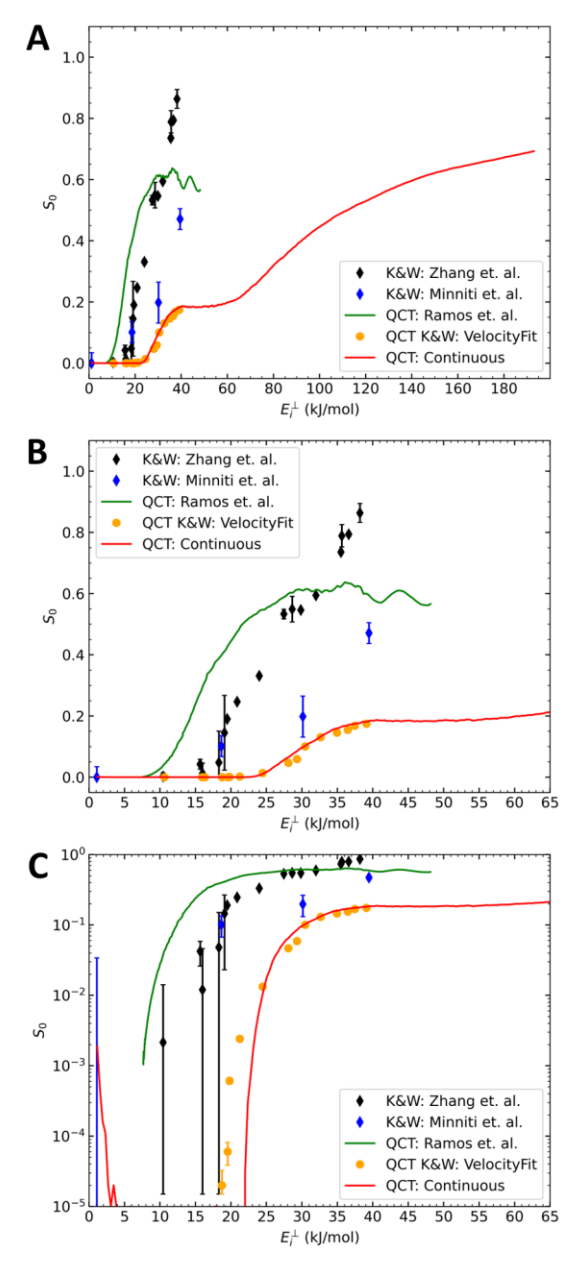


**Figure 5.3**: Sticking probabilities as a function of normal incidence energy; **A**: normal axes; **B**: normal axes, shorter range of the x-axis; **C**: Log y-axis, shorter range of the x-axis. Black diamonds: experimental K&W results taken from Ref.  $^{325}$ ; Blue diamonds: experimental K&W results taken from Ref.  $^{319}$ ; Orange dots: QCT results of present work for the molecular beam with stream velocities based on the fit of the Zhang et al. TOF data using Equation 5.11, 500k trajectories per point; Red line: continuous single  $E_i^\perp$  QCT results of present work based on 100k trajectories per point, one point every 0.39 kJ/mol.

The disagreement with the experiment is more substantial than we would have hoped, however, this is not disheartening. These are, so far as we are aware, the only DFT-based results for the sticking of  $O_2$  + Cu(111) that underestimate experimental results, where thus far, even the least reactive (RPBE) DF would still overestimate the measured sticking probability. This means that the admixing of exact exchange with semi-local exchange in the exchange-correlation DF is a working method to increase the barrier heights for the reaction and to reduce the overall reactivity of the DF. Moreover, as the DF without exact exchange overestimates the sticking probability and the DF with an exact exchange fraction of 1/2 underestimates the reactivity, we may very well be able to find a DF with a lower exact exchange fraction with which we can reproduce the experimental sticking probabilities far more closely.

As already noted in the Introduction, there are fairly large differences between the sticking probabilities measured by Zhang et al. 325 and Minniti et al. 324. These differences occur at high incidence energies but not at low energies, in a region where the sticking probabilities are large (Figure 5.3A and 3B). The observed differences seem consistent with a difference between the cleanliness and the histories of the crystals used in the different experiments as speculated by Zhang et al. 325, and not with the influence of defects like steps that could occur at low surface concentrations. Specifically, one might speculate that with the exposure times in the experiments of Minniti et al. at high incidence energies sticking could occur with averaging over non-zero oxygen pre-coverages, leading to lower sticking probabilities. However, this is mere speculation, and, even worse, speculation by theorists on the origin of experimental differences. At the time of publication of the paper on which this chapter is based, we noted: "Nonetheless, it would be good if additional molecular beam experiments were done on the benchmark  $O_2$  + Cu(111) systems that would conclusively establish both the reactivity of Cu(111) towards  $O_2$  and the origin of the differences between the current experiments." Additionally, calculations could be done looking at the effect of oxygen pre-coverage on sticking, to predict under which regime of oxygen pre-coverages (and therefore molecular beam exposure times) measured sticking probabilities could be significantly smaller than at zero precoverage conditions.

Meanwhile, after the publication of the paper on which this chapter is based, new sticking experiments by Wu  $et~al.^{331}$  have shown good agreement with the sticking probabilities of Zhang  $et~al.^{325}$ . The validation of the results of Zhang et~al. implies that their sticking results can be considered the benchmark for  $O_2$  on Cu(111) over the work of Minniti  $et~al.^{324}$ . Nevertheless, the work presented in this chapter still underestimates all experiments, and therefore the discussions and conclusions of this chapter remain consistent with the original paper that this chapter is based on.

# 5.3.3 Direct or indirect dissociation and normal energy scaling in the QCT dynamics

We have also looked into the two possible reaction mechanisms of  $O_2$  dissociating on Cu(111) that have been discussed in the literature. To do so we have disentangled the mono-energetic  $S_0(E_i^\perp)$  in contributions due to specific events (as discussed in Section 5.2.5) and presented those in **Figure 5.4**.

As discussed before,  $S_0$  can be separated into components  $P_E$  due to several different events. The first is the probability of physisorption or non-dissociative chemisorption in the form of molecular trapping  $(P_t)$ , which may be considered a non-reactive form of sticking. The other part of the sticking probability is dissociative  $(P_r^T)$  and can again be separated into a direct  $(P_r^D)$  and an indirect  $(P_r^T)$  component. All definitions and conditions for these states are discussed in detail in Section 5.2.5. **Figure 5.4** presents mono-energetic probabilities of each of these events for  $E_r^T$  ranging from 12 meV to 2000 meV, for every 4 meV, where 100k trajectories were run per  $E_r^T$ .

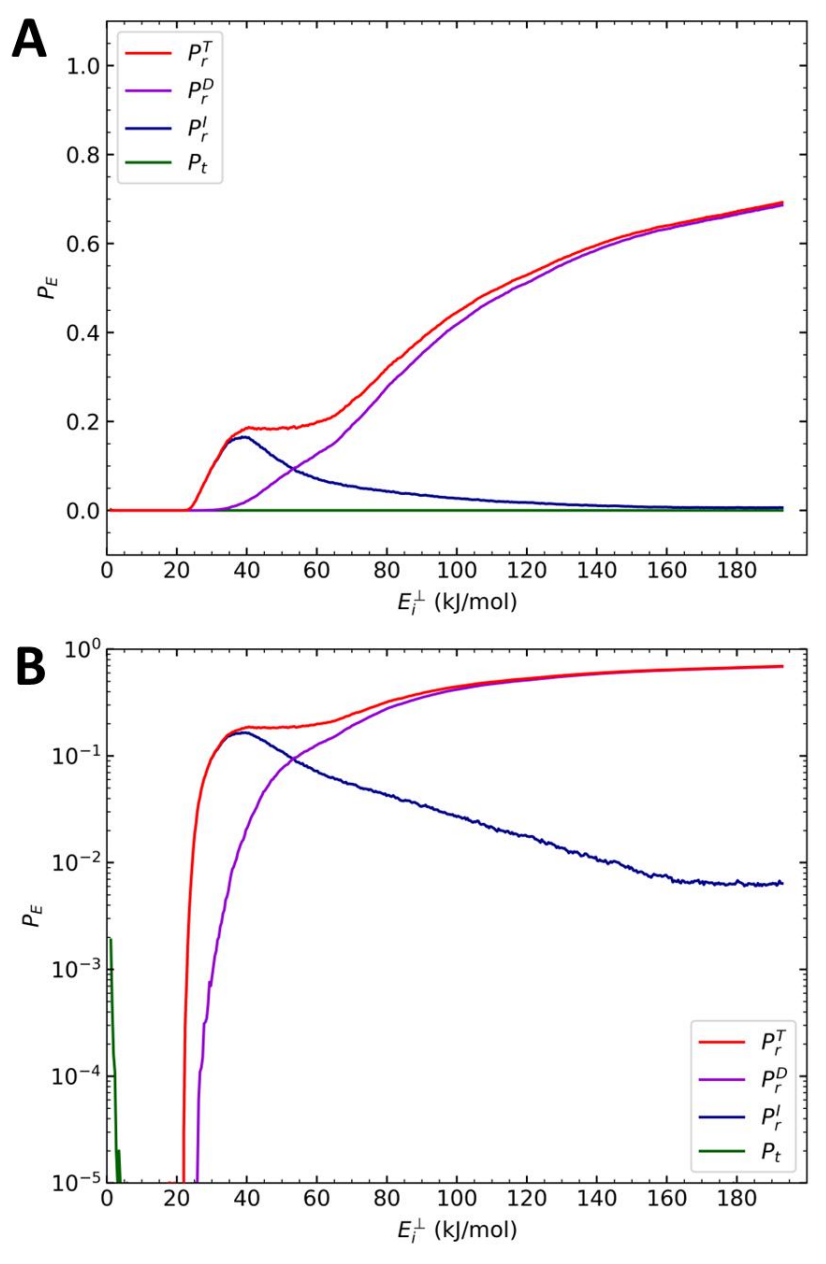


**Figure 5.4**: Decoupled event probabilities as a function of normal incidence energy;  $P_r^T$  is the total reaction probability;  $P_r^D$  is the direct reaction probability;  $P_r^D$  is the indirect reaction probability;  $P_t$  is the trapping probability;  $P_t$ : Event probability;  $P_t$ : log plot of event probability; propagation time of 1 ns per trajectory, 100k trajectories per point, point per  $E_r^D$ : 0.004 eV (0.38 kJ/mol).

**Figure 5.4** shows that, similarly to the findings of Martin-Gondre *et al.* (on Cu(100))<sup>318</sup>, there is both indirect and direct DC. The indirect reaction takes off from  $E_i^{\perp} = 22.0 \, kJ/mol$  and increases in importance up to about  $E_i^{\perp} = 39.5 \, kJ/mol$ . After this, an increase in the  $E_i^{\perp}$  leads to a decreased probability of the indirect reaction, which is reduced to~ $6\cdot10^{-3}$  at  $E_i^{\perp} = 180 \, kJ/mol$ . The direct dissociation reaction takes off at  $E_i^{\perp} = 26.0 \, kJ/mol$  and its probability slowly increases until a kink occurs at  $E_i^{\perp} = 65.0 \, kJ/mol$ , beyond which the reaction probability increases more rapidly to eventually smoothly approach an asymptotic reaction probability of about 0.7 for very high  $E_i^{\perp}$ .

The interplay of these two mechanisms means that the indirect mechanism is dominant for  $E_i^{\perp} \leq 53 \text{ kJ/mol}$  after which the direct mechanism takes over. Furthermore, this change of mechanism causes a plateau to form in the total reaction probability because the decrease of the indirect dissociation is matched roughly by the increase of the direct dissociation. As a result, the total reaction probability remained roughly constant in the range of  $E_i^{\perp} = 45 - 65 \text{ kJ/mol}$ . Furthermore, it is tempting to speculate that the dominance of the direct mechanism seen in **Figure 5.4A** (for  $E_i^{\perp} > 53 \text{ kJ/mol}$ ) could somehow be related to the observation of Cu<sub>2</sub>O formation observed in recent molecular beam experiments of Taleb et al. for incidence energies greater than 0.48 eV332(46 kJ/mol). This formation might result as a consequence of the fast dissociation of oxygen atoms resulting from direct dissociation with subsequent ballistic motion, from clean patches of Cu(111) to patches where the bulk oxide formation takes place<sup>332</sup>. However, firm theoretical evidence for this would have to come from simulations modelling subsurface adsorption and adsorption of atomic oxygen following DC, as well as bulk oxide formation. Such calculations, while certainly of high interest, would require a far larger scale, both in space and in time, than modelled here, and such a comparison is therefore outside the scope of this chapter.

Additionally, **Figure 5.4B** shows non-zero values of  $S_0$  (as seen in **Figure 5.3B**) for  $E_i^{\perp} < 5$  kJ/mol that, with the definitions we use, are attributed to trapping. The trapping probability we determined would strongly change had we used a different maximum propagation time. With a propagation time of 10 ps, it rises to 0.1, but its maximum decreases to about 0.02 for a maximum propagation

time of 100 ps, and to about 0.002 for the propagation time limit used here of 1 ns (see Figure 5.11 in Section 5.5.3). The observed trapping can thus be considered temporary. It is likely due to the physisorption of the O<sub>2</sub> molecule in the Van der Waals well observed in the elbows in Figure 5.2, as was also observed for the trapping of O<sub>2</sub> on Ag(111)<sup>162</sup>. In the relevant mechanism, the molecule is most likely trapped temporarily in the physisorption well due to energy transfer from the translational motion normal to the surface to parallel translational motion or the rotation of the molecule. As there is no mechanism for energy loss in the BOSS model, at some point, the energy flows back to the translational motion normal to the surface, and the molecule is desorbed. However, as also argued in Ref. <sup>162</sup>, the energy dissipation of the molecule needs to be modelled to describe trapping events properly. Energy dissipation of the molecule via interaction with surface atom motion is most likely 131,162,333 as electron-hole-pair excitations are less influential for larger diatomic molecules<sup>334</sup>. Trapping was not considered further here as how it proceeds here should largely be an artefact of the BOSS model used, and would not necessarily reflect reality.

The presence of the indirect mechanism for dissociation (as evident from Figure **5.4** for  $E_i^{\perp} > 22 \, kJ/mol$ ) can be supported along similar lines as argued in Ref. <sup>319</sup> by a brief look at the PES, see Figure 5.2. Ramos et al. 319 showed that the indirect mechanism was driven by O<sub>2</sub> adsorbing parallel to the surface on the bridge site, as this has the lowest barrier for adsorption. After adsorption this precursor O<sub>2</sub> could move to the FCC site where it dissociates without a second barrier<sup>319</sup>. In our case, Figure 5.2 indicates that the FCC site does have a second barrier to dissociation. However, a rotation to  $\varphi = 90^{\circ}$  (see Section 5.2.1 and Figure 5.2E) on the bridge site seems to result in a path to reaction with only a low second barrier. We do reiterate that our grid in r may not be sufficiently large to investigate such a pathway in greater detail, as also discussed in Section 5.3.1, because the expansion of the r-grid would come at very high computational costs. It may be interesting to investigate the sticking with an extended r-grid when using a DF with a lower fraction of exact exchange admixed in the exchange-correlation DF. Because such a DF may yield better agreement with experiments, it could then be worth the additional computational resources to

expand the r-grid to exclude inaccuracy in the  $S_0$  due to the present use of a small grid.

It is interesting to study whether NES is maintained for dissociative chemisorption. As such, **Figure 5.5** presents the  $\Theta$  (incidence angle) dependent reaction probability for six different constant normal incidence energies. To keep the  $E_i^{\perp}$  constant the total incidence energy ( $E_i$ ) needs to increase for increasing  $\Theta$  such that

$$E_i^{\perp} = E_i \cos^2(\Theta) \tag{5.12}.$$

**Figure 5.5** shows to what extent NES of the total dissociation probability is obeyed for different values of  $E_i^{\perp}$ . At the lowest  $E_i^{\perp}$  for which non-zero results are shown ( $24 \, kJ/mol$ ), NES is not obeyed. This appears to be due to NES not being obeyed for indirect reactions, which is the dominant reaction mechanism for this  $E_i^{\perp}$ . At the highest  $E_i^{\perp}$  for which results are shown ( $\geq 72 \, kJ/mol$ ), NES is obeyed rather well. This appears to be due to NES being obeyed for direct dissociation, which is the dominant mechanism for these high  $E_i^{\perp}$ . At the intermediate  $E_i^{\perp}$  of  $48 \, kJ/mol$ , NES is also obeyed rather well, but now this appears to be due to opposing trends of indirect and direct reaction, with the indirect reaction probability decreasing and the direct reaction probability increasing with  $\Theta$ .

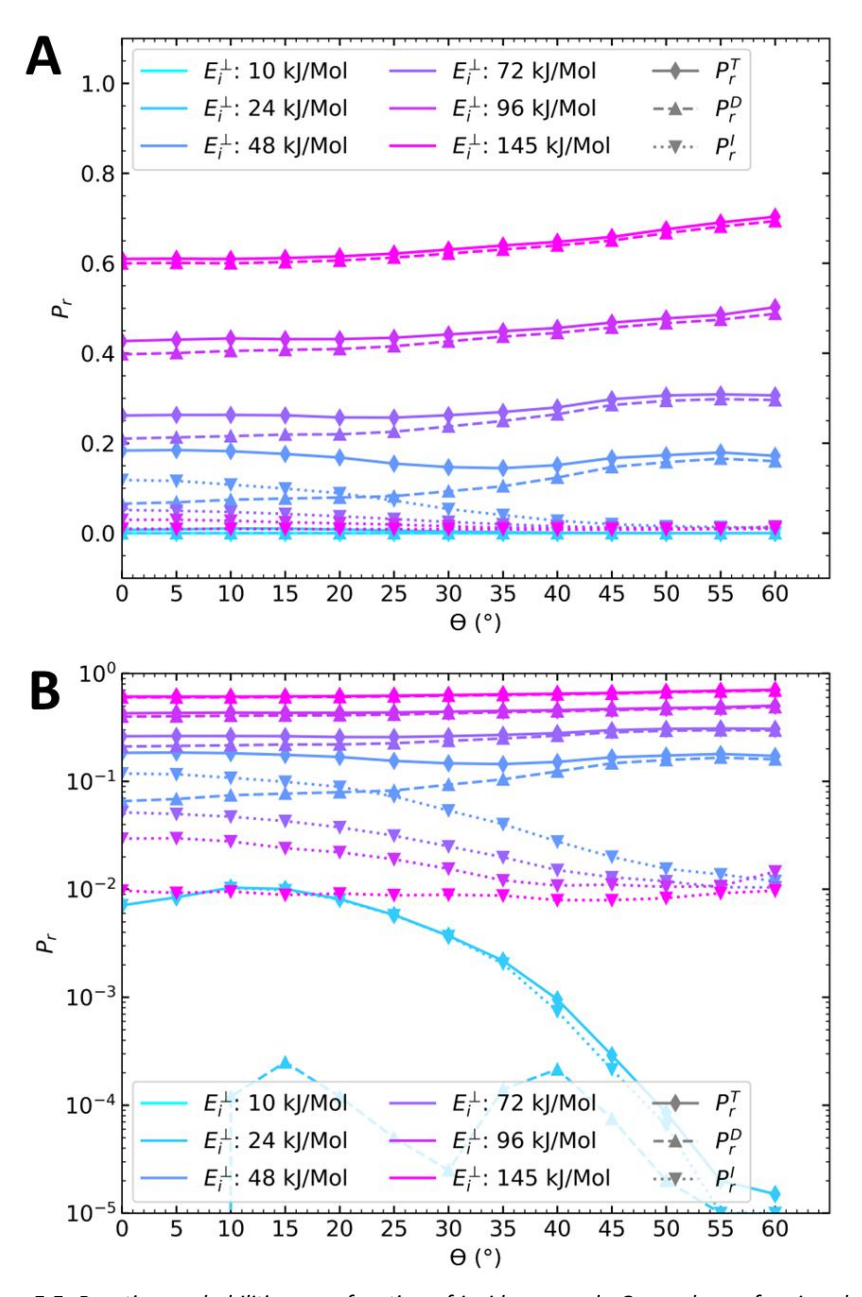


**Figure 5.5**: Reaction probabilities as a function of incidence angle  $\Theta$  are shown for six values of constant normal incidence energy  $(E_r^{\perp})$ ;  $P_r^{\top}$  is the total reaction probability,  $P_r^{D}$  is the direct reaction probability; **A**: reaction probability; **B**: Log plot of the reaction probability; **a** propagation time of 1 ns per trajectory was used, 200k trajectories were run per point.

#### 5.3.4 Discussion

To reiterate, the computed reaction probabilities for  $O_2 + Cu(111)$  using the HSE06-1/2x-vdWDF2 DF are the first DFT results that systematically underestimate the experimentally determined reaction probabilities. However, within the scope of the BOSS model, i.e., a O K static Cu(111) surface, this work also shows the possibility for both precursor-mediated dissociation as well as direct dissociation. The QCT results show that the incidence energy of  $O_2$  is a key factor in the interplay between these two mechanisms: the majority of the molecules with  $E_i^{\perp} < 53$  kJ/mol dissociate via a precursor state, but most of the molecules with  $E_i^{\perp} > 53$  kJ/mol dissociate directly. These results do not necessarily contradict the results and conclusions of Zhang  $et\ al.^{325}$ , as they explicitly stated that they could not rule out a transient, non-equilibrated molecular precursor with their experiments.

Some experiments have shown evidence for a molecular adsorbed O<sub>2</sub> species at  $T_{\rm S}$  < 160  $K^{\rm 322}$ , or indicate the possible presence of precursor-mediated dissociation for low  $T_5^{313,315}$ . These experiments are supported by previous theoretical work at the GGA level of theory that included  $T_S$  modelling<sup>319</sup>. Ramos et al. observed that for  $T_S = 100 \text{ K}$  most of  $S_0$  was non-dissociative<sup>319</sup>. We speculate based on the similarities in the shape of our PES (Section 5.3.1) and that of Ramos et al. 319 that for a PES based on the HSE06-1/2x-VdWDF2 DF, Ts may play a key role, similar to  $E_i^{\perp}$ , in the dissociation mechanism or type of  $S_0$ . Confirming this speculation would require  $T_s$  and atom surface motion to be included in the dynamics calculations. This would also be insightful for the possible trapping or physisorption at low  $E_i^{\perp}$  (Section 5.3.3).  $T_S$  and surface atom motion are also needed to reproduce the experimentally observed linear dependence of  $S_0$  on  $T_s^{325}$  and whether this linear dependency can be attributed to the recoil effect<sup>335</sup>, i.e., whether surface atom motion could help O<sub>2</sub> overcome the second barrier at higher T<sub>S</sub>, as proposed by both Hall et al. 326 and Zhang et al. 325. Therefore in future work  $T_S$  and surface atom motion need to be included for more definite conclusions on their influence on the sticking mechanisms.

Moving beyond a static surface can be difficult, especially with the already substantial computational costs involved in constructing the current static surface PES. A tried and tested method of including surface atom motion would

be to switch to a high dimensional neural-network (HDNN) PES<sup>123,303,336,337</sup>, which will allow for surface atom motion to be included in the PES. However, the training of such neural networks often requires large datasets and is a more serial process meaning that the computational expense of the hybrid HSE06-1/2x-VdWDF2 DF will make this a very time-demanding task. Another option could be the use of the GLO method, as Ramos  $et~al.^{319}$  did; this would not require any additional DFT calculations. Additionally, trying the dynamic corrugation (DCM) method, or if the sudden approximation were to be maintained the static corrugation (SCM) method, for modelling surface temperature may be an option, which was previously thoroughly and successfully tested for  $H_2 + Cu(111)^{109,110,159,160}$ .

Lastly, whilst using our current DF does not yield chemical accuracy, our results do suggest that a DF with high accuracy is within reach. The most obvious path forward is to reduce the fraction of exact exchange. As the work of Ramos et al. used a semi-local DF (i.e.,  $\alpha = 0$ ) and overestimated the reaction probabilities and this work ( $\alpha = 1/2$ ) underestimates the reaction probabilities, it seems that the truth may be somewhere in the middle. Ironically, it could turn out that the original HSE06 DF (with  $\alpha = 1/4$ ) will be a more accurate DF for this system. However, guessing the needed fraction of the exact exchange may result in a repetition of our current mistake. It may be necessary to scan more thoroughly for different allowed fractions of exact exchange  $(1/n, \text{ for } n = 2, 3, 4, 5, \text{ etc.})^{152}$  to test which one will result in the best agreement with the experiments. But we also note that scanning different fractions of exact exchange by constructing new PESs will be computationally very expensive at this moment. Thus, it may be fruitful to first test the accuracy of the non-self-consistent-field (NSCF) method as previously tested for  $O_2$  + Al(111)<sup>280</sup> (see Chapter 3). If this NSCF version produces results closely resembling the results of this chapter, it may be possible to scan across different fractions of exact exchange using the NSCF approach. Using the NSCF approach would dramatically reduce the computational costs of such a scan. From this scan, the ideal exact exchange fraction can then be estimated and used in the construction of a new fully self-consistent PES. The determination of this ideal fraction is best done in calculations also modelling  $T_s$ and surface atom motion. Otherwise agreement with experiment might come

from error cancellation, and the barrier height extracted from optimising the agreement with experiment could be incorrect.

## 5.4 Summary, conclusions, and outlook

This chapter presented the first implementation of a screened hybrid Van der Waals DF PES to quasi-classically model the sticking of  $O_2$  on Cu(111). The HSE06-1/2x-VdWDF2 DF was used to construct a 6D BOSS PES, using the CRP method to fit the DFT data. QCT calculations were performed using this PES to generate sticking probabilities for  $O_2$  + Cu(111) while simulating the experimental conditions of Zhang *et al.*<sup>325</sup>, also investigating the dependence of sticking on normal incidence energy and the angle of incidence. Furthermore, we were able to distinguish between different events in the QCT to disentangle contributions from trapping, direct, and indirect reactions.

The non-local HSE06-1/2x-VdWDF2 DF is the first DF to underestimate the sticking probability compared to experimental results. DFT studies based on semi-local GGA exchange (i.e. excluding exact exchange) always overestimated the sticking probability. This indicates that a similar screened hybrid DF with a lower fraction of exact exchange may exist that can describe the  $O_2 + Cu(111)$  dissociative chemisorption with high accuracy.

Moreover, this chapter shows evidence for the presence of two distinct mechanisms for dissociation. In our calculations, an indirect mechanism leads to dissociation of  $O_2$  when  $E_i^{\perp} > 22$  kJ/mol, becoming more important with an increase of the incidence energy up to  $E_i^{\perp} = 39.5$  kJ/mol, after which the probability of indirect reaction decreases. Meanwhile, the direct dissociative chemisorption starts to occur at  $E_i^{\perp} > 26$  kJ/mol, initially slowly but as the likelihood of the indirect mechanism decreases at higher incidence energies direct reaction eventually becomes the dominant mechanism for dissociation at  $E_i^{\perp} > 55$  kJ/mol. The interplay of the two mechanisms results in a plateau in the total reactivity of the system in the incidence energy range of 45 - 65 kJ/mol where the change of mechanism occurs from predominantly indirect to predominantly direct dissociation.

Lastly, in conjunction with other studies, this chapter suggests that the temperature of the Cu(111) surface may additionally play a key role in the interplay between the two possible mechanisms, as evidence for both has been readily found in literature but it is yet unclear which mechanism is dominant. However, the current study is unable to shine further light on the influence of surface temperature as this would require incorporating Cu surface atom motion into the PES. The computational costs of the BOSS-PES were already quite high so the proper modelling of the surface temperature effect at this level of DFT may prove challenging.

## 5.5 Appendices

The appendices contain three sections. In Section 5.5.1 the fitting of the  $O_2$  flux-weighted velocity distributions of the work of Zhang *et al.*<sup>325</sup> are presented and discussed. This section additionally presents both the resulting fitting parameters and the resulting average incidence energies. Section 5.5.2 presents one-dimensional potential energy "cuts" as a function of  $O_2$  above the surface for a constant bond length, showing the influence of molecular geometry on the Van der Waals well. Section 5.5.3 presents the log plot of the probabilities of the decoupled reactive events as a function of incidence energy of  $O_2$  for three different QCT propagation times.

## 5.5.1 Flux weighted velocity distribution fit

In the computation of sticking probabilities for comparison with supersonic molecular beam experiments, the molecular beam velocity distributions can be described by

$$N(V)dV = K_V V^3 e^{-\frac{(V - V_S)^2}{(\Delta V_S)^2}} dV$$
 (5.13),

where V is the velocity of the molecule,  $K_V$  is a normalisation constant,  $V_S$  is the stream velocity and  $\Delta V_S$  the width of the distribution width<sup>67</sup>. Additionally, the average velocity ( $V_{av}$ ) of the molecular beam can be defined as

$$V_{av} = \frac{\int V * N(V)dV}{\int N(V) dV}$$
 (5.14).

Similarly, the average energy of O<sub>2</sub> molecules in the beam can be computed using

$$E_{av} = \frac{\int \left(\frac{1}{2}m_{O2}V^2\right) * N(V)dV}{\int N(V)dV}$$
 (5.15),

where  $m_{O2}$  is the mass of the oxygen molecule.

The work of Zhang  $et~al.^{325}$  used four different  $O_2$  in He seeding ratios, resulting in four different velocity distributions. These four different velocity distributions were used in combination with different incidence angles to obtain  $S_0$  results for a range of different normal incidence energies. Below all four different distributions and the flux-weighted analytical distribution fits are plotted. The analytical fits are produced using a non-linear least squared fitting method, as implemented in the SciPy Python package. The integral for computing the average velocities and energies is based on the SciPy implementation of the quadpack fortran subroutine<sup>338</sup>.

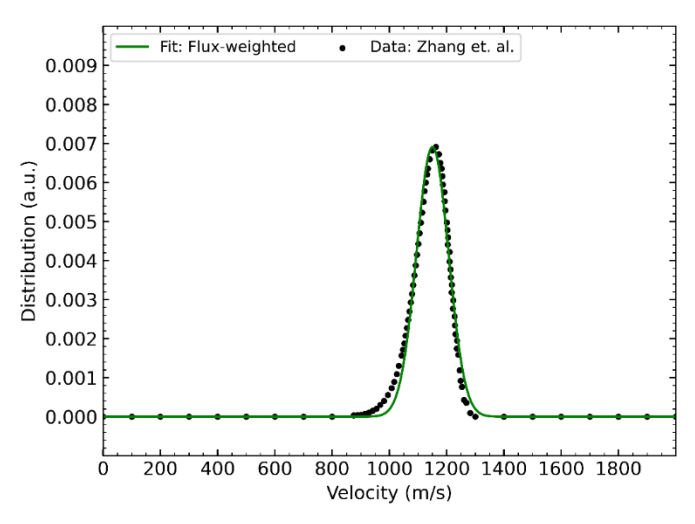


**Figure 5.6**:  $O_2$  molecular beam velocity distribution for the reported average incidence energy of 216 meV<sup>325</sup>. Black dots are the data as extracted from Ref. <sup>325</sup>, and green solid lines are the fluxweighted analytical distribution fits.

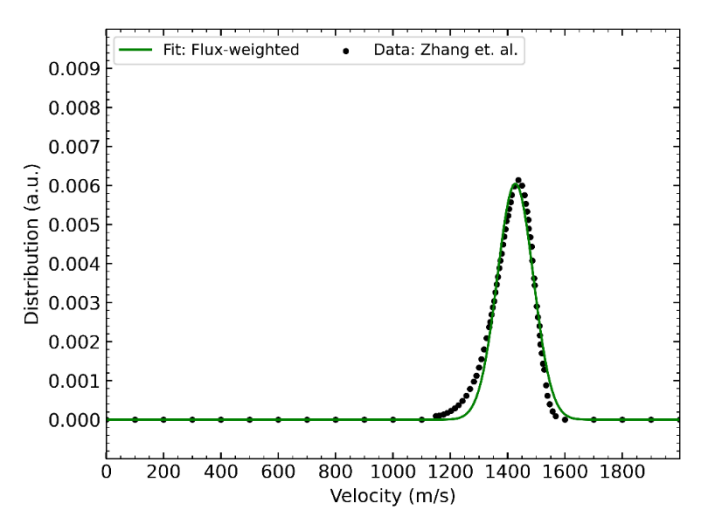


**Figure 5.7:**  $O_2$  molecular beam velocity distribution for the reported average incidence energy of 332 meV<sup>325</sup>. Black dots are the data as extracted from Ref. <sup>325</sup>, and green solid lines are the fluxweighted analytical distribution fits.

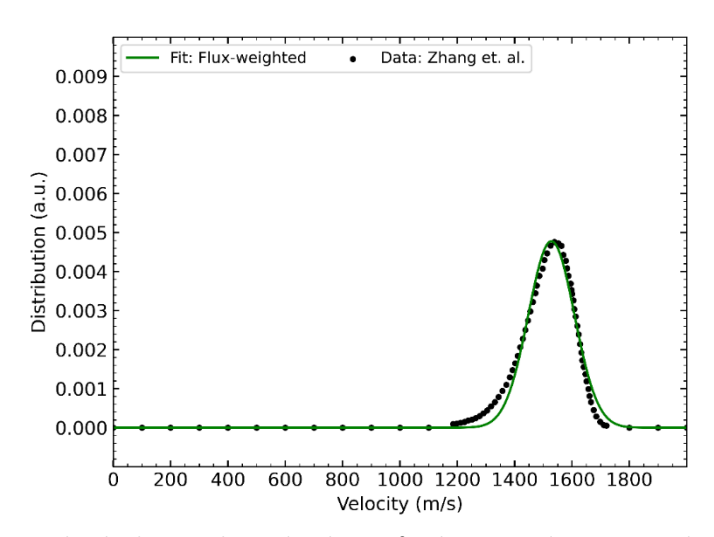


**Figure 5.8**:  $O_2$  molecular beam velocity distribution for the reported average incidence energy of 379 meV<sup>325</sup>. Black dots are the data as extracted from Ref. <sup>325</sup>, and green solid lines are the fluxweighted analytical distribution fits.

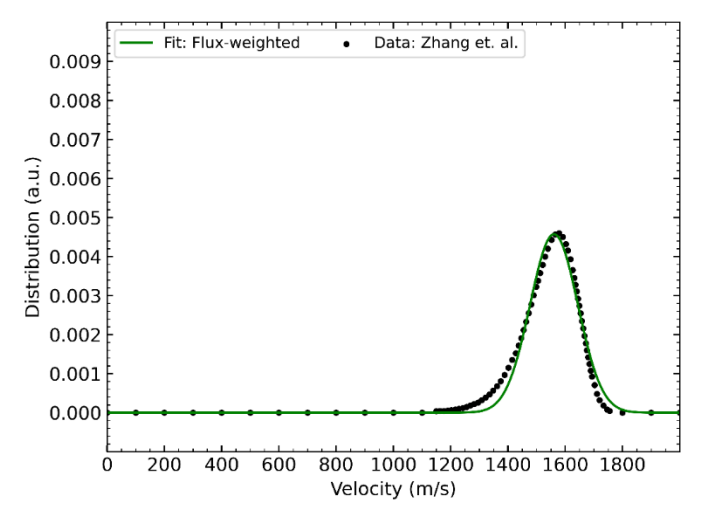


**Figure 5.9:**  $O_2$  molecular beam velocity distribution for the reported average incidence energy of 396 meV<sup>325</sup>. Black dots are the data as extracted from Ref. <sup>325</sup>, and green solid lines are the fluxweighted analytical distribution fits.

None of the four fits to the measured velocity distributions of Zhang *et al.*<sup>325</sup> are perfect. However, the average velocity and energy, peak velocity, and velocity width are all decently described by the flux-weighted fit. **Table 5.2** below shows all parameters of those fits that were used for our QCT dynamics.

**Table 5.2**: Comparison of the reported and fitted average energies of the molecular beam velocity distribution per experimental seeding ratio<sup>325</sup>. Additionally shown are the average velocities  $V_{av}$ , the fitted  $V_{sv}$   $\Delta V_{s}$  as used in the QCT dynamics, and the corresponding  $E_{s}$ , and  $\Delta E_{s}$ .

Seeding Ratios <sup>325</sup> O <sub>2</sub> /He	Reported  E <sub>av</sub> <sup>325</sup> (meV)	Fitted <i>E<sub>av</sub></i> ( <i>meV</i> )	Fitted $V_{av}$ ( $m/s$ )	Vs(m/s)	ΔVs (m/s)	Es (meV)	ΔEs (meV)
0.233	216	220.07	1150.65	1142.368	79.613	213	29.9
0.070	332	338.32	1426.98	1418.647	88.975	334	41.9
0.028	379	388.34	1528.21	1515.405	114.054	381	57.3
0.014	396	405.18	1560.92	1547.396	118.446	397	60.8

Furthermore, **Table 5.3** shows all the average normal incidence energies  $(E_i^{\perp})$  used as a result of varying the incidence angle  $\Theta$  such that:

$$E_i^{\perp} = E_i \cos{(\Theta)^2} \tag{5.16}.$$

**Table 5.3**: All normal incidence energies  $E_i^{\perp}$  in eV used per total incidence energy  $E_i$  (meV) and incidence angle  $\Theta$  in  $^{\circ}$ .

$E_i$ (meV)	<b>⊕</b> (°)	$E_{l}^{\perp}$ (eV)		
220.07	00	0.22007		
220.07	15	0.20533		
220.07	30	0.16505		
220.07	45	0.11004		
338.32	00	0.33832		
338.32	15	0.31566		
338.32	30	0.25374		
338.32	45	0.16916		
388.34	00	0.38834		
388.34	15	0.36233		
388.34	30	0.29126		
388.34	45	0.19417		
405.18	00	0.40518		
405.18	15	0.37804		
405.18	30	0.30389		
405.18	45	0.20259		

## 5.5.2 Physisorption, Van der Waals, well

The physisorption wells that most likely result from the Van der Wells (VdW) correlation are shown in **Figure 5.10** for different molecular geometries and a constant bond length. These results clearly show that the VdW-well is almost independent of the impact site of  $O_2$  on the surface for parallel orientations to the surface. However, the depth of the well is influenced by  $\theta$ , the polar orientation angle of the molecule. The well is shallower if the molecule is oriented along the surface normal, and for such orientations, the minimum of the well also occurs further away from the surface.

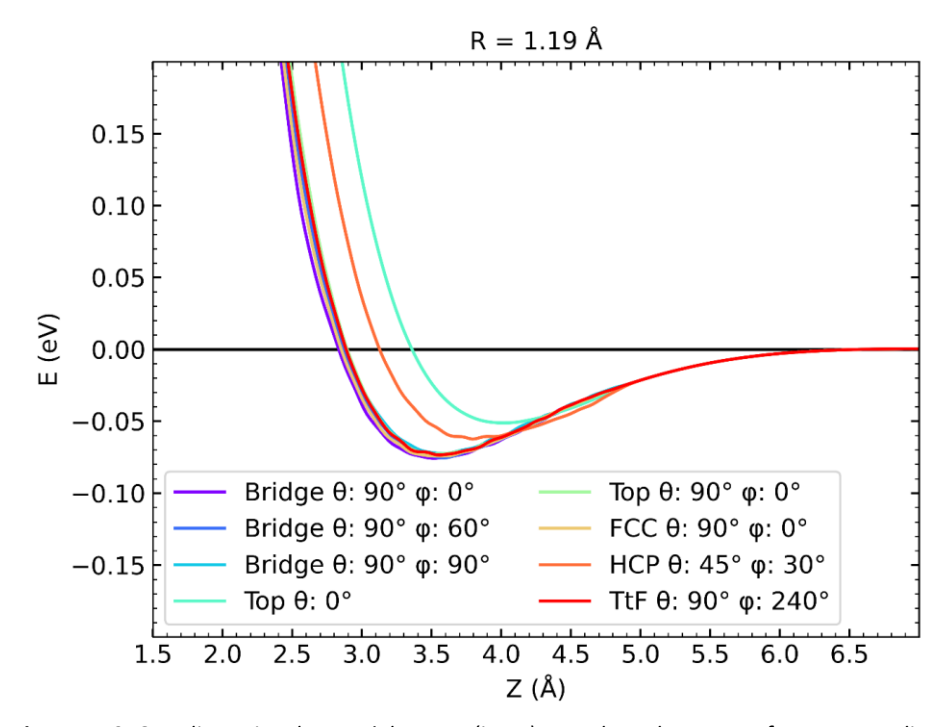


**Figure 5.10**: One-dimensional potential energy (in eV) cuts along the centre of mass Z-coordinate for an  $O_2$  bond length of 1.19 Å at different U, V-locations and for different molecular orientations  $(\theta, \varphi)$ .

## 5.5.3 Propagation-time dependent trapping

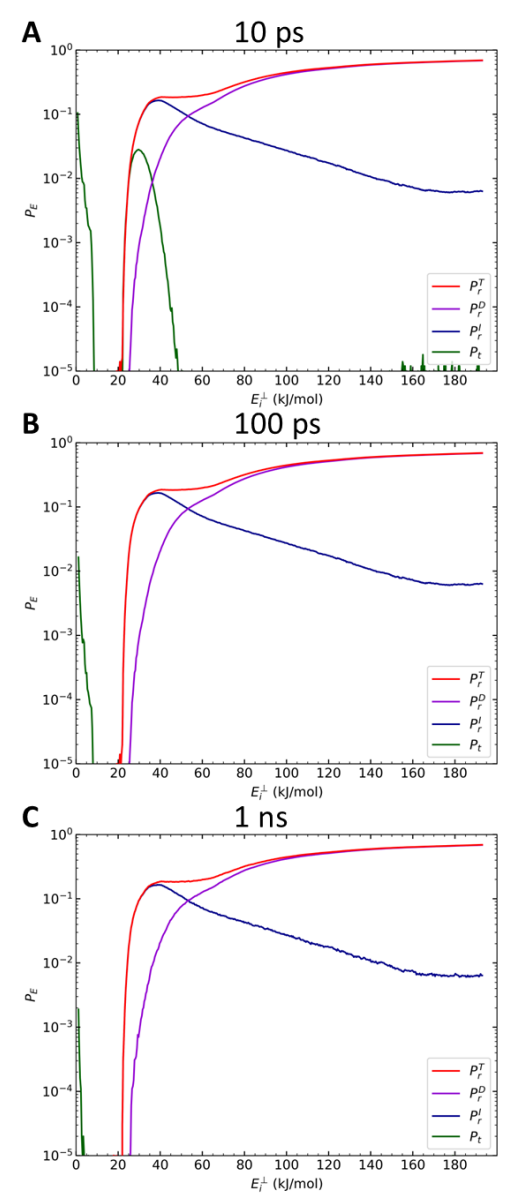


**Figure 5.11**: Log plot of the decoupled event probabilities as a function of normal incidence energy;  $P_r^T$  is the total reaction probability;  $P_r^D$  is the direct reaction probability;  $P_r^I$  is the indirect reaction probability;  $P_t$  is the trapping probability. Trajectories were run for every 4 meV (0.38 kJ/mol); **A**: 500k trajectories per  $E_r^I$ , propagation time of 10 ps; **B**: 500k trajectories per  $E_r^I$ , propagation time of 100 ps; **C**: 100k trajectories per  $E_r^I$ , propagation time of 1 ns.

## References

- (1) Ertl, G. Reactions at Surfaces: From Atoms to Complexity (Nobel Lecture). Angew. Chemie Int. Ed. 2008, 47 (19), 3524–3535. https://doi.org/10.1002/anie.200800480.
- (2) Palmer, T.; Bonner, P. L. Enzymes: Biochemistry, Biotechnology, Clinical Chemistry; Elsevier, 2007.
- (3) Braslavsky, S. E. Glossary of Terms Used in Photochemistry, 3rd Edition (IUPAC Recommendations 2006). Pure Appl. Chem. 2007, 79 (3), 293–465. https://doi.org/10.1351/pac200779030293.
- (4) Smil, V. Detonator of the Population Explosion. *Nature* 1999, 400 (6743), 415–415. https://doi.org/10.1038/22672.
- (5) Ertl, G. Primary Steps in Catalytic Synthesis of Ammonia. J. Vac. Sci. Technol. A Vacuum, Surfaces, Film. 1983, 1 (2), 1247–1253. https://doi.org/10.1116/1.572299.
- (6) Ertl, G. Elementary Steps in Heterogeneous Catalysis. Angew. Chemie Int. Ed. English 1990, 29 (11), 1219–1227. https://doi.org/10.1002/anie.199012191.
- (7) Bagot, P. A. J. Fundamental Surface Science Studies of Automobile Exhaust Catalysis. Mater. Sci. Technol. 2004, 20 (6), 679–694. https://doi.org/10.1179/026708304225016789.
- (8) van Dishoeck, E. F. Astrochemistry: Overview and Challenges. Proc. Int. Astron. Union 2017, 13 (S332), 3–22. https://doi.org/10.1017/S1743921317011528.
- (9) Catalyst. In *The IUPAC Compendium of Chemical Terminology*; International Union of Pure and Applied Chemistry (IUPAC): Research Triangle Park, NC, **2019**. https://doi.org/10.1351/goldbook.C00876.
- (10) Engel, T.; Reid, P. Physical Chemistry, 3rd ed.; Pearson Education Limited: Harlow, 2014.
- (11) Taylor, H. S. Catalysis. Encyclopedia Britannica.; 2024.
- (12) Wisniak, J. The History of Catalysis. From the Beginning to Nobel Prizes. Educ. Química 2010, 21 (1), 60–69. https://doi.org/10.1016/S0187-893X(18)30074-0.
- (13) Fulhame, E. An Essay on Combustion: With a View to a New Art of Dying and Painting: Wherein the Phlogistic and Antiphlogistic Hypotheses Are Proved Erroneous; author, 1794.
- (14) Li, Y.; Somorjai, G. A. Nanoscale Advances in Catalysis and Energy Applications. *Nano Lett.* 2010, 10 (7), 2289–2295. https://doi.org/10.1021/nl101807g.
- (15) Eley, D. D.; Haag, W. O.; Gates, B. C.; Knoezinger, H. *Advances in Catalysis*; ISSN; Elsevier Science, **1998**.
- (16) Cheng, K.; Kang, J.; King, D. L.; Subramanian, V.; Zhou, C.; Zhang, Q.; Wang, Y. Advances in Catalysis for Syngas Conversion to Hydrocarbons; 2017; pp 125–208. https://doi.org/10.1016/bs.acat.2017.09.003.
- (17) Daza, Y. A.; Kuhn, J. N. CO2 Conversion by Reverse Water Gas Shift Catalysis: Comparison of Catalysts, Mechanisms and Their Consequences for CO2 Conversion to Liquid Fuels. RSC Adv. 2016, 6 (55), 49675–49691. https://doi.org/10.1039/c6ra05414e.
- (18) Kaiser, P.; Unde, R. B.; Kern, C.; Jess, A. Production of Liquid Hydrocarbons with CO2 as Carbon Source Based on Reverse Water-Gas Shift and Fischer-Tropsch Synthesis. Chemie-Ingenieur-Technik 2013, 85 (4), 489–499. https://doi.org/10.1002/cite.201200179.
- (19) Birdja, Y. Y.; Pérez-Gallent, E.; Figueiredo, M. C.; Göttle, A. J.; Calle-Vallejo, F.; Koper, M. T. M. Advances and Challenges in Understanding the Electrocatalytic Conversion of Carbon Dioxide to Fuels. *Nat. Energy* 2019, 4 (9), 732–745. https://doi.org/10.1038/s41560-019-0450-y.
- (20) Angelici, R. J. Heterogeneous Catalysis of the Hydrodesulfurization of Thiophenes in

- Petroleum: An Organometallic Perspective of the Mechanism. *Acc. Chem. Res.* **1988**, *21* (11), 387–394. https://doi.org/10.1021/ar00155a001.
- (21) Hettinger, W. P. Contribution to Catalytic Cracking in the Petroleum Industry. *Appl. Clay Sci.* **1991**, *5* (5–6), 445–468. https://doi.org/10.1016/0169-1317(91)90017-4.
- (22) Satterfield, C. N. Heterogeneous Catalysis in Industrial Practice. 2nd Edition.
- (23) Fatima, S. S.; Zuraiqi, K.; Zavabeti, A.; Krishnamurthi, V.; Kalantar-Zadeh, K.; Chiang, K.; Daeneke, T. Current State and Future Prospects of Liquid Metal Catalysis. *Nat. Catal.* 2023, 6 (12), 1131–1139. https://doi.org/10.1038/s41929-023-01083-3.
- (24) Schlögl, R. Heterogeneous Catalysis. Angew. Chemie Int. Ed. 2015, 54 (11), 3465–3520. https://doi.org/10.1002/anie.201410738.
- (25) Fechete, I.; Wang, Y.; Védrine, J. C. The Past, Present and Future of Heterogeneous Catalysis. Catal. Today 2012, 189 (1), 2–27. https://doi.org/10.1016/j.cattod.2012.04.003.
- (26) Smith, C.; Hill, A. K.; Torrente-Murciano, L. Current and Future Role of Haber–Bosch Ammonia in a Carbon-Free Energy Landscape. *Energy Environ. Sci.* 2020, 13 (2), 331–344. https://doi.org/10.1039/C9EE02873K.
- (27) Waugh, K. C. Methanol Synthesis. Catal. Today 1992, 15 (1), 51–75. https://doi.org/10.1016/0920-5861(92)80122-4.
- (28) Rostrup-Nielsen, J. R.; Sehested, J.; Nørskov, J. K. Hydrogen and Synthesis Gas by Steamand CO2 Reforming; Advances in Catalysis; Academic Press, **2002**; Vol. 47, pp 65–139. https://doi.org/10.1016/S0360-0564(02)47006-X.
- (29) Ali, K. A.; Abdullah, A. Z.; Mohamed, A. R. Recent Development in Catalytic Technologies for Methanol Synthesis from Renewable Sources: A Critical Review. *Renew. Sustain. Energy Rev.* **2015**, *44*, 508–518. https://doi.org/10.1016/j.rser.2015.01.010.
- (30) Zhou, G.; Dai, B.; Xie, H.; Zhang, G.; Xiong, K.; Zheng, X. CeCu Composite Catalyst for CO Synthesis by Reverse Water-Gas Shift Reaction: Effect of Ce/Cu Mole Ratio. *J. CO2 Util.* 2017, 21 (April), 292–301. https://doi.org/10.1016/j.jcou.2017.07.004.
- (31) Chen, C. S. S.; Cheng, W. H. H.; Lin, S. S. S. Mechanism of CO Formation in Reverse Water-Gas Shift Reaction over Cu/Al2O3 Catalyst. *Catal. Letters* **2000**, *68* (1–2), 45–48. https://doi.org/10.1023/A:1019071117449.
- (32) Bustamante, F.; Enick, R. M. M.; Cugini, A. V. V.; Killmeyer, R. P. P.; Howard, B. H. H.; Rothenberger, K. S. S.; Ciocco, M. V. V.; Morreale, B. D. D.; Chattopadhyay, S.; Shi, S. High-Temperature Kinetics of the Homogeneous Reverse Water-Gas Shift Reaction. AIChE J. 2004, 50 (5), 1028–1041. https://doi.org/10.1002/aic.10099.
- (33) Iglesia, E. Design, Synthesis, and Use of Cobalt-Based Fischer-Tropsch Synthesis Catalysts. *Appl. Catal. A Gen.* **1997**, *161* (1–2), 59–78. https://doi.org/10.1016/S0926-860X(97)00186-5.
- (34) Dry, M. E. The Fischer Tropsch Process: 1950 2000. **2002**, 71, 227–241.
- (35) Jager, B.; Espinoza, R. Advances in Low Temperature Fischer-Tropsch Synthesis. *Catal. Today* **1995**, *23* (1), 17–28. https://doi.org/10.1016/0920-5861(94)00136-P.
- (36) Schulz, H. Short History and Present Trends of Fischer-Tropsch Synthesis. *Appl. Catal. A Gen.* **1999**, *186* (1–2), 3–12. https://doi.org/10.1016/S0926-860X(99)00160-X.
- (37) Weckhuysen, B. M. Determining the Active Site in a Catalytic Process: Operando Spectroscopy Is More than a Buzzword. *Phys. Chem. Chem. Phys.* **2003**, *5* (20), 4351. https://doi.org/10.1039/b309650p.
- (38) Bentrup, U. Combining in Situ Characterization Methods in One Set-up: Looking with More Eyes into the Intricate Chemistry of the Synthesis and Working of Heterogeneous Catalysts. *Chem. Soc. Rev.* **2010**, *39* (12), 4718. https://doi.org/10.1039/b919711g.
- (39) Zambelli, T.; Barth, J. V. V.; Wintterlin, J.; Ertl, G. Complex Pathways in Dissociative Adsorption of Oxygen on Platinum. *Nature* **1997**, *390* (6659), 495–497.

- https://doi.org/10.1038/37329.
- (40) Diebold, U. The Surface Science of Titanium Dioxide. Surf. Sci. Rep. 2003, 48 (5–8), 53–229. https://doi.org/10.1016/S0167-5729(02)00100-0.
- (41) Diebold, U.; Li, S.-C.; Schmid, M. Oxide Surface Science. Annu. Rev. Phys. Chem. 2010, 61
   (1), 129–148. https://doi.org/10.1146/annurev.physchem.012809.103254.
- (42) Oura, K.; Lifshits, V. G.; Saranin, A. A.; Zotov, A. V; Katayama, M. *Surface Science: An Introduction*; Advanced Texts in Physics; Springer Berlin Heidelberg, **2013**.
- (43) Markovic, N. Surface Science Studies of Model Fuel Cell Electrocatalysts. Surf. Sci. Rep. 2002, 45 (4–6), 117–229. https://doi.org/10.1016/S0167-5729(01)00022-X.
- (44) Somorjai, G. A. Modern Surface Science and Surface Technologies: An Introduction. *Chem. Rev.* **1996**, *96* (4), 1223–1236. https://doi.org/10.1021/cr950234e.
- (45) Zaera, F. The Surface Chemistry of Metal-Based Hydrogenation Catalysis. ACS Catal. 2017, 7 (8), 4947–4967. https://doi.org/10.1021/acscatal.7b01368.
- (46) Kiselev, V. F.; Krylov, O. V. *Adsorption and Catalysis on Transition Metals and Their Oxides*; Springer Series in Surface Sciences; Springer Berlin Heidelberg, **2012**.
- (47) Kittel, C.; McEuen, P. Introduction to Solid State Physics; Wiley, 2018.
- (48) Britannica, T. E. of E. The Fermi-Level. Encyclopedia Britannica; 2006.
- (49) Cantor, B. The Fermi Level. In *The Equations of Materials*; Oxford University Press, **2020**; pp 267–300. https://doi.org/10.1093/oso/9780198851875.003.0013.
- (50) Somorjai, G. A.; York, R. L.; Butcher, D.; Park, J. Y. The Evolution of Model Catalytic Systems; Studies of Structure, Bonding and Dynamics from Single Crystal Metal Surfaces to Nanoparticles, and from Low Pressure (<10 –3 Torr) to High Pressure (>10 –3 Torr) to Liquid Interfaces. *Phys. Chem. Chem. Phys.* **2007**, *9* (27), 3500–3513. https://doi.org/10.1039/B618805B.
- (51) Auras, S. V.; van Bree, R. A. B.; Bashlakov, D. L.; van Lent, R.; Juurlink, L. B. F. It's Not Just the Defects – a Curved Crystal Study of H 2 O Desorption from Ag. *Phys. Chem. Chem. Phys.* 2019, 21 (28), 15422–15430. https://doi.org/10.1039/C9CP02609F.
- (52) Ashcroft, N. W.; Mermin, N. D. Solid State Physics; Cengage Learning, 2011.
- (53) Horuiti, J.; Polanyi, M. Catalytic Interchange of Hydrogen between Water and Ethylene and between Water and Benzene. *Nature* **1934**, *134* (3384), 377–378. https://doi.org/10.1038/134377b0.
- (54) Horiuti, I.; Polanyi, M. Exchange Reactions of Hydrogen on Metallic Catalysts. *Trans. Faraday Soc.* **1934**, *30*, 1164. https://doi.org/10.1039/tf9343001164.
- (55) Kroes, G.-J.; Díaz, C. Quantum and Classical Dynamics of Reactive Scattering of H 2 from Metal Surfaces. Chem. Soc. Rev. 2016, 45 (13), 3658–3700. https://doi.org/10.1039/C5CS00336A.
- (56) Kroes, G.-J. Computational Approaches to Dissociative Chemisorption on Metals: Towards Chemical Accuracy. *Phys. Chem. Chem. Phys.* 2021, 23 (15), 8962–9048. https://doi.org/10.1039/D1CP00044F.
- (57) Muller, P. Glossary of Terms Used in Physical Organic Chemistry (IUPAC Recommendations 1994). Pure Appl. Chem. 1994, 66 (5), 1077–1184. https://doi.org/10.1351/pac199466051077.
- (58) Jackson, J. M.; Howarth, A. Exchange of Energy between Diatomic Gas Molecules and a Solid Surface. *Proc. R. Soc. London. Ser. A Math. Phys. Sci.* **1935**, *152* (877), 515–529. https://doi.org/10.1098/rspa.1935.0206.
- (59) Shenvi, N.; Roy, S.; Tully, J. C. Dynamical Steering and Electronic Excitation in NO Scattering from a Gold Surface. *Science* (80-. ). 2009, 326 (5954), 829–832. https://doi.org/10.1126/science.1179240.
- (60) Bunermann, O.; Jiang, H.; Dorenkamp, Y.; Kandratsenka, A.; Janke, S. M.; Auerbach, D. J.; Wodtke, A. M. Electron-Hole Pair Excitation Determines the Mechanism of Hydrogen

- Atom Adsorption. *Science* (80-. ). **2015**, 350 (6266), 1346–1349. https://doi.org/10.1126/science.aad4972.
- (61) Blanco-Rey, M.; Juaristi, J. I.; Díez Muiño, R.; Busnengo, H. F.; Kroes, G. J.; Alducin, M. Electronic Friction Dominates Hydrogen Hot-Atom Relaxation on Pd(100). Phys. Rev. Lett. 2014, 112 (10), 1–5. https://doi.org/10.1103/PhysRevLett.112.103203.
- (62) Estermann, I.; Stern, O. Beugung von Molekularstrahlen. *Zeitschrift fur Phys.* **1930**, *61* (1–2), 95–125. https://doi.org/10.1007/BF01340293.
- (63) Singh, R. C. V. Raman and the Discovery of the Raman Effect. Phys. Perspect. 2002, 4 (4), 399–420. https://doi.org/10.1007/s000160200002.
- (64) Heisenberg, W. Ober Den Anschaulichen Inhalt Der Quantentheoretischen Kinematik Und Mechanik. Zeitschrift fur Phys. Phys. 1927, 43 (3–4), 172–198. https://doi.org/10.1007/BF01397280.
- (65) Cao, K.; van Lent, R.; Kleyn, A. W.; Kurahashi, M.; Juurlink, L. B. F. Steps on Pt Stereodynamically Filter Sticking of O2. *Proc. Natl. Acad. Sci. U. S. A.* 2019, 116 (28), 13862–13866. https://doi.org/10.1073/pnas.1902846116.
- (66) Kroes, G.-J. Toward a Database of Chemically Accurate Barrier Heights for Reactions of Molecules with Metal Surfaces. J. Phys. Chem. Lett. 2015, 6 (20), 4106–4114. https://doi.org/10.1021/acs.jpclett.5b01344.
- (67) Michelsen, H. A.; Auerbach, D. J. A Critical Examination of Data on the Dissociative Adsorption and Associative Desorption of Hydrogen at Copper Surfaces. J. Chem. Phys. 1991, 94 (11), 7502–7520. https://doi.org/10.1063/1.460182.
- (68) Michelsen, H. A.; Rettner, C. T.; Auerbach, D. J.; Zare, R. N. Effect of Rotation on the Translational and Vibrational Energy Dependence of the Dissociative Adsorption of D2 on Cu(111). J. Chem. Phys. 1993, 98 (10), 8294–8307. https://doi.org/10.1063/1.464535.
- (69) King, D. A.; Wells, M. G. Molecular Beam Investigation of Adsorption Kinetics on Bulk Metal Targets: Nitrogen on Tungsten. Surf. Sci. 1972, 29 (2), 454–482. https://doi.org/10.1016/0039-6028(72)90232-4.
- (70) Kleyn, A. W. Molecular Beams and Chemical Dynamics at Surfaces. Chem. Soc. Rev. 2003. 32 (2), 87–95. https://doi.org/10.1039/b105760i.
- (71) Luntz, A. C.; Brown, J. K.; Williams, M. D. Molecular Beam Studies of H 2 and D 2 Dissociative Chemisorption on Pt(111). *J. Chem. Phys.* **1990**, *93* (7), 5240–5246. https://doi.org/10.1063/1.459669.
- (72) Balooch, M.; Cardillo, M. J.; Miller, D. R.; Stickney, R. E. Molecular Beam Study of the Apparent Activation Barrier Associated with Adsorption and Desorption of Hydrogen on Copper. Surf. Sci. 1974, 46 (2), 358–392. https://doi.org/10.1016/0039-6028(74)90315-X.
- (73) Kurahashi, M.; Yamauchi, Y. Production of a Single Spin-Rotational State [(J,M)=(2,2)] Selected Molecular Oxygen (Σ3g-) Beam by a Hexapole Magnet. *Rev. Sci. Instrum.* 2009, 80 (8), 083103. https://doi.org/10.1063/1.3206299.
- (74) Yoder, B. L.; Bisson, R.; Beck, R. D. Steric Effects in the Chemisorption of Vibrationally Excited Methane on Ni(100). Science (80-. ). 2010, 329 (5991), 553–556. https://doi.org/10.1126/science.1191751.
- (75) Vattuone, L.; Savio, L.; Pirani, F.; Cappelletti, D.; Okada, M.; Rocca, M. Interaction of Rotationally Aligned and of Oriented Molecules in Gas Phase and at Surfaces. *Prog. Surf. Sci.* **2010**, *85* (1–4), 92–160. https://doi.org/10.1016/j.progsurf.2009.12.001.
- (76) Chadwick, H.; Somers, M. F.; Stewart, A. C.; Alkoby, Y.; Carter, T. J. D.; Butkovicova, D.; Alexandrowicz, G. Stopping Molecular Rotation Using Coherent Ultra-Low-Energy Magnetic Manipulations. *Nat. Commun.* 2022, *13* (1), 2287. https://doi.org/10.1038/s41467-022-29830-3.

- (77) Hanbicki, A. T.; Baddorf, A. P.; Plummer, E. W.; Hammer, B.; Scheffler, M. The Interaction of Hydrogen with the (110) Surface of NiAl. Surf. Sci. 1995, 331–333, 811– 817. https://doi.org/10.1016/0039-6028(95)00376-2.
- (78) Smith, R. S.; Huang, C.; Wong, E. K. L.; Kay, B. D. The Molecular Volcano: Abrupt CCl4 Desorption Driven by the Crystallization of Amorphous Solid Water. *Phys. Rev. Lett.* 1997, 79 (5), 909–912. https://doi.org/10.1103/PhysRevLett.79.909.
- (79) Henzler, M. LEED-Investigation of Step Arrays on Cleaved Germanium (111) Surfaces. *Surf. Sci.* **1970**, *19* (1), 159–171. https://doi.org/10.1016/0039-6028(70)90115-9.
- (80) Van Hove, M. A.; Somorjai, G. A. A New Microfacet Notation for High-Miller-Index Surfaces of Cubic Materials with Terrace, Step and Kink Structures. Surf. Sci. 1980, 92 (2–3), 489–518. https://doi.org/10.1016/0039-6028(80)90219-8.
- (81) Chang, C. C. Auger Electron Spectroscopy. Surf. Sci. 1971, 25 (1), 53–79. https://doi.org/10.1016/0039-6028(71)90210-X.
- (82) Mathieu, H. J. Surface Analysis The Principal Techniques; Vickerman, J. C., Gilmore, I. S., Eds.; Wiley, 2009. https://doi.org/10.1002/9780470721582.
- (83) Wagner, C. D.; Zatko, D. A.; Raymond, R. H. Use of the Oxygen KLL Auger Lines in Identification of Surface Chemical States by Electron Spectroscopy for Chemical Analysis. Anal. Chem. 1980, 52 (9), 1445–1451. https://doi.org/10.1021/ac50059a017.
- (84) Mathieu, H. J.; Landolt, D. Quantitative Auger Electron Spectroscopy Analysis of Ag-Pd and Ni-Pd Alloys. Surf. Sci. 1975, 53 (1), 228–240. https://doi.org/10.1016/0039-6028(75)90126-0.
- (85) Hall, P. M.; Morabito, J. M. Matrix Effects in Quantitative Auger Analysis of Dilute Alloys. Surf. Sci. 1979, 83 (2), 391–405. https://doi.org/10.1016/0039-6028(79)90052-9.
- (86) Hall, P. M.; Morabito, J. M.; Conley, D. K. Relative Sensitivity Factors for Quantitative Auger Analysis of Binary Alloys. Surf. Sci. 1977, 62 (1), 1–20. https://doi.org/10.1016/0039-6028(77)90424-1.
- (87) Langeron, J. P.; Minel, L.; Vignes, J. L.; Bouquet, S.; Pellerin, F.; Lorang, G.; Ailloud, P.; Le Héricy, J. An Important Step in Quantitative Auger Analysis: The Use of Peak to Background Ratio. Surf. Sci. 1984, 138 (2–3), 610–628. https://doi.org/10.1016/0039-6028(84)90269-3.
- (88) Shimizu, R. Quantitative Analysis by Auger Electron Spectroscopy. *Jpn. J. Appl. Phys.* **1983**, *22* (11R), 1631. https://doi.org/10.1143/JJAP.22.1631.
- (89) Liday, J.; Hofmann, S.; Harman, R. Quantitative Auger Electron Analysis of Homogeneous Binary Alloys of Cr, Fe and Ni. Vacuum 1992, 43 (4), 331–339. https://doi.org/10.1016/0042-207X(92)90166-T.
- (90) Siegbahn, K.; Edvarson, K. β-Ray Spectroscopy in the Precision Range of 1: 105. Nucl. Phys. 1956, 1 (8), 137–159. https://doi.org/10.1016/S0029-5582(56)80022-9.
- (91) Andrade, J. D. X-Ray Photoelectron Spectroscopy (XPS). In Surface and Interfacial Aspects of Biomedical Polymers; Springer US: Boston, MA, 1985; pp 105–195. https://doi.org/10.1007/978-1-4684-8610-0\_5.
- (92) Powell, C. J.; Seah, M. P. Precision, Accuracy, and Uncertainty in Quantitative Surface Analyses by Auger-Electron Spectroscopy and x-Ray Photoelectron Spectroscopy. *J. Vac. Sci. Technol. A Vacuum, Surfaces, Film.* **1990**, *8* (2), 735–763. https://doi.org/10.1116/1.576956.
- (93) Fadley, C. S. X-Ray Photoelectron Spectroscopy: Progress and Perspectives. *J. Electron Spectros. Relat. Phenomena* **2010**, *178–179* (C), 2–32. https://doi.org/10.1016/j.elspec.2010.01.006.
- (94) Greczynski, G.; Hultman, L. X-Ray Photoelectron Spectroscopy: Towards Reliable Binding Energy Referencing. *Prog. Mater. Sci.* **2020**, *107*, 100591. https://doi.org/10.1016/j.pmatsci.2019.100591.

- (95) Schatz, G. C.; Wodtke, A. M.; Yang, X. Spiers Memorial Lecture: New Directions in Molecular Scattering. Faraday Discuss. 2024, 251, 9–62. https://doi.org/10.1039/D4FD00015C.
- (96) Laidler, K. J. A Glossary of Terms Used in Chemical Kinetics, Including Reaction Dynamics (IUPAC Recommendations 1996). Pure Appl. Chem. 1996, 68 (1), 149–192. https://doi.org/10.1351/pac199668010149.
- (97) Binnig, G.; Rohrer, H.; Gerber, C.; Weibel, E. Surface Studies by Scanning Tunneling Microscopy. *Phys. Rev. Lett.* **1982**, *49* (1), 57–61. https://doi.org/10.1103/PhysRevLett.49.57.
- (98) Binnig, G.; Rohrer, H. Scanning Tunneling Microscopy. *Surf. Sci.* **1983**, *126* (1–3), 236–244. https://doi.org/10.1016/0039-6028(83)90716-1.
- (99) Chen, C. J. Scanning Tunneling Microscopy: A Chemical Perspective. *Scanning Microsc.* **1993**, *7* (3), 793–804.
- (100) Chen, C. J. Introduction to Scanning Tunneling Microscopy; Oxford University PressOxford, 2007. https://doi.org/10.1093/acprof:oso/9780199211500.001.0001.
- (101) Laegsgaard, E.; Österlund, L.; Thostrup, P.; Rasmussen, P. B.; Stensgaard, I.;
   Besenbacher, F. A High-Pressure Scanning Tunneling Microscope. *Rev. Sci. Instrum.* 2001, 72 (9), 3537–3542. https://doi.org/10.1063/1.1389497.
- (102) Rößler, M.; Geng, P.; Wintterlin, J. A High-Pressure Scanning Tunneling Microscope for Studying Heterogeneous Catalysis. *Rev. Sci. Instrum.* 2005, 76 (2). https://doi.org/10.1063/1.1841951.
- (103) Tao, F.; Tang, D.; Salmeron, M.; Somorjai, G. A. A New Scanning Tunneling Microscope Reactor Used for High-Pressure and High-Temperature Catalysis Studies. *Rev. Sci. Instrum.* **2008**, *79* (8). https://doi.org/10.1063/1.2960569.
- (104) Herbschleb, C. T.; van der Tuijn, P. C.; Roobol, S. B.; Navarro, V.; Bakker, J. W.; Liu, Q.; Stoltz, D.; Cañas-Ventura, M. E.; Verdoes, G.; van Spronsen, M. A.; Bergman, M.; Crama, L.; Taminiau, I.; Ofitserov, A.; van Baarle, G. J. C.; Frenken, J. W. M. The ReactorSTM: Atomically Resolved Scanning Tunneling Microscopy under High-Pressure, High-Temperature Catalytic Reaction Conditions. *Rev. Sci. Instrum.* 2014, 85 (8). https://doi.org/10.1063/1.4891811.
- (105) Prabhu, M. K.; Boden, D.; Rost, M. J.; Meyer, J.; Groot, I. M. N. Structural Characterization of a Novel Two-Dimensional Material: Cobalt Sulfide Sheets on Au(111). J. Phys. Chem. Lett. 2020, 11 (21), 9038–9044. https://doi.org/10.1021/acs.jpclett.0c02268.
- (106) Wenzel, S.; Groot, I. M. N. ZnO (1010) Is Unstable in Moderate Pressures of Water. *Surf. Sci.* **2022**, *715*, 121940. https://doi.org/10.1016/j.susc.2021.121940.
- (107) Wenzel, S.; Boden, D.; van Lent, R.; Motaee, E.; Prabhu, M. K.; Achour, H.; Groot, I. M. N. Spectroscopic Investigation of a Co(0001) Model Catalyst during Exposure to H 2 and CO at near-Ambient Pressures. *Phys. Chem. Chem. Phys.* 2023, 25 (37), 25094–25104. https://doi.org/10.1039/D3CP02739B.
- (108) Chadwick, H.; Alexandrowicz, G. Temperature Dependent Stereodynamics in Surface Scattering Measured through Subtle Changes in the Molecular Wave Function. Faraday Discuss. 2024, 251, 76–91. https://doi.org/10.1039/D4FD00007B.
- (109) Smits, B.; Somers, M. F. The Quantum Dynamics of H2 on Cu(111) at a Surface Temperature of 925 K: Comparing State-of-the-Art Theory to State-of-the-Art Experiments 2. J. Chem. Phys. 2023, 158 (1), 014704. https://doi.org/10.1063/5.0134817.
- (110) Smits, B.; Somers, M. F. The Quantum Dynamics of H2 on Cu(111) at a Surface Temperature of 925 K: Comparing State-of-the-Art Theory to State-of-the-Art Experiments. J. Chem. Phys. 2022, 157 (13), 134704.

- https://doi.org/10.1063/5.0112036.
- (111) Wodtke, A. M. Chemistry in a Computer: Advancing the in Silico Dream. *Science (80-. ).* **2006**, *312* (5770), 64–65. https://doi.org/10.1126/science.1124924.
- (112) Cramer, C. J. Essentials of Computational Chemistry Theories and Models, 2nd ed.; John Wiley & Sons, Ltd, 2017.
- (113) Doblhoff-Dier, K.; Meyer, J.; Hoggan, P. E.; Kroes, G.-J.; Wagner, L. K. Diffusion Monte Carlo for Accurate Dissociation Energies of 3d Transition Metal Containing Molecules. J. Chem. Theory Comput. 2016, 12 (6), 2583–2597. https://doi.org/10.1021/acs.jctc.6b00160.
- (114) Doblhoff-Dier, K.; Meyer, J.; Hoggan, P. E.; Kroes, G.-J. Quantum Monte Carlo Calculations on a Benchmark Molecule—Metal Surface Reaction: H 2 + Cu(111). *J. Chem. Theory Comput.* **2017**, *13* (7), 3208–3219. https://doi.org/10.1021/acs.jctc.7b00344.
- (115) Powell, A. D.; Gerrits, N.; Tchakoua, T.; Somers, M. F.; Busnengo, H. F.; Meyer, J.; Kroes, G.; Doblhoff-Dier, K. Best-of-Both-Worlds Predictive Approach to Dissociative Chemisorption on Metals. J. Phys. Chem. Lett. 2024, 307–315. https://doi.org/10.1021/acs.jpclett.3c02972.
- (116) Zhao, Q.; Zhang, X.; Martirez, J. M. P.; Carter, E. A. Benchmarking an Embedded Adaptive Sampling Configuration Interaction Method for Surface Reactions:
   H2Desorption from and CH4Dissociation on Cu(111). J. Chem. Theory Comput. 2020, 16 (11), 7078–7088. https://doi.org/10.1021/acs.jctc.0c00341.
- (117) Born, M.; Oppenheimer, R. Zur Quantentheorie Der Molekeln. Ann. Phys. 1927, 389 (20), 457–484. https://doi.org/10.1002/andp.19273892002.
- (118) Filot, I. A. W. Elements of Electronic Structure Theory, 1st ed.; 2022.
- (119) Sherrill, C. D. The Born-Oppenheimer Approximation. Sch. Chem. Biochem. Georg. Inst. Technol. 2005, 242.
- (120) Dewar, M. J. S.; Kelemen, J. LCAO MO Theory Illustrated by Its Application to H2. *J. Chem. Educ.* **1971**, *48* (8), 494. https://doi.org/10.1021/ed048p494.
- (121) Hohenberg, P.; Kohn, W. Inhomogeneous Electron Gas. Phys. Rev. 1964, 136 (3B), B864–B871. https://doi.org/10.1103/PhysRev.136.B864.
- Kohn, W.; Sham, L. J. Self-Consistent Equations Including Exchange and Correlation Effects. *Phys. Rev.* **1965**, *140* (4A), A1133–A1138. https://doi.org/10.1103/PhysRev.140.A1133.
- (123) Gerrits, N.; Shakouri, K.; Behler, J.; Kroes, G.-J. Accurate Probabilities for Highly Activated Reaction of Polyatomic Molecules on Surfaces Using a High-Dimensional Neural Network Potential: CHD 3 + Cu(111). *J. Phys. Chem. Lett.* **2019**, *10* (8), 1763–1768. https://doi.org/10.1021/acs.jpclett.9b00560.
- (124) Gerrits, N.; Smeets, E. W. F.; Vuckovic, S.; Powell, A. D.; Doblhoff-Dier, K.; Kroes, G.-J. Density Functional Theory for Molecule–Metal Surface Reactions: When Does the Generalized Gradient Approximation Get It Right, and What to Do If It Does Not. J. Phys. Chem. Lett. 2020, 11 (24), 10552–10560. https://doi.org/10.1021/acs.jpclett.0c02452.
- (125) Gerrits, N.; Geweke, J.; Smeets, E. W. F.; Voss, J.; Wodtke, A. M.; Kroes, G.-J. Closing the Gap Between Experiment and Theory: Reactive Scattering of HCl from Au(111). *J. Phys. Chem. C* 2020, 124 (29), 15944–15960. https://doi.org/10.1021/acs.jpcc.0c03756.
- (126) Smeets, E. W. F.; Kroes, G.-J. Designing New SRP Density Functionals Including Non-Local VdW-DF2 Correlation for H 2 + Cu(111) and Their Transferability to H 2 + Ag(111), Au(111) and Pt(111). Phys. Chem. Chem. Phys. 2021, 23 (13), 7875–7901. https://doi.org/10.1039/D0CP05173J.
- (127) Tchakoua, T.; Smeets, E. W. F.; Somers, M.; Kroes, G.-J. Toward a Specific Reaction Parameter Density Functional for H 2 + Ni(111): Comparison of Theory with Molecular Beam Sticking Experiments. J. Phys. Chem. C 2019, 123 (33), 20420–20433.

- https://doi.org/10.1021/acs.jpcc.9b05928.
- (128) Smeets, E. W. F.; Voss, J.; Kroes, G.-J. Specific Reaction Parameter Density Functional Based on the Meta-Generalized Gradient Approximation: Application to H 2 + Cu(111) and H 2 + Ag(111). J. Phys. Chem. A 2019, 123 (25), 5395–5406. https://doi.org/10.1021/acs.ipca.9b02914.
- (129) Tchakoua, T.; Gerrits, N.; Smeets, E. W. F.; Kroes, G.-J. SBH17: Benchmark Database of Barrier Heights for Dissociative Chemisorption on Transition Metal Surfaces. J. Chem. Theory Comput. 2023, 19 (1), 245–270. https://doi.org/10.1021/acs.jctc.2c00824.
- (130) Smeets, E. W. F.; Kroes, G. J. Performance of Made Simple Meta-GGA Functionals with RVV10 Nonlocal Correlation for H2 + Cu(111), D2 + Ag(111), H2 + Au(111), and D2 + Pt(111). J. Phys. Chem. C 2021, 125 (17), 8993–9010. https://doi.org/10.1021/acs.jpcc.0c11034.
- (131) Nattino, F.; Costanzo, F.; Kroes, G.-J. N2 Dissociation on W(110): An Ab Initio Molecular Dynamics Study on the Effect of Phonons. J. Chem. Phys. 2015, 142 (10). https://doi.org/10.1063/1.4913979.
- (132) Migliorini, D.; Nattino, F.; Kroes, G.-J. Application of van Der Waals Functionals to the Calculation of Dissociative Adsorption of N2 on W(110) for Static and Dynamic Systems. J. Chem. Phys. 2016, 144 (8), 084702. https://doi.org/10.1063/1.4942198.
- (133) Nattino, F.; Migliorini, D.; Kroes, G.-J.; Dombrowski, E.; High, E. A.; Killelea, D. R.; Utz, A. L. Chemically Accurate Simulation of a Polyatomic Molecule-Metal Surface Reaction. J. Phys. Chem. Lett. 2016, 7 (13), 2402–2406. https://doi.org/10.1021/acs.jpclett.6b01022.
- (134) Migliorini, D.; Chadwick, H.; Nattino, F.; Gutiérrez-González, A.; Dombrowski, E.; High, E. A.; Guo, H.; Utz, A. L.; Jackson, B.; Beck, R. D.; Kroes, G. J. Surface Reaction Barriometry: Methane Dissociation on Flat and Stepped Transition-Metal Surfaces. J. Phys. Chem. Lett. 2017, 8 (17), 4177–4182. https://doi.org/10.1021/acs.jpclett.7b01905.
- (135) Díaz, C.; Pijper, E.; Olsen, R. A.; Busnengo, H. F.; Auerbach, D. J.; Kroes, G. J. Chemically Accurate Simulation of a Prototypical Surface Reaction: H2 Dissociation on Cu(111). Science (80-.). 2009, 326 (5954), 832–834. https://doi.org/10.1126/science.1178722.
- (136) Füchsel, G.; Del Cueto, M.; Díaz, C.; Kroes, G. J. Enigmatic HCl + Au(111) Reaction: A Puzzle for Theory and Experiment. J. Phys. Chem. C 2016, 120 (45), 25760–25779. https://doi.org/10.1021/acs.jpcc.6b07453.
- (137) Peverati, R.; Truhlar, D. G. Quest for a Universal Density Functional: The Accuracy of Density Functionals across a Broad Spectrum of Databases in Chemistry and Physics. Philos. Trans. R. Soc. A Math. Phys. Eng. Sci. 2014, 372 (2011), 20120476. https://doi.org/10.1098/rsta.2012.0476.
- (138) Goerigk, L.; Kruse, H.; Grimme, S. Benchmarking Density Functional Methods against the S66 and S66x8 Datasets for Non-Covalent Interactions. *ChemPhysChem* 2011, 12 (17), 3421–3433. https://doi.org/10.1002/cphc.201100826.
- (139) Mardirossian, N.; Head-Gordon, M. Thirty Years of Density Functional Theory in Computational Chemistry: An Overview and Extensive Assessment of 200 Density Functionals. *Mol. Phys.* 2017, 115 (19), 2315–2372. https://doi.org/10.1080/00268976.2017.1333644.
- (140) Spiegel, M.; Gamian, A.; Sroka, Z. A Statistically Supported Antioxidant Activity DFT Benchmark—The Effects of Hartree–Fock Exchange and Basis Set Selection on Accuracy and Resources Uptake. *Molecules* **2021**, *26* (16), 5058. https://doi.org/10.3390/molecules26165058.
- (141) Marcel Swart. Average results for the 2010-2023 editions of the Annual DFT Popularity Poll. https://www.marcelswart.eu/dft-poll/results.html (accessed 2024-08-28).
- (142) Nour Ghassemi, E.; Wijzenbroek, M.; Somers, M. F.; Kroes, G.-J. Chemically Accurate Simulation of Dissociative Chemisorption of D2 on Pt(1 1 1). Chem. Phys. Lett. 2017,

- 683, 329-335. https://doi.org/10.1016/j.cplett.2016.12.059.
- (143) Ghassemi, E. N.; Somers, M. F.; Kroes, G.-J. Assessment of Two Problems of Specific Reaction Parameter Density Functional Theory: Sticking and Diffraction of H 2 on Pt(111). J. Phys. Chem. C 2019, 123 (16), 10406–10418. https://doi.org/10.1021/acs.ipcc.9b00981.
- (144) Boereboom, J. M.; Wijzenbroek, M.; Somers, M. F.; Kroes, G. J. Towards a Specific Reaction Parameter Density Functional for Reactive Scattering of H2 from Pd(111). J. Chem. Phys. 2013, 139 (24). https://doi.org/10.1063/1.4851355.
- (145) Gerrits, N.; Smeets, E. W. F.; Vuckovic, S.; Powell, A. D.; Doblhoff-Dier, K.; Kroes, G.-J. Correction to "Density Functional Theory for Molecule–Metal Surface Reactions: When Does the Generalized Gradient Approximation Get It Right, and What to Do If It Does Not." J. Phys. Chem. Lett. 2022, 13 (45), 10575–10576. https://doi.org/10.1021/acs.jpclett.2c03223.
- (146) Cohen, A. J.; Mori-Sánchez, P.; Yang, W. Insights into Current Limitations of Density Functional Theory. *Science* (80-. ). 2008, 321 (5890), 792–794. https://doi.org/10.1126/science.1158722.
- (147) Kim, M.-C.; Sim, E.; Burke, K. Understanding and Reducing Errors in Density Functional Calculations. *Phys. Rev. Lett.* **2013**, *111* (7), 073003. https://doi.org/10.1103/PhysRevLett.111.073003.
- (148) Song, S.; Vuckovic, S.; Sim, E.; Burke, K. Density Sensitivity of Empirical Functionals. J. Phys. Chem. Lett. 2021, 12 (2), 800–807. https://doi.org/10.1021/acs.jpclett.0c03545.
- (149) Vuckovic, S.; Song, S.; Kozlowski, J.; Sim, E.; Burke, K. Density Functional Analysis: The Theory of Density-Corrected DFT. J. Chem. Theory Comput. 2019, 15 (12), 6636–6646. https://doi.org/10.1021/acs.jctc.9b00826.
- (150) Kaplan, A. D.; Shahi, C.; Bhetwal, P.; Sah, R. K.; Perdew, J. P. Understanding Density-Driven Errors for Reaction Barrier Heights. J. Chem. Theory Comput. 2023, 19 (2), 532– 543. https://doi.org/10.1021/acs.jctc.2c00953.
- (151) Kanungo, B.; Kaplan, A. D.; Shahi, C.; Gavini, V.; Perdew, J. P. Unconventional Error Cancellation Explains the Success of Hartree–Fock Density Functional Theory for Barrier Heights. J. Phys. Chem. Lett. 2024, 15 (1), 323–328. https://doi.org/10.1021/acs.jpclett.3c03088.
- (152) Perdew, J. P.; Ernzerhof, M.; Burke, K. Rationale for Mixing Exact Exchange with Density Functional Approximations. J. Chem. Phys. 1996, 105 (22), 9982–9985. https://doi.org/10.1063/1.472933.
- (153) Adamo, C.; Barone, V. Toward Reliable Density Functional Methods without Adjustable Parameters: The PBEO Model. J. Chem. Phys. 1999, 110 (13), 6158–6170. https://doi.org/10.1063/1.478522.
- (154) Perdew, J. P.; Burke, K.; Ernzerhof, M. Generalized Gradient Approximation Made Simple. Phys. Rev. Lett. 1996, 77 (18), 3865–3868. https://doi.org/10.1103/PhysRevLett.77.3865.
- (155) Henderson, T. M.; Izmaylov, A. F.; Scuseria, G. E.; Savin, A. The Importance of Middle-Range Hartree-Fock-Type Exchange for Hybrid Density Functionals. J. Chem. Phys. 2007, 127 (22), 221103. https://doi.org/10.1063/1.2822021.
- (156) Krukau, A. V.; Vydrov, O. A.; Izmaylov, A. F.; Scuseria, G. E. Influence of the Exchange Screening Parameter on the Performance of Screened Hybrid Functionals. *J. Chem. Phys.* **2006**, *125* (22), 224106. https://doi.org/10.1063/1.2404663.
- (157) Brütting, M.; Bahmann, H.; Kümmel, S. Hybrid Functionals with Local Range Separation: Accurate Atomization Energies and Reaction Barrier Heights. *J. Chem. Phys.* **2022**, *156* (10), 104109. https://doi.org/10.1063/5.0082957.
- (158) Gao, W.; Abtew, T. A.; Cai, T.; Sun, Y. Y.; Zhang, S.; Zhang, P. On the Applicability of

- Hybrid Functionals for Predicting Fundamental Properties of Metals. *Solid State Commun.* **2016**, *234*–*235*, 10–13. https://doi.org/10.1016/j.ssc.2016.02.014.
- (159) Smits, B.; Somers, M. F. Beyond the Static Corrugation Model: Dynamic Surfaces with the Embedded Atom Method. J. Chem. Phys. 2021, 154 (7), 074710. https://doi.org/10.1063/5.0036611.
- (160) Smits, B.; Litjens, L. G. B.; Somers, M. F. Accurate Description of the Quantum Dynamical Surface Temperature Effects on the Dissociative Chemisorption of H2 from Cu(111). J. Chem. Phys. 2022, 156 (21), 214706. https://doi.org/10.1063/5.0094985.
- (161) Kroes, G.; Meyer, J. Best-of-Both-Worlds Computational Approaches to Difficult-to-Model Dissociation Reactions on Metal Surfaces. Chem. Sci. 2025, 16 (2), 480–506. https://doi.org/10.1039/D4SC06004K.
- (162) Goikoetxea, I.; Beltrán, J.; Meyer, J.; Iñaki Juaristi, J.; Alducin, M.; Reuter, K. Non-Adiabatic Effects during the Dissociative Adsorption of O 2 at Ag(111)? A First-Principles Divide and Conquer Study. New J. Phys. 2012, 14 (1), 013050. https://doi.org/10.1088/1367-2630/14/1/013050.
- (163) Daru, J.; Forbert, H.; Behler, J.; Marx, D. Coupled Cluster Molecular Dynamics of Condensed Phase Systems Enabled by Machine Learning Potentials: Liquid Water Benchmark. *Phys. Rev. Lett.* 2022, 129 (22), 226001. https://doi.org/10.1103/PhysRevLett.129.226001.
- (164) Jensen, F. Introduction to Computational Chemistry, 2nd ed.; John Wiley & Sons, Ltd, 2007.
- (165) Schrödinger, E. An Undulatory Theory of the Mechanics of Atoms and Molecules. *Phys. Rev.* **1926**, *28* (6), 1049–1070. https://doi.org/10.1103/PhysRev.28.1049.
- (166) Born, M. Zur Quantenmechanik Der Stossvorgange. Zeitschrift fur Phys. 1926, 37 (12), 863–867. https://doi.org/10.1007/BF01397477.
- (167) Dirac, P. A. M. A New Notation for Quantum Mechanics. *Math. Proc. Cambridge Philos. Soc.* 1939, 35 (3), 416–418. https://doi.org/10.1017/S0305004100021162.
- (168) Hartree, D. R. The Wave Mechanics of an Atom with a Non-Coulomb Central Field. Part I. Theory and Methods. Math. Proc. Cambridge Philos. Soc. 1928, 24 (1), 89–110. https://doi.org/10.1017/S0305004100011919.
- (169) Nienhaus, H.; Bergh, H. S.; Gergen, B.; Majumdar, A.; Weinberg, W. H.; McFarland, E. W. Direct Detection of Electron-Hole Pairs Generated by Chemical Reactions on Metal Surfaces. *Surf. Sci.* **2000**, *445* (2–3), 335–342. https://doi.org/10.1016/S0039-6028(99)01078-X.
- (170) Spiering, P.; Meyer, J. Testing Electronic Friction Models: Vibrational De-Excitation in Scattering of H2 and D2 from Cu(111). J. Phys. Chem. Lett. 2018, 9 (7), 1803–1808. https://doi.org/10.1021/acs.jpclett.7b03182.
- (171) Spiering, P.; Shakouri, K.; Behler, J.; Kroes, G. J.; Meyer, J. Orbital-Dependent Electronic Friction Significantly Affects the Description of Reactive Scattering of N2 from Ru(0001). J. Phys. Chem. Lett. 2019, 10 (11), 2957–2962. https://doi.org/10.1021/acs.jpclett.9b00523.
- (172) Pauli, W. Über Den Zusammenhang Des Abschlusses Der Elektronengruppen Im Atom Mit Der Komplexstruktur Der Spektren. *Zeitschrift für Phys.* **1925**, *31* (1), 765–783. https://doi.org/10.1007/BF02980631.
- (173) Atkins, P.; Friedman, R. *Molecular Quantum Mechanics*, 4th ed.; Oxford University Press: New York, NY, **2005**.
- (174) Slater, J. C. The Theory of Complex Spectra. Phys. Rev. 1929, 34 (10), 1293–1322. https://doi.org/10.1103/PhysRev.34.1293.
- (175) Boys, S. F. Electronic Wave Functions I. A General Method of Calculation for the Stationary States of Any Molecular System. Proc. R. Soc. London. Ser. A. Math. Phys. Sci.

- 1950, 200 (1063), 542–554. https://doi.org/10.1098/rspa.1950.0036.
- (176) Slater, J. C. Atomic Shielding Constants. *Phys. Rev.* 1930, 36 (1), 57–64. https://doi.org/10.1103/PhysRev.36.57.
- (177) Averill, F. W.; Ellis, D. E. An Efficient Numerical Multicenter Basis Set for Molecular Orbital Calculations: Application to FeCl4. J. Chem. Phys. 1973, 59 (12), 6412–6418. https://doi.org/10.1063/1.1680020.
- (178) Thomas, L. H. The Calculation of Atomic Fields. Math. Proc. Cambridge Philos. Soc. 1927, 23 (5), 542–548. https://doi.org/10.1017/S0305004100011683.
- (179) Fermi, E. Un Metodo Statistico per La Determinazione Di Alcune Priorieta Dell'atome. *Rend. Accad. Naz. Lincei* **1927**, *6* (602–607), 32.
- (180) Dirac, P. A. M. Note on Exchange Phenomena in the Thomas Atom. *Math. Proc. Cambridge Philos. Soc.* 1930, 26 (3), 376–385. https://doi.org/10.1017/S0305004100016108.
- (181) Bloch, F. Uber Die Quantenmechanik Der Elektronen in Kristallgittern. *Zeitschrift fur Phys.* **1929**, *52* (7–8), 555–600. https://doi.org/10.1007/BF01339455.
- (182) Lundqvist, B. I.; Andersson, Y.; Shao, H.; Chan, S.; Langreth, D. C. Density Functional Theory Including Van Der Waals Forces. *Int. J. Quantum Chem.* 1995, 56 (4), 247–255. https://doi.org/10.1002/qua.560560410.
- (183) Dion, M.; Rydberg, H.; Schröder, E.; Langreth, D. C.; Lundqvist, B. I. Van Der Waals Density Functional for General Geometries. *Phys. Rev. Lett.* 2004, 92 (24), 246401. https://doi.org/10.1103/PhysRevLett.92.246401.
- (184) Sabatini, R.; Gorni, T.; de Gironcoli, S. Nonlocal van Der Waals Density Functional Made Simple and Efficient. *Phys. Rev. B* 2013, 87 (4), 041108. https://doi.org/10.1103/PhysRevB.87.041108.
- (185) Grimme, S. Semiempirical GGA-type Density Functional Constructed with a Long-range Dispersion Correction. J. Comput. Chem. 2006, 27 (15), 1787–1799. https://doi.org/10.1002/jcc.20495.
- (186) Grimme, S.; Antony, J.; Ehrlich, S.; Krieg, H. A Consistent and Accurate Ab Initio Parametrization of Density Functional Dispersion Correction (DFT-D) for the 94 Elements H-Pu. J. Chem. Phys. 2010, 132 (15), 154104. https://doi.org/10.1063/1.3382344.
- (187) Vydrov, O. A.; Van Voorhis, T. Nonlocal van Der Waals Density Functional: The Simpler the Better. J. Chem. Phys. 2010, 133 (24), 244103. https://doi.org/10.1063/1.3521275.
- (188) Perdew, J. P.; Chevary, J. A.; Vosko, S. H.; Jackson, K. A.; Pederson, M. R.; Singh, D. J.; Fiolhais, C. Atoms, Molecules, Solids, and Surfaces: Applications of the Generalized Gradient Approximation for Exchange and Correlation. *Phys. Rev. B* 1992, 46 (11), 6671–6687. https://doi.org/10.1103/PhysRevB.46.6671.
- (189) Heyd, J.; Scuseria, G. E.; Ernzerhof, M. Hybrid Functionals Based on a Screened Coulomb Potential. J. Chem. Phys. 2003, 118 (18), 8207–8215. https://doi.org/10.1063/1.1564060.
- (190) Heyd, J.; Scuseria, G. E.; Ernzerhof, M. Erratum: "Hybrid Functionals Based on a Screened Coulomb Potential" [J. Chem. Phys. 118, 8207 (2003)]. J. Chem. Phys. 2006, 124 (21), 219906. https://doi.org/10.1063/1.2204597.
- (191) Berland, K.; Hyldgaard, P. Exchange Functional That Tests the Robustness of the Plasmon Description of the van Der Waals Density Functional. *Phys. Rev. B Condens. Matter Mater. Phys.* **2014**, *89* (3), 1–8. https://doi.org/10.1103/PhysRevB.89.035412.
- (192) Berland, K.; Jiao, Y.; Lee, J. H.; Rangel, T.; Neaton, J. B.; Hyldgaard, P. Assessment of Two Hybrid van Der Waals Density Functionals for Covalent and Non-Covalent Binding of Molecules. *J. Chem. Phys.* **2017**, *146* (23). https://doi.org/10.1063/1.4986522.
- (193) Shukla, V.; Jiao, Y.; Lee, J.; Schröder, E.; Neaton, J. B.; Hyldgaard, P. Accurate

- Nonempirical Range-Separated Hybrid van Der Waals Density Functional for Complex Molecular Problems, Solids, and Surfaces. *Phys. Rev. X* **2022**, *12* (4), 041003. https://doi.org/10.1103/PhysRevX.12.041003.
- (194) Shukla, V.; Jiao, Y.; Frostenson, C. M.; Hyldgaard, P. VdW-DF-Ahcx: A Range-Separated van Der Waals Density Functional Hybrid. J. Phys. Condens. Matter 2022, 34 (2), 025902. https://doi.org/10.1088/1361-648X/ac2ad2.
- (195) Lee, K.; Murray, É. D.; Kong, L.; Lundqvist, B. I.; Langreth, D. C. Higher-Accuracy van Der Waals Density Functional. *Phys. Rev. B Condens. Matter Mater. Phys.* 2010, 82 (8), 3–6. https://doi.org/10.1103/PhysRevB.82.081101.
- (196) Vanderbilt, D. Soft Self-Consistent Pseudopotentials in a Generalized Eigenvalue Formalism. *Phys. Rev. B* **1990**, *41* (11), 7892–7895. https://doi.org/10.1103/PhysRevB.41.7892.
- (197) Laasonen, K.; Car, R.; Lee, C.; Vanderbilt, D. Implementation of Ultrasoft Pseudopotentials in Ab Initio Molecular Dynamics. *Phys. Rev. B* **1991**, *43* (8), 6796–6799. https://doi.org/10.1103/PhysRevB.43.6796.
- (198) Pyykkö, P. Relativistic Effects in Chemistry: More Common Than You Thought. Annu. Rev. Phys. Chem. 2012, 63 (1), 45–64. https://doi.org/10.1146/annurev-physchem-032511-143755.
- (199) Blöchl, P. E. Projector Augmented-Wave Method. *Phys. Rev. B* 1994, 50 (24), 17953–17979. https://doi.org/10.1103/PhysRevB.50.17953.
- (200) Kresse, G.; Joubert, D. From Ultrasoft Pseudopotentials to the Projector Augmented-Wave Method. *Phys. Rev. B* 1999, 59 (3), 1758–1775. https://doi.org/10.1103/PhysRevB.59.1758.
- (201) Busnengo, H. F.; Salin, A.; Dong, W. Representation of the 6D Potential Energy Surface for a Diatomic Molecule near a Solid Surface. J. Chem. Phys. 2000, 112 (17), 7641–7651. https://doi.org/10.1063/1.481377.
- (202) Olsen, R. A.; Busnengo, H. F.; Salin, A.; Somers, M. F.; Kroes, G. J.; Baerends, E. J. Constructing Accurate Potential Energy Surfaces for a Diatomic Molecule Interacting with a Solid Surface: H2+Pt(111) and H2+Cu(100). J. Chem. Phys. 2002, 116 (9), 3841–3855. https://doi.org/10.1063/1.1446852.
- (203) Wijzenbroek, M. Hydrogen Dissociation on Metal Surfaces, Leiden Univercity, 2016. https://hdl.handle.net/1887/39935.
- (204) Smeets, E. W. F. Development of Highly Accurate Density Functionals for H2 Dissociation on Transition Metals, Leiden Univercity, 2021. https://hdl.handle.net/1887/3193529.
- (205) Verlet, L. Computer "Experiments" on Classical Fluids. I. Thermodynamical Properties of Lennard-Jones Molecules. *Phys. Rev.* **1967**, *159* (1), 98–103. https://doi.org/10.1103/PhysRev.159.98.
- (206) Bulirsch, R.; Stoer, J. Numerical Treatment of Ordinary Differential Equations by Extrapolation Methods. *Numer. Math.* 1966, 8 (1), 1–13. https://doi.org/10.1007/BF02165234.
- (207) Stoer, J.; Bulirsch, R. Introduction to Numerical Analysis; Texts in Applied Mathematics; Springer New York: New York, NY, 2002; Vol. 12. https://doi.org/10.1007/978-0-387-21738-3.
- (208) Richardson, L. F. IX. The Approximate Arithmetical Solution by Finite Differences of Physical Problems Involving Differential Equations, with an Application to the Stresses in a Masonry Dam. Philos. Trans. R. Soc. London. Ser. A, Contain. Pap. a Math. or Phys. Character 1911, 210 (459–470), 307–357. https://doi.org/10.1098/rsta.1911.0009.
- (209) Smits, B. Surface Temperature and the Dynamics of H2 on Cu(111), Leiden Univercity, 2023. https://hdl.handle.net/1887/3628423.

- (210) Karplus, M.; Porter, R. N.; Sharma, R. D. Exchange Reactions with Activation Energy. I. Simple Barrier Potential for (H, H 2). J. Chem. Phys. 1965, 43 (9), 3259–3287. https://doi.org/10.1063/1.1697301.
- (211) Raff, L. M.; Karplus, M. Theoretical Investigations of Reactive Collisions in Molecular Beams: K+CH 3 I and Related Systems. J. Chem. Phys. 1966, 44 (3), 1212–1229. https://doi.org/10.1063/1.1726808.
- (212) Sabbe, M. K.; Reyniers, M.-F.; Reuter, K. First-Principles Kinetic Modeling in Heterogeneous Catalysis: An Industrial Perspective on Best-Practice, Gaps and Needs. *Catal. Sci. Technol.* **2012**, *2* (10), 2010–2024. https://doi.org/10.1039/c2cy20261a.
- (213) Wolcott, C. A.; Medford, A. J.; Studt, F.; Campbell, C. T. Degree of Rate Control Approach to Computational Catalyst Screening. J. Catal. 2015, 330, 197–207. https://doi.org/10.1016/j.jcat.2015.07.015.
- (214) Gartland, P. O. Adsorption of Oxygen on Clean Single Crystal Faces of Aluminium. *Surf. Sci.* **1977**, *62* (1), 183–196. https://doi.org/10.1016/0039-6028(77)90436-8.
- (215) Roberts, M. W. Chemisorption and Reaction Pathways at Metal Surfaces: The Role of Surface Oxygen. Chem. Soc. Rev. 1989, 18, 451–475. https://doi.org/10.1039/cs9891800451.
- (216) Lundgren, E.; Mikkelsen, A.; Andersen, J. N.; Kresse, G.; Schmid, M.; Varga, P. Surface Oxides on Close-Packed Surfaces of Late Transition Metals. J. Phys. Condens. Matter 2006, 18 (30), R481–R499. https://doi.org/10.1088/0953-8984/18/30/R01.
- (217) Stampfl, C.; Soon, A.; Piccinin, S.; Shi, H.; Zhang, H. Bridging the Temperature and Pressure Gaps: Close-Packed Transition Metal Surfaces in an Oxygen Environment. *J. Phys. Condens. Matter* **2008**, *20* (18), 184021. https://doi.org/10.1088/0953-8984/20/18/184021.
- (218) Montemore, M. M.; van Spronsen, M. A.; Madix, R. J.; Friend, C. M. O 2 Activation by Metal Surfaces: Implications for Bonding and Reactivity on Heterogeneous Catalysts. Chem. Rev. 2018, 118 (5), 2816–2862. https://doi.org/10.1021/acs.chemrev.7b00217.
- (219) Jacobsen, J.; Hammer, B.; Jacobsen, K. W.; Nørskov, J. K. Electronic Structure, Total Energies, and STM Images of Clean and Oxygen-Covered Al(111). *Phys. Rev. B* 1995, 52 (20), 14954–14962. https://doi.org/10.1103/PhysRevB.52.14954.
- (220) Darling, G. R.; Holloway, S. The Dissociation of Diatomic Molecules at Surfaces. *Reports Prog. Phys.* 1995, 58 (12), 1595–1672. https://doi.org/10.1088/0034-4885/58/12/001.
- (221) Wijzenbroek, M.; Somers, M. F. Static Surface Temperature Effects on the Dissociation of H2 and D2 on Cu(111). J. Chem. Phys. 2012, 137 (5), 054703. https://doi.org/10.1063/1.4738956.
- (222) Batra, I. P.; Kleinman, L. Chemisorption of Oxygen on Aluminum Surfaces. *J. Electron Spectros. Relat. Phenomena* **1984**, *33* (3), 175–241. https://doi.org/10.1016/0368-2048(84)80020-1.
- (223) Kerkar, M.; Fisher, D.; Woodruff, D. P.; Cowie, B. Adsorption Site Determination for Oxygen on Al(111) Using Normal Incidence Standing X-Ray Wavefield Absorption. Surf. Sci. 1992, 271 (1–2), 45–56. https://doi.org/10.1016/0039-6028(92)90860-9.
- (224) Österlund, L.; Zoric-acute, I.; Kasemo, B. Dissociative Sticking of O2 on Al(111). *Phys. Rev. B* **1997**, *55* (23), 15452–15455. https://doi.org/10.1103/PhysRevB.55.15452.
- (225) Zhukov, V.; Popova, I.; Yates, J. T. Initial Stages of Al(111) Oxidation with Oxygen— Temperature Dependence of the Integral Reactive Sticking Coefficient. Surf. Sci. 1999, 441 (2–3), 251–264. https://doi.org/10.1016/S0039-6028(99)00614-7.
- (226) Liu, H.-R.; Xiang, H.; Gong, X. G. First Principles Study of Adsorption of O 2 on Al Surface with Hybrid Functionals. J. Chem. Phys. 2011, 135 (21), 214702. https://doi.org/10.1063/1.3665032.
- (227) Kurahashi, M.; Yamauchi, Y. Steric Effect in O2 Sticking on Al(111): Preference for

- Parallel Geometry. *Phys. Rev. Lett.* **2013**, *110* (24), 246102. https://doi.org/10.1103/PhysRevLett.110.246102.
- (228) Libisch, F.; Huang, C.; Liao, P.; Pavone, M.; Carter, E. A. Origin of the Energy Barrier to Chemical Reactions of O2 on Al(111): Evidence for Charge Transfer, Not Spin Selection. Phys. Rev. Lett. 2012, 109 (19), 198303. https://doi.org/10.1103/PhysRevLett.109.198303.
- (229) Cheng, J.; Libisch, F.; Carter, E. A. Dissociative Adsorption of O 2 on Al(111): The Role of Orientational Degrees of Freedom. J. Phys. Chem. Lett. 2015, 6 (9), 1661–1665. https://doi.org/10.1021/acs.jpclett.5b00597.
- (230) Yin, R.; Zhang, Y.; Libisch, F.; Carter, E. A.; Guo, H.; Jiang, B. Dissociative Chemisorption of O 2 on Al(111): Dynamics on a Correlated Wave-Function-Based Potential Energy Surface. J. Phys. Chem. Lett. 2018, 9 (12), 3271–3277. https://doi.org/10.1021/acs.jpclett.8b01470.
- (231) Behler, J.; Delley, B.; Lorenz, S.; Reuter, K.; Scheffler, M. Dissociation of O2 at Al(111): The Role of Spin Selection Rules. *Phys. Rev. Lett.* **2005**, *94* (3), 036104. https://doi.org/10.1103/PhysRevLett.94.036104.
- (232) Fan, X. L.; Lau, W. M.; Liu, Z. F. Comment on "Dissociation of O2 at Al(111): The Role of Spin Selection Rules." Phys. Rev. Lett. 2006, 96 (7), 079801. https://doi.org/10.1103/PhysRevLett.96.079801.
- (233) Behler, J.; Reuter, K.; Scheffler, M. Behler, Reuter, and Scheffler Reply. *Phys. Rev. Lett.* **2006**, *96* (7), 79802. https://doi.org/10.1103/PhysRevLett.96.079802.
- (234) Carbogno, C.; Behler, J.; Groß, A.; Reuter, K. Fingerprints for Spin-Selection Rules in the Interaction Dynamics of O2 at Al(111). *Phys. Rev. Lett.* **2008**, *101* (9), 096104. https://doi.org/10.1103/PhysRevLett.101.096104.
- (235) Carbogno, C.; Behler, J.; Reuter, K.; Groß, A. Signatures of Nonadiabatic O2- Dissociation at Al(111): First-Principles Fewest-Switches Study. *Phys. Rev. B* **2010**, *81* (3), 035410. https://doi.org/10.1103/PhysRevB.81.035410.
- (236) Sasaki, T.; Ohno, T. Calculations of the Potential-Energy Surface for Dissociation Process of O2 on the Al(111) Surface. Phys. Rev. B 1999, 60 (11), 7824–7827. https://doi.org/10.1103/PhysRevB.60.7824.
- (237) Honkala, K.; Laasonen, K. Oxygen Molecule Dissociation on the Al(111) Surface. *Phys. Rev. Lett.* **2000**, *84* (4), 705–708. https://doi.org/10.1103/PhysRevLett.84.705.
- (238) Yourdshahyan, Y.; Razaznejad, B.; Lundqvist, B. I. Adiabatic Potential-Energy Surfaces for Oxygen on Al(111). Phys. Rev. B 2002, 65 (7), 075416. https://doi.org/10.1103/PhysRevB.65.075416.
- (239) Hammer, B.; Hansen, L. B.; Nørskov, J. K. Improved Adsorption Energetics within Density-Functional Theory Using Revised Perdew-Burke-Ernzerhof Functionals. *Phys. Rev. B* **1999**, *59* (11), 7413–7421. https://doi.org/10.1103/PhysRevB.59.7413.
- (240) Behler, J.; Reuter, K.; Scheffler, M. Nonadiabatic Effects in the Dissociation of Oxygen Molecules at the Al(111) Surface. *Phys. Rev. B* 2008, 77 (11), 115421. https://doi.org/10.1103/PhysRevB.77.115421.
- (241) Huang, C.; Pavone, M.; Carter, E. A. Quantum Mechanical Embedding Theory Based on a Unique Embedding Potential. J. Chem. Phys. 2011, 134 (15), 154110. https://doi.org/10.1063/1.3577516.
- (242) Andersson, K.; Malmqvist, P. A.; Roos, B. O.; Sadlej, A. J.; Wolinski, K. Second-Order Perturbation Theory with a CASSCF Reference Function. J. Phys. Chem. 1990, 94 (14), 5483–5488. https://doi.org/10.1021/j100377a012.
- (243) Andersson, K.; Malmqvist, P.-Å.; Roos, B. O. Second-Order Perturbation Theory with a Complete Active Space Self-Consistent Field Reference Function. *J. Chem. Phys.* **1992**, *96* (2), 1218–1226. https://doi.org/10.1063/1.462209.

- (244) Perdew, J. P.; Parr, R. G.; Levy, M.; Balduz, J. L. Density-Functional Theory for Fractional Particle Number: Derivative Discontinuities of the Energy. *Phys. Rev. Lett.* **1982**, *49* (23), 1691–1694. https://doi.org/10.1103/PhysRevLett.49.1691.
- (245) Perdew, J. P.; Zunger, A. Self-Interaction Correction to Density-Functional Approximations for Many-Electron Systems. *Phys. Rev. B* **1981**, *23* (10), 5048–5079. https://doi.org/10.1103/PhysRevB.23.5048.
- (246) Menezes, F.; Kats, D.; Werner, H.-J. Local Complete Active Space Second-Order Perturbation Theory Using Pair Natural Orbitals (PNO-CASPT2). J. Chem. Phys. 2016, 145 (12). https://doi.org/10.1063/1.4963019.
- (247) McCreery, J. H.; Wolken, G. A Model Potential for Chemisorption: H 2 +W(001). *J. Chem. Phys.* **1975**, *63* (6), 2340–2349. https://doi.org/10.1063/1.431663.
- (248) Martin-Gondre, L.; Crespos, C.; Larrégaray, P.; Rayez, J. C.; Conte, D.; van Ootegem, B. Detailed Description of the Flexible Periodic London–Eyring–Polanyi–Sato Potential Energy Function. Chem. Phys. 2010, 367 (2–3), 136–147. https://doi.org/10.1016/j.chemphys.2009.11.012.
- (249) Wei, Z.; Martirez, J. M. P.; Carter, E. A. Introducing the Embedded Random Phase Approximation: H2 Dissociative Adsorption on Cu(111) as an Exemplar. *J. Chem. Phys.* **2023**, *159* (19), 194108. https://doi.org/10.1063/5.0181229.
- (250) Mori-Sánchez, P.; Cohen, A. J.; Yang, W. Many-Electron Self-Interaction Error in Approximate Density Functionals. J. Chem. Phys. 2006, 125 (20). https://doi.org/10.1063/1.2403848.
- (251) Mori-Sánchez, P.; Cohen, A. J.; Yang, W. Localization and Delocalization Errors in Density Functional Theory and Implications for Band-Gap Prediction. *Phys. Rev. Lett.* 2008, 100 (14), 146401. https://doi.org/10.1103/PhysRevLett.100.146401.
- (252) Zheng, J.; Zhao, Y.; Truhlar, D. G. The DBH24/08 Database and Its Use to Assess Electronic Structure Model Chemistries for Chemical Reaction Barrier Heights. *J. Chem. Theory Comput.* **2009**, *5* (4), 808–821. https://doi.org/10.1021/ct800568m.
- (253) Sim, E.; Song, S.; Burke, K. Quantifying Density Errors in DFT. J. Phys. Chem. Lett. **2018**, 9 (22), 6385–6392. https://doi.org/10.1021/acs.jpclett.8b02855.
- (254) Karikorpi, M.; Holloway, S.; Henriksen, N.; Nørskov, J. K. Dynamics of Molecule-Surface Interactions. Surf. Sci. Lett. 1987, 179 (1), L41–L48. https://doi.org/10.1016/0167-2584(87)90235-0.
- (255) Perdew, J. P.; Ruzsinszky, A.; Tao, J.; Staroverov, V. N.; Scuseria, G. E.; Csonka, G. I. Prescription for the Design and Selection of Density Functional Approximations: More Constraint Satisfaction with Fewer Fits. J. Chem. Phys. 2005, 123 (6), 062201. https://doi.org/10.1063/1.1904565.
- (256) Wijzenbroek, M.; Kroes, G. J. The Effect of the Exchange-Correlation Functional on H2 Dissociation on Ru(0001). J. Chem. Phys. 2014, 140 (8). https://doi.org/10.1063/1.4865946.
- (257) Cohen, A. J.; Mori-Sánchez, P.; Yang, W. Challenges for Density Functional Theory. *Chem. Rev.* **2012**, *112* (1), 289–320. https://doi.org/10.1021/cr200107z.
- (258) Kresse, G.; Hafner, J. Ab Initio Molecular Dynamics for Liquid Metals. *Phys. Rev. B* **1993**, 47 (1), 558–561. https://doi.org/10.1103/PhysRevB.47.558.
- (259) Kresse, G.; Hafner, J. Ab Initio Molecular-Dynamics Simulation of the Liquid-Metal-Amorphous-Semiconductor Transition in Germanium. *Phys. Rev. B* 1994, 49 (20), 14251–14269. https://doi.org/10.1103/PhysRevB.49.14251.
- (260) Kresse, G.; Hafner, J. Norm-Conserving and Ultrasoft Pseudopotentials for First-Row and Transition Elements. J. Phys. Condens. Matter 1994, 6 (40), 8245–8257. https://doi.org/10.1088/0953-8984/6/40/015.
- (261) Kresse, G.; Furthmüller, J. Efficiency of Ab-Initio Total Energy Calculations for Metals

- and Semiconductors Using a Plane-Wave Basis Set. *Comput. Mater. Sci.* **1996**, *6* (1), 15–50. https://doi.org/10.1016/0927-0256(96)00008-0.
- (262) Kresse, G.; Furthmüller, J. Efficient Iterative Schemes for Ab Initio Total-Energy Calculations Using a Plane-Wave Basis Set. *Phys. Rev. B* 1996, 54 (16), 11169–11186. https://doi.org/10.1103/PhysRevB.54.11169.
- (263) Wijzenbroek, M.; Klein, D. M.; Smits, B.; Somers, M. F.; Kroes, G. J. Performance of a Non-Local van Der Waals Density Functional on the Dissociation of H2 on Metal Surfaces. J. Phys. Chem. A 2015, 119 (50), 12146–12158. https://doi.org/10.1021/acs.jpca.5b06008.
- (264) Kuebler, N. A.; Robin, M. B.; Yang, J. J.; Gedanken, A.; Herrick, D. R. Fully Resolved Zeeman Pattern in the Stern-Gerlach Deflection Spectrum of O2 (3g-, K=1). *Phys. Rev. A* 1988, 38 (2), 737–749. https://doi.org/10.1103/PhysRevA.38.737.
- (265) Powell, M. J. *Numerical Methods for Nonlinear Algebraic Equations*; Rabinowitz, P., Ed.; Gordon and Breach: New York, 1970.
- (266) Garbow, B. S.; Hillstorm, K. E.; More, J. J. MINPACK Subroutine HYBRD. 1980.
- (267) Schmid, M.; Leonardelli, G.; Tscheließnig, R.; Biedermann, A.; Varga, P. Oxygen Adsorption on Al(111): Low Transient Mobility. Surf. Sci. 2001, 478 (3), L355–L362. https://doi.org/10.1016/S0039-6028(01)00967-0.
- (268) Wahnström, G.; Lee, A. B.; Strömquist, J. Motion of "Hot" Oxygen Adatoms on Corrugated Metal Surfaces. J. Chem. Phys. 1996, 105 (1), 326–336. https://doi.org/10.1063/1.471877.
- (269) Binetti, M.; Weiße, O.; Hasselbrink, E.; Komrowski, A. J.; Kummel, A. C. Abstractive Chemisorption of O2 on Al(111). *Faraday Discuss.* **2000**, *117* (111), 313–320. https://doi.org/10.1039/b004006l.
- (270) Binetti, M.; Weiße, O.; Hasselbrink, E.; Katz, G.; Kosloff, R.; Zeiri, Y. The Role of Nonadiabatic Pathways and Molecular Rotations in the Oxygen Abstraction Reaction on the Al(111) Surface. Chem. Phys. Lett. 2003, 373 (3–4), 366–371. https://doi.org/10.1016/S0009-2614(03)00586-4.
- (271) Binetti, M.; Hasselbrink, E. Abstraction of Oxygen from Dioxygen on Al(111) Revealed by Resonant Multiphoton Ionization Laser Spectrometry. J. Phys. Chem. B 2004, 108 (38), 14677–14684. https://doi.org/10.1021/jp049197y.
- (272) Strandberg, M. W. P.; Tinkham, M. Theory of the Fine Structure of the Molecular. *Phys. Rev.* **1955**, *97* (4), 937–966.
- (273) Polanyi, J. C. Some Concepts in Reaction Dynamics. *Science (80-. ).* **1987**, *236* (4802), 680–690. https://doi.org/10.1126/science.236.4802.680.
- (274) Tiwari, A. K.; Nave, S.; Jackson, B. Methane Dissociation on Ni(111): A New Understanding of the Lattice Effect. *Phys. Rev. Lett.* 2009, 103 (25), 253201. https://doi.org/10.1103/PhysRevLett.103.253201.
- (275) Tiwari, A. K.; Nave, S.; Jackson, B. The Temperature Dependence of Methane Dissociation on Ni(111) and Pt(111): Mixed Quantum-Classical Studies of the Lattice Response. J. Chem. Phys. 2010, 132 (13), 134702. https://doi.org/10.1063/1.3357415.
- (276) Luntz, A. C.; Williams, M. D.; Bethune, D. S. The Sticking of O2 on a Pt(111) Surface. *J. Chem. Phys.* **1988**, *89* (7), 4381–4395. https://doi.org/10.1063/1.454824.
- (277) Jacobse, L.; den Dunnen, A.; Juurlink, L. B. F. The Molecular Dynamics of Adsorption and Dissociation of O2 on Pt(553). J. Chem. Phys. 2015, 143 (1). https://doi.org/10.1063/1.4923006.
- (278) Gostein, M.; Sitz, G. O. Rotational State-Resolved Sticking Coefficients for H2 on Pd(111): Testing Dynamical Steering in Dissociative Adsorption. J. Chem. Phys. 1997, 106 (17), 7378–7390. https://doi.org/10.1063/1.473699.
- (279) Perdew, J. P. Climbing the Ladder of Density Functional Approximations. MRS Bull.

- 2013, 38 (9), 743-750. https://doi.org/10.1557/mrs.2013.178.
- (280) van Bree, R. A. B.; Gerrits, N.; Kroes, G.-J. Dissociative Chemisorption of O 2 on Al(111): Dynamics on a Potential Energy Surface Computed with a Non-Self-Consistent Screened Hybrid Density Functional Approach. *Faraday Discuss.* 2024, 251, 361–381. https://doi.org/10.1039/D3FD00165B.
- (281) Juaristi, J. I.; Alducin, M.; Muiño, R. D.; Busnengo, H. F.; Salin, A. Role of Electron-Hole Pair Excitations in the Dissociative Adsorption of Diatomic Molecules on Metal Surfaces. Phys. Rev. Lett. 2008, 100 (11), 116102. https://doi.org/10.1103/PhysRevLett.100.116102.
- (282) Berland, K.; Cooper, V. R.; Lee, K.; Schröder, E.; Thonhauser, T.; Hyldgaard, P.; Lundqvist, B. I. Van Der Waals Forces in Density Functional Theory: A Review of the VdW-DF Method. Reports Prog. Phys. 2015, 78 (6), 066501. https://doi.org/10.1088/0034-4885/78/6/066501.
- (283) Moldabekov, Z. A.; Lokamani, M.; Vorberger, J.; Cangi, A.; Dornheim, T. Non-Empirical Mixing Coefficient for Hybrid XC Functionals from Analysis of the XC Kernel. J. Phys. Chem. Lett. 2023, 14 (5), 1326–1333. https://doi.org/10.1021/acs.jpclett.2c03670.
- van Bree, R. A. B.; Kroes, G. J. O 2 Dissociation on Cu(111) Dynamics on a Novel Screened Hybrid van Der Waals DFT Potential Energy Surface. *J. Phys. Chem. C* 2024, 128 (45), 19182–19196. https://doi.org/10.1021/acs.jpcc.4c05466.
- (285) Klimeš, J.; Bowler, D. R.; Michaelides, A. A Critical Assessment of Theoretical Methods for Finding Reaction Pathways and Transition States of Surface Processes. J. Phys. Condens. Matter 2010, 22 (7), 074203. https://doi.org/10.1088/0953-8984/22/7/074203.
- (286) Klimeš, J.; Bowler, D. R.; Michaelides, A. Van Der Waals Density Functionals Applied to Solids. Phys. Rev. B 2011, 83 (19), 195131. https://doi.org/10.1103/PhysRevB.83.195131.
- (287) Teter, M. P.; Payne, M. C.; Allan, D. C. Solution of Schrödinger's Equation for Large Systems. *Phys. Rev. B* **1989**, *40* (18), 12255–12263. https://doi.org/10.1103/PhysRevB.40.12255.
- (288) Bylander, D. M.; Kleinman, L.; Lee, S. Self-Consistent Calculations of the Energy Bands and Bonding Properties of B12C3. *Phys. Rev. B* 1990, 42 (2), 1394–1403. https://doi.org/10.1103/PhysRevB.42.1394.
- (289) PRECFOCK VASP Wiki. https://www.vasp.at/wiki/index.php/PRECFOCK (accessed 2025-01-13).
- (290) Haas, P.; Tran, F.; Blaha, P. Calculation of the Lattice Constant of Solids with Semilocal Functionals. *Phys. Rev. B* 2009, 79 (8), 085104. https://doi.org/10.1103/PhysRevB.79.085104.
- (291) Noonan, J. R.; Davis, H. L. Confirmation of an Exception to the "General Rule" of Surface Relaxations. J. Vac. Sci. Technol. A Vacuum, Surfaces, Film. 1990, 8 (3), 2671– 2676. https://doi.org/10.1116/1.576692.
- (292) Schöchlin, J.; Bohnen, K. P.; Ho, K. M. Structure and Dynamics at the Al(111)-Surface. Surf. Sci. 1995, 324 (2–3), 113–121. https://doi.org/10.1016/0039-6028(94)00710-1.
- (293) Marcus, R. A. On the Analytical Mechanics of Chemical Reactions. Classical Mechanics of Linear Collisions. J. Chem. Phys. 1966, 45 (12), 4500–4504. https://doi.org/10.1063/1.1727529.
- (294) McCullough, E. A.; Wyatt, R. E. Quantum Dynamics of the Collinear (H, H2) Reaction. *J. Chem. Phys.* **1969**, *51* (3), 1253–1254. https://doi.org/10.1063/1.1672133.
- (295) Oudot, B.; Doblhoff-Dier, K. Reaction Barriers at Metal Surfaces Computed Using the Random Phase Approximation: Can We Beat DFT in the Generalized Gradient Approximation? J. Chem. Phys. 2024, 161 (5), 054708.

- https://doi.org/10.1063/5.0220465.
- (296) Goerigk, L.; Grimme, S. Efficient and Accurate Double-Hybrid-Meta-GGA Density Functionals—Evaluation with the Extended GMTKN30 Database for General Main Group Thermochemistry, Kinetics, and Noncovalent Interactions. J. Chem. Theory Comput. 2011, 7 (2), 291–309. https://doi.org/10.1021/ct100466k.
- (297) Baule, B. Theoretische Behandlung Der Erscheinungen in Verdünnten Gasen. *Ann. Phys.* **1914**, *349* (9), 145–176. https://doi.org/10.1002/andp.19143490908.
- (298) Golibrzuch, K.; Bartels, N.; Auerbach, D. J.; Wodtke, A. M. The Dynamics of Molecular Interactions and Chemical Reactions at Metal Surfaces: Testing the Foundations of Theory. Annu. Rev. Phys. Chem. 2015, 66 (1), 399–425. https://doi.org/10.1146/annurev-physchem-040214-121958.
- (299) Head-Gordon, M.; Tully, J. C. Molecular Dynamics with Electronic Frictions. *J. Chem. Phys.* **1995**, *103* (23), 10137–10145. https://doi.org/10.1063/1.469915.
- (300) Alducin, M.; Díez Muiño, R.; Juaristi, J. I. Non-Adiabatic Effects in Elementary Reaction Processes at Metal Surfaces. *Prog. Surf. Sci.* 2017, 92 (4), 317–340. https://doi.org/10.1016/j.progsurf.2017.09.002.
- (301) White, J. D.; Chen, J.; Matsiev, D.; Auerbach, D. J.; Wodtke, A. M. Conversion of Large-Amplitude Vibration to Electron Excitation at a Metal Surface. *Nature* 2005, 433 (7025), 503–505. https://doi.org/10.1038/nature03213.
- (302) Shenvi, N.; Roy, S.; Tully, J. C. Nonadiabatic Dynamics at Metal Surfaces: Independent-Electron Surface Hopping. J. Chem. Phys. 2009, 130 (17), 174107. https://doi.org/10.1063/1.3125436.
- (303) Shakouri, K.; Behler, J.; Meyer, J.; Kroes, G.-J. Accurate Neural Network Description of Surface Phonons in Reactive Gas—Surface Dynamics: N 2 + Ru(0001). *J. Phys. Chem. Lett.* **2017**, *8* (10), 2131–2136. https://doi.org/10.1021/acs.jpclett.7b00784.
- (304) Liu, Q.; Zhou, X.; Zhou, L.; Zhang, Y.; Luo, X.; Guo, H.; Jiang, B. Constructing High-Dimensional Neural Network Potential Energy Surfaces for Gas-Surface Scattering and Reactions. J. Phys. Chem. C 2018, 122 (3), 1761–1769. https://doi.org/10.1021/acs.jpcc.7b12064.
- (305) Scoles, G. Atomic and Molecular Beam Methods, v. 1.; Oxford University Press, 1988.
- (306) Gattinoni, C.; Michaelides, A. Atomistic Details of Oxide Surfaces and Surface Oxidation: The Example of Copper and Its Oxides. Surf. Sci. Rep. 2015, 70 (3), 424–447. https://doi.org/10.1016/j.surfrep.2015.07.001.
- (307) Over, H.; Kim, Y. D.; Seitsonen, A. P.; Wendt, S.; Lundgren, E.; Schmid, M.; Varga, P.; Morgante, A.; Ertl, G. Atomic-Scale Structure and Catalytic Reactivity of the RuO 2 (110) Surface. Science (80-.). 2000, 287 (5457), 1474–1476. https://doi.org/10.1126/science.287.5457.1474.
- (308) Berger, H. F.; Leisch, M.; Winkler, A.; Rendulic, K. D. A Search for Vibrational Contributions to the Activated Adsorption of H2 on Copper. Chem. Phys. Lett. 1990, 175 (5), 425–428. https://doi.org/10.1016/0009-2614(90)85558-T.
- (309) Rettner, C. T.; Michelsen, H. A.; Auerbach, D. J. Quantum-State-Specific Dynamics of the Dissociative Adsorption and Associative Desorption of H2 at a Cu(111) Surface. J. Chem. Phys. 1995, 102 (11), 4625–4641. https://doi.org/10.1063/1.469511.
- (310) Hou, H.; Gulding, S. J.; Rettner, C. T.; Wodtke, A. M.; Auerbach, D. J. The Stereodynamics of a Gas-Surface Reaction. *Science* (80-. ). 1997, 277 (5322), 80–82. https://doi.org/10.1126/science.277.5322.80.
- (311) Murphy, M. J.; Hodgson, A. Adsorption and Desorption Dynamics of H2 and D2 on Cu(111): The Role of Surface Temperature and Evidence for Corrugation of the Dissociation Barrier. J. Chem. Phys. 1998, 108 (10), 4199–4211. https://doi.org/10.1063/1.475818.

- (312) Kaufmann, S.; Shuai, Q.; Auerbach, D. J.; Schwarzer, D.; Wodtke, A. M. Associative Desorption of Hydrogen Isotopologues from Copper Surfaces: Characterization of Two Reaction Mechanisms. J. Chem. Phys. 2018, 148 (19), 194703. https://doi.org/10.1063/1.5025666.
- (313) Habraken, F. H. P. M.; Kieffer, E. P.; Bootsma, G. A. A Study of the Kinetics of the Interactions of O2 and N2O with a Cu(111) Surface and of the Reaction of CO with Adsorbed Oxygen Using Aes, LEED and Ellipsometry. *Surf. Sci.* **1979**, *83* (1), 45–59. https://doi.org/10.1016/0039-6028(79)90479-5.
- (314) JUNELL, P.; AHONEN, M.; HIRSIMÄKI, M.; VALDEN, M. INFLUENCE OF SURFACE MODIFICATION ON THE ADSORPTION DYNAMICS OF O 2 ON Cu {100}. Surf. Rev. Lett. **2004**, *11* (04n05), 457–461. https://doi.org/10.1142/S0218625X0400627X.
- (315) Hodgson, A.; Lewin, A. K.; Nesbitt, A. Dissociative Chemisorption of O2 on Cu(110). *Surf. Sci.* **1993**, *293* (3), 211–226. https://doi.org/10.1016/0039-6028(93)90315-B.
- (316) Zhu, L.; Zhang, Y.; Zhang, L.; Zhou, X.; Jiang, B. Unified and Transferable Description of Dynamics of H 2 Dissociative Adsorption on Multiple Copper Surfaces via Machine Learning. Phys. Chem. Chem. Phys. 2020, 22 (25), 13958–13964. https://doi.org/10.1039/DOCP02291H.
- (317) Galparsoro, O.; Kaufmann, S.; Auerbach, D. J.; Kandratsenka, A.; Wodtke, A. M. First Principles Rates for Surface Chemistry Employing Exact Transition State Theory: Application to Recombinative Desorption of Hydrogen from Cu(111). *Phys. Chem. Chem. Phys.* 2020, 22 (31), 17532–17539. https://doi.org/10.1039/D0CP02858D.
- (318) Martin-Gondre, L.; Crespos, C.; Larrégaray, P. Dynamics of Dissociative Chemisorption of O2 on Cu(100) Surface: A Theoretical Study. Surf. Sci. 2019, 688, 45–50. https://doi.org/10.1016/j.susc.2019.05.006.
- (319) Ramos, M.; Díaz, C.; Martínez, A. E.; Busnengo, H. F.; Martín, F. Dissociative and Non-Dissociative Adsorption of O 2 on Cu(111) and Cu ML /Ru(0001) Surfaces: Adiabaticity Takes Over. Phys. Chem. Chem. Phys. 2017, 19 (16), 10217–10221. https://doi.org/10.1039/C7CP00753A.
- (320) Fallaque, J. G.; Ramos, M.; Busnengo, H. F.; Martín, F.; Díaz, C. Normal and Off-Normal Incidence Dissociative Dynamics of O 2 (v, J) on Ultrathin Cu Films Grown on Ru(0001). Phys. Chem. Chem. Phys. 2021, 23 (13), 7768–7776. https://doi.org/10.1039/D0CP03979A.
- (321) Mondal, A.; Wijzenbroek, M.; Bonfanti, M.; Díaz, C.; Kroes, G. J. Thermal Lattice Expansion Effect on Reactive Scattering of H2 from Cu(111) at Ts = 925 K. *J. Phys. Chem. A* 2013, 117 (36), 8770–8781. https://doi.org/10.1021/jp4042183.
- (322) Sueyoshi, T.; Sasaki, T.; Iwasawa, Y. Molecular and Atomic Adsorption States of Oxygen on Cu(111) at 100–300 K. Surf. Sci. 1996, 365 (2), 310–318. https://doi.org/10.1016/0039-6028(96)00738-8.
- (323) Xu, Y.; Mavrikakis, M. Adsorption and Dissociation of O2 on Cu(111): Thermochemistry, Reaction Barrier and the Effect of Strain. Surf. Sci. 2001, 494 (2), 131–144. https://doi.org/10.1016/S0039-6028(01)01464-9.
- (324) Minniti, M.; Farías, D.; Perna, P.; Miranda, R. Enhanced Selectivity towards O2 and H2 Dissociation on Ultrathin Cu Films on Ru(0001). J. Chem. Phys. 2012, 137 (7), 074706. https://doi.org/10.1063/1.4746942.
- (325) Zhang, D.; Jansen, C.; Kleyn, A. W.; Juurlink, L. B. F. Adsorption Dynamics of O 2 on Cu(111): A Supersonic Molecular Beam Study. *Phys. Chem. Chem. Phys.* **2023**, *25* (21), 14862–14868. https://doi.org/10.1039/D3CP01215H.
- (326) Hall, J.; Saksager, O.; Chorkendorff, I. Dissociative Chemisorption of O2 on Cu(100). Effects of Mechanical Energy Transfer and Recoil. *Chem. Phys. Lett.* **1993**, *216* (3–6), 413–417. https://doi.org/10.1016/0009-2614(93)90119-L.

- (327) Busnengo, H. F.; Di Césare, M. A.; Dong, W.; Salin, A. Surface Temperature Effects in Dynamic Trapping Mediated Adsorption of Light Molecules on Metal Surfaces: H2 on Pd(111) and Pd(110). Phys. Rev. B 2005, 72 (12), 125411. https://doi.org/10.1103/PhysRevB.72.125411.
- (328) Zhang, Y.; Yang, W. A Challenge for Density Functionals: Self-Interaction Error Increases for Systems with a Noninteger Number of Electrons. J. Chem. Phys. 1998, 109 (7), 2604– 2608. https://doi.org/10.1063/1.476859.
- (329) Lynch, B. J.; Fast, P. L.; Harris, M.; Truhlar, D. G. Adiabatic Connection for Kinetics. J. Phys. Chem. A 2000, 104 (21), 4811–4815. https://doi.org/10.1021/jp000497z.
- (330) Chae, K. H.; Lu, H. C.; Gustafsson, T. Medium-Energy Ion-Scattering Study of the Temperature Dependence of the Structure of Cu(111). *Phys. Rev. B* **1996**, *54* (19), 14082–14086. https://doi.org/10.1103/PhysRevB.54.14082.
- (331) Wu, L. Y.; Roman, M. J.; Heazlewood, B. R.; Kurahashi, M. Steric Effects in the Adsorption of O 2 on a Cu(111) Surface. Phys. Chem. Chem. Phys. 2025. https://doi.org/10.1039/D4CP04595E.
- (332) Taleb, A. Al; Schiller, F.; Vyalikh, D. V.; María Pérez, J.; Auras, S. V.; Farías, D.; Ortega, J. E. Simulating High-Pressure Surface Reactions with Molecular Beams. *Phys. Chem. Chem. Phys.* **2023**, *26* (3), 1770–1776. https://doi.org/10.1039/d3cp05071h.
- (333) Zhou, Y.; Zhou, L.; Hu, X.; Xie, D. Dynamics Studies of O 2 Collision on Pt(111) Using a Global Potential Energy Surface. J. Phys. Chem. C 2020, 124 (19), 10573–10583. https://doi.org/10.1021/acs.jpcc.0c01247.
- (334) Goikoetxea, I.; Juaristi, J. I.; Alducin, M.; Díez Muiño, R. Dissipative Effects in the Dynamics of N 2 on Tungsten Surfaces. *J. Phys. Condens. Matter* **2009**, *21* (26), 264007. https://doi.org/10.1088/0953-8984/21/26/264007.
- (335) Hand, M.; Harris, J. Recoil Effects in Surface Dissociation. *J. Chem. Phys.* **1990**, *92* (12), 7610–7617. https://doi.org/10.1063/1.458198.
- (336) Behler, J.; Parrinello, M. Generalized Neural-Network Representation of High-Dimensional Potential-Energy Surfaces. *Phys. Rev. Lett.* 2007, 98 (14), 146401. https://doi.org/10.1103/PhysRevLett.98.146401.
- (337) Behler, J. Perspective: Machine Learning Potentials for Atomistic Simulations. *J. Chem. Phys.* **2016**, *145* (17), 170901. https://doi.org/10.1063/1.4966192.
- (338) Piessens, R.; de Doncker-Kapenga, E.; Überhuber, C. W.; Kahaner, D. K. *Quadpack*; Springer Series in Computational Mathematics; Springer Berlin Heidelberg: Berlin, Heidelberg, **1983**; Vol. 1. https://doi.org/10.1007/978-3-642-61786-7.

# List of abbreviations, acronyms, and symbols

A list of abbreviations, acronyms, and symbols commonly used in the thesis:

AES: Auger electron spectroscopy
AIMD: Ab initio molecular dynamics

BOA: Born-Oppenheimer approximation
BOMD: Born-Oppenheimer molecular dynamics
BOSS: Born-Oppenheimer static surface

**BuSA**: Burlisch–Stoer algorithm

**CRP**: Corrugation reducing procedure

**COM**: Centre-of-mass

DC:Dissociative chemisorptionDCM:Dynamic corrugation model

**DF**: Density functional

**DFT**: Density functional theory **DOF**: Degrees of freedom

**EA**: Electron affinity

 $E_{av}$ : Average energy of the molecular beam

Ecr:Charge transfer energy;  $\phi$  - EAECW:Embedded correlated wavefunctionEHF:Hartree Fock exchange energy

**Ehp**: Electron-hole-pair **E**<sub>i</sub>: Incidence energy

 $\mathbf{E}_{L}^{\perp}$ : Normal incidence energy

 Ekin:
 Kinetic energy

 Ero:
 Rotational energy

 Erovib:
 Rovibrational energy

 $E_s$ : Stream energy of the molecular beam

E<sub>vib</sub>: Vibrational energy

**E**xchange-correlation energy

**FCC**: Face-centred cubic **FFT**: Fast-Fourier transform

**GGA**: Generalised gradient approximation **GLO**: Generalised Langevin oscillator

**HDNN**: High dimensional neural-network

**HK**: Hohenberg-Kohn **HF**: Hartree-Fock

**HREELS**: High-resolution electron energy loss spectroscopy

K&W: King & Wells KS: Kohn-Sham

LDA: Local density approximation
LEED: Low energy electron diffraction

MD: Molecular dynamics

mGGA: Meta-generalised gradient approximation

N: Normal orientation;  $\theta = 0^{\circ}$ NSCF: Non-self-consistent field NES: Normal energy scaling

P:Parallel orientation;  $θ = 90^\circ$ PAW:Projector augmented wavePBC:Periodic Boundary Conditions

P<sub>E</sub>: Event probability PES: Potential energy surface Pr: Reaction probability  $P_r^D$ : Direct reaction probability  $P_r!$ Indirect reaction probability  $P_r^T$ : Total reaction probability Scattering probability  $P_s$ :  $P_t$ : Trapping probability

QCT: Quasi-classical trajectory
QD: Quantum dynamics

**Ref**.: Reference

RMSE: Root mean squared error

 $S_0$ :Sticking probability;  $1 - P_s$ SCF:Self-consistent fieldSCM:Static corrugation model $S_H$ : $S_0$  of helicoptering molecules $S_P$ : $S_0$  of perpendicular molecules

**T**: Tilted orientation;  $\theta = 45^{\circ}$ 

T<sub>N</sub>: Nozzle temperature
 TOF: Time-of-flight
 T<sub>s</sub>: Surface temperature
 TS: Transitions state

VASP: Vienna Ab Initio Simulation Package
Vav: Average velocity of the molecular beam

VdW: Van der Waals

 $V_s$ : Stream velocity of the molecular beam

XC: Exchange-correlation
XPS: X-ray photon spectroscopy

**ZPE**: Zero-point energy

 $\Delta E_s$ : Distribution width of the energy of the molecular beam  $\Delta V_s$ : Distribution width of the velocity of the molecular beam

**Θ**: Incidence angle of the molecular beam

φ: Work function

#### Samenvatting

Naar een juiste beschrijving van elektronen in  $O_2$  op metaalsystemen

Katalyse is een uiterst belangrijk proces binnen de chemie. Door de toevoeging van kleine hoeveelheden katalysator kan een chemische reactiesnelheid met meerdere orders van grootte toenemen. Dit gebeurt zonder dat de katalysator verbruikt of verloren gaat. Hierdoor speelt katalyse niet alleen een cruciale rol bij veel chemisch industriële toepassingen maar is het ook de drijvende motor achter de chemie van het leven. Een katalysator werkt omdat de stabiliteit van tussenproducten in de chemische reactie geoptimaliseerd wordt, waardoor een efficiënter reactiepad beschikbaar komt. Na de omvorming van dit tussenproduct tot het eindproduct wordt de katalysator vervolgens idealiter volledig geregenereerd. Hierdoor is de katalysator snel beschikbaar om de volgende reactie te versnellen. Over het algemeen kan katalyse in drie verschillende categorieën ingedeeld worden: homogene katalyse, biokatalyse en heterogene katalyse. In dit proefschrift ligt de aandacht volledig bij de heterogene katalyse

Bij heterogene katalyse zit er een faseverschil tussen enerzijds reactanten en producten en anderzijds de katalysator. Dat wil zeggen dat de reactanten en producten meestal vloeibaar of gasvormig zijn en de katalysator meestal wordt toegevoegd als vaste stof. Het voordeel hiervan is dat de katalysator en reactieproducten makkelijk van elkaar te scheiden zijn, wat erg aantrekkelijk is voor industriële toepassingen. Het nadeel is dat er minder efficiënte menging plaatsvindt tussen katalysator en reactanten, wat op zijn beurt de efficiëntie van de katalysator nadelig kan beïnvloeden. Desalniettemin wordt heterogene katalyse op massale schaal in de chemische industrie toegepast en verbetering van het katalytische proces kan tot aanzienlijke verbetering van de efficiëntie van chemische processen leiden of zelfs deuren openen naar hele nieuwe chemische reacties die cruciaal kunnen worden voor bijvoorbeeld de huidige energietransitie.

Verbeteringen van de heterogene katalyse worden echter veelal nog op een proefondervindelijke basis uitgevoerd. Dit komt omdat een heterogeen katalytische proces een complex netwerk vormt van chemische reactiestappen die allemaal van de chemische omgeving, temperatuur, druk en toestand van de katalysator af zullen hangen. Het zou ideaal zijn als verbeteringen van katalysatoren of het vinden van nieuwe katalysatoren juist geleid zou kunnen worden door fundamentele inzichten in de samenhang van al deze variabelen. Daarom is er grote wetenschappelijke baat bij het doorgronden van onder andere de elementaire chemische reacties die plaats vinden, de samenhang van die verschillende stappen, en de effecten van externe factoren op diezelfde stappen. Om deze kwesties beter te kunnen doorgronden en tot nieuwe inzichten te komen, worden er in de heterogene katalyse twee keer verschillende velden uitgesplitst.

De eerste splitsing betreft de tweesprong tussen het bestuderen van de katalysator onder industriële condities (ook wel *in situ* genoemd) en het bestuderen van de componenten van de katalytische reactie in een zo gecontroleerd mogelijke omgeving (veelal oppervlaktechemie genoemd). Hierna volgt voor beide velden de tweede splitsing, beide onderzoeksvelden kunnen namelijk uitgevoerd worden door middel van experimenten of op basis van theorie en simulaties. Voor dit proefschrift geld voor beide splitsingen de laatste keuze. Dat wil zeggen dat dit proefschrift gaat over de theoretische oppervlaktechemie van heterogene katalyse.

In **Hoofdstuk 1** van dit proefschrift wordt de oppervlaktechemie breed, vanuit zowel de experimentele als theoretische kant, toegelicht. In het kort gaat het binnen de oppervlaktechemie erom dat de onderzoeker volledige, of zo volledig mogelijke, controle heeft over alle variabelen die van invloed kunnen zijn op de reactie. Hierdoor kan de onderzoeker vervolgens zo precies mogelijk observeren wat de invloeden van deze variabelen zijn. Zowel voor experimentele als theoretische onderzoeken wordt de katalysator gereduceerd tot een versimpelde vorm van zijn actieve component, dat wil zeggen de component die zorgt voor de versnelling van chemische reactie. Deze actieve component is meestal een metaal, waarbij het belangrijk is dat het oppervlak van dit metaal zeer goed gedefinieerd is en weinig van de perfecte vorm af zal wijken. Hierdoor

kan de invloed van de oppervlakstructuur bepaald worden, en kunnen de vormen van interactie tussen de reactanten en het metaaloppervlak onderzocht worden.

Om het oppervlak, de reactanten, en de reactiecondities zo goed mogelijk te definiëren werkt de experimentele oppervlaktechemie veelal in ultrahoog vacuüm (UHV) condities, zodat er zo weinig mogelijk interacties van moleculen, anders dan de reactanten, met het metaal kunnen plaats vinden. Ook moeten de toestanden van de reactanten zo exact mogelijk bepaald worden door middel van bijvoorbeeld moleculaire bundelexperimenten. Vervolgens moet de reactie of het reactieproduct zeer gedetailleerd gemeten kunnen worden, waarvoor verschillende experimentele technieken beschikbaar zijn. Voor dit proefschrift is het zogenaamde King en Wells (K&W) experiment het belangrijkste type meting. In een K&W experiment wordt een moleculaire gas bundel op een metaaloppervlak afgeschoten en door middel van strategisch in de tijd gescheiden onderbrekingen van deze bundel kan de kans dat de moleculen blijven plakken op het oppervlakte (de plakkans, *So*), direct worden gemeten.

De gemeten  $S_0$  kan door de theoretische oppervlaktechemie bepaald worden door middel van moleculaire dynamica (MD) berekeningen. In een dergelijke simulatie kunnen de omstandigheden namelijk goed gedefinieerd worden omdat het voor theoretisch chemici makkelijk is om de reactiecondities te controleren. Een belangrijk punt voor de theoretische chemie is echter de afweging tussen de nauwkeurigheid van de berekening en de hoeveelheid rekenkracht die nodig is om een simulatie uit te kunnen voeren. Meer rekenkracht kost namelijk meer tijd, energie en geld. In principe zijn de kwantummechanische postulaten zodanig bekend dat deze toegepast en doorgerekend kunnen worden om de chemie volledig te kunnen simuleren. Echter, de hoeveelheid rekenkracht die beschikbaar is voor zo'n simulatie is niet genoeg om dat op meer dan zeer kleine schaal te kunnen doen. Daarom moet er in de theoretische chemie, en ook voor dit proefschrift, een balans gezocht worden tussen de hoeveelheid rekenkracht die we besteden en het zo nauwkeurig mogelijk maken van de chemische simulatie.

In Hoofdstuk 2 worden de onderliggende basis onderdelen en theorieën van moderne chemische simulatietechnieken behandeld. Voor theoretische oppervlaktechemie wordt er in veel, maar niet alle, simulaties uit gegaan van een, op de massa van de deeltjes gebaseerde, scheiding van variabelen, ofwel de zogenaamde Born-Oppenheimer benadering (BOB). Kort geschreven, is het door het massaverschil tussen de elektronen en atoomkernen mogelijk om de energie van de elektronen te ontkoppelen van de beweging van de atoomkernen. Dit maakt de reactiesimulaties makkelijker omdat de kernen dan los van de elektronen behandeld kunnen worden en veelal kunnen de bewegingsvergelijken van de kernen zelfs met klassieke baanberekeningen of quasi-klassieke baanberekeningen (QKB) opgelost worden. Dit betekent dat de gecompliceerde kwantummechanica alleen gebruikt hoeft te worden voor het beschrijven van de elektronen in het system. De oplossing van het elektronische systeem kan vervolgens gebruikt worden als een potentieel energie-oppervlak (PEO) om zo de krachten op de atoomkernen uit te rekenen.

In het veld van de oppervlaktechemie is de dichtheidsfunctionaaltheorie (DFT) de meest gebruikte methode om de elektronenstructuur te berekenen. In deze theorie worden de elektronen niet als afzonderlijke eenheden behandeld, maar wordt er gekeken naar de elektronendichtheid van het systeem. Met het werk van Hohenberg en Kohn (HK) is bewezen dat er een directe relatie moet bestaan tussen de golffunctie, de energieoperator van de elektronen in het systeem en de dichtheid van de elektronen, echter is niet bewezen of bekend wat deze relatie is. Daarom zijn er aannames nodig in de manier waarop zowel de elektronendichtheid als de energie uit die elektronendichtheid berekend kunnen worden. werk van het onderzoek binnen de Veel theoretische oppervlaktechemie is dan ook gericht op het correct afstellen van de aannames binnen de DFT, zo als ook in dit proefschrift.

Met behulp van het werk van Kohn en Sham (KS) is het mogelijk om de fouten binnen de aannames van DFT te reduceren tot een klein deel van onbekenden binnen de dichtheidsfunctionaal (DF). Het deel van onbekenden wordt ook wel de uitwisseling-en-correlatie-dichtheidsfunctionaal (UC-DF) genoemd, en meestal als men spreekt over de details van de DF, spreekt men over de UC-DF. Binnen de oppervlaktechemie is de vorm van de gegeneraliseerde gradiënt

benadering (GGB) op de UC-DF veelal het beste compromis gebleken. In deze benadering hangt de UC-DF af van een lokale dichtheidsbeschrijving alsmede van de eerste lokale afgeleide van de dichtheid. GGB is in staat om de elektronen in het oppervlak van het metaal goed te beschrijven en kan meestal de elektronen in de overgangstoestand van de reactanten ook goed genoeg beschrijven. Hierdoor kan op basis van door GGB beschreven elektronen een PEO gemaakt worden waarmee QKB berekeningen uit te voeren zijn die voor veel systemen de experimentele  $S_0$  tot chemische nauwkeurigheid ( $\pm 1 \, kcal/mol$ ) kunnen benaderen met behulp van een semi-empirische DF.

Alhoewel de GGB voor veel molecuul-metaal systemen succesvol lijkt, blijken er echter een aantal molecuul-metaal systemen te zijn waarvoor het niet mogelijk is om op basis van de GGB nauwkeurige reactiekansen ( $S_0$ ) te berekenen. Recent onderzoek suggereert dat de GGB zal falen voor systemen waarin de ladingsoverdrachtsenergie ( $E_{LO}$ ) kleiner is dan  $7 \, eV$ .  $E_{LO}$  wordt gedefinieerd als de uittreearbeid van het metaaloppervlak min de elektronenaffiniteit van het molecuul. De waarde van  $E_{LO}$  geeft een beeld van de waarschijnlijkheid dat ladingsoverdracht van het metaal naar het molecuul zal optreden tijdens de reactieve verstrooiing van het molecuul aan het metaaloppervlak. Voorbeelden van systemen met een  $E_{LO}$  lager dan  $7 \, eV$  die in dit proefschrift worden behandeld zijn  $O_2 + Al(111)$  en  $O_2 + Cu(111)$ .

 $O_2$  + Al(111) is al langere tijd een systeem met een voorbeeldfunctie voor de geactiveerde dissociatieve chemisorptie (DC) van  $O_2$  op metalen. Er is echter nog geen enkel werk op basis van DFT geweest dat de DC van  $O_2$  op Al(111) binnen chemische nauwkeurigheid heeft kunnen berekenen. Sterker nog, de meeste QKB berekeningen op basis van GGB DFT voorspellen dat de reactiekans onafhankelijk van de energie van het  $O_2$  molecuul altijd gelijk zal zijn aan één. Dit is in tegenstelling tot de experimenten die wel degelijk een afhankelijkheid van  $S_0$  van de invalsenergie ( $E_i$ ) observeren. De aanname is dat dit falen van de GGB komt door de hierboven genoemde reden ( $E_{LO} < 7 \ eV$ ). Ook is gebleken dat de meta-GGB (mGGB) benadering van DFT, waarin ook de tweede afgeleiden van de elektronendichtheid worden meegenomen, niet heel veel beter presteert. Echter is er bij het gebruik van mGGB in ieder geval wel sprake van een

geactiveerde reactie, dat wil zeggen er is een zekere afhankelijkheid van  $E_i$ , en de  $S_0$  is niet gelijk aan één bij lage  $E_i$ .

Voor het  $O_2$  + Cu(111) systeem hebben theoretische simulaties met het gebruik van verschillende GGB gebaseerde rekenmethodes de gemeten reactiekansen altijd overschat. Er blijft bij dit systeem echter ook nog extra onduidelijkheid aangezien verschillende experimenten geen consensus bereiken over de  $E_i$  afhankelijke reactiekans en er heerst onduidelijkheid over de onderliggende reactiemechanismes. Het is voor dit systeem dus ook zeer belangrijk dat de theorie deze reactie nauwkeurig kan gaan simuleren zodat er uitsluitsel gegeven kan worden over zowel de geactiveerde reactiekansen als de onderliggende mechanismes.

Uiteindelijk hebben onderzoeken voorgaand aan dit proefschrift beide systemen dus nooit kunnen beschrijven, waarschijnlijk omdat de eerder binnen de oppervlaktechemie gebruikte DFT methodes niet in staat blijken om dit soort  $E_{LO}$ < 7 eV systemen te beschrijven. Een deel van de voorgaande onderzoeken suggereren wel dat er mogelijke oplossingen voor dit probleem gevonden kunnen worden binnen de DFT. Voor O2 + Al(111) heeft werk met een afgeschermde hybride DF een semi-kwantitatieve overeenkomst met de experimentele S<sub>0</sub> kunnen bereiken voor energieën dicht bij de drempelwaarde van de reactiekans. Bij een hybride DF wordt er een fractie van de exacte uitwisselingsenergie, ofwel Hartree-Fock (HF) uitwisselingsenergie, bij de UC-DF van een GGB (of mogelijk mGGB) DF gemengd. Hiermee wordt de uitwisselingsenergie beter beschreven en kan er ook gecorrigeerd worden voor mogelijk zelfinteractiefouten die plaats kunnen vinden bij gebruik van een GGB DF. Het idee is dat deze hybride DFs, net zoals voor gasfasereacties, de reactiebarrières daardoor beter kunnen beschrijven en de fout in de beschrijving van experimentele plakkansen verminderd wordt. Het is echter bij metaaloppervlakken wel belangrijk dat de elektronenuitwisseling op lange afstand afgeschermd wordt, en daarom wordt in het algemeen een afgeschermde hybride DF gebruikt voor de interacties van een molecuul met een metaaloppervlak.

Op dit moment is het gebruik van (afgeschermde) hybride DFen voor molecuulmetal reacties nog niet een grondig geteste methode. Alhoewel de resultaten van voorgaand onderzoek al een substantiële verbetering in de beschrijving van de  $O_2$  + Al(111) reactie opleveren zijn aan deze berekeningen ook meer (twee orders van grootte meer) rekentijd en rekenkosten verbonden. Ook is de beschrijving van de  $O_2$  + Al(111) reactie nog niet chemisch nauwkeurig. In dit proefschrift wordt er gekeken naar mogelijkheden om zowel de benodigde rekenkracht te verminderen als naar mogelijkheden om de UC-DF verder te verbeteren en zodoende een hogere nauwkeurigheid in de beschrijving van de  $O_2$  + Al(111) en  $O_2$  + Cu(111) systemen te bereiken.

In Hoofdstuk 3 wordt nieuw onderzoek gepresenteerd naar de mogelijkheden om een niet-zelfconsistent-veld (NZCV) berekening uit te voeren aan O<sub>2</sub> + Al(111) met een afgeschermde hybride DF. Met deze methode wordt een afgeschermde hybride DFT energie berkend door middel van een correctie die wordt bepaald op basis van een enkele berekening aan de elektronendichtheid, die op zijn beurt berekend is met een zelfconsistent-veld (ZCV) GGB berekening. De nauwkeurigheid van deze NZCV methode wordt onderzocht aan de hand van de HSE03-1/3x@RPBE DF. Met andere woorden, een NZCV HSE03 hybride DF met een fractie van 1/3 HF uitwisselingsenergie wordt toegepast op een ZCV RPBE elektronen dichtheid. Uit deze berekeningen wordt door middel van de Born-Oppenheimer statisch oppervlak (BOSO) benadering een PEO opgebouwd en geïnterpoleerd door middel van de golvingsreductieprocedure (GRP). Met het hieruit volgende PEO worden vervolgens de QKB berekeningen die zijn uitgevoerd voor de ZCV HSE03-1/3x berekeningen gereproduceerd. De QKB resultaten laten zien dat de NZCV methode de ZCV resultaten tot binnen 2 kcal/mol, dat wil zeggen bijna met chemische nauwkeurigheid, kunnen reproduceren. Alhoewel volledige overeenstemming eleganter geweest zou zijn, suggereren de resultaten wel dat de NZCV methode mogelijk een nuttige methode zou kunnen zijn om verkennend onderzoek te doen voor systemen waarbij het gebruik van de ZCV methode veel rekenkracht kost.

Een analyse van het PEO in **Hoofdstuk 3** laat zien waarom er een verschil in  $S_0$  resultaten tussen de ZCV en NZCV methodes optreedt. De barrières voor reactie op de PEO, zoals brekend met de NZCV methode, hebben namelijk allemaal een

hogere energie. Hierbij liggen enkele barrières in de buurt van de ZCV resultaten, maar sommige juist tientallen kJ/mol hoger. Hierdoor zal de reactiviteit niet alleen afnemen maar zal de  $S_0$  curve ook iets breder uitvallen, wat overeenstemt met de QKB resultaten zoals eerder genoemd. Als laatste is ook het 'gatmodel' gebruikt om de invloed van de dynamica op de reactie te bestuderen. In het gatmodel wordt de reactiekans ingeschat op basis van de interne energie van het molecuul en de complete verzameling van reactiebarrièrehoogtes op het PEO zonder daadwerkelijk dynamica uit te voeren. Niet alleen levert deze methode een mogelijkheid om een schatting te krijgen van reactiekansen zonder QKB berekeningen te doen, deze methode vereist in principe niet een volledige PEO. Dit kan de methode geschikt maken voor verkenden onderzoek met dure DFen. Het gatmodel resulteert in een bredere  $S_0$ -curve, waarbij die curve sterk afhangt van de keuze of de nulpuntsenergie van het molecuul meegenomen mag worden bij het overbruggen van de reactiebarrière. Hierbij moet de nulpuntsenergie voor een deel meegenomen worden om tot de beste overeenstemming te komen met de QKB berekeningen.

In Hoofdstuk 4 wordt voor O<sub>2</sub> + Al(111) vervolgens geprobeerd om de overeenkomst van de  $S_0$  curve met de experimentele resultaten te verbeteren door langeafstand Van der Waals (VdW) correlatie energie mee te nemen in de afgeschermde hybride UC-DF. De hypothese achter het meenemen van nietlokale VdW correlatie energie is dat deze de reactiebarrière afhankelijkheid van de geometrie van het O<sub>2</sub> molecuul doet toenemen, waardoor de verschillende reactiebarrières verder uit elkaar komen te liggen en zo de So curve wordt verbreed, en dus beter met de experimentele curve overeen zal gaan komen. Om dit te testen is in **Hoofdstuk 4** een HSE06-1/2x-VdWDF2 UC-DF toegepast om op basis van de BOSO benadering een PEO uit te rekenen. In tegenstelling tot Hoofdstuk 3 is deze DF dus wel een ZCV DF, heeft het een hogere fractie exacte uitwisselingsenergie en is de Van der Waals DF2 niet-lokale correlatie DF gebruikt. Op basis van de PEO zijn dan wederom QKB berekeningen uitgevoerd. De toevoeging van VdW correlatie energie in de DF heeft er voor gezorgd dat er in de PEO een VdW put ontstaat voor de reactiebarrière, dat wil zeggen, in het entree-kanaal van de reactie. Ook blijken de reactiebarrières met kleine hoeveelheden energie te veranderen ten opzichte van die berekend met de HSE03-1/3x DF. Hierdoor is de afhankelijkheid van de barrière van de geometrie van het molecuul ten opzichte van het oppervlak licht toegenomen, al zijn de meeste veranderingen kleiner dan  $1 \, kcal/mol$ . Uit de QKB berekeningen komt vervolgens ook een ligt verbrede  $S_0$  curve, en daarmee een iets betere overeenstemming met de experimentele curve. De verbetering is echter niet heel groot. De kleine verbetering, voor nog steeds zeer hoge rekenkosten, doet twijfelen aan de mogelijkheden van de BOSO gebaseerde DFT aanpak om de  $O_2$  + Al(111) reactie met hoge nauwkeurigheid te kunnen beschrijven.

Het werk van zowel **Hoofdstuk 3** als **Hoofdstuk 4** suggereert dat de verbreding die nodig lijkt in de  $S_0$  curve alleen door veranderingen in de PEO kan komen als deze veranderingen zeer ingrijpend zullen zijn. Op dit moment is het moeilijk in te zien wat voor veranderingen in de BOSO gebaseerde DFT aanpak nog mogelijk zijn om dit soort ingrijpende veranderingen in de PEO tot stand te brengen, in het besef dat geavanceerdere UC-DF vormen naar waarschijnlijkheid (vooralsnog) te hoge rekenkosten met zich mee zullen brengen. Het is op basis van dit proefschrift dan ook voor de toekomst aan te raden eerst te kijken naar de effecten die de BOSO benadering heeft op de reactie van  $O_2 + Al(111)$  voordat wederom een nieuwe, dure, UC-DF geprobeerd wordt. Er kan bijvoorbeeld gekeken worden naar het effect van de beweging van de Al atomen in het oppervlak, naar elektron-gat-paar excitaties van elektronen in het Al oppervlak, of naar andere effecten die door het BOSO model uitgesloten worden.

Als laatste wordt in **Hoofdstuk 5** gekeken naar de effecten van diezelfde, dat wil zeggen, HSE06-1/2x-VdWDF2, UC-DF op de beschrijving van de  $O_2$  + Cu(111) DC reactie. Wederom is hiervoor een op de GRP gebaseerde PEO opgezet, waarna QKB berekeningen zijn uitgevoerd om de kwaliteit van de DF te testen ten opzichte van andere theoretische maatstaven en de verschillende experimentele resultaten. De resultaten laten zien dat de  $S_0$  curve, berekend met deze DF, de experimentele reactiekansen onderschat. Dit is, voor zover bekend, de eerste keer dat theoretische resultaten de plakkansen van  $O_2$  op Cu(111) onderschatten in plaats van overschatten. Alhoewel het reproduceren van de experimentele resultaten een nog beter resultaat geweest zou zijn doet dit resultaat wel suggereren dat er in ieder geval een hybride VdW DF moet bestaan die de experimentele  $S_0$  curve met hoge nauwkeurigheid kan reproduceren. Daarbij laten de resultaten ook bewijs zien dat sprake lijkt van zowel directe als indirecte

DC.  $O_2$  moleculen met lage  $E_i$  lijken te reageren via een indirect mechanisme. Het molecuul blijft in een indirect mechanisme eerst in moleculaire vorm op het Cu(111) oppervlakte hangen, waarna het pas na enkele botsingen tot volledige dissociatie overgaat. Bij toenemende  $E_i$  neemt de indirecte reactiekans initieel toe tot een maximum bereikt is, waarna de indirecte reactiekans weer afneemt. De kans op directe DC blijft met hogere  $E_i$  wel verder toenemen waardoor er een plateau optreedt in de totale berekende  $S_0$  curve. De effecten van deze mechanismes en uitsluitsel ten aanzien van de discussie over deze mechanismes tussen experimentatoren kunnen pas echt begrepen en verkregen worden als de effecten van oppervlakteatoombewegingen en oppervlaktetemperatuur in een toekomstig model daadwerkelijk worden meegenomen.

Al met al resulteert het gebruik van een afgeschermde hybride-VdW UC-DF in een verbetering voor de beschrijving van molecuul-metaal reacties met  $E_{LO} < 7$ eV. Hierbij lijkt het mogelijk om in de toekomst tot een DF te komen die de O<sub>2</sub> + Cu(111) reactie met hoge nauwkeurigheid kan beschrijven. Vervolgens zou een DF dan door middel van nieuwe technieken die verder gaan dan de BOSO benadering eindelijk uitsluitsel kunnen geven in de discussie over de bestaande mechanismes die van toepassing zijn op de reactie. Vooralsnog lijkt de kans echter wel klein dat een BOSO gebaseerde DFT methode ook in staat zal zijn om de reactie van O<sub>2</sub> met Al(111) met hoge nauwkeurigheid te beschrijven. Ook blijft de benodigde rekenkracht voor het toepassen van afgeschermde hybride berekeningen een probleem dat verholpen zal moeten worden als deze methode op grotere schaal toegepast moet worden. Alhoewel de NZCV methode hierin kan helpen om een voorselectie te maken van UC-DFen, lijkt het vooralsnog niet als een-op-een vervanging voor ZCV berekeningen gebruikt te kunnen worden, waardoor het probleem van de hoge rekeneisen voor een PEO nog niet direct verholpen kunnen worden.

## Lijst van Nederlandstalige afkortingen, acroniemen en symbolen

Lijst van afkortingen, acroniemen en symbolen die in het Nederlands anders zijn dan in het Engels. De andere afkortingen zijn in het Engels en Nederlands hetzelfde. Zie 'List of abbreviations, acronyms, and symbols' voor diezelfde afkortingen.

**BOB**: Born-Oppenheimer benadering

**BOSO**: Born-Oppenheimer statisch oppervlakte

 $E_{LO}$ : Ladingsoverdrachtenergie

**GGB**: Gegeneraliseerde gradiënt benadering

**GRP**: Golvingsreductieprocedure

mGGB: Meta-GGB

NZCV: Niet-zelfconsistent-veld
PEO: Potentieel energie-oppervlak
QKB: Quasi-klassieke baanberekeningen

**UC-DF**: Uitwisseling-en-correlatie dichtheidsfunctionaal

**ZCV**: Zelfconsistent-veld

### Curriculum vitae

Robert A. B. van Bree is geboren op 25 juni 1997 te Haarlem. Op 11 juni 2015 heeft hij zijn VWO diploma gehaald aan het Rijnlands Lyceum Oegstgeest in Oegstgeest. In datzelfde jaar is hij begonnen aan de Bachelor opleiding Molecular Science and Technology aan zowel de Universiteit Leiden als de TU Delft. In de Bachelor heeft hij zijn BSc. verslag geschreven over onderzoek aan experimentele oppervlaktechemie gedaan bij dr. Ludo B. F. Juurlink en dr. Sabine V. Auras in de groep "Catalysis and Surface Chemistry", aan de Universiteit Leiden. Op 31 juli 2018 heeft hij deze opleiding Cum Laude afgerond en is direct daarna begonnen aan zijn Master opleiding "Chemistry" aan de Universiteit Leiden. Tijdens deze opleiding heeft hij een literatuuronderzoek gedaan betreffende de elektrolyse van zeewater onder begeleiding van prof. dr. Marc T. M. Koper bij "Catalysis and Surface Chemistry". Zijn MSc. verslag betrof het fitten van een analytisch EAM model voor Cu(111), het onderzoek is gedaan en het verslag geschreven onder begeleiding van dr. Mark F. Somers en dr. Bauke Smits in de Theoretische Chemiegroep aan de Universiteit Leiden. Het MSc. diploma heeft hij op 30 oktober 2020 Cum Laude behaald. Per 1 November 2020 is hij begonnen aan zijn promotieonderzoek onder begeleiding van prof. dr. Geert-Jan Kroes in dezelfde Theoretische Chemiegroep. Dat onderzoek resulteerde in het proefschrift wat u hier nu leest. Tijdens deze promotie heeft hij in 2022 meegedaan aan de Han-Sur-Lesse winterschool voor theorie en spectroscopie in Han-Sur-Lesse, België. Ook heeft hij op 20 april 2023 de cursus 'scientific conduct' afgerond bij de 'Graduate School of Science'. Ook was Robert plenaire spreker bij het 2023 HRSMC symposium in Leiden en heeft hij wetenschappelijke posters gepresenteerd op o.a. het CHAINS congres van 2022 in Veldhoven, het HRSMC symposium van 2022 in Amsterdam, en op de Faraday Discussions over 'New Directions in Molecular Scattering' van 2024 in Edinburgh, VK. Daarnaast heeft hij ook deelgenomen aan de "High Dimensional Quantum Dynamics" conferentie en workshop van 2022 in Groningen en de N3C conferentie van 2022 in Noordwijkerhout. Na het promotieonderzoek is Robert per 1 juni 2025 verder gegaan bij de Luchtverkeersleiding Nederland (LVNL) als Product Engineer.

Robert A. B. van Bree was born on the 25<sup>th</sup> of June 1997 in Haarlem, the Netherlands. He graduated high school (VWO) on the 11th of June 2015 at the Rijnlands Lyceum Oegstgeest in Oegstgeest. In the same year he started his Bachelor of Science Molecular Science and Technology a joint degree program between Leiden University and the TU Delft. During his BSc. he wrote his BSc. thesis in experimental surface science under the supervision of Dr. Ludo B. F. Juurlink and Dr. Sabine V. Auras in the group of Catalysis and Surface Chemistry at Leiden University, and he received his Cum Laude degree on the 31st of July 2018. Thereafter, he immediately started his Masters of Science Chemistry degree at Leiden University. In his MSc. program he wrote a literature research report regarding the electrolysis of seawater under the supervision of Prof. Dr. Marc T. M. Koper, also at the Catalysis and Surface Chemistry group. Additionally, he wrote his MSc. thesis regarding the fitting of analytical EAM models for Cu(111) under the supervision of Dr. Mark F. Somers and Dr. Bauke Smits at the Theoretical Chemistry group at Leiden University. He received his Cum Laude MSc. degree on the 30<sup>th</sup> of October 2020. Quickly thereafter, on the 1<sup>st</sup> of November he started his work as a PhD Student under supervision of Prof. Dr. Geert-Jan Kroes in the same Theoretical Chemistry group. This work has resulted in the thesis that you are reading right now. During his PhD he has also attended the 2022 edition of the Han-Sur-Lesse winter school for theory and spectroscopy in Han-Sur-Lesse, Belgium. On the 20th of April 2023 he completed a course on 'scientific conduct' at the 'Graduate School of Science'. Robert was a plenary speaker at the 2023 HRSMC symposium in Leiden and has presented several scientific posters at events including, but not limited to: CHAINS 2022 at Veldhoven, the HRSMC symposium of 2022 in Amsterdam, and the Faraday Discussions on 'New Directions in Molecular Scattering' in 2024, Edinburgh, UK. Lastly, he also took part in the "High Dimensional Quantum Dynamics" conference and workshop of 2022 in Groningen and the N3C conference of 2022 Noordwijkerhout. After his PhD Robert has started Luchtverkeersleiding Nederland (LVNL) as a Product Engineer on June 1st 2025.

#### List of publications

- van Bree, R. A. B.; Kroes, G. J. Limits of BOSS DFT: O<sub>2</sub> + Al(111) Dynamics on a Screened Hybrid Van der Waals DFT Potential Energy Surface. *J. Phys. Chem. C* 2025, 129 (11), 5408–5421. https://doi.org/10.1021/acs.jpcc.5c00327.
- van Bree, R. A. B.; Kroes, G. J. O<sub>2</sub> Dissociation on Cu(111) Dynamics on a Novel Screened Hybrid Van der Waals DFT Potential Energy Surface. *J. Phys. Chem. C* 2024, 128 (45), 19182–19196. https://doi.org/10.1021/acs.jpcc.4c05466.
- van Bree, R. A. B.; Gerrits, N.; Kroes, G.-J. Dissociative Chemisorption of O<sub>2</sub> on Al(111): Dynamics on a Potential Energy Surface Computed with a Non-Self-Consistent Screened Hybrid Density Functional Approach. *Faraday Discuss.* 2024, 251, 361–381. https://doi.org/10.1039/D3FD00165B.
- Auras, S. V.; van Bree, R. A. B.; Bashlakov, D. L.; van Lent, R.; Juurlink, L. B. F. It's Not Just the Defects a Curved Crystal Study of H<sub>2</sub>O Desorption from Ag. *Phys. Chem. Chem. Phys.* 2019, 21 (28), 15422–15430. https://doi.org/10.1039/C9CP02609F.

#### **Afterword**

In writing these word I am writing what will be the final words of this thesis, and some of the last blank pages that needed to be overcome. The last four and half years have been far from easy, starting a PhD in a time that turned out to be the height of a global pandemic was a demanding task. Thereafter, as some things have gotten better whilst others may have gotten worse, both work and life has continued. As such, this thesis is now being wrapped up, both from the author's and the reader's perspective, but before it does end I would like to (at risk of maybe forgetting some people) say my thanks.

First and foremost, I thank my promoters Prof. Dr. Geert-Jan Kroes and Dr. Jörg Meyer without whom this thesis could never have existed, nor would I have learned to write, analyse and practice science as I now do.

I wish also to thank Dr. Mark Somers, who started out as my mentor during my MSc. in the TC-group and has never let that role go when I moved on to doing a PhD. Neither would my knowledge of HPC, computers, programming, systematism in work, beers, bars, and hiking be what it is without his enthusiasm, guidance and assistance.

Furthermore, I would like to thank all the students who have worked on my many small, preliminary, research projects which were instrumental in showing us the things we should do or more often the things we should *not* do. These students include but are not limited to my BSc. student Floris Löffler, and MSc. students Laura Viaud and Sanne Starmans

I would also like to thank Bauke Smits for first supervising my MSc. degree and then welcoming me as a valued colleague. Additionally, I thank Joan Enrique Romero, Theophile Tchakoua, Lukas Hückmann, Jonathon Cottom, Floris van den Bosch, Brian Ferrari, and Nick Gerrits for the fun and insightful discussions on all things (surface) science. I would also like to thank Carson Mize, with whom the discussions were often more joyful and ridiculous than necessarily insightful. And of course I also thank: Guido Smeets, Paul Spiering, Justina Moss, Thanja

Lamberts, Marten Raaphorst, Darío Barreiro Lage, and the rest of the TC group for the amazing years working among them.

Additionally, I would also like to thank Koen, Laurens, Quintijn, Sjoerd, Ischa, Frair, Teunis, Jasper, Marijn and many more friends who have been with me through the good and the bad times of not just this PhD.

Last but absolutely not least, I would like to greatly thank my family: Carla, Joost, and Mathijs who have always been there for me.